IDŐJÁRÁS

VOLUME 98 * 1994

BUDAPEST, HUNGARY

AUTHOR INDEX

TABLE OF CONTENTS

I. Papers

II. Book review

III. News

Contents of journal Atmospheric Environment, 1994

IV. SUBJECT INDEX

The asterisk denotes book reviews

A

NOTES TO CONTRIBUTORS

The purpose of *Időjárás* is to publish papers in the field of theoretical and applied meteorology. These may be reports on new results of scientific investigations, critical review articles summarizing current problems in certain subject, or shorter contributions dealing with a specific question. Authors may be of any nationality but papers are published only in English.

Papers will be subjected to constructive criticism by unidentified referees.

* * *

The manuscript should meet the following formal requirements:

Title should contain the title of the paper, the names(s) of the author(s) with indication of the name and address of employment.

The title should be followed by an *abstract* containing the aim, method and conclusions of the scientific investigation. After the abstract, the *key-words* of the content of the paper must be given.

Three copies of the manuscript, typed with double space, should be sent to the Editor-in-Chief: *P.O. Box 39, H-1675 Budapest,* Hungary.

References: The text citation should contain the name(s) of the author(s) in Italic letter or underlined and the year of publication. In case of one author: *Miller* (1989), or if the name of the author cannot be fitted into the text: *(Miller,* 1989); in the case of two authors: *Gamov* and *Cleveland* (1973); if there are more than two authors: *Smith et al.* (1990). When referring to several papers published in the same year by the same author, the year of publication should be followed by letters a,b etc. At the end of the paper the list of references should be arranged alphabetically. For an article: the name(s) of author(s) in Italics or underlined, year, title of article, name of journal, volume number (the latter two in Italics or underlined) and pages. E.g. *Nathan, K. K.,* 1986: A note on the relationship between photosynthetically active radiation and cloud amount. *Időjárás 90,* 10-13. For a book: the name(s) of author(s), year, title of the book (all in Italics or underlined with except of the year), publisher and place of publication. E.g. *Junge, C. E.,* 1963: *Air Chemistry and Radioactivity.* Academic Press, New York and London.

Figures should be prepared entirely in black India ink upon transparent paper or copied by a good quality copier. A series of figures should be attached to each copy of the manuscript. The legends of figures should be given on a separate sheet. Photographs of good quality may be provided in black and white.

Tables should be marked by Arabic numbers and provided on separate sheets together with relevant captions. In one table the column number is maximum 13 if possible. One column should not contain more than five characters.

Mathematical formulas and *symbols:* non-Latin letters and hand-written marks should be explained by making marginal notes in pencil.

The final text should be submitted both in manuscript form and on *diskette.* Use standard 3.5" or 5.25" DOS formatted diskettes for this purpose. The following word processors are supported: WordPerfect 5.1, WordPerfect for Windows 5.1, Microsoft Word 5.5, Microsoft Word for Windows 2.0. In all other cases the preferred text format is ASCII.

* * *

Authors receive 30 *reprints* free of charge. Additional reprints may be ordered at the authors' expense when sending back the proofs to the Editorial Office.

Published by the Hungarian Meteorological Service

Budapest, Hungary

INDEX: 26 361

HU ISSN 0324-6329

IDŐJÁRÁS

QUARTERLY JOURNAL
OF THE HUNGARIAN METEOROLOGICAL SERVICE

CONTENTS

VOL. 98 * NO. 1 * JANUARY–MARCH 1994

IDŐJÁRÁS

Quarterly Journal of the Hungarian Meteorological Service

Editorial Office: P.O. Box 39, H–1675 Budapest

Subscription from customers in Hungary should be sent to the Financial Department of the Hungarian Meteorological Service Kitaibel Pál u. 1, 1024 Budapest. The subscription rate is HUF 2000.

Abroad the journal can be purchased from the distributor: KULTURA, P.O. Box 149, H–1389 Budapest. The annual subscription rate is USD 56.

IDŐJÁRÁS

Quarterly Journal of the Hungarian Meteorological Service
Vol. 98, No. 1, January–March 1994

Comparison of initialization methods in a barotropic model

I. Csigó[1] and **G. Radnóti**[2]

[1] *Department of Meteorology, Eötvös Loránd University, Ludovika tér 2, H-1083 Budapest, Hungary*
[2] *Hungarian Meteorological Service, Kitaibel Pál u. 1, H-1024 Budapest, Hungary*

(Manuscript received 10 December 1993; in final form 28 February 1994)

Abstract—This paper discusses the application and comparison of digital filter and nonlinear normal mode initialization within a one- and a two-dimensional barotropic model. The basic ideas of the compared initialization techniques and the short description of the applied models are presented together with some details of implementation.

Experiments made on the two models are discussed. The results prove that the recently developed digital filter initialization technique is an efficient method and can serve as a good alternative of the widely applied nonlinear normal mode initialization.

Key-words: initialization, digital filter, nonlinear normal modes, barotropic model.

1. Introduction

The aim of initialization of a numerical model is to remove spurious high frequency oscillations which could occur during the solution of primitive equation models. Since the first attempts on numerical weather prediction (NWP) numerous methods have been developed for eliminating these inertial-gravity waves (*Bengtsson*, 1975; *Daley*, 1981; *Daley*, 1991). Recently the most widely applied initialization method is the nonlinear normal mode initialization (NNMI), which was firstly introduced by *Machenhauer* (1977), and *Baer* and *Tribbia* (1977). Its relatively cheap computational costs and clear theoretical foundation are good reasons why this method has become almost uniquely used in most operational centers. Nevertheless, among other reasons, the increasing horizontal and vertical resolution, the more and more sophisticated parameterization of physical processes and the variety of vertical discretizations in recent NWP models raise some difficulties with NNMI, which

are mostly related to the stability and convergence of its iterative algorithm, the number and interpretation of initialized vertical modes and the inclusion of diabatic processes within the initialization procedure. A recently developed initialization based on digital filters (*Lynch* and *Huang*, 1992) being free of all these problems is therefore of particular interest. First experiments by the use of digital filter initialization (DFI) carried out in some NWP centres (such as the HIRLAM project of Northern European countries, the ARPEGE/ALADIN project of France and Central-Eastern-European countries, those at the Canadian Meteorological Service and at NOAA/FSL, USA) prove that, besides its extreme simplicity, the method is really efficient in removing gravity wave noises. Present paper intends to provide a short introduction of the method of DFI and to illustrate its effectiveness on a simple barotropic model. As a reference method to this experiment NNMI has been chosen.

2. The method of DFI

The basic idea of DFI is that high frequencies occuring in a time series can be filtered out if coefficients in the Fourier transform corresponding to these frequencies are set to zero and then the modified time series is recomputed by an inverse Fourier transform. This procedure formally means that the $F(\omega)$ Fourier transform of the function $f(t)$ is multiplied by the step function $H(\omega)$, where

$$H(\omega) = \begin{cases} 1, \; if \; |\omega| \leq |\omega_c|; \\ 0, \; if \; |\omega| > |\omega_c|. \end{cases} \tag{1}$$

It follows from the convolution theorem for Fourier series (*Folland*, 1992) that for the filtered function $f^*(t)$

$$f^*(t) = \int_{-\infty}^{\infty} h(\tau) f(t-\tau) \, d\tau \tag{2}$$

holds, where h is the inverse Fourier transform of $H(\omega)$, i.e.

$$h(t) = \frac{\sin(\omega t)}{\pi t}. \tag{3}$$

By the use of the discrete analogue of (2) and a truncation of the corresponding infinite sum at a level of N

$$f_n^* = \sum_{k=-N}^{N} h_k \, f_{n-k} \tag{4}$$

is obtained with

$$h_k = \frac{\sin(n\omega_c \Delta t)}{n\pi}. \tag{5}$$

To reduce the effect of Gibbs oscillation, which occurs due to the truncation of Fourier series, the weight function h can be multiplied by a window function, e.g. the well known Lanczos window function of the form of

$$w_n = \frac{\sin \frac{n\pi}{N+1}}{\frac{n\pi}{N+1}}. \tag{6}$$

Reduction of Gibbs oscillation can also be achieved by the use of an "optimum filter", which minimizes the distance between the step function (ideal filter response) and its reconstruction from finite elements in the Fourier series according to L_∞ norm. On the other hand, pure truncation minimizes the distance of the two responses in L_2 norm (*Huang* and *Lynch*, 1993).

3. The barotropic model

(a) 2-Dimensional case

For testing the algorithms of different initialization procedures and their filter efficiencies a tempting way is to implement the methods for a relatively simple model such as a 2-D barotropic model solving the shallow water equations, i.e. those governing the motion of an incompressible, homogeneous, non-viscous, quasi-static, rotating fluid with a flat bottom and a free top surface. These equations provide a closed system with 3 unknown variables, the horizontal wind components u, v and the geopotential height Φ

$$\partial_t u = -\partial_x K + (f+\xi)v - \partial_x \Phi + \sigma_u, \tag{7}$$

$$\partial_t v = -\partial_y K - (f+\xi)u - \partial_y \Phi + \sigma_v, \tag{8}$$

$$\partial_t \Phi = -u\partial_x \Phi - v\partial_y \Phi - \Phi D + \sigma_\Phi, \tag{9}$$

where ∂ represents partial derivatives according to its subscript, $K=0.5(u^2+v^2)$ is the kinetic energy, $D=\partial_x u + \partial_y v$ is the divergence and $\xi=\partial_x v - \partial_y u$ is the vorticity and σ represents any forcing term (in the basic case the only forcing taken into account is diffusion). Eqs. (7)–(9) do not contain diabatic terms, but in order to simulate diabatic processes, in some extent, σ was included which originates irreversibly in the model.

A simple spectral model integrating Eqs. (7)–(9) using double Fourier spectral representation for computing spatial derivatives and a semi-implicit leapfrog scheme for time discretization has been developed within the frame of the ARPEGE/ALADIN project in Toulouse, France and later implemented on a Hewlett Packard-710 workstation at the Weather Forecast Division of the Hungarian Meteorological Service. Initialization experiments have been carried out with different versions of NMI and DFI, both implemented for this model. Model experiments with simulating orographic and diabatic forcing have been also realized by modifying the basic equations, i.e. adding forcing terms to Eqs. (7)–(9).

(*b*) *1-Dimensional case*

To see the impacts of filter for an even simpler model, the 1-D version of the barotropic equations has also been coded. These equations are derived from system (7)-(9) by omitting derivatives with respect to y. This model, just like the 2-D one, computes derivatives in Fourier spectral space while the time discretization is carried out by an explicit leapfrog scheme. For initialization experiments different DFI versions have been implemented for this very simple model as well.

4. Implementation of digital filter and normal mode initialization techniques within the barotropic model

As it was mentioned above, DFI has been implemented both for the 1-D and for the 2-D version of the barotropic model while NMI only for the 2-D one. In this section details of implementation in the 2-D system will be discussed.

4.1 Implementation of DFI

An initialization using a non-recursive digital filter can be easily developed by using Eq. (2) for the initial time (n=0). Then the different filter "strategies" mean different choices of the h_k coefficients. Once this strategy is decided the set of h_k coefficients can be computed and stored in file. Then the application of Eq. (2) requires past and future model states around the initial time. This can be achieved by backward and forward integration of the model starting from the original initial state and applying Eq. (2) for each prognostic variable at each gridpoint independently.

In the case of adiabatic DFI (ADFI) both backward and forward integrations are carried out without diabatic terms. Thus the steps of ADFI procedure can be summarized as

– adiabatic backward integration from $t=0$ to $t=-T/2$;

- adiabatic forward integration from $t=0$ to $t=T/2$, starting from the original initial fields.

During the backward and forward integration the filtered state is being accumulated by adding the current state with the current weight to the sum, as prescribed by Eq. (2).

When the filter is diabatic (DDFI) the procedure described above needs some modification because diabatic processes can't be taken into account during backward integration. In this case the procedure starts with an adiabatic backward model integration just to establish the starting state from where the forward diabatic integration will start and the accumulation of the filtering sum will be realized along the forward diabatic model trajectory. This can be summarized in the following points

- adiabatic backward integration from $t=0$ to $t=-T/2$ without accumulation of filter sum;
- diabatic forward integration from $t=-T/2$ to $t=T/2$ with accumulation of filter sum.

It should be remarked that the diabatic forward trajectory, which follows the adiabatic backward one and starts from the endpoint of the backward one, does not exactly pass through the original initial state. Though this brings some inaccuracy into the procedure, the benefit of inclusion of diabatic processes is much more important, especially for a model with sophisticated physics in it. All this is not expected to be proven by such a simple barotropic model where the only irreversible process is horizontal diffusion.

4.2 Implementation of NMI

To have reference for evaluating the performance of DFI, NMI has also been implemented for the 2-D barotropic model. The method, which has been applied, is based on Machenhauer's explicit algorithm (*Machenhauer*, 1977). For the present barotropic spectral model this can be summarized as follows. Let

$$\underline{X} = \begin{pmatrix} u \\ v \\ \Phi \end{pmatrix} \tag{10}$$

denote the state vector of the model. Then the evolution equation of the model can be written as

$$\frac{d\underline{X}}{dt} = F(\underline{X}) = L(\underline{X}) + N(\underline{X}), \tag{11}$$

where L represents the linear and N the nonlinear part of the model. For the

barotropic model this decomposition of the vector field $F(\underline{X})$ can be of the form

$$\underline{\underline{L}} = \begin{pmatrix} 0 & f & -\partial_x \\ -f & 0 & \partial_y \\ -\Phi_0\partial_x & -\Phi_0\partial_y & 0 \end{pmatrix}, \tag{12}$$

where f is the Coriolis parameter and Φ_0 is the reference geopotential height. In the case of bi-Fourier spectral representation the operator $\underline{\underline{L}}$ can be considered separately for each wavenumber-pair (m,n) and can be written as

$$\underline{\underline{L}}^{(m,n)} = \begin{pmatrix} 0 & f & -ikm \\ -f & 0 & iln \\ -ikm\Phi_0 & -iln\Phi_0 & 0 \end{pmatrix}, \tag{13}$$

where i is the imaginary unit, $k=2\pi/L_x$, $l=2\pi/L_y$ and L_x and L_y are the sizes of the model domain in x and y directions, respectively. The normal modes of the linearized system are the eigenvectors of $\underline{\underline{L}}$, which can be decomposed into rotational and gravity modes, here defined as eigenvectors corresponding to zero and non-zero eigenvalues, respectively. For the operators in (13) the eigenvalues are

$$\mu_1^{(m,n)} = 0, \quad \mu_{2,3}^{(m,n)} = \pm i\sqrt{l^2n^2\Phi_0 + k^2m^2\Phi_0 + f^2} \tag{14}$$

and the corresponding eigenvectors are the columns of the eigenvector matrix

$$\underline{\underline{W}}^{(m,n)} = \begin{pmatrix} -inl & km\lambda - inlf & -km\lambda - ilnf \\ ikm & nl\lambda + ikmf & -nl\lambda + ikmf \\ f & -l^2n^2\Phi_0 - k^2m^2\Phi_0 & -l^2n^2\Phi_0 - k^2m^2\Phi_0 \end{pmatrix}, \tag{15}$$

where

$$\lambda = \sqrt{l^2n^2\Phi_0 + k^2m^2\Phi_0 + f^2}. \tag{16}$$

To get the normed form of $\underline{\underline{W}}$ the first column must be multiplied by

$$1/[l^2n^2 + k^2m^2 + f^2)^{0.5}]$$

while the second and third columns both by

$$1/[\{k^2m^2\lambda^2 + l^2n^2f^2 + l^2n^2\lambda^2 + k^2m^2f^2 + (l^2n^2\Phi_0 + k^2m^2\Phi_0)^2\}^{0.5}].$$

The normal modes span the whole phase space of the truncated system (here

truncation means that finite number of m and n is considered) and they provide a basis in the phase space determining two linear manifolds G and R spanned by the gravitational and rotational normal modes respectively.

When performing linear normal mode initialization (LNMI), the initial states are chosen from the manifold R, i.e. an arbitrary initial state vector is projected onto R. Due to the presence of the nonlinear part N of the model, however, this choice of initial state does not guarantee that during the temporal evolution of the system the phase space trajectory remains within R. Therefore, in the case of NNMI, instead of this, an initial state for which

$$\left[\frac{d\underline{X}}{dt}\right]_G = 0 \tag{17}$$

is prescribed, where the subscript G represents projection of any vector in the phase space onto the manifold G. The iteration procedure given by

$$\underline{X}_G^{(p+1)} = \underline{X}_G^{(p)} - L_G^{-1}\left(\frac{d\underline{X}^{(p)}}{dt}\right)_G ; \quad \underline{X}_R^{(p+1)} = \underline{X}_R^{(p)} , \tag{18}$$

where the subscript R represents the projection of any vector in the phase space onto the manifold R, provided it converges, leads to a state satisfying the above requirement and at the same time the iteration does not touch rotational modes. In Eq. (18) L_G represents the linear transformation of the manifold G for which $L_G(\underline{y})=L(\underline{X})_G$, $\underline{y} \in G$ where $\underline{X}$ is the vector in the phase space for which $\underline{X}_G=\underline{y}$ and $\underline{X}_R=0$. In each iteration step the tendencies on the right hand side of the first Eq. of (18) can be derived by a single timestep integration of the model with Eulerian explicit tendencies. In this case with $\Delta t=1$, the differences between the fields gained after and before a single timestep Eulerian explicit integration of the model directly provide the desired tendencies. The correction term for one iteration step can be written for each wavenumber-pair as

$$(\underline{X}^{(p+1)} - \underline{X}^{(p)})^{(m,n)} = -\underline{\underline{W}}^{(m,n)} \begin{pmatrix} 0 & 0 & 0 \\ 0 & 1/\mu_2{}^{(m,n)} & 0 \\ 0 & 0 & 1/\mu_3{}^{(m,n)} \end{pmatrix} \underline{\underline{W}}^{(m,n)^{-1}} \frac{d\underline{X}^{(p)(m,n)}}{dt} . \tag{19}$$

This transformation of the tendency vector is a sequence of three linear operations, which are

- a basis transformation from the basis of spectral prognostic variables to that of normal modes;
- transformation representing the correction term of an iteration step written in the transformed (normal mode) space;
- inverse basis transformation.

It should be noted that this transformation can be carried out in the same manner for each wavenumber-pair, except for (0,0), for which the eigen-problem has only one nontrivial solution and this corresponds to the rotational mode. It means that the iteration procedure does not touch this wavenumber-pair, involving that field-averages remain unchanged during the initialization.

In the LNMI case the initialization formula is non-iterative and can be written as

$$\underline{X}^{(m,n)}_{initialized} = \underline{X}^{(0)(m,n)} - \underline{\underline{W}}^{(m,n)} \begin{pmatrix} 0 & 0 & 0 \\ 0 & 1 & 0 \\ 0 & 0 & 1 \end{pmatrix} \underline{\underline{W}}^{(m,n)-1} \underline{X}^{(0)(m,n)} . \qquad (20)$$

As the tranformation matrices in (19) and (20) depend only on the geometry of the model and the reference geopotential height, they can be computed and stored preliminarily to model run. The major steps of NNMI can be summarized as

- one timestep integration of the model;
- computation of tendencies of prognostic variables;
- sequence of direct FFT-s (Fast Fourier Transformation) to transform tendencies to spectral space;
- computation of correction terms;
- inverse FFT-s;
- convergence test;
- updating prognostic fields.

These steps for LNMI are very similar, just the multiplier matrix is of different form and there is no iteration.

5. Results

In this section the results of digital filtering technique and its comparison with those of the nonlinear normal mode technique will be described for the above mentioned two models.

5.1 1-Dimensional case

This model works over the whole latitudinal circle 45°N with 72 grid points. Thus the resolution is 393.6 km (5°). The time step for the integration is 8 minutes, which satisfies the Courant-Friedrichs-Lewy condition. The filter span is chosen to be 8.6 hours and the filter coefficients are calculated according to optimum filter.

To demonstrate the efficiency of DFI technique the model was integrated from different initial conditions. The time evolution of geopotential height for the first 24 hours (180 time steps) of two different initial conditions at a certain grid point is shown in *Figs. 1* and *2*. The mean initial geopotential height is

30,000 J/kg. The wind components were derived by adding an analytical ageostrophic term to the geostrophic wind components. The uninitialized trajectory shows that the high frequency oscillations are not damped during the time integration so the 1-D model itself is not able to adjust mass and momentum fields. In Fig. 2 a strong initial "shock" can be observed at the examined gridpoint and this effect together with the high frequency noises are successfully removed by DFI. The curves corresponding to DFI also prove that lower frequency oscillations are not removed by DFI and that the separation of waves is well controlled by DFI parameters: stop and pass edges of optimum filter were chosen to be 3 and 12 hours respectively and this is in agreement with the results in Figs. 1 and 2, which show that the highest frequencies occuring after DFI are of the order of 50 timesteps (6.5 hours).

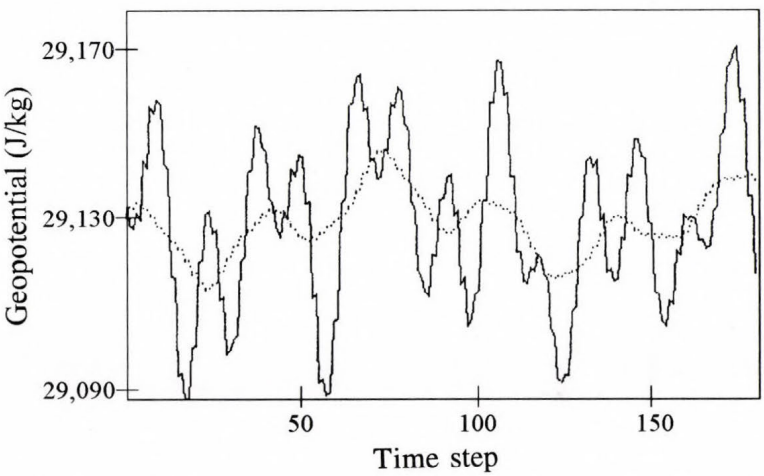

Fig. 1. Time evolution of geopotential height at a certain grid point gained by the 1-D model without initialization (solid line) and with DFI (dotted line).

5.2 2-Dimensional case

This model is launched over a 64×36 point grid with cca 50 km resolution in both directions and the timestep is 5 minutes. The Coriolis parameter is assumed constant. The DFI time span is 8.3 hours and the filter coefficients are determined by Lanczos windowing with a 6 hour cutoff period. Periodic lateral boundary values are applied in both directions by this making possible the bi-Fourier spectral representation. The mean geopotential value is 30,000 J/kg.

The first experiment shown in this paper starts from simple geostrophic initial conditions (*Fig. 3*). The initial field corresponding to this experiment varies in x and y direction as well. The geostrophic initial condition is produced by adjusting the initial wind field to the geopotential field. The two curves in Fig. 3 represent the time evolution of geopotential height for the first 288 time steps (24 hours) starting from initialized and uninitialized initial fields. The

smooth curve represents in fact two cases, one gained by DFI and another gained by NNMI, but they evolve completely identically. It is important to distinguish the two sorts of NMI procedures, the linear and nonlinear one, because in this case they yield significantly different solutions (LNMI does never make any modification on geostrophic initial conditions). As it can be

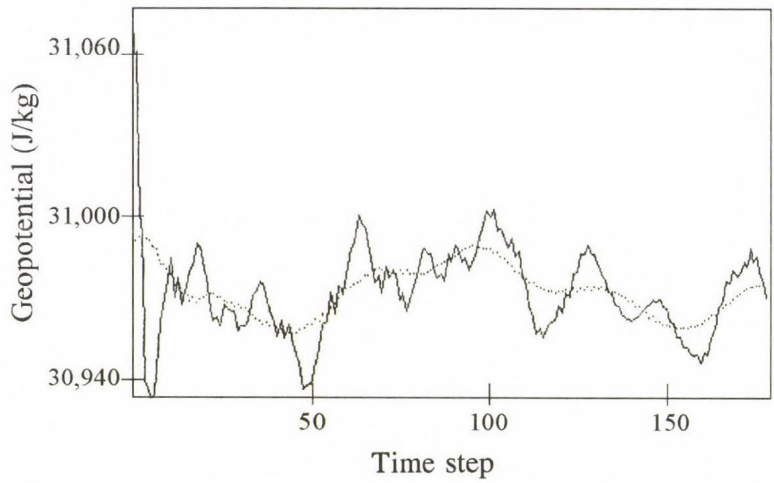

Fig. 2. Time evolution of geopotential height at a certain grid point gained by the 1-D model in uninitialized case (solid line) and initialized with DFI (dotted line).

seen in Fig. 3, in contrast with the 1-D results, gravity wave oscillations are damped by the model as the time evolves. Some further experiments were made with one-dimensional initial fields, i.e. for which initial fields vary only in x direction.

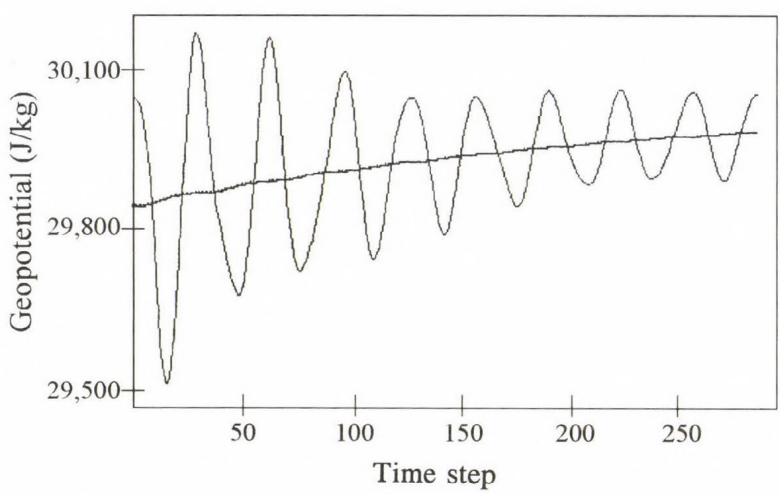

Fig. 3. Time evolution of geopotential height at a central grid point of the 2-D model domain in unfiltered (solid line) and initialized NMI and DFI (smooth line) cases.

After establishing the fields satisfying geostrophic relationship the geopotential field was modified in the central region of the domain (*Fig. 4a*). As it is seen in *Figs. 4b, c*, the two kinds of initialization simply remove this perturbation from the geopotential field setting back the original one-dimensional field. *Fig. 4d* shows the corresponding evolution of geopotential height at a gridpoint within the area of perturbation and this figure indicates that both initializations exhibit good filter efficiency. It should be remarked that this initial state would involve stationary solution if there were no horizontal diffusion in the model.

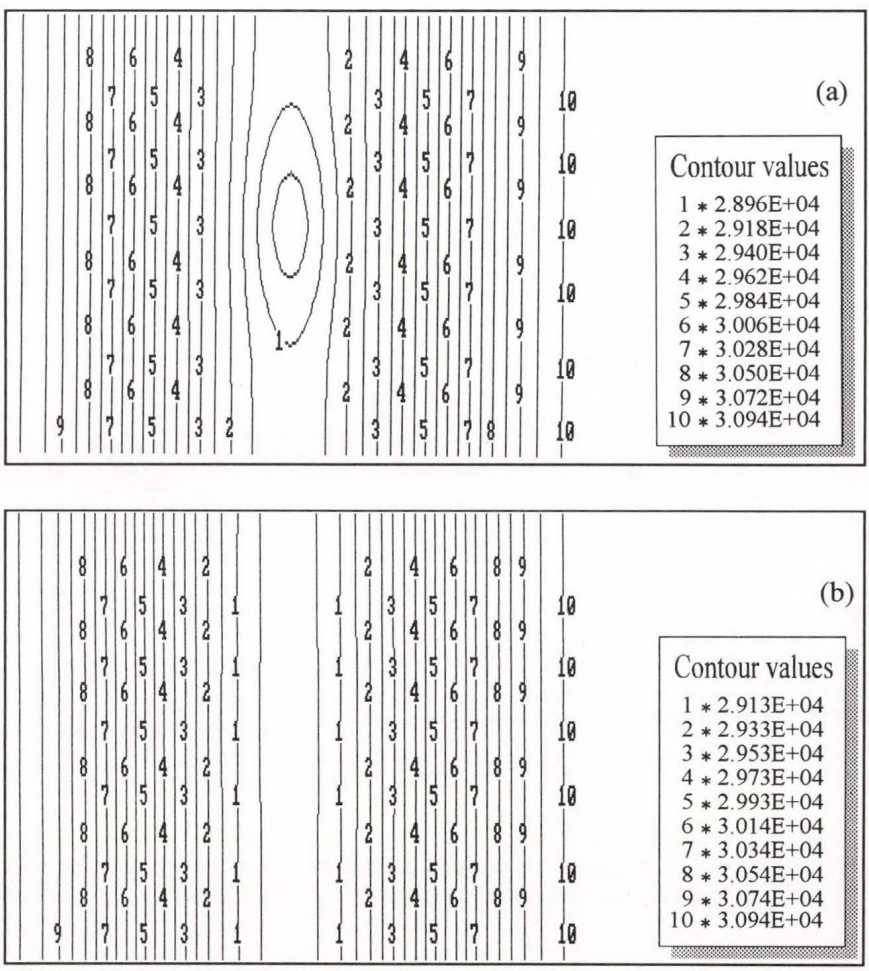

Fig. 4a, b. Initial geopotential field of the 2-D model gained by (*a*) no initialization, (*b*) DFI.

The experiment presented in *Fig. 5a, b* also applies a one-dimensional basic state, but now the introduced perturbation consists of a single gridpoint

disturbance and a superposed noise. In the uninitialized case this involves a strong initial "shock". DFI and NMI removes this shock as well as the high frequency oscillations from the evolution.

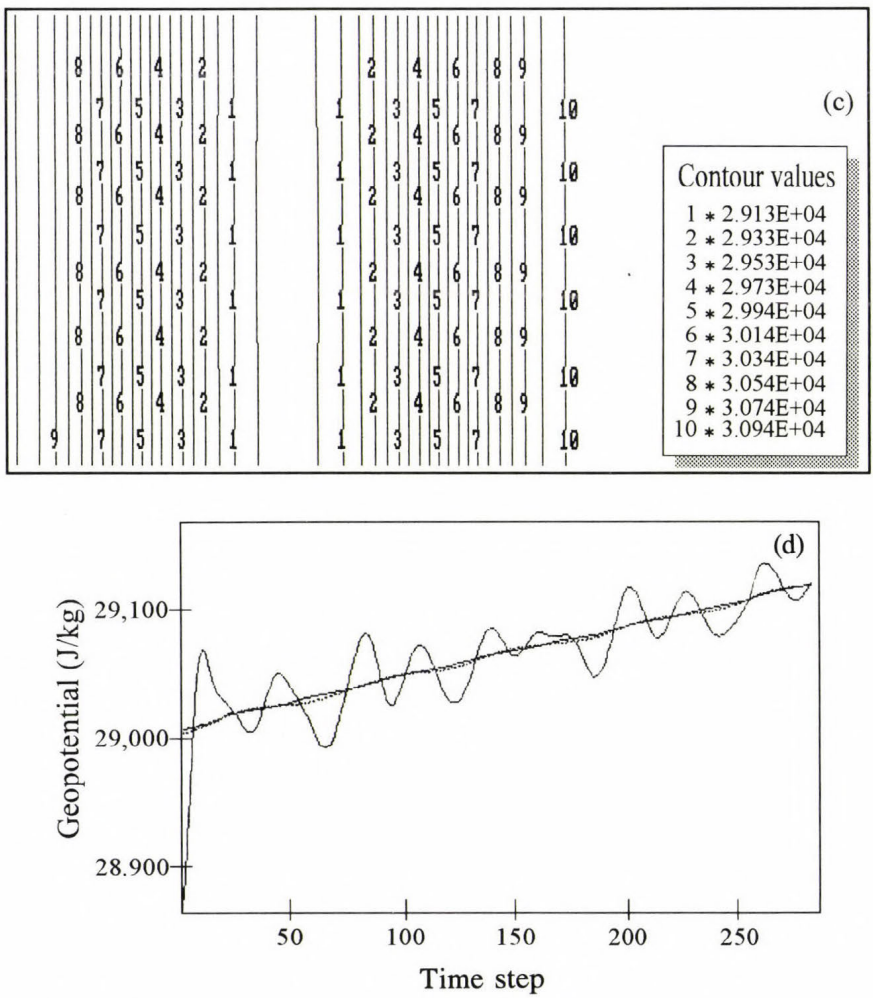

Fig. 4c, d. Initial geopotential field of the 2-D model gained by (*c*) NNMI, (*d*) the corresponding time evolutions at a single grid point of the domain: no initialization (solid line), DFI (dotted line) and NNMI (smooth solid line).

6. Summary and concluding remarks

The aim of the experiments presented in this paper was to get an idea about the applicability of the recently developed digital filter initialization technique. The vehicle for this experiments were simple one- and two-dimensional

barotropic models. Unbalanced initial fields were created and DFI and NMI methods were used to remove gravity wave noises.

All the experiments described in this paper show very similar performance of NNMI and DFI. This proves that the ideas behind digital filter work well in practice and the technique is adequate for initialization purposes in numerical weather prediction.

However, in order to see more specific properties of the method, with especial regard to diabatic aspects, one probably has to carry out experiments on a more realistic prognostic model with sophisticated physical parameterization.

Acknowledgments – Present study is based on the model developed within the frame of the ALADIN project of METEO-FRANCE and some Central-Eastern-European meteorological services. We thank all ALADIN staff and project leaders for the support.

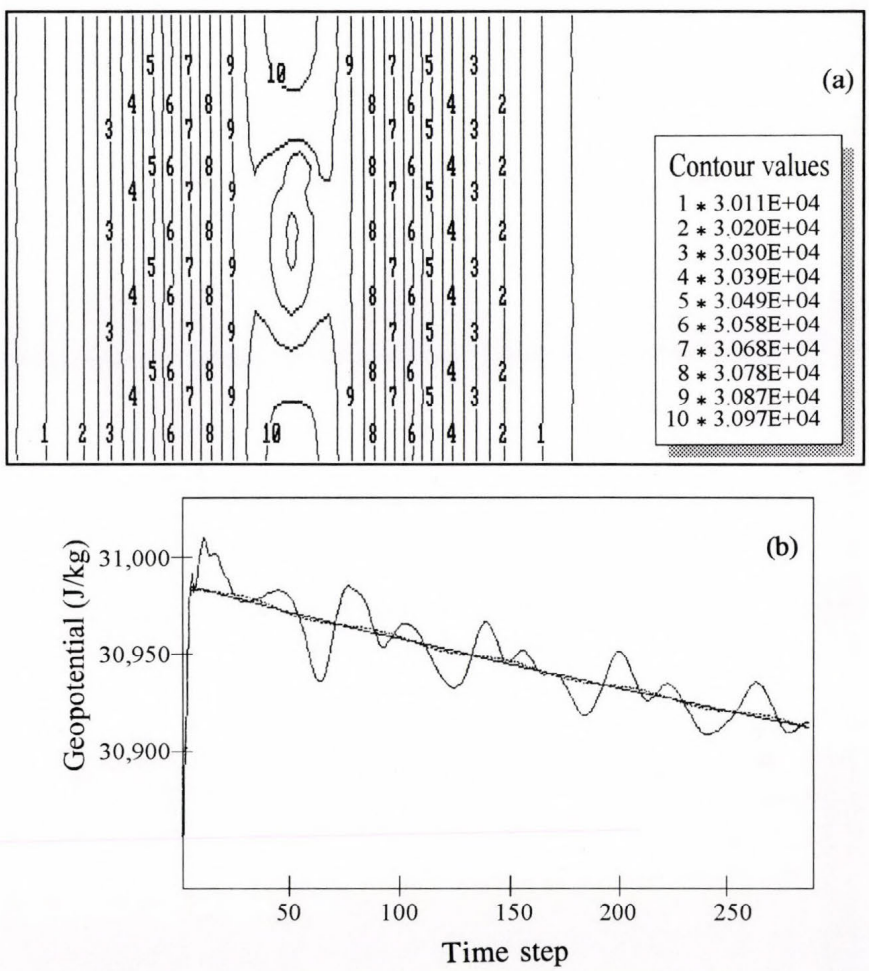

Fig. 5. (*a*) Initial geopotential field of the 2-D model, (*b*) time evolution at a single gridpoint without initialization (solid line), with NNMI (smooth solid line) and DFI (dotted line).

References

Baer, F., 1977: Adjustment of initial conditions required to suppress gravity oscillations in non-linear flows. *Beitr. Phys. Atmos. 50*, 358-366.

Baer, F. and *Tribbia, J.*, 1977: On complete filtering of gravity modes through nonlinear initialization. *Mon. Wea. Rev. 105*, 1536-1539.

Bengtsson, L., 1975: 4-dimensional assimilation of meteorological observations. *GARP Publ. Ser.*, No. 15. *WMO/ICSU Joint Organizing Committee.*

Daley, R., 1981: Normal mode initialization. *Rev. Geophys. Space Phys. 19*, 450-468.

Daley, R., 1991: *Atmospheric data analysis*. Cambridge University Press, Cambridge.

Folland, G.B., 1992: *Fourier analysis and its applications*. Wadsworth and Brooks/-Cole, Pacific Grove.

Huang, X.Y. and *Lynch, P.*, 1993: Diabatic digital-filtering initialization: application to the HIRLAM model. *Mon. Wea. Rev. 121*, 589-603.

Lynch, P. and *Huang, X.Y.*, 1992: Initialization of the HIRLAM model using a digital filter. *Mon. Wea. Rev. 120*, 1019-1034.

Machenhauer, B., 1977: On the dynamics of gravity oscillations in a shallow water model with application to normal mode initialization. *Beitr. Phys. Atmos. 50*, 253-271.

IDŐJÁRÁS

Quarterly Journal of the Hungarian Meteorological Service
Vol. 98, No. 1, January–March 1994

Air cleaning by low frequency acoustic wave

A. Sadigzadeh

Radiation Protection Department, Atomic Energy Organization of Iran
P.O. Box 14155-4494, Tehran, Iran

(Manuscript received 10 February 1994)

Abstract—The aim of this work is to study the granular beds, with and without an acoustic wave used in air cleaning processes. In the absence of an acoustic field our experimental results are in a good agreement with the theory developed by *Otani et al.* (1989). In the presence of a high acoustic pressure level (APL $\geq$ 130 dB), our experiments show an increase in granular bed efficiency. The efficiency shows a large rise from a threshold value in acoustic pressure level.

Key-words: granular bed, filter efficiency, acoustic wave.

1. Introduction

Sonic treatment of aerosol particles in waste gases is an advanced industrial emission control technique. Under the high-temperature, high pressure, corrosive and explosive environment, the necessity for elimination of the aerosols makes the acoustic filter one of the primary gas cleaning devices. The depressurization of the enclosure at high pressure (nuclear industry), residual particle removal in the inflammable environment (petroleum and combustible gas industry), etc. are the examples of recent application of acoustic gas cleaning devices. An acoustic filter is composed of two parts (*Fig. 1*):

(1) an acoustic agglomeration chamber (AAC),

(2) a granular bed.

Application of acoustic waves increases the kinetic energy of aerosol particles in the gas medium. This becomes important above a certain threshold value in acoustic pressure level, it increases the probability of the collisions between the particles themselves, and the obstacles. The acoustic field increases the efficiency of an acoustic filter at two stages:

– An increase of aerosol particles diameter by increasing coagulation

factor, for example, with an acoustic field of f=1 kHz, APL=165 dB, the increase of the diameter of the initial monodisperse aerosol particles (D_p=3.34 μm) by a factor of 3 (*Malherbe,* 1987).

– An increase in the overall efficiency of the granular bed, by increasing the aerosol particles diameter and by adding an important aerosol capture mechanism due to the induced force in the medium which acts on the aerosol particles.

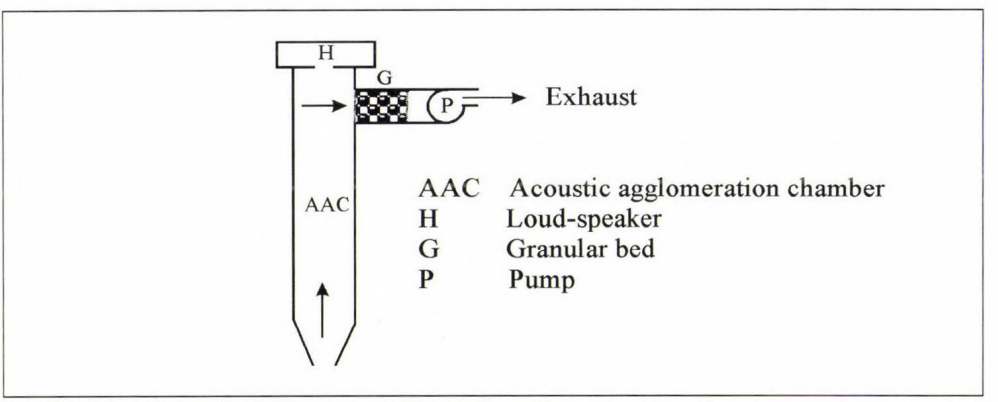

Fig. 1. The schematic diagram of an acoustic filter.

2. Efficiency of a granular bed

The theoretical expression for the capture efficiency of the aerosol particles (E) by a granular bed is a function of its depth (L) and porosity (ε), as well as the diameter (D_s) and the total single collector efficiency η_t of spherical collectors (*Tardos et al.*, 1974)

$$E = 1 - \exp\left[-\frac{3(1-\varepsilon)L}{2\,\varepsilon\,D_s}\eta_t\right]. \tag{1}$$

If we neglect the interactions between the different collection mechanisms, electrostatic and sieve effect; η is obtained by adding the contribution of individual collection mechanisms: sedimentation (η_s), inertial impact (η_{imp}), direct interception (η_i) and diffusion (η_d). Consequently

$$\eta_t = \eta_s + \eta_{imp} + \eta_i + \eta_d. \tag{2}$$

In the absence of an acoustic field, our experimental results agree with the theoretical results developed by *Otani et al.* (1989) and by *Sadigzadeh* (1989). In the relations 3 to 6, the principal expressions are summarized

$$\eta_I = \frac{St_{eff}^{\ 3}}{0.014 + St_{eff}^{\ 3}}, \tag{3}$$

where

$$St_{eff} = \left[1 + \frac{1.75\,Re\,(1-\alpha)}{150\alpha}\right] St,$$

$$\eta_{Int} = 16R^{\left(2 - \frac{Re}{Re^{1/3}+1}\right)^3}, \tag{4}$$

$$\eta_s = \frac{G}{1+G}, \tag{5}$$

$$\eta_D = 8\,Pe^{-2/3} \quad \text{for } Re \to 0, \qquad \eta_D = 2.1\,Pe^{-1/2} \quad \text{for } Re \to \infty. \tag{6}$$

(The denotations are explained at the end of the paper.)

3. The effect of the acoustic field on aerosol particles

Application of an acoustic wave with a level more than 130 dB generates the occurrence of a number of complex and violent motions by the particles, in addition to the motions such as Brownian or settling that a particle has in a gas medium. This is due to the fact that the particles take some part in the vibration of the gas, in the translation motion or "drift" and acoustic turbulence induced by the acoustic field in the gas. These phenomena act on the suspended particles and affects their movements.

The motion of the aerosols in a vibrating carrier gas can be described by the entrainment factor μ_p (*Mednikov,* 1965). For an isolated spherical particle of aerodynamic diameter D_p moving in a sonic field of frequency (f), the entrainment factor is

$$\mu_p = \frac{A_p}{A_g} = \frac{1}{(1+\omega^2\tau^2)^{1/2}}, \tag{7}$$

where A_p, A_g are the amplitude of a particle and gas vibration in the acoustic wave, while $\omega(\omega=2\pi f)$ and $\tau(\tau=\rho_p D_p^{\ 2}/18\eta_g)$ denote the angular frequency of the acoustic wave and the relaxation time of the aerosol, respectively. According to the angular frequency we can differentiate the following cases:

- $\omega\tau \ll 1$, in this case, the amplitude of acoustic oscillations of an aerosol and of the carrier gas molecules are equal ($A_p \approx A_g$).
- $\omega\tau \gg 1$, in this case, $A_p \approx 0$.

Above the pressure level of 158 dB (see *Cheng et al.*, 1983; *Boulaud et al.*, 1984), the acoustic turbulence becomes important enough to induce a force that

favours the probability of collision between the particles, and the particles and an obstacle such as an element of the constituent media. The overall efficiency of the granular media in the presence of an acoustic field (E_T) is given by the following relation

$$E_T = 1 - \exp\left[\frac{3(1-\varepsilon)}{2\varepsilon D_s}\eta_T L\right]; \quad \eta_T = \eta_t + \eta_{ac}, \tag{8}$$

where η_T is the total single collector efficiency in the presence of an acoustic wave, while η_{ac} is the acoustic efficiency of a spherical collector; this is dependent on the frequency and sound pressure level of the acoustic waves and the spherical collector and particles size.

4. Experimental apparatus and measurement

The schematic diagram of the experimental set up is shown in *Fig. 2*. The granular bed used consisted of spherical glass collectors. This was set up inside of a glass column of 1 m height and 6.7 cm internal diameter. In our experiments, we used monodisperse aerosols of dioctyle phtalate (DOP) and dioctyle sebacate (DES) produced by a two stage aerosol generator (TSI; model 3072, and 3076) and a MAGE (for particles larger than 1 μm), respectively. The acoustic waves are generated by a high power loud-speaker (maximum effective power 120 watts). The sinusoidal signal is fed by an electric signal generator, and amplified by an audio-amplifier before supplying the loud-speaker.

An original dilution system *Sadigzadeh* (1989), allows us to produce aerosol concentrations ranging from a few to 10^5 particles/cm^3. A pump assures the

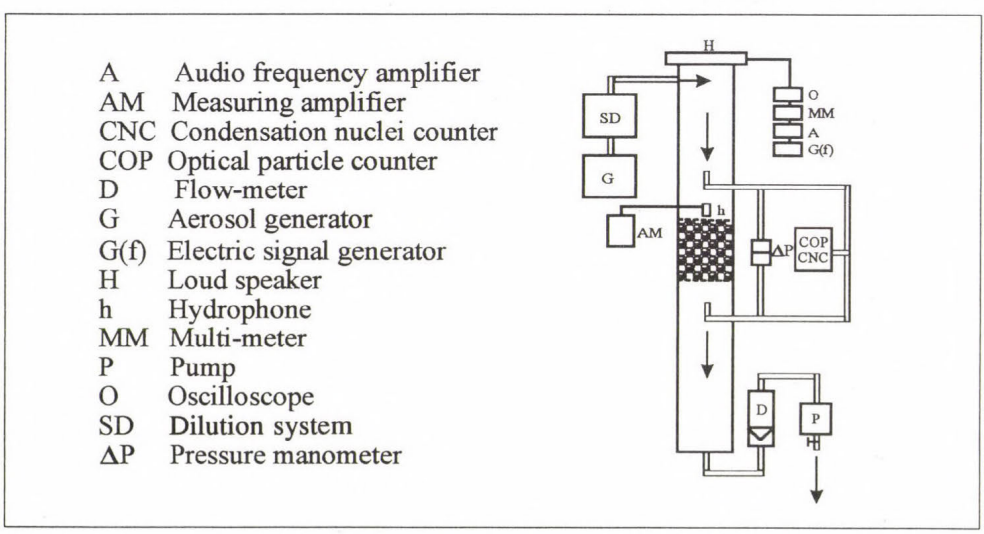

Fig. 2. Experimental device.

clean air circulation in the device. The shape and the power of yielded signal to the loud-speaker is monitored by an oscilloscope and a voltage, and an intensity multimeters. The acoustic pressure level (APL) is measured by a Bruel & Kjær system comprising a hydrophone, a pre-amplifier (BK 2626) and a reading amplifier (BK 2609). The upstream and downstream aerosol volume concentration and size distribution of particles were determined by a condensation nuclei counter (TSI), an optical particle counter (Kratel) and a quartz crystal micro-balance cascade impactor (California measurements INC).

The pressure drop was obtained with and without acoustic wave by a pressure manometer.

5. Experimental results

5.1 Electrical power

The effective electrical power necessary to supply the loud-speaker for obtaining an acoustic field by a given APL was determined. For example, in an experiment a granular bed with following characteristics: L=20 cm, D_s=5 mm and ε=0.38 was made. *Fig. 3* shows the increase of the APL measured in a loop of the acoustic pressure as a function of the effective electrical power supplied to the loud-speaker. The frequencies chosen were those of resonance frequencies of the set-up. For example, we observed that for a fixed frequency of 450 Hz, 24 W effective electrical power is enough for obtaining 160 dB of APL.

5.2 Pressure drop

The pressure drop ΔP of a granular bed rises with the flow rate. In the presence of an acoustic wave, the pressure drop increases. This is in direct proportion to APL and inversely proportional to acoustic frequency. As an example, *Fig. 4* shows the increase of the pressure drop of a granular bed (L=20 cm, D_s=2 mm, ε=0.39), as a function of the APL, for three different frequencies.

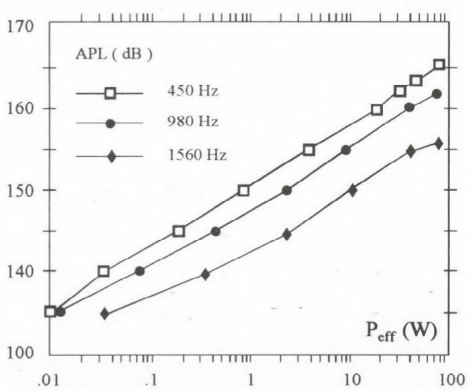

Fig. 3. Acoustic pressure level, versus the effective electric power (P_{eff}).

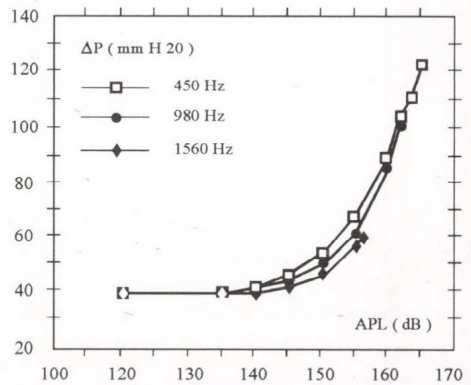

Fig. 4. The pressure drop of the granular bed versus the APL. U_f=18 cm s^{-1}.

5.3 *Efficiency of a granular bed*

We verify our theoretical forecast, by developing a number of experiments to measure the efficiency of the granular bed with and without an acoustic field. The efficiency of different granular beds (L=20 cm, D_s=1, 2 and 5 mm), is determined experimentally for different carrier gas velocities: 4.5, 9, 18 cm s^{-1}. The diameter of DES monodisperse aerosol particles used, are 2,3.3 and 4 μm. In these experiments, the generated acoustic wave frequencies are successively fixed at 450, 980 and 1590 Hz; the APL varies in the range 120 and 164 db.

In *Fig. 5* typical data are illustrated showing the increase in the efficiency of the granular bed (L=20 cm, D_s=2 mm, ε=0.39) as a function of the APL. For two air velocities, the diameter of the monodisperse aerosol used was 2 μm. The acoustic wave frequency was fixed at 450 Hz. The experimental data indicate that the action of acoustic wave on granular bed increases with air flow rate. Our explanation for this phenomena is as follows. The expansion of the turbulent volume because of the transport of the acoustic vortex is locally induced by the carrier gas movement.

The increase of the granular bed (L=20 cm, D_s=5 mm, ε=0.38) efficiency in the presence of an acoustic field of frequency 450 Hz, for three different particle diameters is illustrated in *Fig. 6*. The velocity of air is fixed at 4.5 cm s^{-1}. We observe an increase in the efficiency of granular bed by the APL. There is a great increase from a threshold APL, which is dependent on the aerosol particle size, for the particles of 2, 3.3, 4 μm diameter, this threshold is situated at 150, 145 and 145 dB, respectively.

In order to evaluate the effect of the acoustic wave on the capture efficiency of fine particles by a granular bed, a new series of experiments was carried out to measure the efficiency of a granular bed (L=15 cm, D_s=2 mm, ε=0.39) in

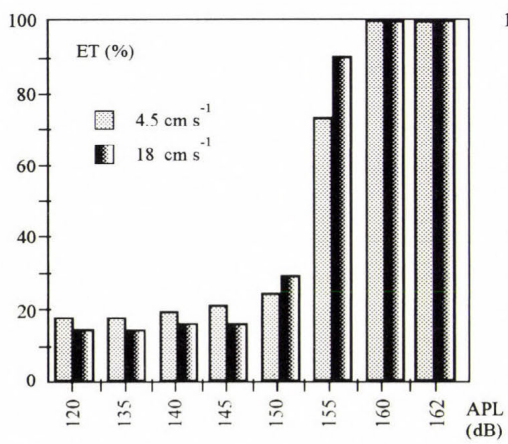

Fig. 5. The overall efficiency of the granular bed versus APL, for different air velocity.

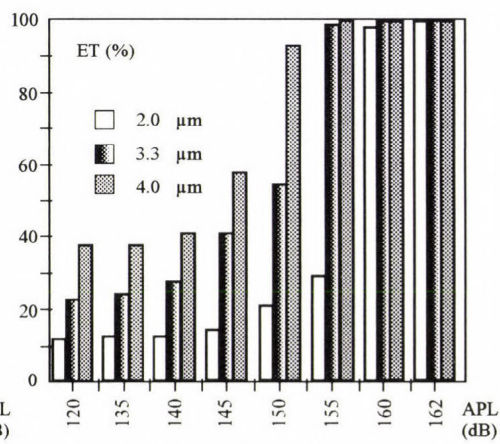

Fig. 6. The overall efficiency of the granular bed, versus APL, for different diameters of aerosol. U_f=4.5 cm s^{-1}.

the presence of an acoustic field for the submicrometric aerosol particles. The velocity of air flow rate was fixed at 7.9 cm s^{-1}, and the diameter of the DOP monodisperse aerosol particles used were 0.1, 0.5, 1 μm. The studied frequencies were 0.2, 0.5, 1, 1.5, 2, 2.5, 3 kHz, and the acoustic pressure level varied in the range of 120–160 dB.

By virtue of example in the histogram of *Fig. 7* the efficiency increase of the granular bed is plotted as a function of APL for the frequency fixed to 1 kHz. The experimental histogram allows us the following comments:

- The acoustic wave act on the efficiency of granular bed from 130 dB, in the diffusional range (D_p=0.1 μm), from 140 dB in the intermediary range (D_p=0.5, 1 μm).
- The acoustic impact on the efficiency is more important for large particles.

6. Conclusions

Our theoretical and experimental exploration for the various air velocities, spherical collector diameters and particle sizes, demonstrate the following results

- Without acoustic waves, our experimental results are in a good agreement with the theory of *Otani et al.* (1989).
- Under the effect of a high acoustic pressure level, the efficiency of a granular bed rises substantially. It is demonstrated that from a threshold in APL, the increase of granular bed efficiency is greater.
- The acoustic impact on granular bed efficiency is more important for large aerosol particles and for spherical collectors of small diameter.
- From 160 dB in acoustic pressure level, the efficiency of the studied granular bed exceeds 97% for the particles of diameter $\geq$0.5 μm.
- The pressure drop of granular bed rises in the presence of an acoustic field. Nevertheless, this was not too high to be used for the industrial filtering application.

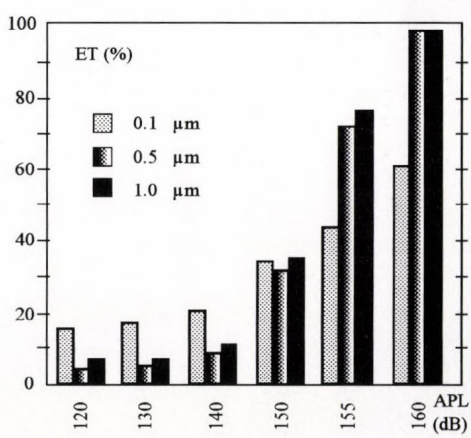

Fig. 7. The overall efficiency of a granular bed (L=15 cm, D_s=2 mm), versus APL. U_f=7.8 cm s^{-1}.

Acknowledgements—I wish to thank *Professor A. Renoux* for the helpful suggestions and discussions.

List of symbols

C Cunningham slip correction
D_s spherical captor diameter
G sedimentation parameter $=2g\rho_p D_p/9\eta_g U_f$
K_B Boltzmann's constant
Pe Peclet number $=D_s U_f/D_B$
Re Reynolds number $=D_s U_i/\nu$
St_{eff} effective Stokes number
U_i interstitielle air velocity $=U_f/\varepsilon$
α solid fraction of bed $=1-\varepsilon$
ε porosity of bed
ν_g kinematic viscosity of carrier gas
τ relaxation time of particle $=2\rho_p R_p^2/9\eta_g$
D_B particle diffusion coefficient $=CK_BT/3\pi\eta_g D_p$
f acoustic frequency
g acceleration of gravity
L depth of granular bed
R interception parameter $=D_p/D_s$
St Stokes effective number $=C\rho_p D_p^2 U_i/9\eta_g D_s$
T temperature
U_f superficial velocity
ΔP pressure drop
η_g fluid viscosity $=\nu_g\rho_g$
ρ_p particle density.

References

Boulaud, D., Frambourt, C., Madelaine, G. and *Malherbe, C.*, 1984: Experimental study of the acoustic agglomeration and precipitation of an aerosol. *J. Aerosol Sci. and Technol. 15*, 247-252.

Cheng, M.T., Lee, P.S., Berner, A. and *Shaw, D.T.*, 1983: Orthokinetic agglomeration in an intense acoustic field. *J. of Coll. and Interface Sci. 91*, 176-187.

Malherbe, C., 1987: Etude du comportement d'un aérosol soumis à un champ sonore. Thèse de doctorat d'état. Université Paris XII.

Mednikov, E.P., 1965: *Acoustic Coagulation and Precipitation of Aerosols*. Consultants Bureau, New York.

Otani, Y., Kanaoka, C. and *Emi, H.*, 1989: Experimental study of aerosol filtration by the granular bed over a wide range of Reynolds numbers. *J. Aerosol Sci. and Technol. 10*, 463-474.

Sadigzadeh, A., 1989: Filtrate acoustic. *6. Journées d'études sur les aérosols* (COFERA), 45-50.

Tardos, G., Gutfinger, C. and *Abuaf, N.*, 1974: Deposition of dust particles in a fluidized bed filter. *Israel J. Technol. 19*, 184-189.

IDŐJÁRÁS

Quarterly Journal of the Hungarian Meteorological Service
Vol. 98, No. 1, January–March 1994

The spectral reflection of different soils and soil ingredients

G. Szász and **V. Zilinyi**

Debrecen Agricultural University,
P.O. Box 36, H-4015 Debrecen, Hungary

(Manuscript received 5 October 1993; in final form 28 January 1994)

Abstract—In this paper the results of 67 soil sample investigations are presented. The spectral brightness coefficients were measured in the direction perpendicular to the surface of the samples. The linear and quadratic coefficients of the wavelength dependence are shown. The effect of different soil ingredients, humidity and roughness are analysed. The final purpose of this work is the application of these measured characteristics when using of data remotely sensed by satellites.

Key-words: reflection spectrum, albedo, soil ingredients, humidity, roughness.

1. Introduction

A part of solar irradiation is reflected by the surface and is spectrally transformed according to its material structural characteristics. The reflected portion and spectral transformation are characteristic of the surface and they are determined by its material composition, structure and condition. Meteorological investigations so far have mainly been restricted to the relationship between the reflection ratio and surface conditions. Material composition can only be deduced by the spectral resolution of the albedo. The spectral composition and dynamics of reflected radiation are very significant for both meteorology and the interpretation of information supplied by remote sensing. The spectral composition of the albedo provides information on the radiation energy utilised by the surface. Investigations in this area involve the technical-methodological development of detection, the reflection characteristics of representative surfaces and their interpretations.

2. *Methods and instruments used in investigations*

The reflection can be characterised by different parameters (see *Fig. 1*). In our investigations the brightness coefficient was determined. The measurement results serve as basis for the albedo definition.

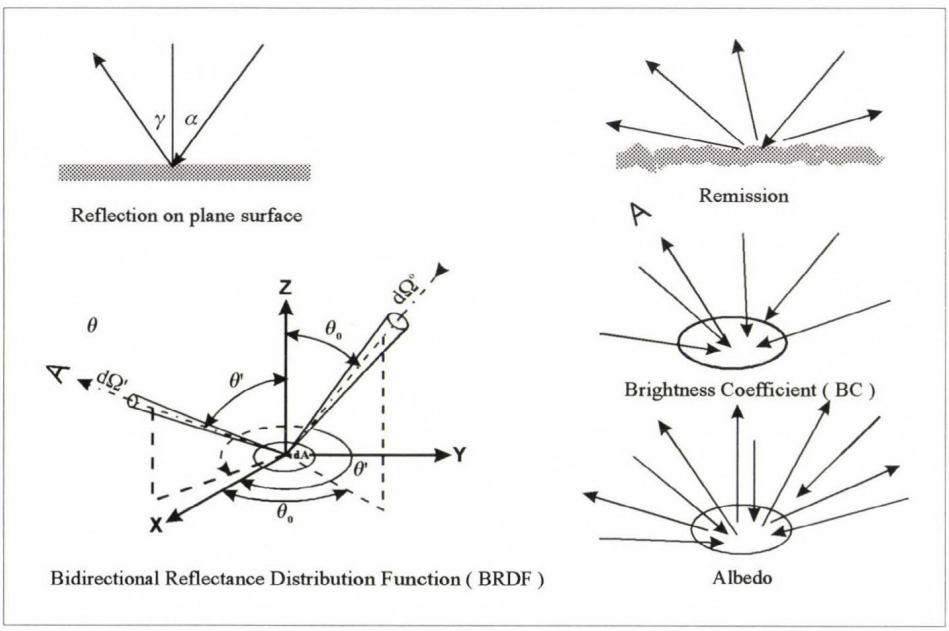

Fig. 1. The types of radiation reflection on surfaces of differing roughness.

Brightness coefficient

In field measurements, in most cases, it is impossible to illuminate the target surface from one direction only, this is why reasonable to introduce the brightness coefficient. The brightness coefficient is the ratio of the radiation energy scattered from δA surface at unit solid angle of θ', Φ' direction to the radiation energy arriving at the surface from total 2π solid angle.

Brightness coefficient mainly depends on the location of the detector as compared to δA surface (θ', Φ'). This does not mean, though, that the same surface examined from the same direction will produce constant values. It will be significantly affected by the distribution formula of the radiation R (θ_0, Φ_0) arriving at the surface.

The albedo

It is the ratio of the radiation energy scattered from δA surface at total 2π solid angle to the radiation energy arriving at the surface from total 2π solid

angle. The albedo can be taken as the weighted average of the brightness coefficientes (*BC*)

$$A = \int_0^{2\pi} BC(\theta', \Phi') \cos\theta' \, d\Omega'.$$

Weighting is necessary because, examined from θ' direction, δA surface will only mean $\delta A \times \cos\theta'$ surface. When calculating the albedo, the zenith point brightness coefficient ($\theta' = 0$, $\cos\theta' = 1$) counts for the most, therefore the brightness coefficient and the albedo concepts cannot be considered as synonymous. This is especially true, when the indicatrix is significantly distorted. Unfortunately, remote sensing-meteorological technical literature very often fails to distinguish between the two values.

In meteorological terminology the concept of albedo is used. Remote sensing detects radiation scattered and reflected at nearly nadir point, consequently, this value does not equal to the albedo.

To produce representative spectra the own-designed SM-1 and SM-2 reflection spectrophotometers, manufactured by LABOR-MIM, were used. The SM-1 and SM-2 are surface devices capable of determining continual spectra of the upgoing radiation reflected by soils and vegetation.

The measurement range of the SM-1 field reflection spectrophotometer is 400–1000 nm.

Major characteristics

- *Opening angle*: 7°, optical grid density: 1200 c/mm, detector: PIn photodiode, reflection standard: Ba SO_4, resolving capacity: 1 nm. The SM-2 is nearly a similar variety, the difference being its two-unit optical system.
- *Visual unit* (VIS): 400-1000 nm, infrared unit (IR): 1000-2400 nm. Characteristics: grid density VIS: 1200 v/mm, IR = 600 v/mm; detector VIS: PIn/Si photodiode, IR: PbS, photoresistor cooled to –38°. Reflection standard VIS: $BaSO_4$, IR: a diffuse surface coated with gold. Control and digital sign processing is carried out by the INTEL 8085 microprocessor.

After the calibration of the spectrometers, the measurement results were compared with internationally used measuring systems. When choosing the ranges, the operative ranges of about 50 spectrometers – produced in different countries – (LICOR, EXOTECH, BARNES) were considered.

The determination of different spectra was carried out in specifically built "black laboratories", using Tungsram sources of light. The dried samples were on a table in horizontal position and they were illuminated by several lamps. The spectrophotometer looked down at the investigated sample, so we actually measured the vertical brightness coefficient in each case.

The examined soil samples were taken in different regions of the country. The number of samples involved in the investigations is 67, their major physical and chemical characteristics were established by laboratory analyses. Thirty six of the samples were provided by the Soil and Agrometeorological Research Institute of the Hungarian Academy of Science, the clay samples were supplied by the Department of Soil Science of Gödöllő Agricultural University. For each measuring ground soil samples were used, providing reliable grounds for comparison making.

3. Measurement

Below the summary of findings follows that can be considered as significant. The results achieved give possibilities of international comparisons.

3.1 The reflection spectrum of soils

The investigations of the reflection spectra of soils were restricted to the analysis of macrophysical characteristics and the effects of soil condition. The representative soil spectrum refers to airdry, ground conditions.

The primary question is: what is the correlation (r) between the characteristic reflection and the wavelength for the Hungarian soils? The analysis of dried and powdered samples shows that the reflection increases as the wavelength grows. In the case of linear fitting, the slope is 0.015–0.041 in the 400–1000 nm interval.

In the range of 400–1000 nm the average reflection of soils in Hungary is

$$R_n(\lambda) = -5.278 + 0.022\,\lambda\,; \quad r = 0.986\,.$$

$R_n(\lambda)$ is the relative value of reflection referred to the wavelength (λ, nm). The high value of correlation coefficient suggests that soil reflection in the referred range is nearly linear. The higher the clay content of the soil is ($\Phi < 0.002$ mm) the stronger the linearity becomes. *Fig. 2* shows the reflection spectra of airdry sandy, loam and clay soils. It supports the view that soil texture has a decisive effect on reflectivity, which is most marked in the range of 500–1000 nm. Parabola can be better fitted to the measurements: r=0.985–0.999. The average quadratic coefficient is $-4.8 \cdot 10^{-5}$ for sandy soils (clay content $<10\%$); and $-2 \cdot 10^{-5}$ for clayey soils (clay content $>40\%$, mass ratio of sand 20%). The final conclusion on basic physical soil types can be described as follows

$$\begin{aligned}
\text{sand:}\quad & R_H\ \%\ (\lambda) = -5.4 \cdot 10^{-5} \times \lambda^2 + 0.124 \times \lambda - 37.1,\\
\text{loam:}\quad & R_V\ \%\ (\lambda) = -3.5 \cdot 10^{-5} \times \lambda^2 + 0.091 \times \lambda - 27.6,\\
\text{clay :}\quad & R_A\ \%\ (\lambda) = -0.6 \cdot 10^{-5} \times \lambda^2 + 0.036 \times \lambda - 11.3,
\end{aligned}$$

where λ is the wavelength. The reflection spectrum of different soils can be

described in different ways, by different parameters. The characteristic parameters used in the measurements are

- reflection in 400 nm,
- slope in the *range* of 400–1000 nm (direction tangent),
- the precision of linear trend fitting,
- the precision of quadratic trend fitting.

The reflection values at 400 nm are significantly different for major physical soil types: sand=3.7–4.6%, loam=2.8–3.5%, clay=1.9–2.6%. The 400 nm reflection value can be considered as a deterministic parameter as it conse-

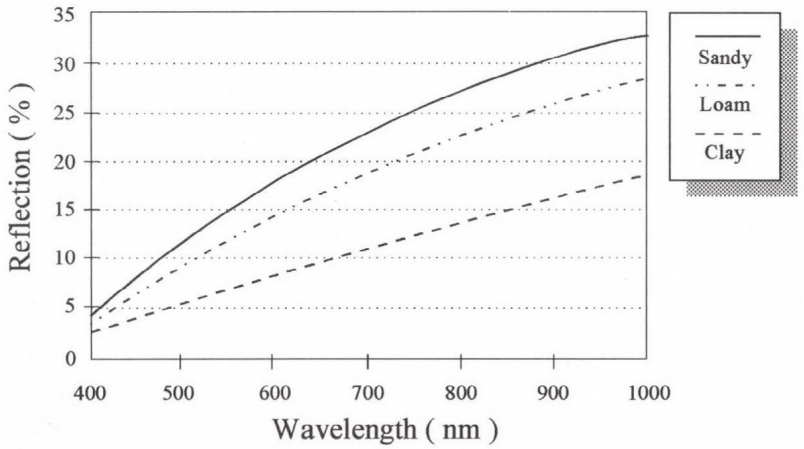

Fig. 2. The spectral reflection of different soils.

quently changes with the clay content ratio. The band 400–1000 nm is the most significant range of the solar spectrum. The lowest reflection value was measured at about 400 nm. Maximum soil reflection was measured in the range of 1200–1300 nm which supports *Baumgardner et al.*'s (1985) findings. The investigations show that the lower the clay fraction ratio, the steeper the referred range of the spectrum. According to the analyses of some 80 soil varieties collected in Hungary, the steepness of reflection spectrum in sandy soils is 3.0%/100 nm, it is 1.5%/100 nm in loam and it is as low as 1.0%/100 nm for clay. This allows to determine the physical type of the soil by its reflexion spectrum.

A linear equation can very well be fit to the referred range of the reflection spectrum. For the examined soils the fit is between r=0.92–0.99 (n=36). For parabolic equations r=0.95–0.99.

This regularity can be used for the categorization of undefined soils. Let's take the definite integral (D_i)

$$D_i = \frac{1}{1000 - 400} \int_{400}^{1000} (Rx\,(\lambda)) - (Ri\,(\lambda))\, d\lambda,$$

where $Rx(\lambda)$ is the spectral reflectivity of the unknown, $Ri(\lambda)$ is the spectral reflectivity of the known soil sample. The smaller the difference will become, the more similar the undefined characteristics is to the known soil type. It was found that, in 70% of the cases, this classification gives the same result as the classification made by granule composition definition. The method can be further developed if the number of the known soil categories is increased.

2.2 The effect of soil ingredients on the reflection spectrum

Soil ingredients are minerals and organic matters produced by different chemical processes. About 95% of materials of mineral origin derive from sedimentary rocks. The mineral ingredients of the soil are oxides, silicates, phosphates, sulphates, carbonates and chlorides (*Di Gleria et al.*, 1957). These materials are present in the form of compounds of different crystal structures. They differ in colour, and so, they have different optical characteristics. Below, some of the spectrometric characteristics of soil ingredients will be discussed. The results refer to airdry conditions.

Humus

It is the most important component of fertile soil, its volume percentage varies between 1–7%. As humus content increases, reflection decreases. Turf is the richest in humus, its reflection being the lowest. This soil nears black body both in the visual and infrared ranges ($R<7\%$).

Clay minerals

They are very important building blocks of the soil, effecting soil nutrient and water management (*Stefanovits*, 1981). The following clay minerals were examined: kaolinite, montmorillonite, illite; they are of fairly different crystal structure, their attitudes to water also differ. They belong to silicates mainly, which is of importance in thermoemission. They do not differ significantly in the visual range, but marked differences (as the effect of hydroxile residue) can be found in the infrared range (*Csákiné Michéli*, 1991). Reflection decrease is the strongest in the montmorillonite (27%), it is weaker in the kaolinite (18%). No difference can be found in the range of the second hydroxile residue (*Figs. 3a, 3b, 3c*).

Soil ingredients represent different volume percentages in the soil which, in turn, affects reflection (*Fig. 4*).

Ferric oxide (Fe_2O_3)

Ferric oxide affects the reflecting capacity of the soil fairly significantly. As it is known, Fe_2O_3 and Fe_3O_4 have very different reflecting characteristics. The reflecting capacity of Fe_3O_4 is constant in the examined range, whereas that of Fe_2O_3 depends on the wavelength. The dominant feature in the 650–760 nm red

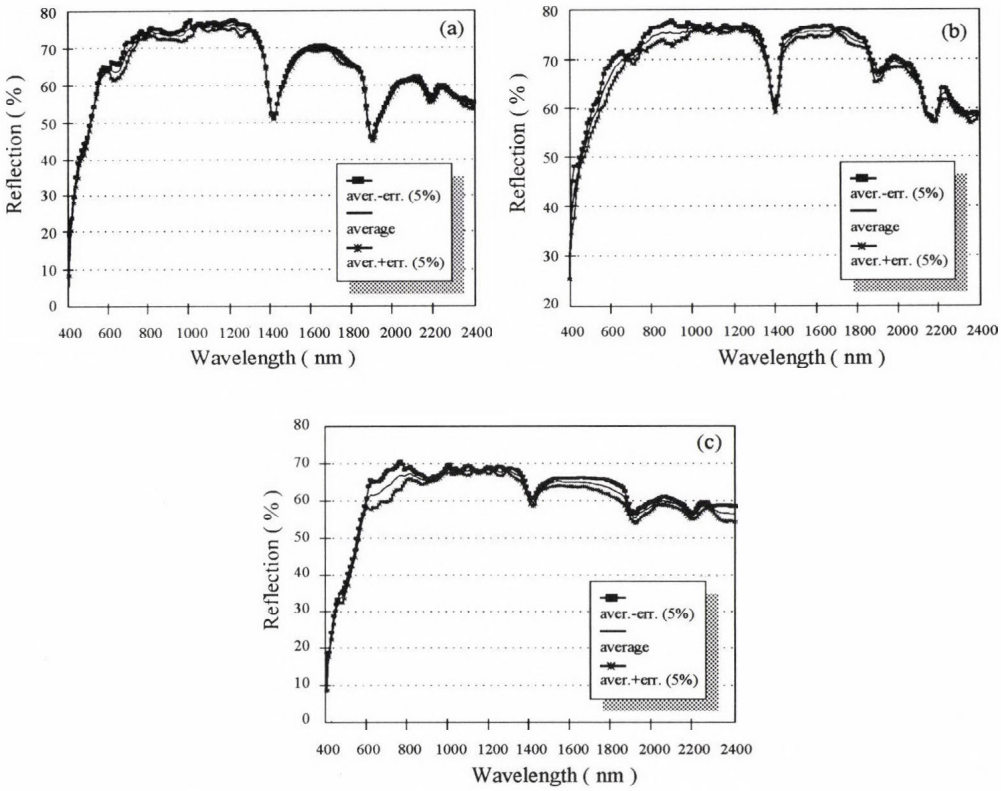

Fig. 3. The spectral reflection of montmorillonite *(a)*, caolinite *(b)* and illite *(c)*.

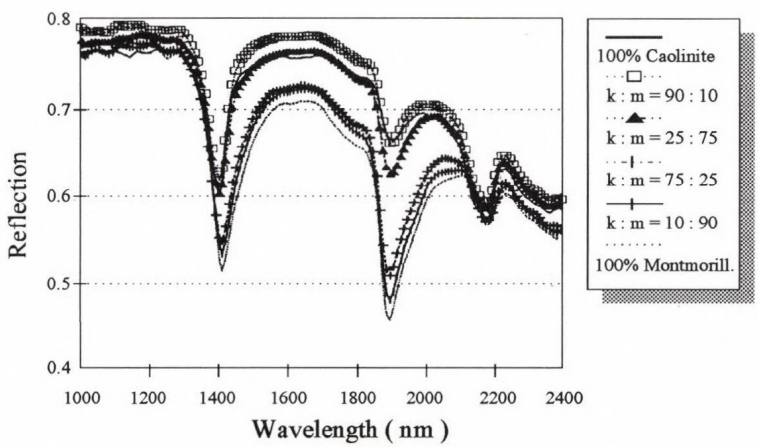

Fig. 4. The spectral reflection of the mixture of montmorrillonite and caolinite of different mass proportions.

range is the reflection, in the 450–500 nm blue range it is the absorption.

Airdry soils contain Fe_2O_3 mainly, and, so, spectral characteristics can be used for the quantitative definition of iron in the soil. The significant differences that exist between the reflection of different physical soil types should not be ignored though, as they may cover up the effect of ferric oxide. Consequently, no relationship generally applicable for all soil types can be established between reflection and Fe_2O_3 content.

Ferric oxid in loom

The majority of the examined samples was loam, so the conclusions below will refer to this soil type. For quantitative determination *Obuhov* and *Orlov* (1964) suggest the $C\% = 17.35 - 0.20\ R\%$ (640) relation between Fe_2O_3 content (C) the reflection value (R) in the 640 nm range. This relation was not proven by our investigations.

A new reflection parameter was introduced in the evaluation process, a *NRB* (normalized red-blue) index, which is defined as follows

$$NRB = \frac{R\%\,(710) - R\%\,(480)}{R\%\,(710) + R\%\,(480)}.$$

$R\%$ (710) is the reflection in 710 nm, $R\%$ (480) is the refleciton in 480 nm. In the samples this index varies between 0.25–0.5 and shows a strong relationship to the iron content of the soils. The equation used for the determination of $C\%$ (Fe_2O_3 content) is this

$$C\% = 1.09 + 11.5\ NRB\ (R = 0.75).$$

It should not be forgotten that this equation refers to loam soils only, where the iron content determined with X-ray fluorescent method is 2–5%. To establish similar relationship for sandy and clay soils is a task to be solved in future.

Soil humidity

It is the soil humidity that can modify the reflection spectrum most strongly. Soils hold their water contents against gravity with the help of capillary and sorption forces. Basically, the reflection effect of water content is expressed by the relationship between clay fraction and spectrum characteristics. The spectral charasteristics effected by humidity are:

- the measure of linearity,
- the R_{400}/R_{1000} quotient, slope,
- the R_{400} value,
- hydrate-adsorption in NIR.

Linearity has already been discussed, now it has to be added that it is increased by the growth of water content. The R_{400}/R_{1000} quotient is a specific parameter. In clay soils (clay fraction >60%) the slope is not significantly

increased by raised water content. The slope changes slightly in loam, but sharply in sand. Consequently, the angle of dry and wet spectra curve serves as a soil type specific parameter (*Fig. 5*).

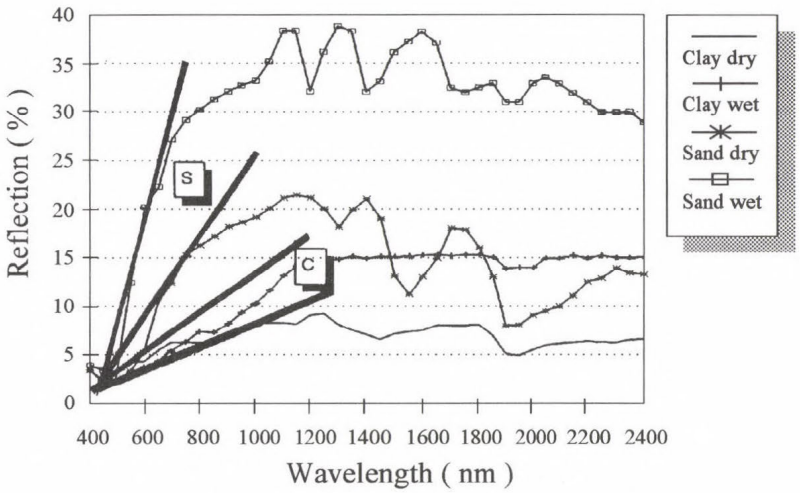

Fig. 5. The spectral reflection of dry and wet sand and clay soils.

Soil roughness

Natural soils, and even laboratory soil samples have more or less rough surfaces. (Even pressed soils are considered rough. This can easily be detected with a simple magnifying glass.)

If the reflections of a relatively smooth surface and those of its roughened variety are compared, the conclusion is that the size of reflection decreases as roughness increases. This can be explained with the following two simple models

(a) Mirroring reflecting surface

Supposing that plane surfaces totally reflect incoming light, according to the law of reflection, radiation will be detected in one direction only. If the rough surface is modelled by triangles, radiation will be detected in several directions, supposing again total reflection from the sides of the triangles.

(b) Lambert surface

The radiation of the real Lambert surface is constant, whichever direction is considered

$$L(\theta, \Phi) = a/\pi \; L_0 \sin\alpha ,$$

where L is the irradiation, a is the albedo of the surface, α is the angle of irradiation, L_0 is the radiation of the source of light.

This means that the *BRDF* (see Fig. 1) of the Lambert-type surface is independent of the direction of lighting and observation, it only depends on the albedo of the surface

$$BRDF\ (\text{Lambert}) = a/\pi.$$

If the rough surface is modelled by triangles whose sides are supposed to be Lambert-type reflecting surfaces , and the irradiation of the surface elements by each other is neglected (this factor is of importance only for bright surfaces—R nears one—and by high β values), the radiation of the surface can be defined in the following way (*Fig. 6*)

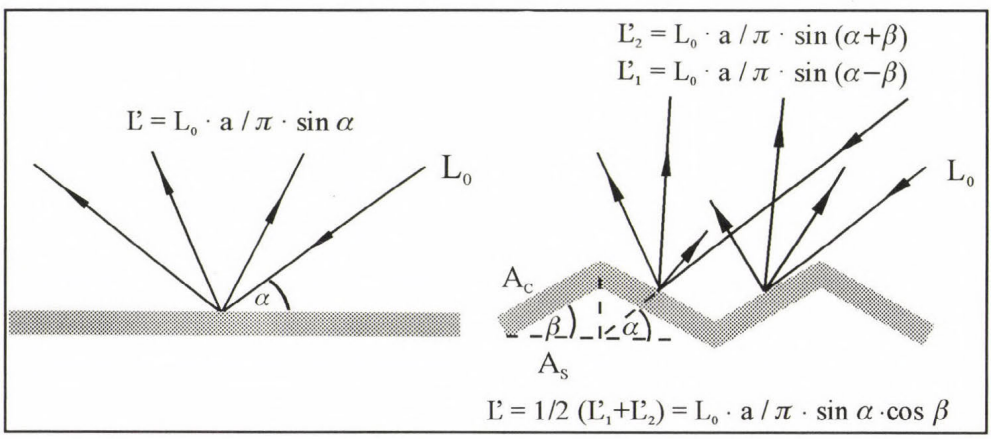

Fig. 6. The diffuse reflection of plane and rough surfaces.

$$L(\theta, \Phi) = R/\pi\ L_0\ \sin\alpha\ \cos\beta;$$

the *BRDF* of rough surfaces, consequently, is

$$BRDF(\text{rough}) = a/\pi\ \cos\beta.$$

If the result is compared with the *BRDF* of plane Lambert surface

$$BRDF(\text{rough}) = BRDF(\text{Lambert})\ \cos\beta.$$

According to Fig. 6 $\cos\beta$ is

$$\cos\beta = A_s(\text{plane})/A_c(\text{rough}),$$

the converse of unit rough surface per unit plane surface. This value is considered as the roughness characteristic.

A rough surface can be taken as a random distribution of elementary plane surfaces (mirroring and Lambert-type), which explains reflection decrease against the increase in roughness.

This method can be improved if soil granules are modelled with spheres. A very reliable model was elaborated by *Cierniewski* (1987), in which soils are modelled by spheres placed on directed surface. Unit sphere surface per unit surface seen from above is taken as roughness factor. The distance between the centres of the spheres is larger than their diameters, and so their reciprocal shading effect, which produces ellipses in this case, has also to be taken into consideration.

A practicable method was also elaborated by *Bunnik* (1987), in whose SOIL model soil surface is modelled by cylinders placed on a horizontal surface. The advantage of this method is its suitability to model for example the reflection of forests by enlarging sizes.

Investigations were made into the question whether roughness modifies the spectral composition of reflected radiation. It was established that roughness decreases reflection in all ranges, but no spectral differences were found.

A further question is whether there are differences between the reflections of parallely and perpendicularly lit surfaces if furrows are cut into the soil samples. This simple modelling was designed to explain the relationship between furrow direction and reflection. (A similar question arises when the effect of the row direction of grown plants on reflection is investigated.) It was found that furrows perpendicular to lighting direction significantly reduce reflection. (This, of course, means radiation reflected into zenith point. Furrows perpendicular to lighting backscatter considerably higher than those parallel to lighting.)

If lighting is homogeneous and the sample is turned around, no statistically provable differences were detected.

4. Discussion of research results

As a conclusion, it can be established that the vertical brightness coefficient measured under equal geometrical conditions expresses several material characteristics of the surface and is strongly modified by the changes in the conditions. This value transformed to π solid angle will give the albedo. Yet, it has to be noted that this value is the *homogeneous albedo*. Obviously, no such homogeneous surface exists in reality, and so, the calculated value will only approximate the conventionally measured albedo.

(1) The albedo of rough surface can be determined as the weighted sum of the measured *BC* values (brightness coefficient). Weighting is made by the cosinus of the angle of observation (θ') by this integral

$$a_r = \int_0^{\pi/2} BC(\theta') \cos\theta' \sin\theta' \, d\theta'.$$

If soil reflection is perfectly Lambert-type, *BC* would give a constant value

independent of direction, and so

$$a_L = \pi\ BC$$

that is, the albedo can be calculated if plumb point *BC* is known.

(2) Soil reflection cannot be considered Lambert-type, not even approximately. The greater the deviation of the soil from the ideal diffuse reflection surface, the more the deviation of the albedo calculated from the actual one. The relation between the two albedoes is characteristic of the soil and is affected mainly by roughness, consequently, it can be considered as the optical roughness parameter (*ORP*)

$$ORP = a_r/a_L = a_r/\pi\ BC.$$

a_r is the albedo of the rough and a_L is that of the Lambert surface. If the roughness parameter is known, the albedo of the surface can be determined by measuring the plumb point *BC*.

(3) The radiation arriving at a given plane and reflected to the total hemisphere, and also the proportion between them, can be measured with pyranometers. This measurement involves the effect of the roughness and the deviation from the Lambert surface. The magnitude of the two effects is

$$\triangle a = a_L - a_m,$$

a_m is the measured albedo value. The smaller the $\triangle a$, the smaller the degree of the roughness of the surface.

The conclusions made above support the view that the spectral analysis of reflection supplies plenty of practical information to increase the efficiency of interpretation.

Acknowledgements—Authors are grateful to *Academician G. Várallyay* director of the Department of Soil and Agrochemical Research Institute of Hungarian Academy of Science and to *Academician P. Stefanovits*, for their contribution with soil samples and clay minerals for the measurements.

This work has been supported by *Hungarian Academy of Sciences* as an OTKA project, contract number: 1173.

References

Baumgardner, M.F., Silva, L.F., Biehl, L.L. and *Stoner, E.R.*, 1985: Reflectance properties of soils. *Adv. Agron. 38*, 1-44.

Bunnik, N.J.J., 1987: The multispectral reflectance of shortwave radiation by agricultural crops in relation with their morphological and optical properties. Mededelingen Lnadbouwhogescholl, Wageningen, The Netherlands, 78-100.

Cierniewski, J., 1987: A model for soil surface roughness influence on the spectral response of bare soil in the visible and near infrared range. *Remote Sens. Environ. 23*, 97-115.

Csákiné Michéli, Erika, 1991: *The Complex Optical Reflectance of Artificial Mineral Humus* (in Hungarian). Ph. D. Thesis. Agricultural University, Gödöllő, Hungary.

Di Gleria, J., Klimes-Szmik, A. and *Dvoracsek, M.*, 1951: *Soil Physics and Soil Colloids* (in Hungarian). Akadémiai Kiadó, Budapest.

Obuhov, A.E. and *Orlov, D.S.*, 1964: Spectral reflectivity of major soil groups and possibility of using diffuse reflections in soil investigations (in Russian). *Soviet Soil Science 1*, 174-184.

Stefanovits, P., 1981: *Soil Science* (in Hungarian). Mezőgazdasági Kiadó, Budapest.

Szász G., 1987: The importance of agricultural remote sensing in agrometeorology (in Hungarian). *Időjárás 91*, 88-103.

IDŐJÁRÁS

Quarterly Journal of the Hungarian Meteorological Service
Vol. 98, No. 1, January–March 1994

Validation of crop simulation model CERES-Maize

M. Hunkár

Agrometeorological Research Station,
P.O. Box 80, H-8361 Keszthely, Hungary

(Manuscript received 14 January 1994; in final form 3 March 1994)

Abstract—A crop simulation model must first be capable of representing the actual performance of crops grown in any particular region before it can be applied to the prediction of agrotechnology or climate change impacts. CERES-Maize model was developed by the United States Department of Agriculture, Agricultural Research Service (USDA-ARS). The model is designed to simulate the effects of cultivar, planting density, weather, soil moisture and nitrogen on crop growth, development and yield. Version 2.1 was used in the present study. Crop analysis of maize was carried out at the Agrometeorological Research Station at Keszthely, Hungary in the years 1976-1991. Measured and simulated data of silking date, maturity date, leaf area maximum, final biomass and grain yield were compared. The average differences between the predicted and observed plant characteristics are not more than 4%. The probability, that of CERES-Maize model simulated yield and biomass agreed within 15% with observed values in a given year, is 80%. A summarized index-value was developed with a scale ranging from 0 to 5. On the basis of 16 years simulation experiments the index-value of CERES-Maize model was 4.23.

Key-words: maize, simulation model, CERES-Maize, validation.

1. Introduction

"Simulation may aid the understanding of important aspects of complex systems in such a way that their behaviour is visualized and a guide to their management is obtained. But solutions are only accepted as such methods to falsify them are available, if they can be verified or their usefulness can be proven" (*Rosenberg et al.*, 1992). Several crop models are known in the literature and most of them is unique concerning their input requirements therefore the adaptation and validation of any models is not an easy task.

The International Benchmark Sites Network for Agrotechnology Transfer (IBSNAT) Project was established in 1982 in the USA (*IBSNAT*, 1990). The IBSNAT project was designed to provide the structure and mechanism to link soil, moisture conditions, weather, crop and management research efforts into

a coherent problem-solving procedure. In the first phase of the project twelve main food crops (maize, rice, sorghum, millet, barley, wheat, soybean, peanut, phaseolus bean, cassava, taro and potato) were identified for model development and simulation. These twelve food crops were divided into three groups on the basis of their similarity structure. The name of model families are CERES for grain crops, SOYGRO for legumes and SUBSTOR for storage plants. All of the models simulate daily incrementing and require daily weather data consisting of maximum and minimum air temperature, solar radiation and rainfall data as driving forces. Local conditions are described by standard soil characterization. Initial values of water content of the soil are also required. This relative simplicity in data requirement and the detailed documentation of the models make possible to run simulation experiments also for Hungarian conditions. In the present paper the evaluation of CERES-Maize model is given.

2. Material and method

2.1 The crop model

CERES-Maize model (*Jones* and *Kiniry*, 1986) is a multipurpose user-oriented simulation model. In order to accurately simulate maize growth, development and yield, the model takes into account the following processes:

- phenological development, especially as it is affected by genetics and weather,
- extension growth of leaves, stems and roots,
- biomass accumulation and partitioning, especially as phenological development affects the development and growth of vegetative and reproductive organs,
- soil water balance and water use by crop,
- soil nitrogen transformations, uptake by the crop, and partitioning among plant parts.

The model calculates crop phasic and morphological development using temperature data, daylength and genetic characteristics. Leaf expansion, growth and plant population provide information for determining the amount of light intercepted, which is assumed to be proportional to biomass production. The biomass is partitioned into various growing organs in the plant using a priority system. A water and nitrogen balance submodel provides feedback that influences the development of growth processes. These are multilayer models. The number and depth of the layers are optional but it is suggested to reach the depth of root system. There is a possibility to switch off the water and nitrogen submodels which means that the nutrition shortage or water shortage is avoided using fertilizer and irrigation on optimum level. In this case the light and temperature conditions form the potential production.

Crop cultivars differ one from another in a whole array of morphological

and other characteristics. The "genetic coefficients" that summarize the way in which a specific crop cultivar divides up its life cycle, respond to different aspects of its environment, or appear changes morphologically. The number of potential genetic coefficients is very large. However, the general aspects of adaptation to any given environment are determined by a few responses, and these have been taken into account in the current models. For maize there are five coefficients. Three are related to the development and progression through the life cycle, while two are related to growth aspects. To choose appropriate genetic coefficients is a crucial process in model adaptation. The model documentation contains the values of genetic coefficients for about 50 varieties of maize.

2.2 Field experiments

Biomass production, leaf area index and grain yield of maize were measured together with phenological observations at the experimental field of the Agrometeorological Research Station of the Hungarian Meteorological Service at Keszthely in the years 1976–1991. The size of the experimental plot is 900 m^2. Sowing density was 70,000 plants/ha. Sowing depth was 5 cm. The soil is a Ramman type brown forest soil, its characteristics are shown in *Table 1*. Only

Table 1. Soil characteristics of Ramman brown forest soil at Keszthely

Layer mm	Wilting point cm^3/cm^3	Field capacity cm^3/cm^3	Saturation moisture content cm^3/cm^3	Moist bulk density g/cm^3
0 - 5	0.070	0.29	0.46	1.71
5 - 15	0.081	0.32	0.45	1.78
15 - 30	0.095	0.35	0.40	1.96
30 - 40	0.091	0.32	0.45	1.79
40 - 50	0.071	0.35	0.45	1.79
50 - 60	0.091	0.33	0.46	1.79
60 - 70	0.091	0.36	0.44	1.79
70 - 90	0.061	0.38	0.43	1.88
90 -120	0.085	0.36	0.39	2.02
120 -150	0.085	0.36	0.39	2.02

one maize variety was grown in each year but it altered several times during this 16 years period. Maize variety SZTC-255 was used in 9 years, Pioneer 45 3901 in three years, Pioneer 3782 in two years, Pioneer 3978 and KSC-360 in one year. The level of nitrogen fertilization was the same in each year, 200

kgN/ha. This amount can be taken to be optimum. There was no irrigation, the plot was rainfed in each year. Initial soil moisture content was measured at the time of sowing by thermo-gravimetric method. Leaf area index (LAI) and the dry weight of above ground biomass were measured several times during the vegetation period using sample plants. In the present study the maximum leaf area index which occurs at the time of silking, and the final amounts of above ground dry biomass and grain yield containing 15% moisture were used.

The daily meteorological data as minimum and maximum air temperature, global radiation and precipitation amount were measured in a standard way next to the experimental field.

2.3 Simulation experiments

The first step in the model adaptation is to choose or determine the genetic coefficients of the given cultivar. In our case the genetic coefficients had to be estimated on the basis of phenological observations. The applied genetic coefficients are shown in *Table 2*. The meanings of denotations are as follows:

- *P1* – growing degree days base 8°C from seedling emergence to the end of the juvenile phase,
- *P2* – photoperiod sensitivity coefficient. Juvenile phase and photoperiodic sensitivity are uncommon in the routine observation system. They were measured for a number of cultivars grown in controlled environments by *Kiniry et al.* (1983a, b). For other cultivars they can be estimated,
- *P5* – growing degree days base 8°C from silking to physiological maturity,
- *G2* – potential kernel number per plant,
- *G3* – potential kernel growth rate in mg/kernel day.

Table 2. Genetic coefficients applied in simulation experiments for the different cultivars of maize

Cultivar	Genetic coefficients				
	P1	P2	P5	G2	G3
SZTC-255	110	0.1	700	780	8.6
PIO 3901	140	0.1	720	600	9.0
PIO 3782	200	0.7	800	650	8.5
PIO 3978	110	0.1	720	700	10.0
KSC-360	165	0.0	600	760	9.6

Because of the lack of the measurements of nitrogen concentration in the soil and in the plant, the nitrogen submodel was switched off. It may not cause too

much error because the amount of applied nitrogen fertilizer – 200 kg N/ha – can be taken to be optimum as it was shown by *Dávid* (1981).

Simulation experiments were carried out for 16 years using the actual weather data, cultivars, sowing depth and density, and initial soil moisture content.

3. Results and discussion

From the model outputs the date of silking and maturity, the final amounts of biomass, the grain yield and the maximum leaf area index were selected for comparing them with observed data.

Before the year by year analysis let's see the differences in the averages. *Table 3* shows a very good agreement between the predicted and observed average values in the 16 years. The differences in silking date are only 0.2 days, in maturity date 3.3 days, in LAI max 0.01, in grain yield 386 kg/ha, in dry biomass 375 kg/ha. Also the standard deviations of the simulated and observed values are well correlated. This extremely good agreement in the averages means that the CERES-Maize works at least as good as a statistical model. The estimation of the effect of weather for longer period gives reliable results.

Table 3. Averages (av) and standard deviations (sd) of predicted and observed plant characteristics

	Predicted		Observed	
	av	sd	av	sd
Silking date (day of the year)	199.7	8.3	199.5	8.0
Maturity date (day of the year)	260.4	14.6	257.0	14.2
Biomass (kg/ha)	17,716	2,552	18,091	3,124
Grain yield (kg/ha)	10,681	2,190	10,294	2,008
LAI max (m^2/m^2)	3.42	0.64	3.43	0.59

Fig. 1 shows the differences in silking date year by year and the differences between the observed and predicted maturity date. According to the silking date there is no systematic error in the prediction. In most of the years the predicted maturity date occurs later than it was observed. The cumulated distribution of the error of the prediction for these phenological stages are shown in *Fig. 2*. The length of the phenological phase from silking to maturity is influenced by the genetic coefficient *P5*. If we choose smaller value for growing degree days the length of this phase will be shorter. But if this period is shorter the biomass production will be less. It would result improvement only in 50% of the years, in the rest of the years the biomass prediction would be worse and also the grain yield would be less which is not required as it is shown in *Fig. 3*. Since

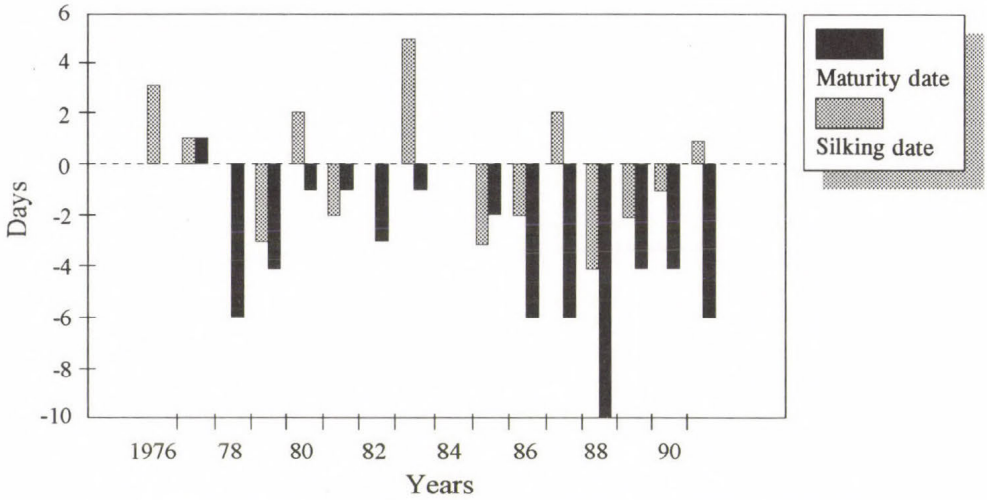

Fig. 1. Differences in silking date and maturity date: observed − predicted.

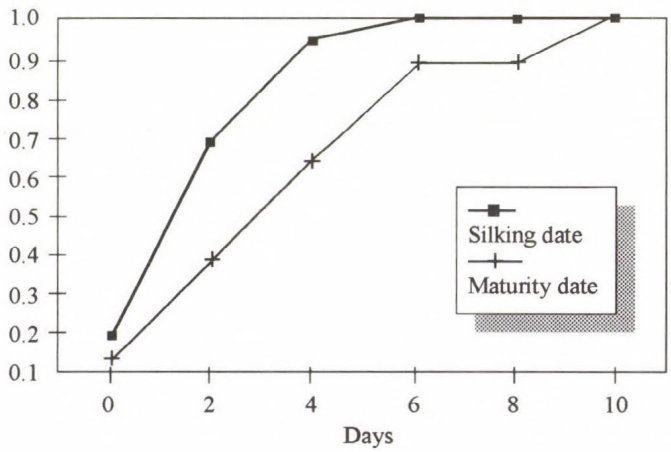

Fig. 2. Cumulative error of model prediction for silking date and maturity date.

the grain yield is the most important output from economical viewpoint in *Fig. 4* also its absolute values are presented year by year. *Fig. 5* shows the cumulative error in percentage for the final amount of biomass and grain yield. The probability, that the differences between the predicted and observed biomass and grain yield are not more than 15%, is at least 80%. The prediction of maximum leaf area can be judged reliable. The differences between the observed and predicted values were larger than one only in 1983 as it can be seen in Fig. 3. The cumulative error for the leaf area maximum can be seen in Fig. 5.

Besides the evaluation of the individual model outputs an index-value was

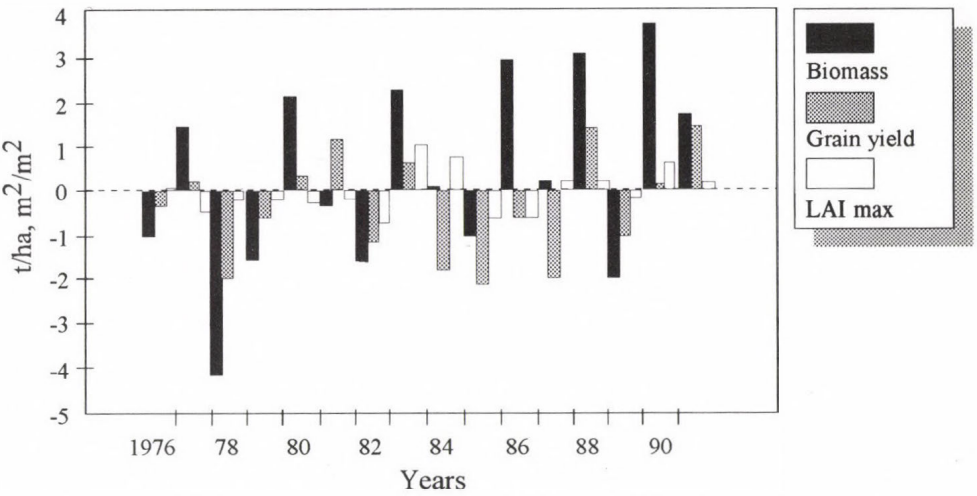

Fig. 3. Differences in the final above ground biomass (t/ha), grain yield (t/ha) and maximum leaf area index (m^2/m^2): observed − predicted.

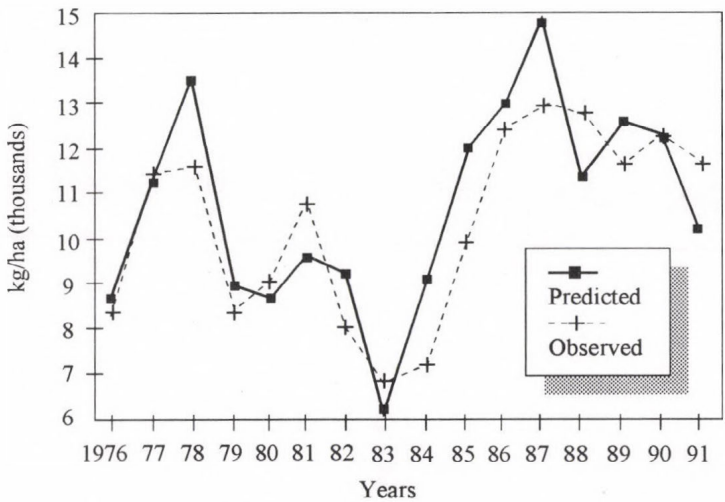

Fig. 4. Predicted and observed grain yield year by year.

created to assess the skilfullness of the model. Considering the differences between the observed and predicted values a more or less arbitrary scale is given for the evaluation. In *Table 4* the skill-score of prediction is presented for the individual outputs. When the predicted value shows a very good agreement with the observed value this output gets 1 point. If the agreement is not so good the output gets a point of less than 1 while a very bad agreement is characterized with 0 point.

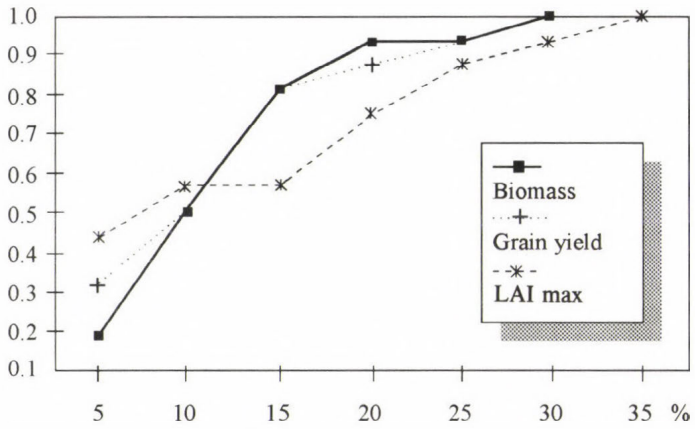

Fig. 5. Cumulative error of model prediction for grain yield, biomass production and maximum leaf area index.

Summing up these points for the five outputs we get an index-value between 0 and 5. In *Table 5* the skill-score of the individual outputs and the index-values of the whole model prediction are presented for each year. In 13 years the index-value is greater than or equal to 4, and its smallest value is 3.5.

Table 4. Scale of skill-scores of prediction

Deviation ± Days	Deviation %	Skill-scores
2	< 5	1.0
3	5 - 10	0.9
4	10 - 15	0.8
5	15 - 20	0.7
6	20 - 25	0.6
7	25 - 30	0.5
8	30 - 35	0.4
9	35 - 40	0.3
10	40 - 45	0.2
11	45 - 50	0.1
> 12	> 50	0.0

4. Conclusions

CERES-Maize model is a comprehensive method for describing growth and development of maize plant. Since the documentation and dissemination of the

Table 5. Skill-scores of model outputs and the index-value for each year

Years	Skill-scores					Index value
	Silking date	Maturity date	Grain yield	Biomass	LAI max	
1976	0.9	1.0	1.0	0.9	1.0	4.8
1977	1.0	1.0	1.0	0.9	0.6	4.5
1978	1.0	0.6	0.7	0.5	1.0	3.8
1979	0.9	0.8	0.9	0.8	1.0	4.4
1980	1.0	1.0	1.0	0.8	0.9	4.7
1981	1.0	1.0	0.8	1.0	1.0	4.8
1982	1.0	0.9	0.8	0.8	0.6	4.1
1983	0.7	1.0	0.9	0.7	0.4	3.7
1984	1.0	1.0	0.5	1.0	0.5	4.0
1985	0.9	1.0	0.6	0.9	0.6	4.0
1986	1.0	0.6	1.0	0.8	0.7	4.1
1987	1.0	0.6	0.7	1.0	1.0	4.3
1988	0.8	0.2	0.8	0.8	0.9	3.5
1989	1.0	0.8	0.9	0.8	1.0	4.5
1990	1.0	0.8	1.0	0.7	0.7	4.2
1991	1.0	0.6	0.8	0.9	1.0	4.3
Averages	0.95	0.81	0.84	0.83	0.81	4.23

model is well organized, the model is well known in a wide area of the world. The effects of meteorological elements are taken into account in explanatory way, and for a longer period the average differences between the predicted and observed plant characteristics are not more than 4%. Considering the extent of this uncertainty the model is suitable for studying climate impact even by this 2.1 version which does not contain the direct effect of atmospheric CO_2 concentration. Recently the model developers have been working on a more sophisticated version for taking into account also the direct effect of the atmospheric CO_2 and other environmental effects including mineral nutrition other than nitrogen and pests as well. It makes possible in the future to study the plant responses to different environmental factors as a part of a whole system.

References

Dávid, A., 1981: Connection between weather, fertilization and characteristics of the development of maize (in Hungarian). *Időjárás 85*, 103-111.

IBSNAT, 1990: *Network Report 1987-1990*, IBSNAT PR., University of Hawaii.

Jones, C. A. and *Kiniry, J.R.* (eds.), 1986: *CERES-Maize A Simulation Model of Maize Growth and Development*. Texas A&M University Press, College Station.

Kiniry, J.R., Ritchie, J.T. and *Musser, R.L.*, 1983a: Dynamic nature of the photoperiod response in maize. *Agron. J. 75*, 700-703.

Kiniry, J.R., Ritchie, J.T., Musser, R.L., Flint, E.P. and *Iwig, W.C.*, 1983b: The photoperiod sensitive interval in maize. *Agron. J. 75*, 687-690.

Rosenberg, N.J., McKenney, M.S., Easterling, W.E. and *Lemon, K.M.*, 1992: Validation of EPIC model simulations of crop responses to current climate and CO_2 conditions: comparisons with census, expert judgement and experimental plot data. *Agricult. Forest Meteorol. 59*, 35-51.

IDŐJÁRÁS

Quarterly Journal of the Hungarian Meteorological Service
Vol. 98, No. 1, January–March 1994

Solar radiation components at Qena, Egypt

Sayed M. El Shazly

Department of Physics, Faculty of Science, Qena University
Qena, A.R. Egypt

(Manuscript received 28 December 1993; in final form 22 February 1994)

Abstract—A solar radiation station has been established in Qena, Upper Egypt. Measurements of hourly global and diffuse solar radiation on a horizontal surface for February and March 1992 have been used to derive formulas that predict the monthly mean of hourly global solar radiation including its diffuse and direct components. A statistical procedure has been developed to compute correlations between the daily global radiation and its diffuse component.

Key-words: solar radiation components, measurements empirical model, statistical correlations, Qena.

1. Introduction

Very precise measurements of different solar radiation components are required for solar energy users in order to design any solar energy system or study of the potential of solar energy in a region. Solar radiation data for most parts of the world are now available (*Lenung,* 1980). However, such information for developing countries is scarce.

Qena is located at the south part of Egypt (ϕ=26°10', λ=32°43', H=78 m asl). She is almost dry and free from clouds all year around, which makes of richly supplied with the available solar energy. The aim of this paper is to describe the station for measuring the global solar radiation and its diffuse component over Qena city, and to present an empirical model derived from the measured data to estimate different solar radiation components.

2. Measurements

Principally, there are three components of paramount importance in solar energy utilization, namely: global (G), diffuse (D) and direct (I) solar radiation.

These components are related to each other according to the following relation (*WMO*, 1983)

$$G = D + I \sin h, \tag{1}$$

where h is the solar elevation angle. In this work both G and D were measured, while I was calculated.

2.1 Measurements and instruments

The solar radiation was measured by two Kipp and Zonen precision pyranometers (Model CM 6B). This type of pyranometers is designed for measuring the irradiance on a plane surface, which consists of the direct and diffuse solar radiation incident from the hemisphere above, and complied with the specification for "first class" pyranometer (*WMO*, 1983). For measuring the diffuse component of solar radiation on the horizontal surface, the direct solar component was shielded semi automatically from one of the two pyranometers, by using shadow band constructed by the author following Kipp and Zonen rules. The band guarantees a stable stand even at high winds. The objective of the shadow band is to intercept the direct radiation of the Sun during the whole day. It intercepts not only the direct radiation but also a small part of the diffuse sky radiation, so the measured data were multiplied by a correction factor (*Latimer* and *Mac Dowall,* 1971) equal to

$$I/(I - F/D), \tag{2}$$

where

$$F/D = \frac{2\omega}{\pi\gamma} \cos^3\delta \, (\sin\phi \, \sin\delta \, H_0 + \cos\phi \, \cos\delta \, \sin H_0). \tag{3}$$

In Eq. (3) ω is the width of the shadow band, γ is its radius, δ is solar declination, ϕ is station latitude, H_0 is the hour angle of the Sun at sunset. For our station and shadow band design (ω=60 mm, γ=610 mm, ϕ=26.10°), the correction factor varies between 1 and 1.14 depending on the measurement date is applied. The setting of the shadow band was checked daily at 11.00 hr making sure of the centering of the Sun image on it. Every few days the band position is adjusted to the declination of the Sun. The pyranometers are securely mounted on steel stands located on the roof of the Faculty of Literature, Qena University (18 m above the ground), free from any obstruction above the plane of the sensing elements. The instruments are not in proximity to light-colored walls or other objects likely to reflect solar radiation on it and it is not exposed to artificial radiation sources.

2.2 Recording system

Two channels solar integrator (Kipp and Zonen, Model CC 12) in

conjunction with the used pyranometers measures the solar irradiance (in W m^{-2}) and calculates the irradiations over selectable periods: 10, 30 or 60 minutes as well as over 24 hr. After requested period (60 minutes), two irradiation values per channel (sub and accumulating totals) and time are available on built in cartridge printer. Along with the solar radiation measurements, all the usual meteorological parameters which include those of particular interest to solar applications, such as temperature, relative humidity, pressure, cloud cover are observed at the same site.

3. Results and discussion

3.1 Monthly mean hourly values

Monthly means of hourly values (expressed in W m^{-2}) are tabulated in *Tables 1* and *2* for February and March 1992 of global (G), diffuse (D) and direct (I) solar radiation as well as the maximum and the minimum values recorded during the hour. The tables include also the standard deviation of the hourly values with respect to its mean, which is a convenient measure of the normal variability of the observed components. It is clear from these tables that the standard deviation is larger, for the same hour in March than in February. This indicates that during March the variability of cloudiness is larger.

The variation of the $\bar{G}$, $\bar{D}$ and $\bar{I}$ with the actual time t, is shown in *Fig. 1*. The curves suggest that the following empirical relations may be written

$$\bar{G} = a_1 + b_1 t + c_1 t^2 , \tag{4}$$

$$\bar{D} = a_2 + b_2 t + c_2 t^2 , \tag{5}$$

$$\bar{I} = a_3 + b_3 t + c_3 t^2 , \tag{6}$$

where a, b and c are constants determined for February and March and given in *Table 3*. It is clear from the figures that a very good fit is obtained between the measured solar radiation data, especially the diffuse component, and their estimation models represented by Eqs. 4, 5 and 6.

3.2 Correlation between the daily global radiation and its diffuse component

For this type of correlation, the most common empirical equations are linear expressions, produced by *Page* (1964)

$$K = 1.00 - 1.13 K_T \tag{7}$$

or cubic ones, suggested by *Klein* (1977), using data from *Liu* and *Jordan* (1960)

Table 1. Monthly means of hourly solar radiation components (W m^{-2}), February 1992. Station: Faculty of Science in Qena

		Time											Total
		7–8	8–9	9–10	10–11	11–12	12–13	13–14	14–15	15–16	16–17	17–18	
Global	Mean	172.0	389.0	586.7	730.0	805.4	814.7	761.5	520.8	422.0	204.8	32.5	5439.4
	Max.	212.4	443.0	643.2	790.0	881.5	898.3	834.8	677.1	470.3	249.7	52.4	
	Min.	130.4	334.4	534.8	677.2	758.0	758.3	710.5	525.1	384.5	175.5	20.9	
	S.D.	23.1	29.4	30.5	31.7	42.1	37.3	33.8	90.8	33.1	19.9	8.6	
Diffuse	Mean	74.7	119.7	142.4	160.7	168.4	171.5	163.6	149.5	124.0	81.6	20.0	1376.1
	Max.	110.4	200.1	191.6	215.4	236.4	244.5	245.4	220.6	180.5	115.2	29.8	
	Min.	62.6	95.3	122.4	141.8	138.4	139.4	144.0	136.0	103.3	71.1	13.9	
	S.D.	13.2	24.2	16.5	20.9	25.4	28.9	29.3	26.3	18.0	11.0	5.2	
Direct	Mean	662	760	838	860	857	839	806	720	594	386	113	7435
	Max.	873	888	896	902	920	913	866	789	692	496	204	
	Min.	167	413	730	767	692	673	662	471	334	280	80	
	S.D.	144	95	38	38	65	63	58	79	83	56	30	

Table 2. Monthly means of hourly solar radiation components (W m^{-2}), March 1992. Station: Faculty of Science in Qena

		Time											Total
		7–8	8–9	9–10	10–11	11–12	12–13	13–14	14–15	15–16	16–17	17–18	
Global	Mean	225.0	480.3	684.3	811.5	886.5	886.3	824.3	678.9	469.3	249.0	56.2	6251.6
	Max.	369.6	604.0	805.0	944.0	1014.0	1012.0	931.0	777.0	574.0	330.0	95.0	
	Min.	145.6	258.0	461.0	403.0	494.0	554.0	558.0	284.0	155.0	58.0	16.0	
	S.D.	50.9	71.0	68.7	110.5	104.7	97.8	77.3	85.7	79.0	48.0	16.0	
Diffuse	Mean	120.9	172.9	213.3	238.4	249.0	259.6	240.6	207.9	174.2	116.6	37.3	2030.6
	Max.	183.9	270.0	354.0	432.0	430.0	437.0	403.0	326.0	247.0	158.0	54.0	
	Min.	86.0	117.0	140.0	127.0	124.0	121.0	117.0	111.0	99.0	52.0	14.0	
	S.D.	27.1	40.0	16.0	78.2	80.8	92.2	72.8	53.1	40.0	24.8	8.8	
Direct	Mean	541.7	669.9	740.5	746.0	746.4	725.7	707.1	650.6	509.3	340.8	110.9	6488.9
	Max.	916	954	974	985	987	973	932	864	769	593	283	
	Min.	80	141	220	64	120	159	189	45	35	16	13	
	S.D.	205.8	196.6	179.0	218.0	198.5	206.8	165.4	161.9	164.7	129.0	62.0	

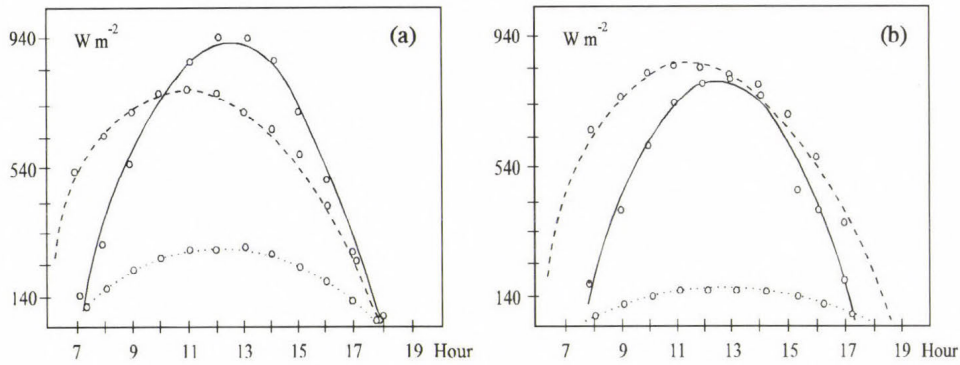

Fig. 1. Mean hourly solar radiation *(a)* for February, *(b)* for March (solid line—global, dotted line—diffuse, dashed line—direct).

$$K = 1.39 - 4.027\,K_T + 5.53\,K_T^2 - 3.108\,K_T^3, \tag{8}$$

where $K=D/G$, $K_T=G/G_0$, G_0 is the daily extraterrestrial, undepleted solar-radiation. The comparison between the values of diffuse ratio K, computed by Eqs. (7) and (8), and the experimental ones has pointed out considerable deviation as displayed in *Fig. 2*. This deviation has been found by other inves-

Table 3. The coefficients a_i, b_i and c_i in Eqs. (4)–(6)

Month	Constant								
	a_1	a_2	a_3	b_1	b_2	b_3	c_1	c_2	c_3
February	-520	-238	346	5660	835	2620	-6000	-886	-3220
March	-334	-393	379	5155	1280	2207	-5548	-1383	-3008

tigators (*Barbaro et al.*, 1981; *Katsoulis* and *Papachristopoulos*, 1978), indicating the important role played by the local influences in the correlation of diffuse radiation with the cloudiness index as has been shown by *LeBaron* and *Dirmhirn* (1983) and *Neuwirth* (1980). In this paper we tried to generate an experimentally derived relationship for Qena, using linear, quadratic and cubic approximations. The best relation was given by the following linear equation

$$K = 1.324 - 1.448\,K_T. \tag{9}$$

The correlation coefficient is 0.98.

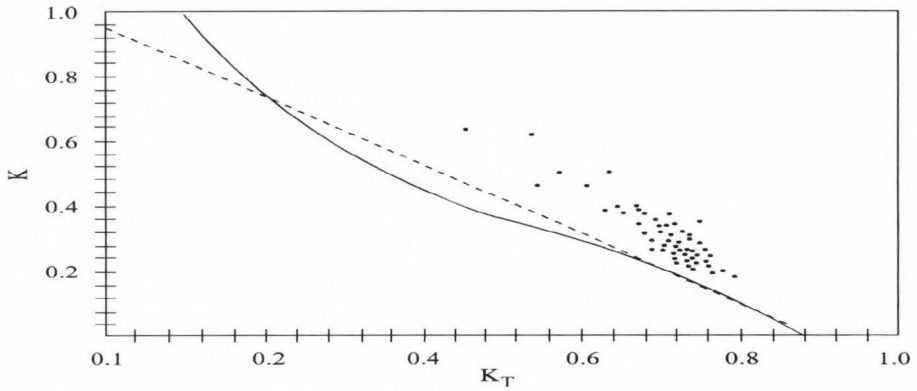

Fig. 2. Relation between daily diffuse ratio K and clearness index K_T.

4. Conclusions

As a first step solar radiation station was established in Qena Upper Egypt, (ideal climate for solar energy projects) to provide information about the available energy in a systematic fashion and with assurances of accuracy. The exposure and installation of the measuring instruments were selected according to the rules given by the World Meteorological Organization.

The analysis of the measurements leads to an empirical model to estimate the global solar radiation with its diffuse and direct components. Correlation between the daily global and diffuse radiation has been studied. The results obtained indicate the effect of locality on the regression formulas. An empirical linear relation was found convenient to fit the measured data in Qena.

The established station will provide intermittently measurements of global and diffuse radiation along with standard meteorological parameters for the future investigations. The data may also serve as a useful reference for system designers and users in other subtropical region of similar climatic conditions.

References

Barbaro, S., Cannata, G., Coppolino, S., Leone, C. and *Sinagra, E.*, 1981: Diffuse solar radiation statistics for Italy. *Solar Energy 26*, 429-435.

WMO, 1983: *Guide to Meteorological Instruments and Method of Observation.* Geneva, Switzerland.

Katsoulis, V.D. and *Papachristopoulos, L.E.*, 1978: Analysis of solar radiation measurements at Athen's observatory and estimates of solar radiation in Greece. *Solar Energy 21*, 217-226.

Klein, S.A., 1977: Calculation of monthly average insolation on tilted surface. *Solar Energy 19*, 325-329.

Latimer, J.R. and *Mac Dowall, J.*, 1971: Radiation measurement, international field year for the Great Lakes. *Technical Manual Series*, No. 2.

LeBaron, B. and *Dirmhirn, I.*, 1983: Strengths

and limitations of the Liu and Jordan model to determine diffuse from global irradiance. *Solar Energy 34*, 167-172.

Lenung, C.T., 1980: The fluctuation of solar irradiance in Hong Kong. *Solar Energy 25*, 485-494.

Liu, Y.H. and *Jordan, R.C.*, 1960: The interrelationship and characteristic distribution of direct, diffuse and total radiation. *Solar Energy 4*, No. 3, 1-19.

Neuwirth, F., 1980: The estimation of global and sky radiation in Austria. *Solar Energy 24*, 421-426.

Page, J.K., 1964: The total estimation of monthly mean values of daily total shortwave radiation on vertical and inclined surfaces from sunshine records for latitude 40°N–40°S. *Proc. UN Conf. New Sources of Energy*, 378-387.

BOOK REVIEW

Wayne, R. P.: **Chemistry of Atmospheres.** Clarendon Press, Oxford. Second edition 1991, reprinted 1992, 1993. pp. 447, 9 chapters.

Since the publication of *Junge*'s classical book on air chemistry in 1963 (Academic Press, New York and London) several volumes have been published on the subject. These volumes differ at least because of two reasons. First, books are different concerning the depth of the discussion of smaller scale air pollution problems. Secondly, some of the books include chapter(s) on ion chemistry in the middle and upper atmosphere, not discussed by *Junge*. Concerning its content and structure the present volume is unique. *Wayne* discusses not only ion chemistry (Chapter 6: *Ions in the atmosphere*) and the chemistry of the airglow (Chapter 7: *The airglow*), but also the properties of *Extraterrestrial atmospheres* (Chapter 8). In addition to this, in Chapter 5 on *The Earth's troposphere* a subsection is devoted to air pollution, while in Chapter 2 (*Atmospheric behaviour as interpreted by physics*) physical and dynamical properties of the Earth's atmosphere are summarized. Consequently, *Wayne*'s publication is the most general textbook of the chemistry of atmospheres (in plural!).

However, the completeness is not the only merit of the author. The text is also clear, relatively short and well-written. This makes the book very useful in teaching the subject at universities according to the author's intentions. The use of the volume by students is facilitated by Chapter 3 which contains the bases of *Photochemistry and kinetics applied to atmospheres.* Further, except figures and tables, literature citations are generally not given in the text. However, very good reference lists follow each chapter, grouped didactically according to subject areas. An other interesting feature of the work reviewed is that the first chapter (*Chemical composition: a preliminary survey*) gives a general survey of the remaining parts of the book. It should be noted that the composition of the Earth's atmosphere is presented in comparison with the gaseous covers of the solar system bodies and the importance of the linkage between the biosphere and the atmosphere on our planet is emphasized. Since the aim of the author is also to present man-made effects on our atmosphere, Chapter 4 entitled *Ozone in Earth's stratosphere* discusses—among other things—ozone trends and the ozone hole problem. In accordance with this aim the last chapter *Evolution and change in atmospheres and climates* contains subsections on the past and future of our atmosphere including possible anthropogenic modifications. In this respect *Wayne* argues that some prospect is the controlled nuclear fusion and he concludes that global warming should

be mitigated by "...harnessing, as a source of energy, the process out of which the Sun, planets and atmospheres were born".

The reviewer believes that even this short discussion is sufficient to demonstrate that the present book is excellent. After reviewing it one can understand why it was published in two editions and the second edition was reprinted two times. Thus, *Wayne's* book is proposed to students, professors and research workers and to everybody who wants to get acquainted easily with the problems of the chemistry of *all* the planets and moons in the Solar System.

E. Mészáros

NEWS

"Science Advice"

Round table discussion in the Club of the Hungarian Academy of Sciences

On 18 January 1994, in the morning, a small round table discussion took place in the Club of the Hungarian Academy of Sciences. The topic was: 'science advice', namely how technical expertise is being provided for decision making in general and in particular in connection with issues such as technological development and environmental change. Participants included the keynote speaker: *Jesse Huntley Ausubel* (Director, Programme for the Human Environment, The Rockefeller University, New York), *Professor Helga Nowotny* (Permanent Fellow, Collegium Budapest), *Professor Ricardo Galli* (Scientific Advisor, Ministry of Universities and Scientific Research, Rome), and a number of Hungarian scientists representing a wide range of disciplines from social to technical sciences, also including meteorology. The round table was chaired by the undersigned.

Jesse Ausubel in his introductory talk provided an outline of the organizational ecology of science advice in America. As he pointed out, one way that the American government has changed in the past 50 years was through the establishment and expansion of organizations providing technical expertise for decision making. He noted that the US government may be these days probably the largest employer of scientists in the world (in 1990 the federal government directly employed 112,000 scientists and 111,000 engineers full-time.)

The vantage point of the keynote speaker from which he overviewed the working of this vast machinery may be considered indeed as quite exceptional. He had been working during the last five years as Director of Studies of the Carnegie Commission on Science, Technology and Government, and this job offered him a particularly deep insight into the whole area. His chosen approach in his keynote lecture was to look at the four essential perspectives identified in the 'cultural theory' of science advice, developed by *Douglas et al.*. Applying this approach he analysed the widely differing views about science advice of the 'elites' (the President and top politicians), the 'bureaucracies', the 'general public', and the 'independent (activist) groups'.

All four perspectives are associated with certain characteristic views on 'science advice' and the corresponding actors (elites, bureaucracies, etc.) all have their own specific views on where the shortcomings of the existing mechanisms for science advice may be. These views are widely divergent and sometimes even conflicting, which may be in itself a very interesting subject for closer analysis.

While we cannot go into the details, it may be interesting to mention here—with special regard to global environmental issues—a strong critical remark about the US research community, which is usually voiced by the so-called 'organized activists'. They say that the research community has become much less independent of the government than it used to be. Hence, they say, there is too much positive feedback at higher levels: the 'Republic of Science' has been corrupted. This opinion encapsulates a polarized conflict of opinion between the 'independents' and the establishment. In activists' views loss of independence means loss of credibility, whereas in the opinion of the elites (and the bureaucracies as well) more independence goes along with less responsibility.

After the keynote lecture the ensuing lively discussion converged on the problems of science advice in Hungary and on comparisons of approaches in America, in Italy and in Hungary. To summarize such debates in a few words is quite impossible. One could only try to highlight some reflections.

The American model of 'science advice' appears to be based on permanent structures and networks, which all continue working and speak up whenever they see a problem, even if unrequested. On the top of this network there are 60 key scientific positions which are strongly rotated among a much larger group of top scientists in reserve.

Opposite to this, in Hungary, science advice is being provided mainly through ad hoc committees which only exist, work and speak if requested, and they only respond to the questions on which they are requested to speak. These ad hoc groups are changing, but the persons involved are often the same. In Italy a revolving door operates between the government, the universities, the research institutes, etc., and thereby provision is made for the necessary rotation. (However, some outstanding personalities tend to be present everywhere and tend to know everything better, which may be a source of difficulties.)

Concerning the Hungarian side, some comments were also made that perhaps the Academy of Sciences could have the potential of providing an independent voice in science advice, thereby to bridge the credibility gap, but it was also noted that currently there may be difficulties in turning this potential into a reality.

Another point made was that—at least in Hungary—proponents of science may be sometime too anxious to combat against everything that is not 'science proper'. In this effort, along with 'bad science', a potential ally, 'proto-science' is often tactlessly also turned away and alienated (a strong enough reason for public anti-science feelings). Perhaps it would be beneficial for the promotion of a truly effective distribution of scientific information and knowledge to embrace more heartily the proto-professional groups (such as teachers of public schools, or science writers and journalists) in some circles of science proper.

In conclusion it may be most fitting to put on record a remark made during the discussion by *Professor Helga Nowotny*: "...internationalization in science tames partisanship". We trust it does, and we confidently hope that the round table discussion summarized above was a step in this direction.

R. Czelnai

ATMOSPHERIC ENVIRONMENT

an international journal

To promote the distribution of Atmospheric Environment *Időjárás* publishes regularly the *contents* of this important journal. For further information the interested reader is asked to contact *Dr. P. Brimblecombe,* School for Environmental Sciences, University of East Anglia, Norwich NR 7TJ, U.K.

Volume 27A Number 17/18 1993

Arctic Air, Snow and Ice Chemistry

Section II: The Arctic Gas and Aerosol Sampling Program (AGASP)

Section III: Arctic snow and ice chemistry

Section IV: Monitoring programs: atmospheric chemistry and meteorology in the Arctic

Volume 28 Number 1 1994

Surface Ozone

A.S. Lefohn: Introduction: The special issue of *Atmospheric Environment* on surface ozone, 1-2.

C. Cartalis and *C. Varotsos*: Surface ozone in Athens, Greece, at the beginning and at the end of twentieth century, 3-8.

S.J. Oltmans and *H. Levy II*: Surface ozone measurements from a global network, 9-24.

Young Sunwoo, G.R. Carmichael and *H. Ueda*: Characteristics of background surface ozone in Japan, 25-37.

J.F. Austin and *R.P. Midgley*: The climatology of the jet stream and stratospheric intrusions of ozone over Japan, 39-52.

T.D. Davies and *E. Schuepbach*: Episodes of high ozone concentrations at the Earth's surface resulting from transport down from the upper troposphere/lower stratosphere: a review and case studies, 53-68.

V.W.J.H. Kirchhoff and *E.V.A. Marinho*: Layer enhancements of tropospheric ozone in regions of biomass burning, 69-74.

J. Staehelin, J. Thundium, R. Buehler, A. Volz-Thomas and *W. Graber*: Trends in surface ozone concentrations at Arosa (Switzerland), 75-87.

U. Pedersen and *A.S. Lefohn*: Characterizing surface ozone concentrations in Norway, 89-101.

T. Laurila and *H. Lättilä*: Surface ozone exposures measured in Finland, 103-114.

J.S. Bower, K.J. Stevenson, G.F.J. Broughton, J.E. Lampert, B.P. Sweeney and *J. Wilken*: Assessing recent surface ozone concentrations in the U.K., 115-128.

J.P. Beck and *P. Greenfelt*: Estimate of ozone production and destruction over northwestern Europe, 129-140.

P.R. Miller, M. de Lourde de Bauer, A.Q. Nolasco and *T.H. Tejeda*: Comparison of ozone exposure characteristics in forested regions near Mexico City and Los Angeles, 141-148.

D. Kley, H. Geiss and *V.A. Mohnen*: Tropospheric ozone at elevated sites and precursor emissions in the United States and Europe, 149-158.

Chung-Ming Liu, Ching-Ya Huang, Shinn-Liang Shieh and *Ching-Chi Wu*: Important meteorological parameters for ozone episodes experienced in the Taipei Basin, 159-173.

Volume 28 Number 2 1994

N.L. Rose and *S. Juggins*: A spatial relationship between carbonaceous particles in lake sediments and sulphur deposition, 177-183.

J.F. Pankov: An absorption model of gas/particle partitioning of organic compounds in the atmosphere, 185-188.

J.F. Pankow: An absorption model of the gas/aerosol partitioning involved in the formation of secondary organic aerosol, 189-193.

J.C. Dechaux, V. Zimmermann and *V. Nollet*: Sensitivity analysis of the requirements of rate coefficients for the operational models of photochemical oxidants formation in the troposphere, 195-211.

H. Akimoto and *H. Narita*: Distribution of SO_2, NO_x and CO_2 emissions from fuel combustion and industrial activities in Asia with $1° \times 1°$ resolution, 213-225.

J.C. Little, A.T. Hodgson and A.J. Gadgil: Modeling emissions of volatile organic compounds from new carpets, 227-234.

Z. Klimont, M. Amann, J. Cofala, F. Gyárfáš, G. Klaassen and *W. Schöpp*: An emission inventory for the Central European Initiative 1988, 235-246.

R.M. Harrision and *I.M. Msibi*: Validation of techniques for fast response measurement of HNO_3 and NH_3 and determination of the $[NH_3]$ $[HNO_3]$ concentration product, 247-255.

Technical Notes

Short Communications

NOTES TO CONTRIBUTORS

The purpose of *Időjárás* is to publish papers in the field of theoretical and applied meteorology. These may be reports on new results of scientific investigations, critical review articles summarizing current problems in certain subject, or shorter contributions dealing with a specific question. Authors may be of any nationality but papers are published only in English.

Papers will be subjected to constructive criticism by unidentified referees.

* * *

The manuscript should meet the following formal requirements:

Title should contain the title of the paper, the names(s) of the author(s) with indication of the name and address of employment.

The title should be followed by an *abstract* containing the aim, method and conclusions of the scientific investigation. After the abstract, the *key-words* of the content of the paper must be given.

Three copies of the manuscript, typed with double space, should be sent to the Editor-in-Chief: *P.O. Box 39, H-1675 Budapest,* Hungary.

References: The text citation should contain the name(s) of the author(s) in Italic letter or underlined and the year of publication. In case of one author: *Miller* (1989), or if the name of the author cannot be fitted into the text: *(Miller,* 1989); in the case of two authors: *Gamov* and *Cleveland* (1973); if there are more than two authors: *Smith et al.* (1990). When referring to several papers published in the same year by the same author, the year of publication should be followed by letters a,b etc. At the end of the paper the list of references should be arranged alphabetically. For an article: the name(s) of author(s) in Italics or underlined, year, title of article, name of journal, volume number (the latter two in Italics or underlined) and pages. E.g. *Nathan, K. K.,* 1986: A note on the relationship between photosynthetically active radiation and cloud amount. *Időjárás 90,* 10-13. For a book: the name(s) of author(s), year, title of the book (all in Italics or underlined with except of the year), publisher and place of publication. E.g. *Junge, C. E.,* 1963: *Air Chemistry and Radioactivity.* Academic Press, New York and London.

Figures should be prepared entirely in black India ink upon transparent paper or copied by a good quality copier. A series of figures should be attached to each copy of the manuscript. The legends of figures should be given on a separate sheet. Photographs of good quality may be provided in black and white.

Tables should be marked by Arabic numbers and provided on separate sheets together with relevant captions. In one table the column number is maximum 13 if possible. One column should not contain more than five characters.

Mathematical formulas and *symbols:* non-Latin letters and hand-written marks should be explained by making marginal notes in pencil.

The final text should be submitted both in manuscript form and on *diskette.* Use standard 3.5" or 5.25" DOS formatted diskettes for this purpose. The following word processors are supported: WordPerfect 5.1, WordPerfect for Windows 5.1, Microsoft Word 5.5, Microsoft Word for Windows 2.0. In all other cases the preferred text format is ASCII.

* * *

Authors receive 30 *reprints* free of charge. Additional reprints may be ordered at the authors' expense when sending back the proofs to the Editorial Office.

Published by the Hungarian Meteorological Service

Budapest, Hungary

INDEX: 26 361

HU ISSN 0324-6329

IDŐJÁRÁS

QUARTERLY JOURNAL
OF THE HUNGARIAN METEOROLOGICAL SERVICE

CONTENTS

VOL. 98 * NO. 2 * APRIL–JUNE 1994

IDŐJÁRÁS

Quarterly Journal of the Hungarian Meteorological Service

Editorial Office: P.O. Box 39, H–1675 Budapest

Subscription from customers in Hungary should be sent to the Financial Department of the Hungarian Meteorological Service Kitaibel Pál u. 1, 1024 Budapest. The subscription rate is HUF 2000.

Abroad the journal can be purchased from the distributor: KULTURA, P.O. Box 149, H–1389 Budapest. The annual subscription rate is USD 56.

IDŐJÁRÁS

Quarterly Journal of the Hungarian Meteorological Service
Vol. 98, No. 2, April–June 1994

Application of nonlinear dynamics in atmospheric sciences Part II. Some examples

G. Götz

Hungarian Meteorological Service
P.O. Box 38, H-1525 Budapest, Hungary

(Manuscript received 1 March 1994; in final form 20 April 1994)

Abstract—The purpose of this review article is to demonstrate the applicability of chaos theory in the study of the nature of atmospheric behavior. Selected examples are chosen to illustrate how the theory of nonlinear dynamics has improved our understanding of the behavior of the atmosphere, and how new ideas and insights are shaping our way of investigating the prediction problem. The examples presented cover a wide range of the frequency domain of atmospheric variability, extending from the phenomenon of cellular convection up to the glacial-interglacial fluctuations of the Quaternary ice age. Special attention is devoted to the nonlinear dynamical aspects of a global climate change. Finally, the existence of low-dimensional atmospheric attractors, a highly debated subject in these days, is discussed.

Key-words: strange attractor, chaos, fractals, predictability.

1. Introduction

The basic goal of dynamical systems theory is to understand the asymptotic consolidated behavior of a given bounded deterministic system as $t \to \infty$. It is now an accepted notion that many *nonlinear* dissipative dynamical systems do not approach stationary, periodic or quasi-periodic final states as transients monotonically die out. Instead, with appropriate values of their control parameters, they tend towards *strange attractors* in the phase space, on which the spectra of the trajectories are not composed solely of discrete frequencies, but have a continuous, broad-band nature. This noise-like consolidated behavior of a deterministic system has been termed *chaotic* or *strange behavior.*

Strange attractors are not smooth topological manifolds, and do not have integer dimension. Typically, a strange attractor arises when the flow of the

dissipative system does not contract a volume element in all directions of the phase space, but stretches it in some. In order to remain confined to a bounded domain, the volume element gets folded at the same time, so that it has after some time a multisheeted structure. A closer study shows that a choatic attractor finally becomes locally Cantor-set like in some directions, and is accordingly a *fractal construction* in the sense of *Mandelbrot* (1977).

Another property of choatic systems is *sensitive dependence on initial conditions*: initially nearby trajectories diverge at a rate characteristic of the system until, for all practical purposes, they are uncorrelated. In practice, the initial state of a system can never be specified exactly, but only to within some tolerance $\epsilon > 0$. Therefore, no matter how precisely the initial condition is known, the long-term behavior of the system can never be predicted. It is the discovery of this property of chaotic systems, also known as *dynamical instability* with respect to small perturbations, that has eliminated one of the basic tenets of science, the Laplacian idea of long-term deterministic predictability.

In order to make quantitative the notion of 'sensitive dependence on initial conditions', Lyapunov exponents are most frequently used. The Lyapunov exponents λ_i ($i = 1, 2, \ldots, n$) of an n-dimensional dynamical system are determined by $\epsilon_i(t) \approx \epsilon(0)\, e^{\lambda_i t}$, and describe the distortion of a sufficiently small hypersphere in the phase space of radius $\epsilon(0)$ at time $t = 0$ into at ellipsoid of principal semi-axes $\epsilon_i(t)$ at $t = t$. Thus, Lyapunov exponents quantify the long-term average dynamical stability properties of the system's behavior on an attractor by measuring the exponential rates of convergence ($\lambda_i < 0$) or divergence ($\lambda_i > 0$) of initially nearby trajectories. A positive exponent indicates chaotic behavior and a loss of predictability.

One limitation of the Lyapunov exponents is that while they describe the stretching needed to generate a strange attractor, they do not say much about the folding. To eliminate this drawback, the dimension of the attractor is used. There are several ways to generalize the concept of dimension to the fractional case (*Farmer et al.*, 1983; *Grassberger* and *Procaccia*, 1983a,b). The relevant definitions are of two general types, those that depend only on metric properties (e.g. the fractal dimension), and those that depend on the frequency with which a typical trajectory visits different regions of the attractor (e.g. the information dimension and the correlation dimension). Another type of dimension is the Lyapunov dimension, which is defined in terms of Lyapunov exponents, and is usually far easier to calculate than any other definition.

The concept of deterministic randomness has initiated a rapidly developing interdisciplinary field of research called *nonlinear dynamics*. As it was discussed in some details in Part I of this paper (*Götz,* 1992), the atmosphere should be considered as a nonlinear system forced by differential heating of the solar radiation, and kept bounded by dissipation of its total energy due to outgoing thermal radiation and the diffusive effects of friction. Therefore, it seems evident that chaos theory has its natural applications in atmospheric sciences,

leading to new ideas and insights, and offering inspiration for further research. The purpose of this part of the article is to give some examples of these applications aiming at a better understanding of weather and climate processes.

2. *The chaotic behavior of atmospheric processes*

In this section, the asymptotic final-state characteristics of some selected macro-scale motion systems of the atmosphere are discussed, and the problem of predictability in nonlinear dynamics is briefly reviewed.

2.1 The Rayleigh-Bénard convection

Historically the irregular and apparently random behavior of a simple deterministic dynamical system was first demonstrated by *Lorenz* (1963) in his work on Rayleigh-Bénard convection, i.e. the flow occurring in a layer of fluid of uniform depth, when the temperature difference between the upper and lower surfaces is maintained at a constant value. The simplified equations governing this forced dissipative hydrodynamic flow are

$$\left.\begin{aligned} dx/dt &= \sigma y - \sigma x, \\ dy/dt &= rx - y - xz, \\ dz/dt &= xy - bz. \end{aligned}\right\} \tag{1}$$

In this third-order autonomous dynamical system, the state variable x is proportional to the intensity of the convective motion, y is proportional to the temperature difference between the ascending and descending currents, while z is proportional to the distortion of the vertical temperature profile from linearity. Among the control parameters of the system, r is the Rayleigh number, i.e. the forcing parameter, which is proportional to the imposed vertical temperature gradient, σ is the Prandtl number of the fluid, and b is related to the aspect ratio of the domain. The variation of the volume V of a small region in the phase space of the system, as each point in the region is displaced in accordance with (1), is

$$dV/dt = -V(\sigma + b + 1). \tag{2}$$

Hence each small volume shrinks to zero as $t \to \infty$, at a rate independent of the state variables. This does not imply that each small volume shrinks to a point; it may simply become flattened into a surface. Consequently, all sufficiently close trajectories become 'attracted' asymptotically to a specific subset of the phase space having zero volume.

Eqs. (1) possess the steady-state solution $x = y = z = 0$, representing the state of no convection. The criterion for the onset of convection is $r = 1$. When $r > 1$, Eqs. (1) have two additional steady-state solutions $x = y = \pm\sqrt{b(r-1)}$, $z = r - 1$. If $\sigma > b + 1$, the states of steady convection are linearly unstable for sufficiently high Rayleigh numbers.

The surprising, previously unknown behavioral form of the deterministic system (1) appears at the slightly supercritical control parameter value of the thermal forcing $r = 28$. For $b = 8/3$ and $\sigma = 10$, and using a standard fourth-order Runge-Kutta scheme with time increment $\Delta t = 0.01$ to integrate the equations, the graph of x as a function of t obtained for the first 4500 iterations is shown in *Fig. 1*. The initial instability of the state of rest is evident; the strength of the convection grows rapidly. After reaching its early peak, it undergoes systematic amplified oscillation. Then a critical state is reached, and thereafter x changes sign at seemingly irregular intervals, reaching sometimes one, sometimes two, and sometimes three or more extremes of one sign before changing sign again. Projections of the transient-free solution trajectory onto the xy-, xz- and yz-planes of the phase space corresponding to iterations 4001 to 9000 are shown in *Fig. 2*. Characteristically, the trajectory travels around one of the two unstable fixed points of the system (which represent the states of steady convection), and crosses from one spiral to the other at irregular intervals. One of the main conclusions is that there are certain thermally (or mechanically) forced nonconservative hydrodynamical systems exhibiting *irregular behavior* when there is *no* obviously related irregularity in the forcing process (*Lorenz,* 1963). The peculiar geometrical object in Fig. 2, resembling an owl's mask or butterfly's wing, is now known as the *Lorenz attractor* of the Lorenz equations (1).

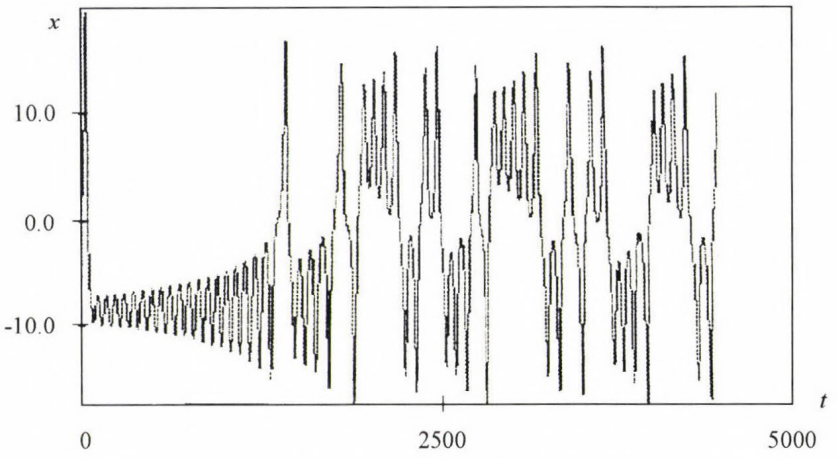

Fig. 1. Numerical solution of the Rayleigh-Bénard convection equations. Graph of x as a function of time for the first 4500 iterations.

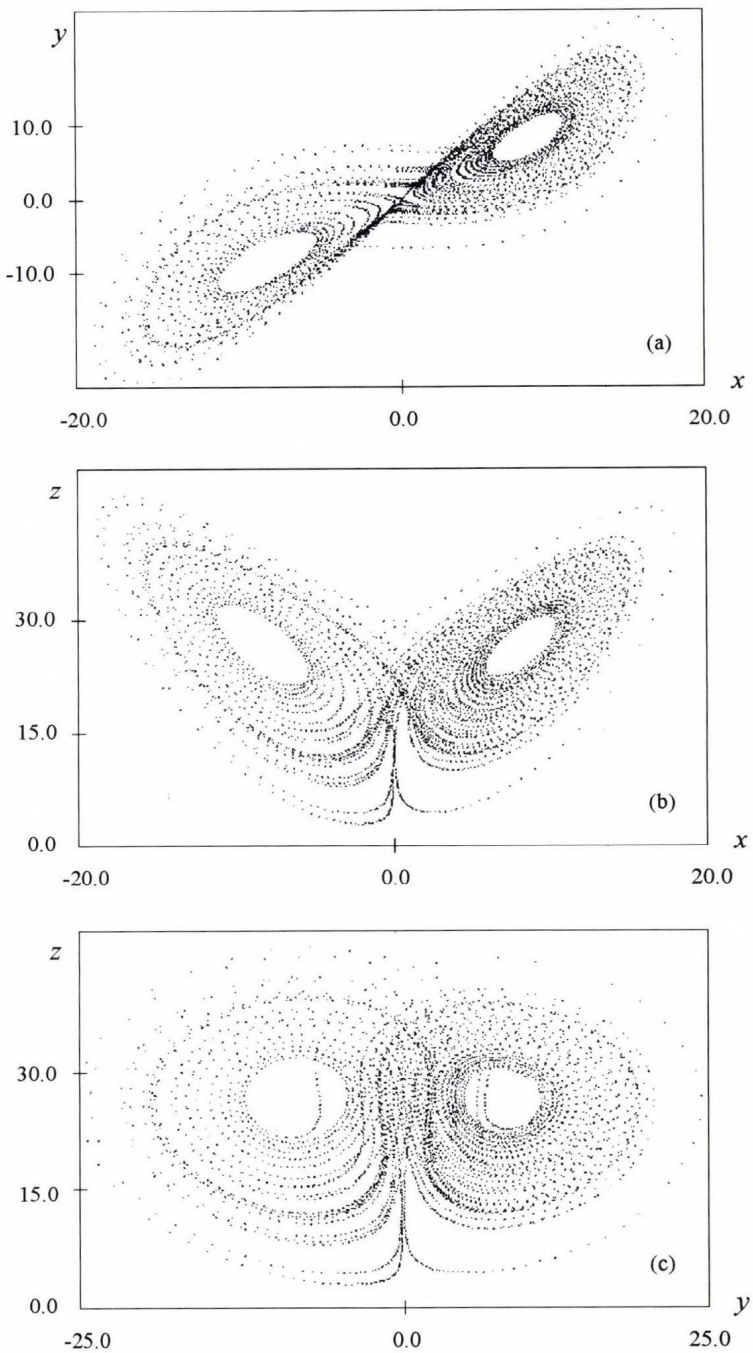

Fig. 2. Numerical solution of the Rayleigh-Bénard convection equations. Projections (*a*) on the *xy*-, (*b*) on the *xz*-, and (*c*) on the *yz*-planes in the phase space of the segment of the trajectory from iteration 4001 to iteration 9000.

To quantify the phase space topology of the Lorenz attractor, first we note from Eq. (2) that the net divergence of the flow is $1/V\,(dV/dt) = -(\sigma + b + 1) = -41/3$. When using the method described by *Nese et al.* (1987), we find the Lyapunov exponents $\lambda_1 = 0.93$, $\lambda_2 = 0$, $\lambda_3 = -14.60$. The Lyapunov dimension of the attractor embedded in the three-dimensional phase space is given by

$$d_L = 2 + \frac{\lambda_+}{|\lambda_-|} = 2.063\,.$$

The existence of one positive Lyapunov exponent indicates the presence of chaos. The relative magnitudes of λ_1 and λ_3 indicate that the contraction of a phase space volume in one principal direction is occurring much faster than the rate of expansion of the volume along another principal axis. This is quantified by the small fractional component of the Lyapunov dimension which, on the other hand, measures the 'strangeness' of the Lorenz attractor.

In his famous paper, *Lorenz* (1963) had not used the terms 'chaos' and 'strange attractor'; they emerged some ten years later. The phrase *strange attractor* first appeared in the article by *Ruelle* and *Takens* (1971), and the word *chaos*, that came to stand for deterministic disorder, was coined and introduced to the mathematical literature by *James A. Yorke* in a paper written with his student *Tien-Yien Li* (*Li* and *Yorke*, 1975). Lorenz's work became widely known only about a decade later than it had been published in a meteorological journal but thereafter, in the thousands of articles that made up the technical literature of chaos, few were cited more often than his one.

2.2 *The general circulation of the atmosphere*

In recent years, it has become increasingly recognized that a deeper understanding of the general circulation of the atmosphere is an essential condition to further major progress in the science of meteorology (*Lorenz,* 1991a). The construction of low-order models of the large-scale atmospheric flow for qualitative analysis of its inherent behavioral characteristics constitutes one possible avenue towards achieving this aim.

Lorenz (1984, 1987) has developed such a model of the general circulation which may well be the simplest possible model capable of representing its most prominent feature, i.e. the nonlinear interaction between the zonal flow (Hadley circulation) and the superposed stationary or migratory disturbances. The model is defined by three ordinary differential equations

$$\left.\begin{aligned} dx/dt &= -y^2 - z^2 - ax + aF, \\ dy/dt &= xy - cxz - y + G, \\ dz/dt &= cxy + xz - z. \end{aligned}\right\} \qquad (3)$$

Here x denotes the intensity of the globally averaged westerly current, which

is identified through the geostrophic relation with the large-scale poleward temperature gradient, while y and z denote the strengths of the cosine and sine phases of a chain of superposed waves, which can be identified with the Rossby waves that transport heat poleward, thus reducing the temperature contrast. The control parameter $c > 1$ allows the displacement of the waves by the westerly current to occur more rapidly than their amplification, while the parameter $a < 1$ allows the westerly current to damp less rapidly than the waves; a suitable choice includes $c = 4$ and $a = 0.25$. F represents the cross-latitude external heating symmetric with respect to the earth's axis, while G represents the asymmetric external thermal forcing due to the heating contrast between the oceans and continents. The time unit equals the damping time for the waves, which is assumed to be five days.

The Eqs. (3) constitute a bounded dynamical system, since it is easily shown that the total energy $(x^2 + y^2 + z^2)/2$ will decrease if it exceeds a certain value. From (3), we also find that the variation of the volume V of an infinitesimal region of the phase space is given by

$$dV/dt = -V(a + 2 - 2x). \tag{4}$$

The right side of (4) is negative only when $x < (1 + a/2)$. Thus, in contrast to the fully dissipative systems, where dV/dt is always negative, there is no assurance that small volumes will shrink to zero, and in particular, that attractors will have zero volume.

For suitable choices of the parameters a, c, F, and G, Eqs. (3) produce chaos, which was studied in details by *Masoller et al.* (1992). Such choices of parameters include $a = 1/4$, $c = 4$, $F = 8$, and $G = 5/4$. Variations of the state variable x in this case will be qualitatively the same as those shown in Fig. 1, i.e. again we will see aperiodic behavior of the system. Therefore, the chief lesson about the atmosphere to be learned from the model is that such fluctuations of the weather need not require external irregularity or even external variability (*Lorenz,* 1984).

Projections of the solution trajectory of Eqs. (3) onto the selected planes of the phase space exhibit the same characteristic configuration of the strange attractor as those displayed in Fig. 2. The solution trajectory moves around the two lobes in an entirely random fashion, but with certain preferred metastable types of behavior: the trajectory spends an extended time (several weeks) in one of the regimes before crossing to the other regime at irregular intervals. We can think about one regime as representing zonal flow, and the other regime as being blocked flow. Therefore, the succession of these episodes may be regarded as modeling the atmospheric index cycle.

As it is known, a linear or quasi-linear description of the large-scale flow of the atmosphere has permitted a qualitative explanation of many of the observed features of the global circulation, but has left others entirely unexplained. In particular, it has not accounted for the persistence of large amplitude

flow anomalies such as blocking. Nor has it explained the existence of the persistent or recurrent weather patterns or types exemplified by the *Grosswetterlage* of *Baur* (1951). Such multiple metastable equilibria (or weather regimes) were first found numerically by *Charney* and *DeVore* (1979) who used another simple nonlinear model in which the external asymmetries were orographic rather than thermal.

The Lyapunov exponents of the dynamical system (3) prove to be $\lambda_1 = 0.18$, $\lambda_2 = 0$, $\lambda_3 = -0.52$. The Lyapunov dimension of the attractor is $d_L = 2.346$. The fractional component of d_L is larger than in the case of the Rayleigh-Bénard convection, indicating that the strange attractor of the general circulation is a more complex construction. The first Lyapunov exponent indicates that, on the average, the *e*-folding time of a small error ϵ in the initial condition is $t = 1/\lambda_1 = 5.55$ time units, or about 28 days. We might add that by real atmospheric standards this growth is unreasonably small. For example, by analyzing the time series of daily surface pressure over the North Atlantic Ocean, *Zeng et al.* (1992) found $\lambda_1 = 0.098$, $\lambda_2 = 0.044$, $\lambda_3 = 0.004$ day^{-1}, i.e. an *e*-folding time of initial error $t = (\lambda_1 + \lambda_2 + \lambda_3)^{-1} = 6.8$ days. (The divergence of initially nearby trajectories in more than one direction in the phase space has been termed *hyper-chaos*.)

2.3 The El Niño-Southern Oscillation phenomenon

An El Niño-Southern Oscillation (ENSO) event may be defined as the appearance of anomalously warm water in the eastern equatorial Pacific. Associated with this is a weakening, and sometimes a reversal, of the trade wind field. An ENSO event has major economic consequences, and much observational and modeling efforts has therefore been devoted to it. The theory elaborated by *Vallis* (1986) differs from others in that the aperiodic occurrence and the variations in intensity of the ENSO are generated internally and deterministically within a simple chaotic dynamical system.

The equatorial ocean is imagined to be a box of fluid characterized by temperatures in the east and west (T_E and T_W), and a current u. The current in the basin of size ΔX is driven by a surface wind, which is in part generated by the temperature gradient $(T_E - T_W)/\Delta X$, so describing a parameterized Walker circulation (i.e. $T_E < T_W$ produces a westward surface wind, because of the tendency of air to rise over warm water), and the temperature field is advected by the current. Thus the nonlinear governing equations of the dynamical system are

$$du/dt = B(T_E - T_W)/2\Delta X - C(u - u^*), \tag{5}$$

$$dT_W/dt = u(\bar{T} - T_E)/2\Delta X - A(T_W - T^*), \tag{6}$$

$$dT_E/dt = u(T_W - \bar{T})/2\Delta X - A(T_E - T^*). \tag{7}$$

Here, the temperature decay time scale A, the influence of ocean temperatures on the wind field B, and the frictional decay time scale C are constants; $-u^* = \text{const}$ is the speed of the mean tropical easterlies, $\bar{T} = \text{const}$ is the temperature below the thermocline, while $T^* = \text{const}$ is the temperature to which the ocean would relax in the absence of motion. In Eq. (5), the terms $B\,(T_E - T_W)/\Delta X + Cu^*$ represent wind-produced stress, and $-Cu$ represents mechanical damping. In Eqs. (6) and (7), the first term on each right-hand side represents horizontal advection, while the second term represents forcing and thermal damping.

With $u^* \neq 0$, Eqs. (5) to (7) have the same structure as the Lorenz equations (1). The physical system resembles that of ordinary convection in that the velocity of circulation is maintained by a horizontal temperature gradient: this sets up a direct circulation in the atmosphere, which forces the ocean. The unusual aspect here is that the oceanic part of the system is able to overturn with warmer water above the cool deep ocean, i.e. a stable configuration because work must be done on the system. Overturning and instability can occur here because the dominant driving of the ocean is mechanical, namely wind stress.

For constant T^*, C and A, all stationary solutions become unstable when B, the thermal forcing of the wind field, is sufficiently large. The system can no longer stably reside anywhere and oscillates apparently randomly between the two least unstable stationary states. Numerical integration of the Eqs. (5) to (7) yields aperiodic behavior plausibly reproducing the basic ENSO event cycle (*Fig. 3*). The system stays in the neighborhood of one unstable stationary solution for many model years before flipping to an ENSO event. These ENSO

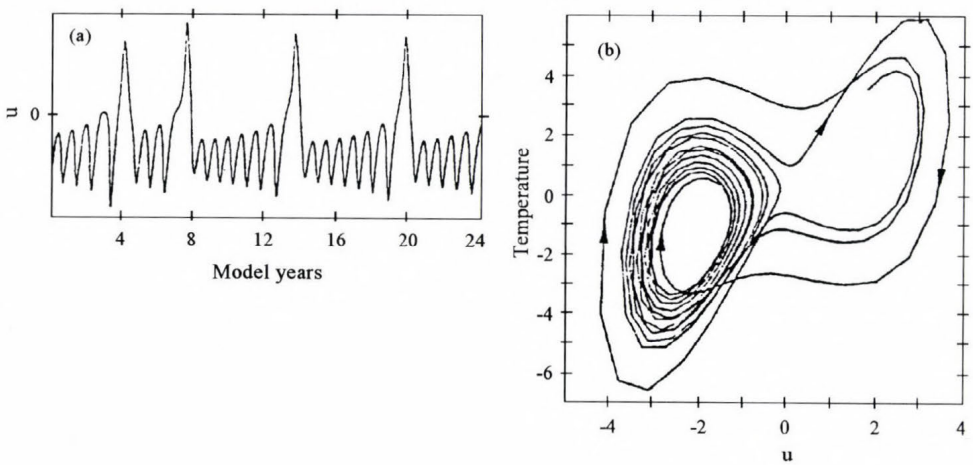

Fig. 3. Numerical solution of the ENSO equations with parameter values $C = 1/4$ month^{-1}, $A = 1$ year^{-1}, $u^* = -0.45$ m s^{-1}, $\Delta X = 7500$ km, and $T^* = 12$°C. (*a*) Graph of u as a function of time. (*b*) Trajectory of the system projected onto the u,$(T_E - T_W)$-plane, over a period of 12 model years. Arrows indicate the direction of the flow. (After *Vallis*, 1986)

states are trajectories around another stationary, but highly unstable, solution and the system quickly returns to its normal, less unstable state.

In summary, this theoretical model clearly demonstrates the underlying dynamics and thereby the possibility of a *purely internal mechanism* for the ENSO. It shows that external triggering or stochastic forcing is not necessarily essential, although such effects may have a role in the real system. Recently, *Elsner* and *Tsonis* (1993) have analyzed a time series describing the ENSO, using the latest techniques of chaos theory. They carried out a strictly empirical investigation of the intrinsic nonlinearity within the atmosphere-ocean system. From the results, nonlinear dynamics in the ENSO have been established at a high confidence level.

2.4 The phase-spatial variation of predictability

The rate at which adjacent trajectories diverge on a chaotic attractor is, in general, not constant, but rather this local divergence rate depends on time and therefore, on location in phase space. Thus, for applications requiring short-term prediction, using only the Lyapunov exponents to measure predictability is inadequate, because any phase-spatially dependent predictability information is essentially eliminated by long-term averaging over the attractor. The local predictability of the Lorenz system (1) from both temporal and phase-spatial viewpoints was studied by *Nese* (1989) to demonstrate how local divergence rates might be used to identify regions of high or low predictability in phase space.

The distribution of local predictability on the Lorenz attractor is summarized qualitatively in *Fig. 4*. We find that initially nearby trajectories converge most rapidly on average as they approach the vicinity of the z-axis on the tops of the wings. Adjacent trajectories diverge most rapidly on average on the bottoms of the wings of the attractor as trajectories swing away from the vicinity of the unstable origin (0,0,0) representing the state of no convection. However, even on a portion of the attractor where predictability is low, there still may be a sense of predictability, because the divergence of nearby trajectories may be a uniform characteristic of that region of the phase space. In these cases, the short-term error growth can be estimated.

Predictability near the z-axis and origin is influenced by two opposing effects. For relatively large values of z, almost all pairs of adjacent trajectories converge temporarily owing to the stabilizing influence of the z-axis, which is part of the two-dimensional stable manifold of the unstable steady state (0,0,0). On the other hand, closer to the origin, the potential for extremely rapid divergence of neighboring trajectories exists, with one trajectory circling each wing. However, this potential is only occasionally realized. Thus the region near the origin, which is the principal source of long-term forecast errors, is only moderately unpredictable in terms of average local divergence rates.

Nonetheless, when catastrophic separation of initially nearby trajectories occurs, the consequences in terms of forecast errors are extremely severe.

The *stable manifold* of a steady state is the set of points **x** in the phase space such that the forward trajectory starting from **x** approaches the steady state. Similarly, the *unstable manifold* of a steady state is the set of points **x** such that the trajectory going backward in time starting from **x** approaches the steady state. Within this context, *Legras* and *Ghil* (1985) suggested a relationship be-

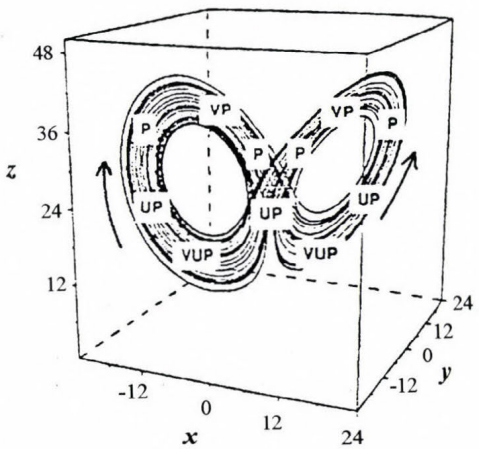

Fig. 4. Distribution of local predictability on the Lorenz attractor in a three-dimensional perspective. The abbreviations VP, P, UP, and VUP denote very predictable, predictable, unpredictable, and very unpredictable regions, respectively. Arrows indicate the direction of the flow. (After *Nese*, 1989)

tween the temporal variation of predictability and the dynamics of weather regimes (quasi-stationary states of the general circulation). They found that at the onset of weather regimes, the rate of divergence of nearby trajectories has a small value, and it has a large value at the transitions between two types of the flow. They explained this variation of the predictability by the local dynamics of the unstable steady state generating quasi-stationary states: persistencies are associated with gradual capture of the trajectory into a contracting phase flow region near the stable manifold of the unstable steady state, and rapid transients with strong instabilities along the unstable manifold.

In order to investigate further the dynamical aspects of the temporal variation of predictability, *Mukougawa et al.* (1991) introduced the *Lorenz index*, which is a measure of the ensemble average of the *linear growth rate* of infinitesimally small initial errors. This index does not depend on the amplitude nor the configuration of initial errors, but directly represents the instability characteristics of the flow. The authors computed the Lorenz index along the stable and unstable manifold of the three unstable stationary points in the Lorenz system, and found that none of these steady states has the property suggested by *Legras* and *Ghil* (1985). This is also implied by the phase-spatial organization of the Lorenz index in *Fig. 5*; we see that the Lorenz index is a smooth function of the state variables, and does not show any distinctive

organization (e.g., a local maximum or minimum value) around the unstable stationary points of the Lorenz system. Therefore, the unstable steady states do not have the same local dynamics.

The nonlinear prediction problem is currently one of the most exciting topics and a very active research area (*c.f.*, *Elsner* and *Tsonis*, 1992).

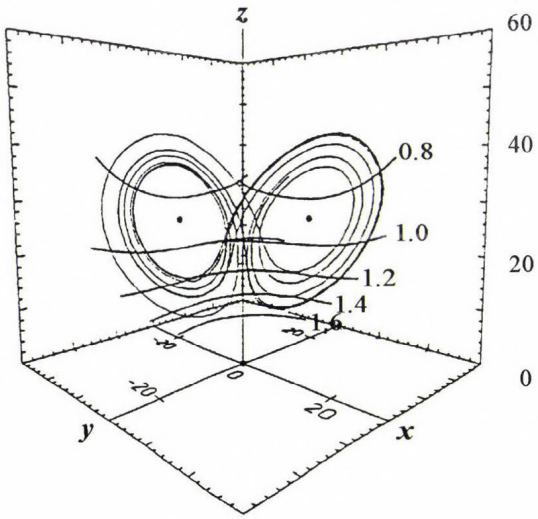

Fig. 5. Distribution of the Lorenz index on the Lorenz attractor in a three-dimensional perspective. A part of the trajectory is indicated by the solid line. The locations of the three unstable stationary points are denoted by dots. (After *Mukougawa et al.*, 1991)

3. Chaotic behavior on climatic time scales

When a dynamical system is an atmospheric model, the points on the attractor represent those states which are compatible with the climate. Physically unrealistic states correspond to points in the phase space which are not on the attractor, while extreme states correspond to points which are in domains of the attractor rarely visited by a trajectory. Within this context, the question of climate becomes a problem of quantifying the attractor, and climate change a matter of how modifications of the boundary conditions lead to altered attractors.

In this section, climate variations on time scales ranging from years to ice-age cycles are interpreted from the viewpoint of nonlinear dynamics, and a modified perspective on global climatic change of anthropogenic origin is outlined.

3.1 Interannual variability

As possible causes for variations in climate, climatologists have often invoked the presumed variations of certain external influences. However, recent numerical studies have uncovered a multitude of autonomous dynamical systems

that undergo variations on a wide range of time scales, without the aid of any varying external influences (see, e.g., *James* and *James*, 1989; *Geller*, 1989). Therefore, some climatic variations may be internally, rather than externally produced, i.e., they are simply the natural internal oscillations in the intricate climate system. Of course the activity of this system requires external thermal forcing, but this is not to say that *variations* in the system require *variations* in the external heating.

In a recent study, *Lorenz* (1990) examined a mechanism that in theory can produce changes on time scales of years, with no variations in external conditions other than the normal seasonal cycle. He presumed that F, representing the cross-latitude external-heating contrast in the geostrophic baroclinic model (3), is greater in winter than in summer. Therefore he identified $F = 6$ with a summer condition, and $F = 8$ with a winter condition. Depending upon the initial conditions, two types of the perpetual summer circulation can develop with the thermal forcing $F = 6$: strong periodic oscillations of the westerly flow x (called *active summer*), and oscillations of x with a much smaller amplitude and a much shorter period than in the former (this type of activity is referred to as *inactive summer*). Extension of the solutions indicated that each type of oscillation, once established, is stable and persists for ever, so that the system can be looked upon as an intransitive system. On the other hand, in the winter case with $F = 8$, different initial conditions lead to strong fluctuations that exhibit chaotic behavior. However, without a *continuous* seasonal change of F, there is no sign of pronounced variations with periods of years or longer.

When a continuous seasonal heating cycle is included by letting F vary sinusoidally between the extreme values 5 and 9, strong interannual variation can appear, with irregular alternations between active and inactive summers. The mechanism that produces the year-to-year variations involves chaotic behavior during the colder months, which assures that a randomly chosen circulation pattern will be present when the warmer months begin. This allows one possible circulation pattern to develop during one summer, while an alternative pattern may develop during another.

Since both summer cases with $F = 6$ are periodic solutions of the Eqs. (3), the two attractors, which *Lorenz* (1990) has called the *strong attractor* and the *weak attractor*, are closed loops (limit cycles) that a trajectory traverses during a single period. A detailed analysis has revealed that the boundary separating the basins of attractions of the two attractors has an extremely complex, fine-scale distribution in the phase space: the two basins are intricately intertwined, and magnification of successively smaller and smaller regions has unveiled a Cantor-set-like, fractal nature of the basin boundary. The existence of such a *fractal basin boundary* can present a serious problem when one attempts to predict the future state of a dynamical system (*Grebogi et al.*, 1987; *Ott*, 1993).

As an extension of Lorenz's work, *Pielke* and *Zeng* (1993) integrated the Eqs. (3) for about 1100 years. Their calculations have revealed that the seasonal cycle itself is sufficient to generate decadal and century time scale variations in climate that are of the same order as interannual variations. No long-term external mechanisms are required to account for substantial long-term deviations in the climatic state. These long-term natural variabilities cannot be predicted deterministically because of the chaotic property of the system (see also *Palmer*, 1993a).

3.2 Long-term variability

The Quaternary ice age has been characterized by repeated alternations between relatively warm interglacial periods and much colder glacial periods. The marked cyclic character of the glaciations has promted many investigators to view long-term climatic variations as a sustained self-oscillation of the limit cycle type. Such self-oscillations were shown to arise quite naturally from the coupling between mean ocean temperature and sea ice, or mean surface temperature and continental ice sheet. Under the presence of a weak external periodic forcing due to Earth-Sun orbital geometry changes, a phase locking can take place, enabling the limit cycle oscillator to adopt the frequency of the forcing or a multiple thereof (see, e.g., *Nicolis*, 1987; *Saltzman* and *Verbitsky*, 1992). Thus, according to this hypothesis, the main climatic variations during the Quaternary are caused by an *internal* property of the climate system, with external forcing playing a relevant role only in determining the phases of the cycles.

As an illustrative example, we recall the work of *Tsonis* and *Elsner* (1990). They considered a simple model of the climate system in which long-term forced damped, nonlinear oscillations are described by the following equation:

$$d^2x/dt^2 + kdx/dt + \beta(x^3 - x) = A\cos\omega t. \tag{8}$$

Here, x is a variable of the climatic state (e.g., global temperature, or ice-sheet extent), k indicates the damping, A is the amplitude of the external forcing, ω is the angular frequency, and $\beta\ (x^3 - x)$ is the nonlinear restoring force. Physically, the damping is related to the tendency of the system to react to changes dictated by some external force (which may be thought of as some astronomical forcing) and the restoring force.

For $k = 0.15$, $\beta = 0.5$, $\omega = 0.833$ and $A = 0.1$ the system exhibits two periodic attractors I and G, which in the one-sided Poincaré map are fixed points $x = \pm 1$, $dx/dt = 0$. In this simplified situation, attractor I may be thought of as describing the dynamics of weather in the interglacial climate, and attractor G in the glacial climate. Depending upon the initial conditions, the system settles down in one of the two attractors.

Numerical experiments on the forced damped pendulum equation show that

fractal basin boundaries are extremely common for this system, causing high sensitivity to initial conditions even if all solutions are found periodic (*Ott*, 1993). Thus, in the presence of noise it is quite possible that a trajectory converging to one attractor will be forced to a point in the fractal boundary which will bring the trajectory to the other attractor. This will indicate a jump from one attractor to the other. Such jumps happen in the system (8) when a random-noise term is added to the right-hand side of the equation. The noise may be thought of as related to short-term internal or external fluctuations. An example of the chaotic evolution of the system is presented in *Fig. 6a*, while *Figs. 6b* and *6c* show the corresponding time variation of x. Fig. 6c indicates, in agreement with several deep-sea core records which represent average climatic conditions over thousands of years, that the climate system has two modes of oscillation. Each oscillation involves a jump from one mode of operation to the other.

The jumps may provide an explanation for the rapid deglaciations and why glacial periods do not last as long as interglacial epochs. In order for that to happen, the coexisting basins of attractions have to be asymmetric. In such a case one attractor will be more attracting than the other, and the residence time on each of the attractors will not be the same. In the case of system (8), the mean residence time of the trajectory for attractor I has indeed proven to be greater than for attractor G.

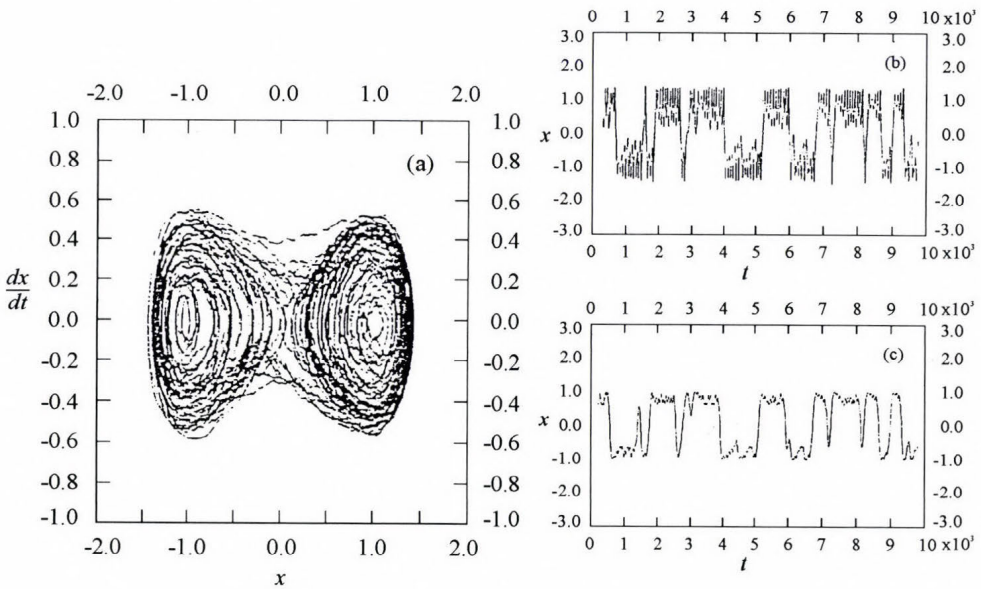

Fig. 6. Numerical solution of the forced damped, nonlinear oscillation equation. (*a*) Trajectory of the system in the phase space whose coordinates are x and dx/dt. (*b*) Graph of x as a function of time. (*c*) A smoothed version of the graph in (*b*). (After *Tsonis* and *Elsner*, 1990)

3.3 A nonlinear dynamical look at climate change

Many of the existing conceptual paradigms about anthropogenic climate change involve linear dynamical thinking. This is embodied in a general perception of the phrases *greenhouse effect* and *global warming* as effectively synonymous. Linear thinking is also implicit in the belief that the effect of increasing atmospheric carbon dioxide concentration will be manifested through a pattern of atmospheric variability that is quite unlike any naturally occurring pattern of variability, e.g. that the greenhouse signal is orthogonal to and independent of the background noise.

In order to put forward a nonlinear dynamical perspective on climate change, *Palmer* (1993b) used the Lorenz model (1) to study predictions of the second kind (i.e., how the statistical properties of the atmosphere change as some control parameter, carbon dioxide content for example, is altered). To do this, he added to the right-hand side of the Eqs. (1) the components of some fixed additional forcing vector **F**, whose strength was governed by a parameter α, and tried to understand conceptually the change in the climate of the Lorenz model as α was increased from zero.

Now, an erroneous linear-thinking analysis of this problem might go as follows. Whilst it is difficult to predict without detailed calculation how an individual trajectory portion might be influenced by the imposed additional forcing, the time-mean state of the system might respond in rough proportion to the forcing **F** itself. The variability in the model might then be approximated by assuming that, relative to the new time-mean state, it is largely unchanged. It might therefore be concluded that the original attractor ($\alpha = 0$) is approximately translated in the direction of the forcing vector **F** to some new position, when $\alpha > 0$.

The actual result of such an additional forcing is shown in *Fig. 7* in terms of the probability distribution function (PDF). This quantity gives the probability of finding the state vector of the system at a given point in the xy-plane of the phase space. *Fig. 7a* gives the values of the PDF with $\alpha = 0$, showing clearly the two weather regimes: the state vector is most likely to be found in two preferred regions of the phase space. We can see that the PDF is symmetric, so that the probability of the trajectory being found in one regime is equal to the probability of its being found in the other regime. *Fig. 7b* shows a PDF when $\alpha > 0$, and the forcing vector **F** is oriented from one regime to the other in the xy-plane. In this case, the PDF is no longer symmetric, the state of the system is more likely to be found in the regime towards which the forcing vector **F** points. However, the phase-space coordinates of the PDF maxima are virtually identical to those in the model with $\alpha = 0$, i.e., the structure of the regime centroids in both the model with $\alpha = 0$ and in the model with forcing $\alpha\mathbf{F}$ is unchanged.

Nonlinear dynamics might also raise questions about the validity of the *Gaia*

hypothesis introduced by *Lovelock* and *Margulis* (1974). It postulated the Earth to be a self-regulating system comprising the biota and their environment with the capacity to maintain the climate and the chemical composition at a steady state favorable for life. A simple model, referred to as Daisyworld, was later developed to illustrate the Gaia concept (*Watson* and *Lovelock*, 1983). Daisyworld is defined as a cloudless planet with negligible atmospheric greenhouse gases, on which the only plants are two species of daisy of different colors. The growth rate of the daisies depends on only one environmental variable, temperature, which the daisies in turn modify because they absorb different amount of solar radiation. The authors concluded that, regardless of the details of the interaction, the effect of daisies is to maintain stable climatic conditions.

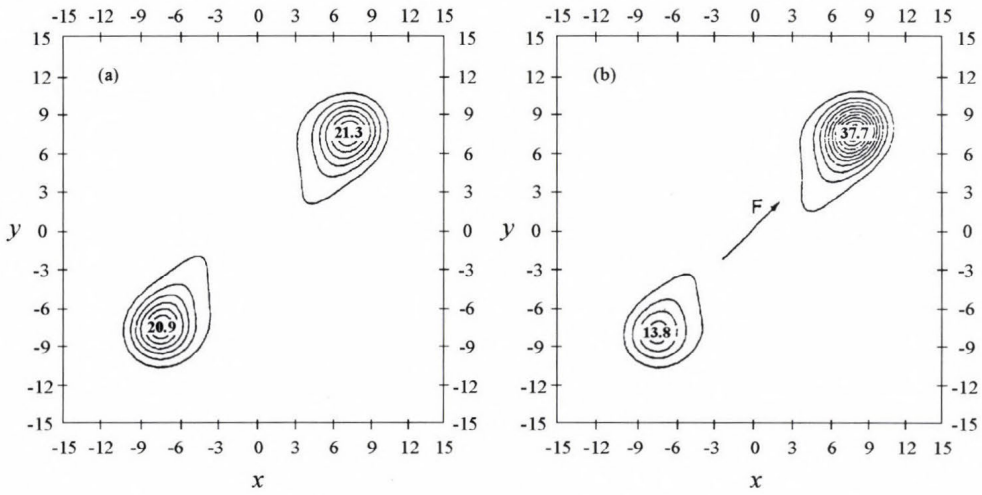

Fig. 7. Probability distribution function of the Lorenz model in the *xy*-plane (*a*) from the model without additional forcing, and (*b*) with a constant additional forcing $F_x = F_y = 1/\sqrt{2}$, $F_z = 0$. (After *Palmer*, 1993b)

In Daisyworld, the comparative growth of the daisies is governed by the logistic map

$$x_{n+1} = rx_n(1 - x_n), \tag{9}$$

where x ($0 \leq x \leq 1$) represents the population density of a given species of daisy, while the growth-rate parameter r depends on the area covered by the given species and on the local temperature. The surprising fact that the iterative mapping of a nonlinear discrete-time equation as simple as Eq. (9) can exhibit apparently aperiodic fluctuations was first described by *May* (1974); population values that look like samples from some random process appear for the control

parameter $r > 3.57$. The presence of chaos in Daisyworld was revealed by *Zeng et al.* (1990). Their results show that this imaginary planet is not always in a steady state as predicted by the Gaia hypothesis; instead, the state of Daisyworld is extremely sensitive to minor fluctuations in the temperature or the areas covered by daisies when in its chaotic regime. Therefore, the biota do not always stabilize the climate, and the remarks made by *Lovelock* (1986), that the inclusion of a negative feedback from the environment appears to lead to steady-state behavior, are also not true in general.

4. Reconstruction of weather and climate attractors

In this section, we present the remarkable fact that allows a strange attractor to be reconstructed from a sampled time series of just one component of the state. The physics behind such a reconstruction is that a nonlinear system is characterized by self-interaction, so that a time series of a single variable can carry the information about the dynamics of the entire multivariable system.

Among the different procedures that have been developed for obtaining a strange attractor, the method of delay coordinates (*Takens*, 1981) is most widely used. Let us suppose that we can only measure one scalar component $y(t)$ of the d-dimensional state vector $\mathbf{x}(t)$. It can be shown that, if n is sufficiently large, then the n-dimensional delay coordinate vector time series

$$y(t_i) = \{y(t_i), y(t_i - \tau), \ldots, y(t_i - (n-1)\tau)\}$$

will be a faithful representation of $\mathbf{x}(t_i)$ where τ is some fixed time interval, and n is the number of delays. In other words, the time trajectory traveling along the sequence of points $\mathbf{y}(t_1)$, $\mathbf{y}(t_2)$,..., $\mathbf{y}(t_n)$ will typically produce a qualitatively similar structure on the Poincaré surface of section in the **y**-space as would be seen had we made our Poincaré section in the original phase space **x**. In this case we say that we have *embedded* the d-dimensional **x**-space into the n-dimensional delay coordinate **y**-space.

Different methods have been suggested to estimate the dimension of the reconstructed attractor, including the correlation-integral method (*Grassberger* and *Procaccia*, 1983a,b) which is most frequently used in atmospheric studies. If the method is correctly applied, the correlation dimension then provides a measure of the number of independent modes excited by the system, that is, it gives the minimum number of coupled nonlinear ordinary differential equations necessary to describe the system (*Procaccia*, 1988a; *Sundermeyer* and *Vallis*, 1993).

Although the method gives no hint as to where these equations might come from and what they might look like, many studies in the field of atmospheric science have concentrated on computing the dimensions of

weather and climate attractors from observational data. To mention just a few, *Nicolis* and *Nicolis* (1984) analyzed the time series of the isotope record of deep-sea cores, and obtained a dimensionality between 3 an 4 for the climate system. Subsequently, *Fraedrich* (1986, 1987), *Essex et al.* (1987), and *Keppenne* and *Nicolis* (1989) analyzed weather data, and have likewise concluded the existence of low-dimensional attractors. From the results obtained for the precipitation and sea-surface temperature, *Hense* (1987) hypothesized the existence of a strange attractor with a fractal dimension between 2.5 and 6.0 for the Southern Oscillation. According to *Tsonis* and *Elsner* (1988), even from the 10-second averages of the vertical wind velocity over a time interval of 11 hours, recorded at Boulder, Colorado, a 7.3-dimensional attractor can be derived.

These unexpected results, suggesting that both long-term climatic processes and phenomena occurring on very short time scales have only a few important modes that govern their dynamics, can stem from one of two reasons. Either there is something fundamental in atmospheric dynamics that we do not understand, which leads to an unexpected simplification of its behavior, or the method of analysis does not apply or is outside its range of validity. Therefore, the existence of low-dimensional atmospheric attractors is currently a highly debated subject. Doubts as to their appropriateness have been expressed even by the originators of the method (*Grassberger*, 1986; *Procaccia*, 1988b), as well as by *Ruelle* (1990). These comments have inspired *Lorenz* (1991b) to apply the procedure to 'data' generated by a mathematical system whose dimension can be evaluated by other means. In this way, he could identify conditions, apparently satisfied by the studies that use real data, in which the method would yield systematic underestimates. Lorenz therefore could see no reason to believe that the global weather and climate systems possess low-dimensional attractors.

In an overview of most recent developments concerning data requirements in estimating the dimension of weather and climate attractors, *Tsonis et al.* (1993) have concluded that due to existing algorithm weaknesses all results present just evidence rather than proof of existence. On the other hand, it should be kept in mind that in weather and climate studies we deal with coarse data in which small-scale processes are absent. These large-scale coarse data are likely to obey to a closed dynamics, which need not appeal to the small-scale processes. Consequently, real-data studies reporting on low-dimensional attractors may not be altogether meaningless; they just need to be reinterpreted.

5. Conclusions

Chaos is a ubiquitous nonlinear phenomenon which permeates all fields of science. Though identified as an important research area only recently, chaos

has been with us from time immemorial. It almost certainly has graced the eyes of many scientists long ago, only to be dismissed as physical noise (*Chua*, 1987). We now know that chaos can readily occur in all natural and living systems where nonlinearity is present. Indeed, chaos has been reported from virtually every scientific discipline: astronomy, biology, biophysics, chemistry, engineering, geology, mathematics, medicine, plasmas, and even social sciences.

In this part of our paper, some examples of the applications of chaos theory to the atmosphere have been presented. In the overview, we have focused our attention mainly on large-scale processes, although areas of application include smaller scale phenomena as well. We now know that the Landau-Hopf route to turbulence is unlikely to occur in nature. Instead, routes through consecutive bifurcations, period doubling cascade, and intermittency have been proposed. Multifractal models of the energy-cascade process have been developed for the understanding of fully developed turbulence. Theories of deterministic chaos have been applied to data in the atmospheric boundary layer, the pulse of thunderstorm rainfall, and some special microphysical systems. More applications can be found in the review article by *Zeng et al.* (1993).

In summary, the grammar of chaos seems to provide a useful way of describing *the nature of dynamically complex phenomena.* Simple models may capture qualitative aspects of a variety of complex atmospheric processes. Whether, and in what sense, the new ideas and physical insights inspired by chaos theory can be used to improve the finite-time prediction of weather and climate is currently one of the most exciting research topics comprising a number of still open questions for the near future.

Acknowledgment—The author would like to thank *Gábor Radnóti* for providing Figs. 1 and 2.

References

Baur, F., 1951: Extended range weather forecasting. In *Compendium of Meteorology* (ed.: *T.F. Malone*). American Meteorological Society, Boston, pp. 814-833.

Charney, J.G. and *DeVore, J.G.*, 1979: Multiple flow equilibria in the atmosphere and blocking. *J. Atmos. Sci. 36*, 1205-1216.

Chua, L.O., 1987: Chaotic systems. *Proc. Inst. Electrical and Electronics Engineers 75*, 979-980.

Elsner, J.B. and *Tsonis, A.A.*, 1992: Nonlinear prediction, chaos, and noise. *Bull. Amer. Meteor. Soc. 73*, 49-60.

Elsner, J.B. and *Tsonis, A.A.*, 1993: Nonlinear dynamics established in ENSO. *Geophys. Res. Lett. 20*, 213-216.

Essex, C., Lookman, T. and *Nerenberg, M. A.H.*, 1987: The climate attractor over short timescales. *Nature 326*, 64-66.

Farmer, J.D., Ott, E. and *Yorke, J.A.*, 1983: The dimension of chaotic attractors. *Physica 7D*, 153-180.

Fraedrich, K., 1986: Estimating the dimensions of weather and climate attractors. *J. Atmos. Sci. 43*, 419-432.

Fraedrich, K., 1987: Estimating weather and climate predictability on attractors. *J. Atmos. Sci. 44*, 722-728.

Geller, M.A., 1989: Variations without forcing. *Nature 342*, 15-16.

Götz, G., 1992: Application of nonlinear dynamics in atmospheric sciences. Part I. Theoretical background. *Időjárás 96*, 121-130.

Grassberger, P., 1986: Do climatic attractors exist? *Nature 323*, 609-612.

Grassberger, P. and *Procaccia, I.*, 1983a: Characterization of strange attractors. *Phys. Rev. Lett. 50*, 346-349.

Grassberger, P. and *Procaccia, I.*, 1983b: Measuring the strangeness of strange attractors. *Physica 9D*, 189-208.

Grebogi, C., Ott, E. and *Yorke, J.A.*, 1987: Chaos, strange attractors, and fractal basin boundaries in nonlinear dynamics. *Science 238*, 632-638.

Hense, A., 1987: On the possible existence of a strange attractor for the Southern Oscillation. *Beitr. Phys. Atmos. 60*, 34-47.

James, I.N. and *James, P.M.*, 1989: Ultra-low-frequency variability in a simple atmospheric circulation model. *Nature 342*, 53-55.

Keppenne, C. and *Nicolis, C.*, 1989: Global properties and local structure of the weather attractor over Western Europe. *J. Atmos. Sci. 46*, 2356-2370.

Legras, B. and *Ghil, M.*, 1985: Persistent anomalies, blocking and variations in atmospheric predictability. *J. Atmos. Sci. 42*, 433-471.

Li, T.-Y. and *Yorke, J.A.*, 1975: Period three implies chaos. *Amer. Math. Mon. 82*, 985-992.

Lorenz, E.N., 1963: Deterministic nonperiodic flow. *J. Atmos. Sci. 20*, 130-141.

Lorenz, E.N., 1984: Irregularity: A fundamental property of the atmosphere. *Tellus 36A*, 98-110.

Lorenz, E.N., 1987: Deterministic and stochastic aspects of atmospheric dynamics. In *Irreversible Phenomena and Dynamical Systems Analysis in Geosciences* (eds.: *C. Nicolis* and *G. Nicolis*). D. Reidel, Dordrecht, pp. 159-179.

Lorenz, E.N., 1990: Can chaos and intransitivity lead to interannual variability? *Tellus 42A*, 378-389.

Lorenz, E.N., 1991a: The general circulation of the atmosphere: An evolving problem. *Tellus 43AB*, 8-15.

Lorenz, E.N., 1991b: Dimension of weather and climate attractors. *Nature 353*, 241-244.

Lovelock, J.E., 1986: Geophysiology: A new look at earth science. *Bull. Amer. Meteor. Soc. 67*, 392-397.

Lovelock, J.E. and *Margulis, L.*, 1974: Atmospheric homeostasis by and for the biosphere: The Gaia hypothesis. *Tellus 26*, 2-10.

Mandelbrot, B. B., 1977: *Fractals–Form, Chance, and Dimension*. W. H. Freeman, San Francisco, 365 pp.

Masoller, C., Sicardi Schifino, A.C. and *Romanelli, L.*, 1992: Regular and chaotic behavior in the new Lorenz system. *Phys. Lett. A167*, 185-190.

May, R.M., 1974: Biological populations with nonoverlapping generations: Stable points, stable cycles, and chaos. *Science 186*, 645-647.

Mukougawa, H., Kimoto, M. and *Yoden, S.*, 1991: A relationship between local error growth and quasi-stationary states: Case study in the Lorenz system. *J. Atmos. Sci. 48*, 1231-1237.

Nese, J.M., 1989: Quantifying local predictability in phase space. *Physica D 35*, 237-250.

Nese, J.M., Dutton, J.A. and *Wells, R.*, 1987: Calculated attractor dimensions for low-order spectral models. *J. Atmos. Sci. 44*, 1950-1972.

Nicolis, C., 1987: Long-term climatic variability and chaotic dynamics. *Tellus 39A*, 1-9.

Nicolis, C. and *Nicolis, G.*, 1984: Is there a climatic attractor? *Nature 311*, 529-532.

Ott, E., 1993: *Chaos in Dynamical Systems*. Cambridge University Press, Cambridge, 385 pp.

Palmer, T.N., 1993a: Extended-range atmospheric prediction and the Lorenz model. *Bull. Amer. Meteor. Soc. 74*, 49-65.

Palmer, T.N., 1993b: A nonlinear perspective on climate change. *Weather 48*, 314-326.

Pielke, R.A. and *Zeng, X.*, 1993: Long term variability of climate. In *Research Activities in Atmospheric and Oceanic Modelling*, Report No. 18 (ed.: *G.J. Boer*). WMO/TD-No. 533, pp. 7.437.44.

Procaccia, I., 1988a: Universal properties of dynamically complex systems: The organization of chaos. *Nature 333*, 618-623.

Procaccia, I., 1988b: Complex or just complicated? *Nature 333*, 498-499.

Ruelle, D., 1990: Deterministic chaos: The science and the fiction. *Proc. Roy. Soc. A 427*, 241-248.

Ruelle, D. and *Takens, F.*, 1971: On the nature of turbulence. *Commun. Math. Phys. 20*, 167-192.

Saltzman, B. and *Verbitsky, M.Y.*, 1993: Multiple instabilities and modes of rhythmicity in the Plio-Pleistocene: A general-theory of late Cenozoic climatic change. *Clim. Dyn. 9*, 1-15.

Sundermeyer, M. and *Vallis, G.K.*, 1993: Correlation dimensions of primitive equation and balanced models. *J. Atmos. Sci. 50*, 2556-2564.

Takens, F., 1981: Detecting strange attractors in turbulence. In *Dynamical Systems and Turbulence* (eds.: *D.A. Rand* and *L.-S. Young*). Springer Lecture Notes in Mathematics, Vol. 898. Springer-Verlag, New York, pp. 366-381.

Tsonis, A. A. and *Elsner, J. B.*, 1988: The weather attractor over very short timescales. *Nature 333*, 545-547.

Tsonis, A.A. and *Elsner, J.B.*, 1990: Multiple attractors, fractal basins and longterm climate dynamics. *Beitr. Phys. Atmos. 63*, 171-176.

Tsonis, A.A., *Elsner, J.B.* and *Georgakakos, K.P.*, 1993: Estimating the dimensions of weather and climate attractors: Important issues about the procedure and interpretation. *J. Atmos. Sci. 50*, 2549-2555.

Vallis, G.K., 1986: El Niño: A chaotic dynamical system? *Science 232*, 243-245.

Watson, A.J. and *Lovelock, J.E.*, 1983: Biological homeostasis of the global environment: The parable of Daisyworld. *Tellus 35B*, 284-289.

Zeng, X., Pielke, R.A. and *Eykholt, R.*, 1990: Chaos in Daisyworld. *Tellus 42B*, 309-318.

Zeng, X., Pielke, R.A. and *Eykholt, R.*, 1992: Estimating the fractal dimension and the predictability of the atmosphere. *J. Atmos. Sci. 49*, 649-659.

Zeng, X., Pielke, R.A. and *Eykholt, R.*, 1993: Chaos theory and its applications to the atmosphere. *Bull. Amer. Meteor. Soc. 74*, 631-644.

IDŐJÁRÁS

Quarterly Journal of the Hungarian Meteorological Service
Vol. 98, No. 2, April–June 1994

The urban modification of acid deposition

D. S. Lee[1] and **J. W. S. Longhurst**[2]

[1] *AEA Technology, National Environmental Technology Centre*
Culham, Oxfordshire OX14 3DB, United Kingdom
[2] *Atmospheric Research and Information Centre,*
Department of Environmental and Geographical Sciences
Manchester Metropolitan University
Chester Street, Manchester M1 5GD, United Kingdom

(Manuscript received 22 April 1994; in final form 24 May 1994)

Abstract—This paper describes the urban modification of precipitation composition in a densely populated region of the United Kingdom. Bulk deposition was compared to wet deposition at a city centre site. Significant differences were found between the collectors, dry deposition contributing less than 20% of the deposition of sulphur and nitrogen species to the bulk collector. However, this sampling artifact was not found to be greatly different to that observed at rural sites in the U.K., confirming the use of carefully sited bulk collectors for these species as valid. Acidity, however, is better assessed with wet-only collectors. Significant spatial variability of concentrations of non-marine sulphate, nitrate, ammonium, calcium and hydrogen ions were found, using a network of 18 bulk collectors. Non-marine sulphate and nitrate were primarily the result of long-range transport with dry deposition of aerosols postulated as being the most likely cause of small, but significant, local variability. Ammonium and calcium in precipitation had local urban sources of precursor species which contributed to their spatial variability which was much stronger than that of non-marine sulphate and nitrate. The spatial variation of acidity was the result of neutralisation by calcium species rather than acidic emissions from local sources. All ions in precipitation showed seasonal variability which was not different to that observed at two nearby rural sites, with the exception of calcium at one of the rural sites, confirming the predominance of meteorology as the controlling factor on seasonal variations. The deposition of ammonium was found to be more episodic than non-marine sulphate or nitrate and back trajectories of two episodes showed that both low pressure and high pressure systems could lead to large deposition.

Key-words: acid deposition, urban rainfall composition, urban bulk/wet deposition.

1. Introduction

The chemical composition of precipitation has been the subject of much discussion over the past two decades because of the impact of wet deposited

sulphur and nitrogen compounds on terrestrial and aquatic ecosystems (*Longhurst et al.*, 1993a; 1993b). However, the effects of emissions from fossil fuel combustion and industrial activity on precipitation composition were recognised as long ago as the late 19th century by Robert Angus Smith (*Smith*, 1852; 1872). Smith described the composition of precipitation at Manchester, Liverpool, Glasgow, London and various rural locations in his book '*Air and Rain–the Beginnings of a Chemical Climatology*' (*Smith*, 1872). Whilst acid deposition was first specifically mentioned in the context of the urban environment by *Smith* (1872), little attention has been paid to acidic deposition in the urban environment other than the work of Gorham and Cauer in the 1940s and 50s (*Gorham*, 1955, 1958; *Cauer*, 1949, 1956).

This paper describes some of the findings of a study of precipitation composition in Greater Manchester, a large urban area of the United Kingdom (*Fig. 1*) with a population of approximately 2.58 million. The aim of the study was to investigate the spatial and temporal variability of precipitation composition and to assess the urban modification of regional precipitation composition and deposition (*Longhurst et al.*, 1987).

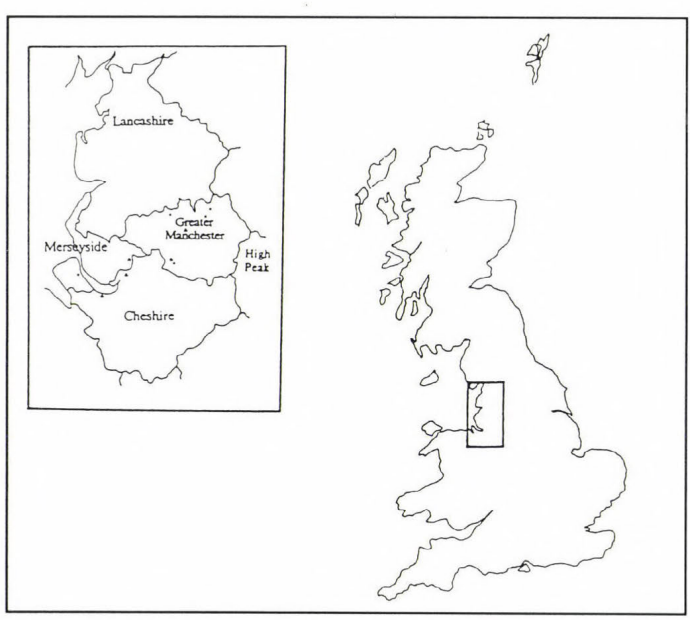

Fig. 1. The north-west of England in relation to the rest of Great Britain.

2. Methods

Samples were collected between January 1987 and December 1988 on a weekly basis from 18 bulk precipitation collectors and despatched to the labo-

ratory for analysis within 24 hours of collection. The network in relation to the geographical extents of Greater Manchester is shown by the crosses in Fig. 3 (see page 94).

An IL 457 spectrophotometer was used for the determination of Ca^{2+}, Mg^{2+} and Zn^{2+}. Sodium and K^+ were determined using a Corning 410 flame photometer. Chloride, SO_4^{2-} and NO_3^- were analysed using a Perkin Elmer ion chromatograph with an LC21 conductivity detector and a Waters IC Pak anion column linked to a LC1-100 Laboratory computing integrator. Hydrogen carbonate and pH were determined within 24 hours of receipt at the laboratory using an Orion EA940 Autochemistry Module fitted with a Ross 8162 electrode. Ammonium was analysed within 24 hours of receipt at the laboratory spectrophotometrically using a Chem Labs Instruments Ltd. autoanalyser.

3. Results and discussion

3.1 Regional emissions estimates

Estimates of emissions of SO_2, NO_x, HCl and NH_3 for Greater Manchester and the north-west of England are given in *Table 1* (see Fig. 1 for geographical extent). These estimates were derived from data on power generation, incinerator plant capacity, fuel usage, animal and human population statistics (*Lee* and *Longhurst*, 1993). The emissions from motor vehicles make up 52% of the NO_x emissions from the north-west of England, whilst those from fossil fuel fired power stations are 20%. The emissions of fossil fuel fired power stations make up 58% of SO_2 emissions from the north-west. A large fossil fuel fired power station is the largest known point source for emissions of SO_2, NO_x and HCl. The largest contribution to NH_3 emissions in the region is from cattle. Humans may contribute some NH_3 to atmospheric emissions (*Atkins* and *Lee*, 1993), as may some other non-agricultural sources (*Lee* and *Dollard*, 1994) but the magnitude of these emissions is highly uncertain.

3.2 Wet and dry deposition

Bulk collectors are continuously open to the atmosphere and collect both wet and dry deposition in the form of gases and aerosols. Bulk deposition collectors provide acceptable estimates of wet deposition at rural background sites but it has been suggested that they are unsuitable for sampling in urban environments (*Gatz*, 1991). Wet-only collectors are expensive and require power, and the operation of a large urban network would be prohibitively expensive. In order to estimate the dry deposition component to the bulk collectors, i.e. the sampling artifact, a wet-only collector was collocated with a bulk collector at one of the sites in the city centre. A comparison of data al-

Table 1. Estimates of emissions of SO_2, NO_x, NH_3 and HCl from Greater Manchester, the north-west of England and the United Kingdom

Source	Greater Manchester* (Gg)	North-west of England* (Gg)	United Kingdom++ (Gg)
SO_2			
Power stations	17	164	2644
Domestic & other	48	119	1055
NO_x			
Power stations	6	41	785
Vehicles & other	70	171	1905
NH_3			
Agriculture	1.2	18.5	300-400#
Industry & other	0.6	1.6	70-100+
HCl			
Power stations	2.0	18.6	244¶
Incinerators & domestic coal burning	3.8	8.7	16¶

* *Lee* and *Longhurst* (1993)
++ *DoE* (1990)
# various estimates, see *Lee* and *Dollard* (1994) for review
+ *Lee* and *Dollard* (1994)
¶ *Lightowlers* and *Cape* (1988)

lowed estimates of the contribution of dry deposition to the bulk collector to be made which are given in *Table 2*. Dry deposition contributed between 15 and 17% to total (wet plus dry) deposition and concentrations of non-marine SO_4^{2-}, NO_3^- and NH_4^+ in the bulk collector and 47% to that of Ca^{2+}. Statistical analyses revealed significant differences between concentrations of ions found in the bulk and wet-only collectors (*Lee* and *Longhurst*, 1992a), but the calculated dry deposition component from gases and aerosols for non-marine SO_4^{2-}, NO_3^- and NH_4^+ found at this urban site was not greatly different to that found at rural sites in the U.K. by *Stedman et al.* (1990). In this particular urban area, the use of bulk collectors did not introduce an unacceptable sampling artifact for S and N species. For acidity, however, it is apparent that the use of a bulk collector introduces a sampling artifact. At the city-centre site, the wet-only collector indicates precipitation weighted mean concentrations of H^+ ion twice those indicated by the use of a bulk collector. It is suggested that such a comparison

Table 2. Measurements of precipitation composition from the collocated bulk and wet-only collectors at the city centre site

	Bulk	Wet	%wet	%dry
Concentration				
non-marine SO_4^{2-}	124.9	106.0	84.9	15.1
NO_3^-	43.9	37.4	85.2	14.8
NH_4^+	58.2	48.2	82.8	17.2
H^+	18.4	37.1	-	-
Ca^{2+}	114.3	61.1	53.4	46.6
Deposition				
non-marine SO_4-S	2.218	1.894	85.4	14.6
NO_3-N	0.683	0.585	85.6	14.4
NH_4-N	0.904	0.754	83.4	16.6
Ca	2.537	1.365	53.8	46.2
mm	1109.7	1116.6	-	-

concentration units = μeq l^{-1}
deposition units = g m^{-2}

would be a requirement for sampling, particularly in more heavily polluted environments where dry deposition may be important. It should, of course, be pointed out that the sampling artifact does not represent dry deposition to natural and urban surfaces.

3.3 Spatial variability

The values of the mean concentrations of non-marine SO_4^{2-}, NO_3^-, NH_4^+ and H^+ across the network are shown in relation to the regional fields of precipitation composition across the U.K. in *Fig. 2* (*RGAR*, 1990). The mean urban network values were not greatly different to those predicted by the U.K. national acid deposition network, which uses bulk collectors sited at rural locations. However, this comparison of data obscures much of the detail from the urban network as the ions in precipitation showed significant spatial variability. Concentrations of non-marine SO_4^{2-}, NO_3^-, NH_4^+, H^+ and Ca^{2+} showed significant spatial variability (*Table 3*) and are shown in *Fig. 3*. This spatial variability demonstrates the potential for local effects of the urban environment and its atmospheric emissions on precipitation composition.

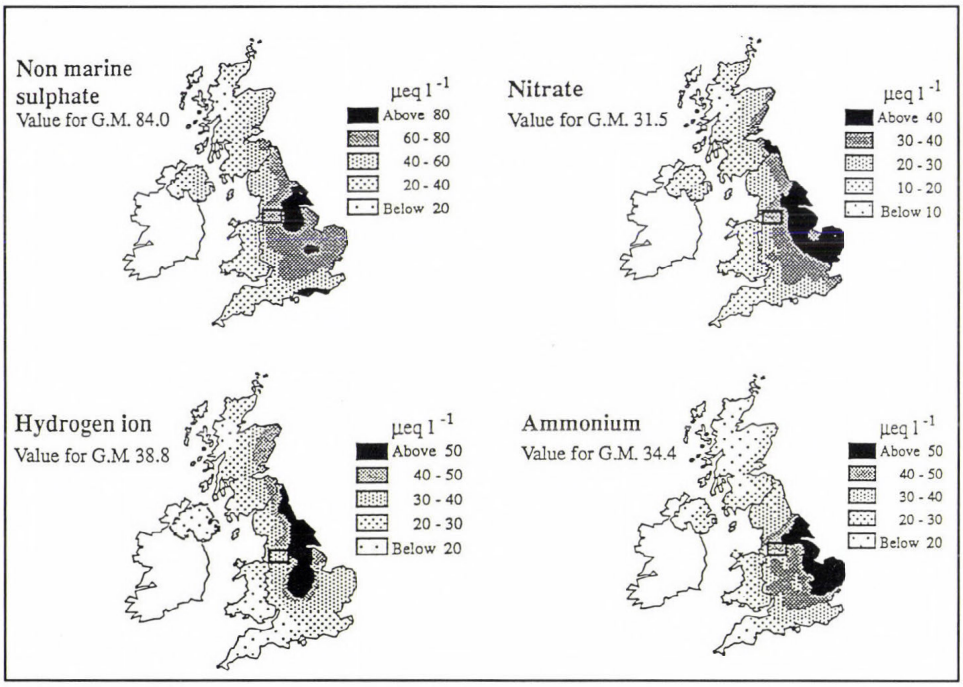

Fig. 2. Mean network values of non-marine sulphate, nitrate, hydrogen and ammonium ions in relation to regional fields of precipitation composition (in μeq l^{-1}).

The spatial variability of non-marine SO_4^{2-} is thought to mainly be the result of the dry deposition of sulphate particles rather than SO_2 gas as the correlation between the dry deposition component of non-marine SO_4^{2-}, evaluated by the difference between the bulk and the wet-only collector, was not significant (*Lee* and *Longhurst*, 1992a). Local variation in the formation of sulphate, and its subsequent removal from the atmosphere, is not feasible on the spatial scale of the network as the oxidation rate is too slow.

Nitrate concentration showed significant spatial variability across the conurbation but this was relatively weak compared to that of other ions in precipitation. Coincident measurements of NO_2 gas concentrations using passive diffusion tube samplers were made at 17 of the 18 sites but the spatial variability of NO_2 was found to be significantly different to that of NO_3^- in precipitation ($r = 0.323$, $P \leq 0.005$). It is concluded that NO_2 gas is not scavenged by precipitation which is in agreement with our current understanding of the atmospheric chemistry of NO_2 and its removal. The spatial variability of NO_3^- in precipitation may be the result of the dry deposition and scavenging of NH_4NO_3 and HNO_3 in the north-east of the study area.

Ammonium concentration was highly variable across the network, which was not random. It is thought that the spatial variability of concentration and

Table 3. Oneway analysis of variance results for periods 1987-1988, 1987, 1988

	1987-1988	1987	1988
non-marine	3.50	2.35	1.66
SO_4^{2-}	< 0.01	< 0.01	0.04
NO_3^-	4.03	2.82	1.95
	< 0.01	< 0.01	0.01
H^+	12.50	6.14	7.52
	< 0.01	< 0.01	< 0.01
NH_4^+	14.70	8.07	9.66
	< 0.01	< 0.01	< 0.01
Ca^{2+}	17.15	8.57	9.51
	< 0.01	< 0.01	< 0.01
mm	1.39	0.80	1.06
	0.13	0.70	0.38

The upper figure is the F ratio, the lower the significance

deposition was not the result of very local sources adjacent to the collectors such as slurry spreading or animal husbandry, as care was taken to locate the collectors away from such sources. Large agricultural sources of NH_3 lie to the south and west of the conurbation in central western England and Wales (*Kruse et al.*, 1989) and the conurbation itself may also be a significant source, as sewage treatment plants and humans, and other urban activities result in emissions of NH_3 (*Lee et al.*, 1992, *Atkins* and *Lee*, 1993, *Lee* and *Dollard*, 1994). The predominant wind direction is from the south-west and the enhanced concentrations and deposition of NH_4^+ in the north-east of the study area may be the result of dry deposition and/or below-cloud scavenging of NH_3 from sources both within and outside the study area.

Calcium concentration showed significant spatial variability with the highest concentrations in the centre of the conurbation. This pattern of variability is thought to be the result of local sources which are intrinsic features of the urban environment. Calcium particles in the atmosphere are generally > 2 μm in diameter so that these large particles are likely to be removed by dry deposition and below-cloud scavenging.

Acidity also showed strong spatial variability which was inversely correlated with Ca^{2+} concentration (*Table 4*). It is likely that calcium compounds in the atmosphere reduce the acidity of precipitation and that the significant spatial variability of H^+ ion concentration is a function of neutralisation by calcium compounds rather than elevated acidity in the fringes of the conurbation.

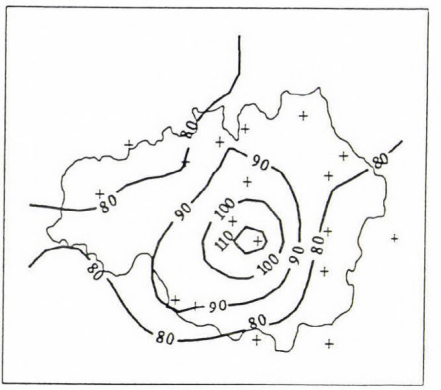

Non-marine sulphate concentrations

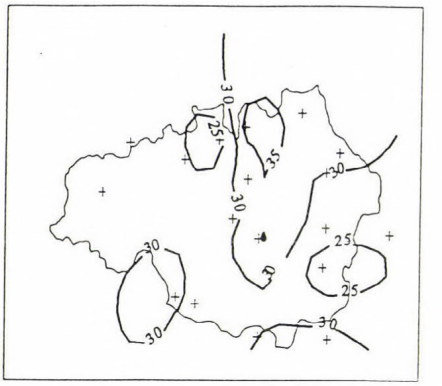

Nitrate concentrations

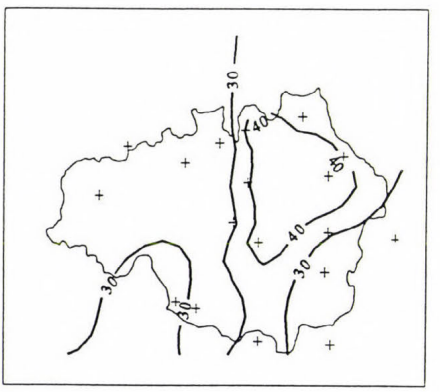

Ammonium concentrations

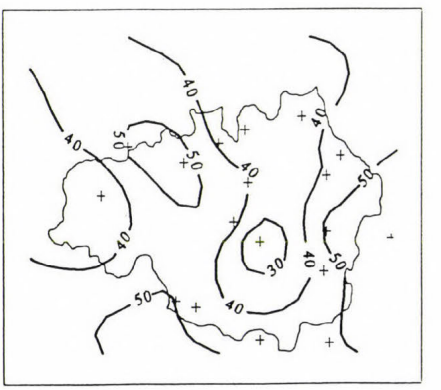

Hydrogen ion concentrations

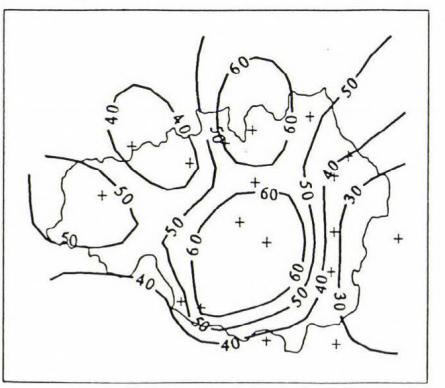

Calcium concentrations

Fig. 3. Concentration fields of non-marine sulphate, nitrate, ammonium, hydrogen and calcium ions across Greater Manchester (in μeq l^{-1}).

Table 4. Correlations between spatial fields of ions in precipitation

	non-marine SO_4^{2-}	NO_3^-	H^+	NH_4^+
NO_3^-	0.296	-	-	-
H^+	- 0.537	- 0.346	-	-
NH_4^+	0.339	0.744*	- 0.329	-
Ca^{2+}	0.836*	0.330	- 0.772*	0.163

* significance less than or equal to 0.005

3.4 Relationships between ions in precipitation

Correlation coefficients calculated between the variables have shown that the data are highly intercorrelated, which hampers interpretation (*Lee*, 1993). Principal Components Analysis (PCA) provides a means of reducing such a large multivariate data set into a series of uncorrelated components which are made up of the original variables. Concentrations of ions in precipitation show a significant inverse correlation with precipitation amount, so that a first-order partial correlation matrix, controlling for precipitation, was used as the basis for the PCA. The PCA was performed on the data from the whole network, rather than by site, and the results are given in *Table 5*. Composite variables of the eigenvectors were selected on the basis of the variable loadings being greater than, or equal to 0.5, (*Gorsuch*, 1983; *Harman*, 1976). The first eigenvector consisted of a marine component (Na^+, Cl^-, Mg^{2+} and K^+) which accounted for 40% of the variation in the data, the second eigenvector of an anthropogenic Ca^{2+}/non-marine SO_4^{2-} component which accounted for 22%, and the third eigenvector of an anthropogenic NH_4^+/NO_3^-, which accounted for 13% of the variation in the data.

Calcium and non-marine sulphate

An analysis of spatial variability clearly shows that Ca^{2+} concentrations are lower at the edge of the urban area (Fig. 3). This phenomenon is not unique to Greater Manchester. Elevated concentrations of Ca^{2+} in urban precipitation have been noted for other cities (e.g. *Clarke* and *Lambert*, 1987; *Lipfert* and *Dupuis*, 1984; *Vermette et al.*, 1988). Calcium is a major component of the fabric of the urban environment, particularly with respect to buildings, and the prevalence of exposed mineral surfaces in towns and cities may have an influence on urban precipitation composition (*Argese* and *Bianchini*, 1989). The wind mediated suspension of coarse particles derived from urban sources such

as erosion of exposed surfaces, extraction industries, construction activities, transportation and combustion may be the source of Ca^{2+} particles in the urban atmosphere. Resuspension of particles occurs as the result of wind (*Nicholson*, 1988) and traffic, both in wet and dry conditions (*Nicholson* and *Branson*, 1990).

Table 5. Results from principal components analysis

Eigenvector	Eigenvalue	% var.	Cum. %
1	3.60853	40.1	40.1
2	2.01505	22.4	62.5
3	1.16865	13.0	75.5
4	0.79473	8.8	84.3

	Eigenvector 1	Eigenvector 2	Eigenvector 3	Eigenvector 4
Cl^-	0.96123			
Na^+	0.92269			
Mg^{2+}	0.87398			
K^+	0.52185			
nm SO_4^{2-}		0.87560		
Ca^{2+}		0.83507		
NH_4^+			0.92410	
NO_3^-			0.74480	
H^+				0.97199

Table 4 shows that the spatial pattern of Ca^{2+} is significantly correlated with that of non-marine SO_4^{2-}. The spatial variability of non-marine SO_4^{2-} (which is significant, but relatively weak) may be the result of an urban source for a fraction of the sulphate. It is suggested that the dry deposition of SO_4^{2-} particles to the bulk collectors results in the spatial variability of non-marine SO_4^{2-}.

Many buildings and other surfaces in towns have been exposed to SO_2, both in the present and the past, which may result in strong sulphation (*Butlin*, 1991). As weathering and other erosive processes occur, particles of both $CaCO_3$ and $CaSO_4$ may be available for suspension.

Other workers have suggested that a relationship between Ca^{2+} and non-marine SO_4^{2-} may be possible in terms of SO_2 reacting with Ca^{2+} bearing

particles in the atmosphere (*Gentilizza* and *Vadjic*, 1986; *Argese* and *Bianchini*, 1989; *Altwicker* and *Mahar*, 1984; *Hooper* and *Peters*, 1989; *Van Borm et al.*, 1989; *Clarke et al.*, 1984). *Buttler* (1988) found conversion rates of samples of $CaCO_3$ to $CaSO_4$ of up to 20% per day from ambient SO_2 at a rural site in the U.S.A. This rate is much slower than the oxidation rate of SO_2 in the atmosphere by either dry or wet oxidation processes which are of the order of per cent per hour (*RGAR*, 1990). Furthermore, any reaction between $CaCO_3$ and SO_2 on particles in the atmosphere will also be limited by the diffusion of the gas into the particle matrix. Thus, the available evidence would suggest that suspension of eroded $CaSO_4$ particles from urban surfaces is more likely to contribute to the spatial variability of SO_4^{2-} particles than atmospheric reaction between SO_2 and $CaCO_3$ particles and subsequent removal of the reaction products.

The origin and form of these SO_4^{2-} particles, however, remains unconfirmed. Other work on particle composition has identified the presence of $CaCO_3$ in the urban atmosphere (*Clarke* and *Karani*, 1992) but *Van Borm et al.* (1989) found that most of the calcium particles are in the sulphate form, rather than the carbonate. *Clarke* and *Karani* (1992) did not, however, quantify the sulphate fraction of the particle phase.

Nitrate and ammonium

The results from the principal components analysis has shown that there is a statistical association between NH_4^+ and NO_3^-. Ammonia may be removed from the atmosphere by wet and dry deposition and atmospheric reactions (*ApSimon et al.*, 1987). It is possible that the elevated concentrations of NH_4^+ in the north-west of the conurbation may be the result of scavenging of NH_3 emissions from animal sources within the conurbation, combined with other sources such as a large sewage treatment plant in the west of the conurbation, humans and other urban sources.

The concentration fields of NO_3^- and NH_4^+ are significantly correlated but the spatial variability of NO_3^- is much weaker than that of NH_4^+ (Tables 3 and 4). The spatial variability of NO_3^- may be the result of the dry deposition of HNO_3. Both NH_3 and HNO_3 are reactive gases with large deposition velocities but HNO_3 is a secondary pollutant formed from the day-time reaction of OH radicals with NO_2 and the night-time reaction with O_3, so that dry deposition is thus unlikely to contribute to spatial variability of concentration and deposition on a local scale, whereas NH_3 is a primary pollutant and is more likely to be spatially variable. The reversible reaction between these two gases to form NH_4NO_3 is also likely to be a sink. The strong correlation between NH_4^+ and NO_3^- concentrations may be the result of this chemical interaction and subsequent precipitation scavenging of NH_4NO_3. This explanation is, however, somewhat speculative.

Neutralisation of acidity by calcium compounds

The acidity of precipitation is a balancing term which responds to concentrations of other ions so that any local source effect increasing H^+ ion concentration would be the result of associated acid nitrate, sulphate or chloride. Furthermore, the acidity will also be altered by the neutralising effect of NH_3, the buffering of NH_4^+ salts or alkaline particles in the atmosphere. This neutralisation effect may mask any acidity enhancement. The spatial pattern of Ca^{2+} concentration appears to 'mirror' that of H^+ ion and they are inversely correlated (Table 4). Thus, it would seem that Ca compounds in the urban atmosphere reduce the acidity of precipitation, so that the spatial variability of the deposition and concentration of H^+ ion is the result of the spatial variability of calcium. The effect of the reduction of acidity from alkaline calcium compounds in the urban atmosphere was also noted by *Casado et al.* (1992) in the urban atmosphere of Vitoria, Spain. However, this apparent neutralisation by Ca compounds is difficult to explain as it has previously been argued that the relationship between Ca^{2+} and non-marine SO_4^{2-} may be the result of SO_2 oxidation on urban surfaces with subsequent suspension and deposition of these particles. Calcium sulphate would not effectively neutralise acidity, whereas $CaCO_3$ would. The only explanation that can be offered is the presence of both these chemical forms which may vary in their spatial distributions. It is suggested that the site of the neutralisation is more likely to be the collector itself, rather than the atmosphere, as the precipitation weighted mean concentration of H^+ ion from the wet-only collector is twice that found in the bulk collector. A likely explanation for this is that Ca^{2+} particles are dry deposited onto the funnel of the bulk collector and are washed in after precipitation events with subsequent neutralisation.

3.5 Temporal variability

Monthly network mean concentrations of non-marine SO_4^{2-}, NO_3^-, NH_4^+, H^+ and Ca^{2+} ions are shown in *Fig. 4*. Mean network concentrations of non-marine SO_4^{2-}, NO_3^-, NH_4^+, and Ca^{2+} ions show more variability in 1988 than in 1987. The exception to this is H^+ ion concentration, for which the converse situation is apparent. It is also apparent that concentrations of NH_4^+ and Ca^{2+} ions are more variable than those of non-marine SO_4^{2-}, NO_3^- and H^+.

Seasonal variability has been shown to exist for concentrations of the major anthropogenic ions in precipitation (i.e. non-marine SO_4^{2-}, NO_3^-, NH_4^+, and H^+) at rural sites across the U.K. where a maximum in concentration is observed in late spring, and a minimum in early winter (*RGAR*, 1983; 1987; 1990; *Skeffington*, 1984) so that the seasonal pattern found at the urban sites is consistent with that found at other rural sites in the U.K.

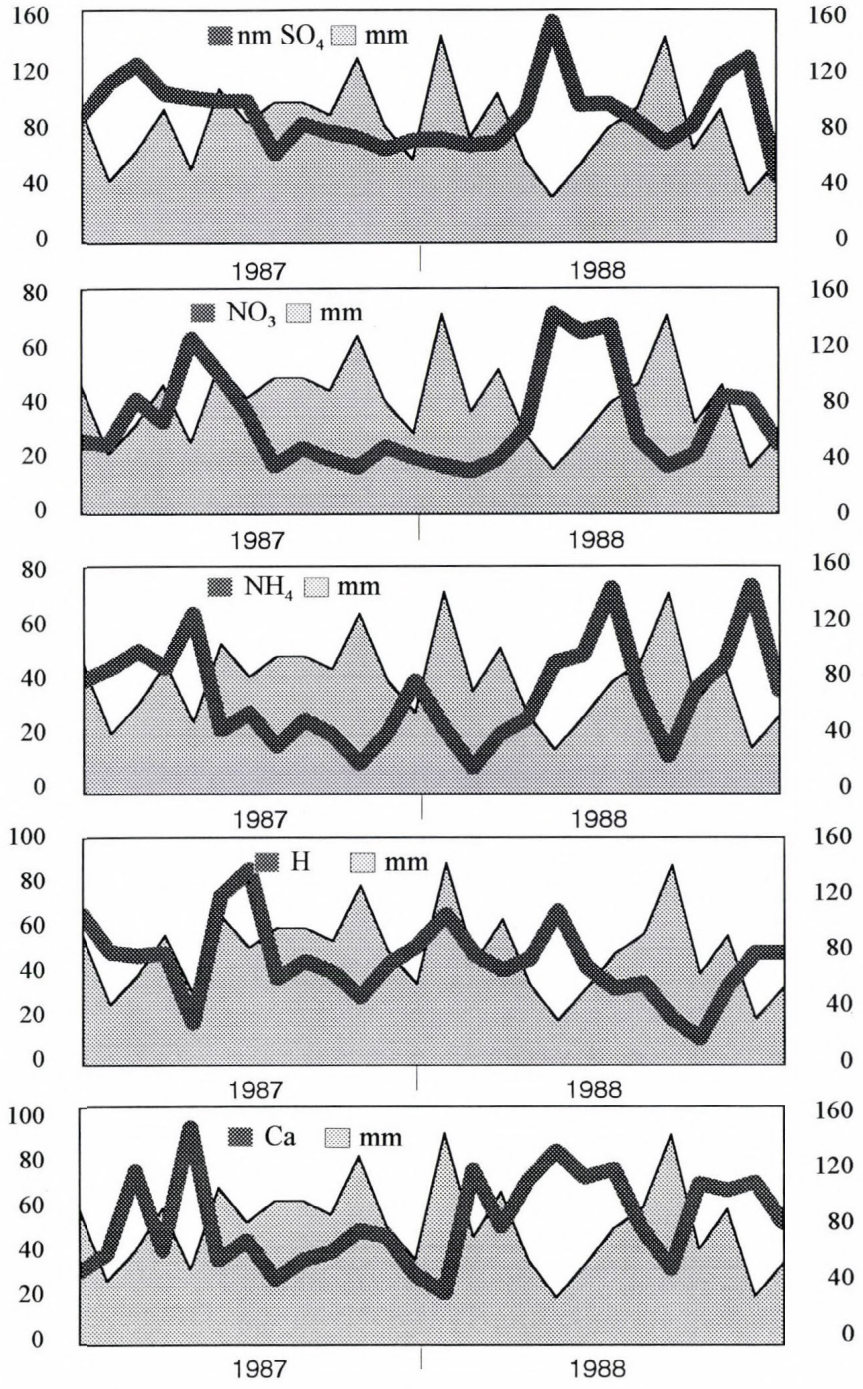

Fig. 4. Four-weekly precipitation weighted mean concentrations (in μeq l^{-1}, left ordinates) of non-marine sulphate, nitrate, ammonium, hydrogen and calcium ions and the precipitation (in mm, right ordinates) 1987-1988 (mean network values).

The temporal variability of concentrations of various ions in precipitation from the urban network was also compared to data collected from two nearby rural sites, Wardlow Hay Cop in Derbyshire and Hebden Bridge in West Yorkshire, some 30 and 15 km distant from the conurbation, and are shown in *Fig. 5*. For concentrations of all species, similarities can be seen between the mean urban network data and data from the two rural sites, with the exception of Ca^{2+} concentration at Wardlow Hay Cop. It is thought that much of the Ca^{2+} ion in precipitation at this site originates from large dust particles from local limestone quarrying, which is extensive in this part of the country, and account for the observed differences (*Lee* and *Longhurst*, 1992b). This comparison of time series plots supports the suggestion of the larger scale influence of meteorology on the temporal variability of species concentration in precipitation (*Davies et al.*, 1990), a factor which also prevails over Greater Manchester.

Whilst the urban area of Greater Manchester is thought to influence spatial patterns of deposition by local emissions adding to meso-scale emissions, temporal variability is considered to be the result of the larger scale influence of meteorology. Identification of the origin of air masses, particularly those which lead to the largest deposition of species, aids the identification of source regions.

One way in which deposition can be considered, is by the identification of episodes. The temporal nature of deposition has so far only been considered in terms of annual cycles. However, wet deposition is made up of discrete events.

In this investigation, bulk deposition was collected on a weekly basis and hence it was only possible to define 'episode weeks' (i.e. those weeks for which 30% of the annual deposition fell) for the whole network rather than individual events. The deposition of non-marine SO_4-S, NO_3-N and NH_4-N were calculated in terms of percentage deposition per week for 1988 and shown in *Fig. 6*. Deposition which lies on or above the horizontal lines shown in these figures indicates the individual weeks which contributed 30% of the annual deposition. The episodicity of a species is defined as the ratio of the number of episode weeks to the number of individual rain days. Across the network, NH_4-N deposition was the most episodic at 13%, the episodicity of NO_3-N was 15% and non-marine SO_4-S was the least episodic at 19%. From Fig. 6 it appears that episode weeks of NH_4-N and NO_3-N tend to occur together, mostly independent of non-marine SO_4-S deposition, particularly in the summer. However, this can only remain speculative as episode weeks are made up of several rain events and it was not possible to attribute deposition quantitatively to any particular trajectory. Two weeks which illustrate the ability of quite different synoptic weather condition to lead to large deposition were weeks 28 and 43. Composite back trajectories constructed for these weeks in which particular conditions prevailed are shown in *Figs. 7* and *8*. In Fig. 7, conditions were dominated by a strong frontal Atlantic low pressure system. As the

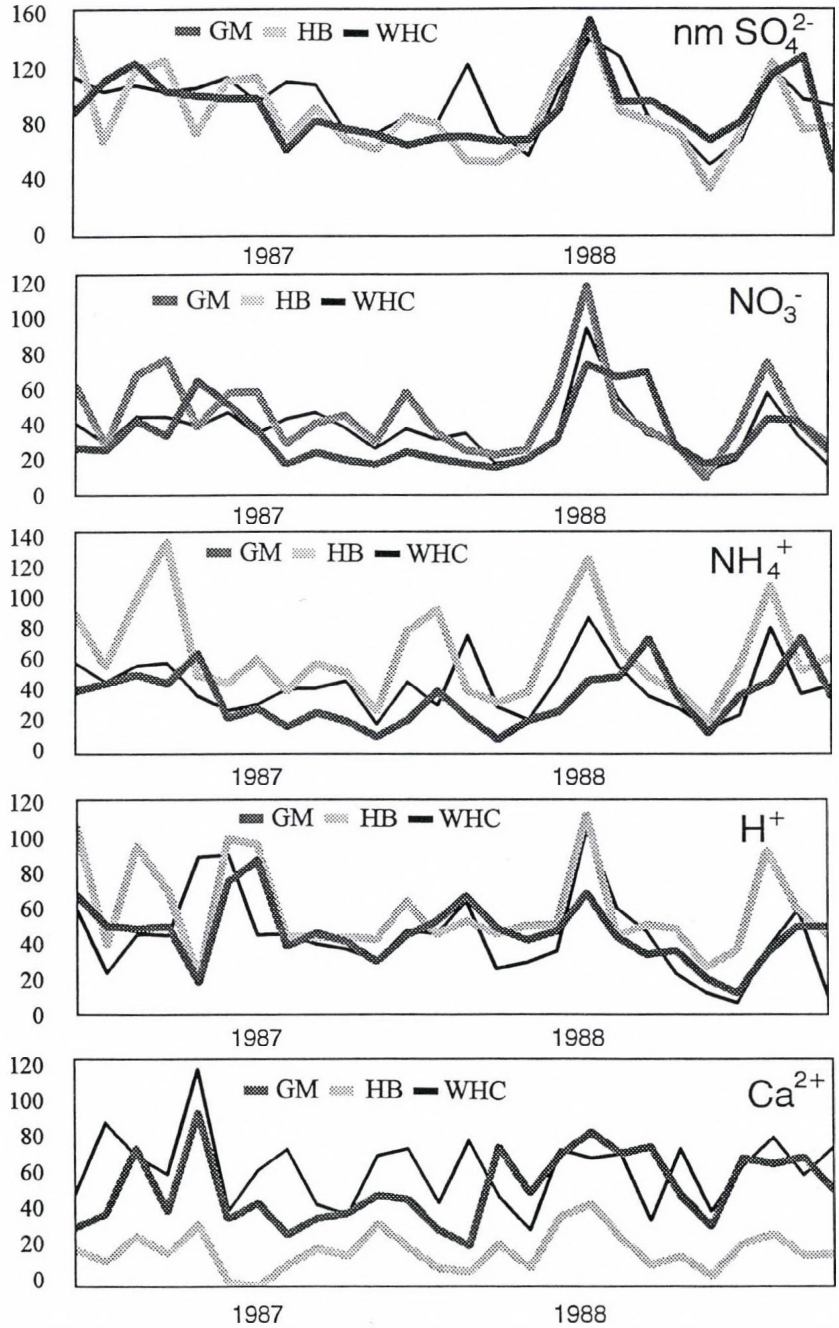

Fig. 5. Four-weekly precipitation weighted mean concentrations (in μeq l^{-1}) of non-marine sulphate, nitrate, ammonium, hydrogen and calcium ions 1987–1988, from the Greater Manchester network and two nearby rural sites, Hebden Bridge and Wardlow Hay Cop.

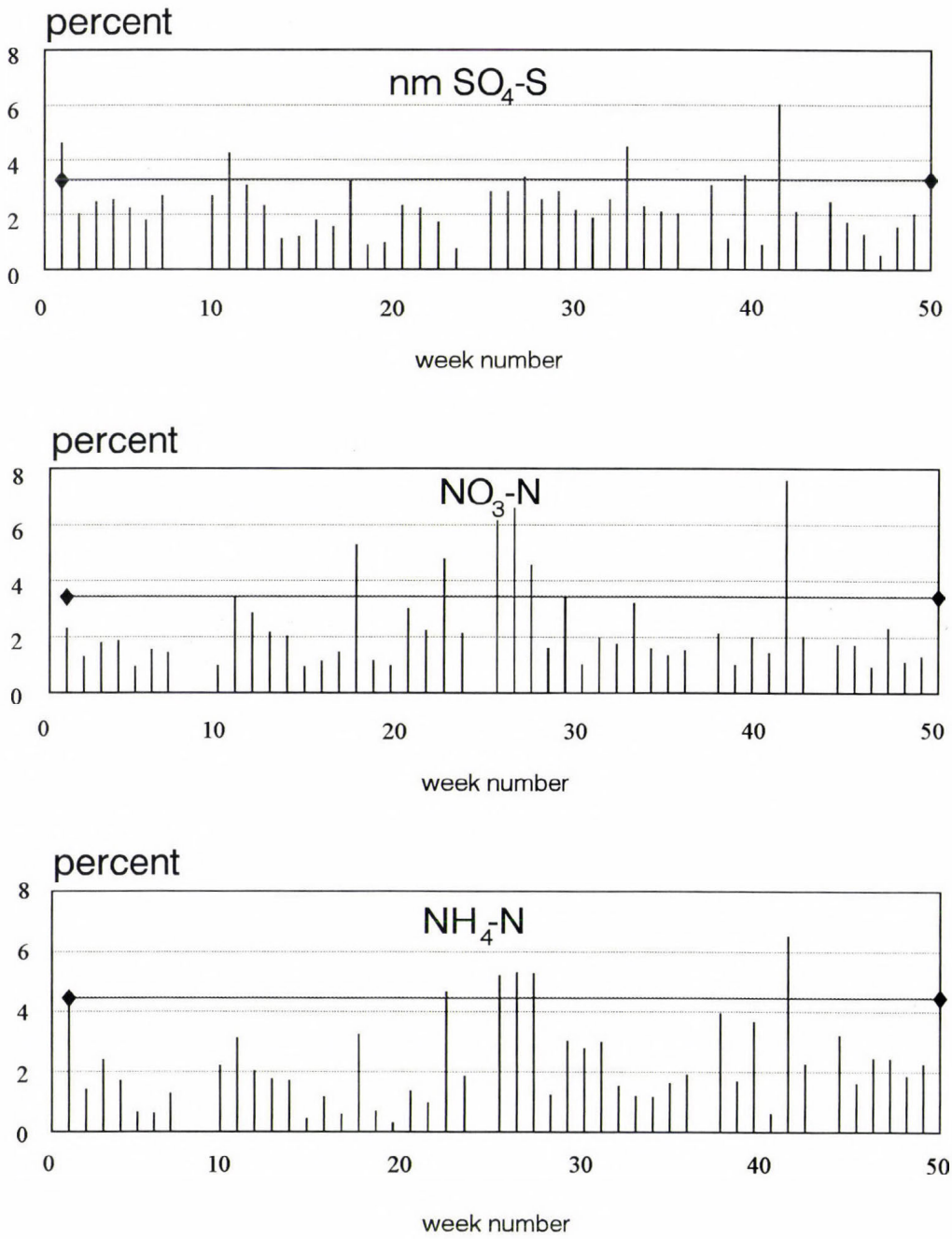

Fig. 6. Weekly network deposition of non-marine sulphate (S), nitrate (N) and ammonium (N). Horizontal lines indicate threshold value for 'episode weeks'.

trajectories indicate, this system drew in air from Europe, which resulted in large concurrent deposition of non-marine SO_4-S, NH_4-N and NO_3-N. In week 43, however, the trajectories which lead to rain events and a large deposition episode of non-marine SO_4-S, NH_4-N and NO_3-N were the result of a high pressure system which drew in air masses directly from central Europe in an easterly flow (Fig. 8).

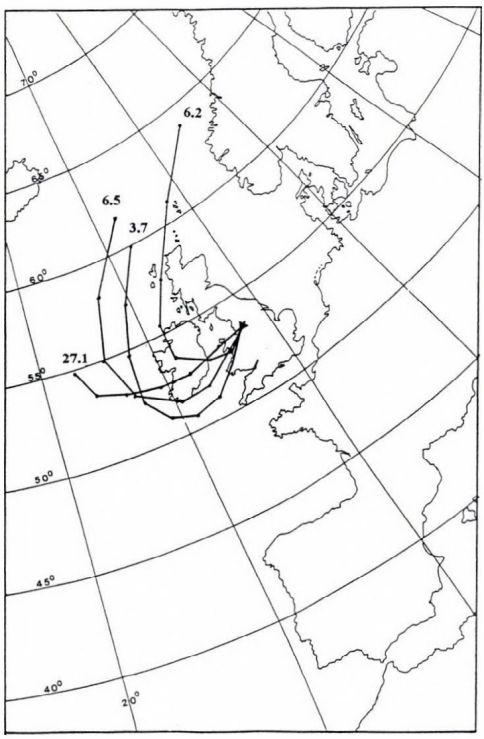

Fig. 7. Composite trajectories for episode week, Atlantic frontal system, showing precipitation amounts for each trajectory (mm).

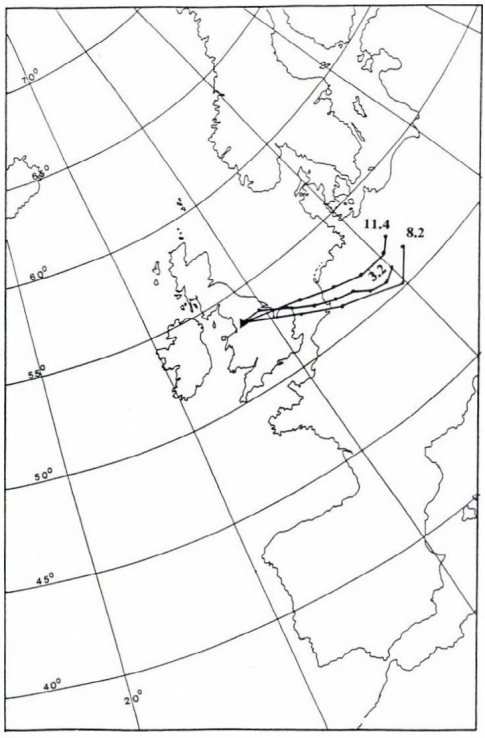

Fig. 8. Composite trajectories for episode week, high pressure system, showing precipitation amounts for each trajectory (mm).

4. Conclusions

Concentrations of non-marine SO_4^{2-}, NO_3^-, NH_4^+, and H^+ in precipitation over Greater Manchester are not greatly different to those predicted by interpolation of data from a national rural network. However, all these ions exhibit significant spatial variability, particularly NH_4^+, Ca^{2+} and H^+. The use of bulk precipitation collectors in the urban environment did not introduce a sampling artifact which was greater than that found at more rural sites in the U.K. for S and N species.

Local sources of SO_2 and NO_x did not result in enhanced concentrations of SO_4^{2-} and NO_3^- in precipitation over the study area, these ions were the result of more regional scale atmospheric chemistry. It is postulated that local sources of Ca^{2+} and NH_3 had an impact on urban precipitation composition. Calcium is thought to have its origin in the suspension of calcium-bearing particles from the erosion of urban surfaces and emissions from construction and industrial activities. Ammonia has urban sources but the magnitude of these are, as yet, uncertain. It is likely, however, that the steep gradient of NH_4^+ ions in precipitation are the result of local sources. Urban precipitation is not generally more acidic than rural precipitation but was found to be rather less so in the centre of the conurbation, as measured by the bulk collector. However, a comparison of data from the wet-only and bulk collectors at the city centre site would indicate that the site of neutralisation is the bulk collector rather than the atmosphere. Calcium carbonate aerosol is probably the main neutralising compound.

The temporal variation of concentrations of the major ions in rainfall was very similar to that observed at two rural monitoring sites, demonstrating that synoptic scale meteorology controls the seasonal variations of all the major ions in urban precipitation. Episodes of deposition were observed, of which NH_4-N, was the most episodic. By constructing back trajectories for selected weeks, it was shown that both high and low pressure systems could result in deposition episodes of S and N species, but that the origin of the emissions was European in both instances.

Acknowledgements–This work was funded by *Tameside Metropolitan Borough Council* on behalf of the *Association of Greater Manchester Authorities Planning and Transportation Committee*. Data from the national network sites were provided *Warren Spring Laboratory* who operate the network on behalf of the *U.K. Department of the Environment*.

References

Altwicker, E.R. and *Mahar, J.T.*, 1984: NH_4/Ca ratio in different forms of atmospheric deposition: interpretative potential. *Atmosph. Environ. 18*, 1875-1883.

ApSimon, H.M., *Kruse, M.* and *Bell, J.N.B.*, 1987: Ammonia emissions and their role in acid deposition. *Atmosph. Environ. 21*, 1939-1946.

Argese, E. and *Bianchini, A.G.*, 1989: Chemical and physical characteristics of rainfall in Venice: influence of the sampling method on the reliability of the data. *Sci. Tot. Environ. 83*, 287-298.

Atkins, D.H.F. and *Lee, D.S.*, 1993: Indoor concentrations of ammonia and the potential contribution of humans to atmospheric budgets. *Atmosph. Environ. 27A*, 1-7.

Butlin, R.N., 1991: Effects of air pollutants on buldings and materials. *Proc. R. Soc. Edin. 97B*, 255-272.

Buttler, T.J., 1988: Composition of particles dry deposited to an inert surface at Ithaca, New York. *Atmosph. Environ. 22*, 895-900.

Casado, H., *Eacinas, D.* and *Lacaux, J.P.*, 1992: The moderating effect of the Ca^{2+} ion on the acidity in precipitation. *Atmosph. Environ. 26*, 1175.

Cauer, H., 1949: Ergebnisse chemisch-meteorologischer Forschung. *Arch.*

Geophys. Bioklimat. S.B.B.I.H, 221-256.

Cauer, H., 1956: Die pH-Werte von Aerosolen und Niederschlägen und ihre lufthygienische und bioklimatische Indikatorbedeutung. *Zeit. Aerosol Forsch. Therapie 6*, 459-509.

Clarke, A.G. and *Karani, G.N.*, 1992: Characterisation of the carbonate content of atmospheric aerosols. *J. Atmosph. Chem. 14*, 119-128.

Clarke, A.G. and *Lambert, D.R.*, 1987: Local factors affecting the chemistry of precipitation. In *Acid Rain: Scientific and Technical Advances* (eds.: *R. Perry, R.M. Harrison, J.N.B. Bell* and *J.N. Lester*). Selper Ltd., London.

Clarke, A.G., Willison, M.J. and *Zeki, E.M.*, 1984: A comparison of urban and rural aerosol composition using dichotomous samplers. *Atmosph. Environ. 18*, 1767-1775.

Davies, T.D., Farmer, G. and *Barthelmie, R.J.*, 1990: Use of simple atmospheric circulation types for the interpretation of precipitation composition at a site (Eskdalemuir) in Scotland, 1978-1984. *Atmosph. Environ. 24A*, 63-72.

DoE, 1990: *Digest of Environmental Protection and Water Statistics No. 12*. Department of the Environment, HMSO, London.

Gatz, D.F., 1991: Urban precipitation chemistry: a review and synthesis. *Atmosph. Environ. 25B*, 1-15.

Gentilizza, M. and *Vadjic, V.*, 1986: The relationship between the mass concentrations of sulphate and sulphur dioxide in air polluted with cement dust. *Sci. Tot. Environ. 48*, 231-237.

Gorham, E., 1955: On the acidity and salinity of rain. *Geochim. et Cosmochim. Acta 7*, 231-239.

Gorham, E., 1958: Atmospheric pollution by hydrochloric acid. *Quart. J. Roy. Meteorol. Soc. 84*, 274-276.

Gorsuch, R.L., 1983: *Factor Analysis*. Lawrence Erlbaum Associates, New Jersey.

Harman, H.H., 1976: *Modern Factor Analysis*. University of Chicago Press, Chicago.

Hooper, R.P. and *Peters, N.E.*, 1989: Use of multivariate analysis for determining sources of solutes found in wet atmospheric deposition in the United States. *Environ. Sci. Technol. 23*, 1263-1268.

Kruse, M., ApSimon, H.M. and *Bell, J.N.B.*, 1989: Validity and uncertainty of an emission inventory for ammonia arising from agriculture in Great Britain. *Environ. Pollut. 56*, 237-257.

Lee, D.S., 1993: The spatial variability of urban precipitation chemistry and deposition; statistical associations between constituents and potential removal processes of precursor species. *Atmosph. Environ. 27B*, 321-337.

Lee, D.S. and *Dollard, G.J.*, 1994: Uncertainties in current estimates of the emissions of ammonia in the United Kingdom. *Environ. Pollut.* (in press).

Lee, D.S. and *Longhurst, J.W.S.*, 1992a: A comparison between wet and bulk deposition at an urban site in the U.K. *Water, Air, and Soil Pollut. 64*, 635-648.

Lee, D.S. and *Longhurst, J.W.S.*, 1992b: A statistical intercomparison between 'urban' and 'rural' precipitation data from Greater Manchester and two nearby secondary national network sites in the United Kingdom. *Atmosph. Environ. 26A*, 2869-2883.

Lee, D.S. and *Longhurst, J.W.S.*, 1993: Estimates of emissions of SO_2, NO_x, HCl and NH_3 from a densely populated region of the U.K. *Environ. Pollut. 79*, 37-44.

Lee, D.S., Nason, P.D. and *Bennett, S.L.*, 1992: Atmospheric ammonia in the vicinity of a sewage treatment plant–results from a preliminary investigation. AEA-EE-0328, AEA Environment and Energy, Harwell Laboratory, Oxon.

Lightowlers, P.J. and *Cape, J.N.* 1988: Sources and fate of atmospheric HCl in the U.K. and western Europe. *Atmosph. Environ. 22*, 7-15.

Lipfert, F.W. and *Dupuis, L.R.*, 1984: Urban and local effects on precipitation chemistry. *Proc. 77th Ann. Meet. Air Pollut. Contr. Assoc.*

Longhurst, J.W.S., Gee, D.R., Lee, D.S. and *Green, S.E.* 1987: The establishment of an urban acid deposition monitoring network. *Environmentalist 7*, 299-307.

Longhurst, J.W.S., Raper, D.W., Lee, D.S., Heath, B.A., Conlan, B. and *King, H.J.*, 1993a: Acid deposition: a select review 1852-1990. 1. Emissions, transport, deposition, effects on freshwater systems and forests. *Fuel 72*, 1261-1280.

Longhurst, J.W.S., Raper, D.W., Lee, D.S., Heath, B.A., Conlan, B. and *King, H. J.*, 1993b: Acid deposition: a select review 1852-1990. 2. Effects on materials and health; abatement strategies and programmes. *Fuel 72*, 1363-1380.

Nicholson, K.W., 1988: A review of particle resuspension. *Atmosph. Environ. 22*, 2639-2651.

Nicholson, K.W. and *Branson, J.R.*, 1990: Factors affecting resuspension by road traffic. *Sci. Tot. Environ. 93*, 349-358.

RGAR, 1983: *Acid Deposition in the United Kingdom.* United Kingdom Review Group on Acid Rain. Warren Spring Laboratory, Stevenage.

RGAR, 1987: *Acid Deposition in the United Kingdom 1981-1985.* A second report of the United Kingdom Review Group on Acid Rain. Warren Spring Laboratory, Stevenage.

RGAR, 1990: *Acid Deposition in the United Kingdom 1986-1988.* A third report of the United Kingdom Review Group on Acid Rain. Warren Spring Laboratory, Stevenage.

Skeffington, R.A., 1984: The chemistry of bulk precipitation at a site in southeast England – I. Small scale spatial variation, frequency distributions and variation with time. *Atmosph. Environ. 18*, 1683-1693.

Smith, R.A., 1852: On the air and rain of Manchester. *Mem. Lit. Phil. Soc. Manchester 10*, 207-217.

Smith, R.A., 1872: *Air and Rain. The Beginnings of a Chemical Climatology.* Longmans Green and Co., London.

Stedman, J.R., Heyes, C.J. and *Irwin, J.G.*, 1990: A comparison of bulk and wet-only precipitation collectors at rural sites in the United Kingdom. *Water, Air, and Soil Pollut. 52*, 377-395.

Van Borm, W.A., Adams, F.C. and *Maenhaut, W.*, 1989: Characterization of individual particles in the Antwerp aerosol. *Atmosph. Environ. 23*, 1139-1151.

Vermette, S.J., Drake, J.J. and *Landsberger, S.*, 1988: Intra-urban precipitation quality: Hamilton, Canada. *Water, Air, and Soil Pollut. 38*, 37-53.

IDŐJÁRÁS

Quarterly Journal of the Hungarian Meteorological Service
Vol. 98, No. 2, April–June 1994

The effect of the droplet size distribution on the reflectivity of boundary layer clouds

I. Csiszár

Satellite Research Laboratory, Hungarian Meteorological Service
P.O. Box 39, H-1675 Budapest, Hungary

(Manuscript received 17 March 1994; in final form 12 May 1994)

Abstract—The principal aim of this study was the assessment of the applicability of the 3.7 μm satellite reflectivity measurements for the retrieval of cloud microphysical properties, with special respect to the *High Resolution Infrared Radiation Sounder* (HIRS) on board the polar orbiter NOAA series. Reflectivities of opaque plane-parallel water clouds have been simulated using a discrete-ordinate radiative transfer model by assuming various droplet size distributions. A small sensitivity to the width of the droplet size spectrum was observed. The effects of the within-cloud horizontal variability were also investigated. The calculations have shown that the fractal re-distribution of the droplet population causes changes in the cloud reflectivity. These phenomena affect not only the effective radius retrieval accuracy, but also have to be taken into account in the parametrization of the near-infrared cloud albedo in general circulation models.

Key-words: radiation balance, cloud microphysics, satellite measurements.

1. Introduction

During the recent years there has been a major concern about the radiative effects of cloudiness on the Earth's energy budget. The net *cloud forcing* (the change of total radiant energy due to the presence of clouds) shows significant variation with cloud type. For example, cirrus clouds exhibit a warming effect because of their high shortwave transmissivity and low longwave emission. Low stratocumulus clouds, on the other hand, reflect large proportion of the shortwave energy with little compensation in the longwave region. Investigations have revealed that 15–20% increase in their amount, 20–35% increase in their liquid water path or 15–20% decrease in their droplet size can balance the radiative perturbation from doubling of the CO_2 content (*Slingo*, 1990). Therefore, the accurate knowledge about these parameters is essential and requires sophisticated retrieval methods.

Meteorological satellites provide a unique opportunity to obtain global information on the state and amount of the cloudiness. The *International Satellite Cloud Climatology Program* (ISCCP, *Rossow* and *Schiffer*, 1991) is aimed at the collection and processing of such data.

In this study we were focusing on the effect of the cloud droplet size distribution on the accuracy of the retrieval of the cloud droplet *effective radius* (r_e). This parameter is the ratio of the total volume to the total surface of the cloud droplets. A commonly used bispectral retrieval approach is based on constructing reflectivity look-up tables by radiative transfer calculations in a visible window and a near-infrared liquid water absorption band for various sun-satellite geometries, cloud optical depth (τ) and effective radius values. Then, the satellite reflectivity measurements at a given viewing geometry provide simultaneously the optical depth and the effective radius of the cloud droplets. However, for relatively thick clouds ($\tau \geq 10$) the reflection in the near-infrared (e.g around 1.65, 2.16 or 3.7 μm) is closely independent of the optical depth (*Nakajima* and *King*, 1990). Hence, in such cases, the effective radius can be directly derived from the near-infrared satellite reflectivity measurements.

Two radiometers on board the polar orbiting operational NOAA satellites carry out measurements in the 3.7 μm band. They are channel 3 of the *Advanced Very High Resolution Radiometer* (AVHRR) and channel 19 of the *High Resolution Infrared Radiation Sounder* (HIRS), having sub-satellite pixel sizes of 1.1 and 17 km, respectively. Both instruments have been used for the retrieval of cloud droplet effective radius (see, for example, *Arking* and *Childs*, 1985; *Gu et al.*, 1992; *Watts*, 1993).

However, the simulated reflectivity values are calculated using several simplifying assumptions. First, the clouds are taken geometrically plane-parallel. Second, within-cloud homogeneity in liquid water content is assumed on a scale comparable to the pixel size of the satellite radiometer. In addition, the effective radius is also taken to be constant on the same scale, and the statistical characteristics of the droplet size spectra in all pixels are fixed. Obviously, in some cases these simplifications are not entirely applicable. Here we will examine the potential error caused by the last assumptions, using in-situ and remote sensing observational data of marine stratocumulus clouds during the *First ISCCP Regional Experiment* (FIRE) off the California Coast in 1987 (*Nakajima et al.*, 1991). We will concentrate on the larger field of view (FOV) of HIRS where the bias is expected to be larger.

In the paper we first introduce the physical basis of the simulation of cloud reflectivities by radiative transfer calculations. After that we investigate the potential retrieval error connected to the assumption of constant droplet spectrum width. In the following section we study the effect of the horizontal cloud inhomogeneity on the reflectivity. That will be followed by some discussion and concluding remarks.

2. *Calculation of simulated reflectivities of opaque plane-parallel water clouds*

In the investigated spectral region the shortwave solar radiation and the longwave terrestrial thermal emission are of comparable magnitude. However, the thermal emission can be easily removed from the measured radiance. Hence, it is sufficient to use the radiative transfer equation for a multiple scattering atmosphere, which describes the change of the radiant intensity I in direction Ω at a given optical depth (*Liou*, 1980)

$$\mu \frac{dI(\tau,\Omega)}{d\tau} = I(\tau,\Omega) - \frac{\varpi}{4\pi} \int_{4\pi} I(\tau,\Omega')\, P(\Omega,\Omega')\, d\Omega' - \frac{\varpi}{4\pi}\, \pi F_0\, P(\Omega, -\Omega_0)\, e^{-\frac{\tau}{\mu_0}}, \tag{1}$$

where $\mu = \cos\Theta$ and $\mu_0 = \cos\Theta_0$ denote the cosines of the observational and solar zenith angles respectively, ϖ is the *single scattering albedo* (the ratio of the scattering and extinction efficiencies), F_0 is the solar flux and P is the *phase function* that describes the angular distribution of the scattering. It is usual to express P in the form of Legendre polynomial expansion:

$$P(\cos\chi) = \sum_{0}^{N} \alpha_l P_l(\cos\chi), \tag{2}$$

where χ is the angle between the incident and scattered beams (scattering angle) and P_l is the lth Legendre polynomial. The first moment of the expansion, α_1 is the *asymmetry factor* (generally denoted as g) that gives at what rate the scattering differs from the isotropic distribution.

In this work the scattering parameters at $\lambda = 3.7$ μm were calculated by the Mie scattering program *MIEV0* developed by *Wiscombe* (1979). This software provides, among other quantities, the single scattering albedo, the asymmetry factor and the coefficients for the Legendre polynomial expansion for a single droplet size and wavelength. To obtain these parameters for a given size distribution an integration over the droplet size spectrum is required. The complex refractive index of water for 3.7 μm was taken from the work by *Paltridge* and *Platt* (1976).

The angular distribution of the radiant intensity on the top of the atmosphere was determined by the discrete-ordinate radiative transfer program *DISORT* (*Stamnes et al.*, 1988), using 24 computational polar angles (streams). A three-layer atmospheric model was applied in which the cloud was located in the middle layer with Rayleigh scattering and weak water vapour absorbtion in the top and bottom layers. The reflectivity was determined from the following formula

$$R(\mu,\mu_0,\Phi) = \frac{\pi I(0,-\mu,\Phi)}{\mu_0 F_0}, \tag{3}$$

in which Φ represents the azimuthal separation of the sun and the satellite. The physical meaning of the reflectivity is what the cloud albedo would be if the reflection were isotropic.

3. Sensitivity of the cloud reflectivity to the width of the droplet size spectrum

Throughout this work it was assumed that the droplet size spectrum of a stratocumulus cloud follows the lognormal distribution. This distribution is understood locally, i.e. the whole spectrum is present in a vertical cloud column having a horizontal dimension that is comparable to or smaller than the pixel (or FOV) size of the satellite sensor. The optical depth of all cloud columns was 32. Since in the case of opaque clouds the remotely sensed cloud microphysical parameter represents the upper third of the cloud (*Nakajima* and *King*, 1990), for simplicity, no vertical inhomogeneity was taken into account. The effects of two parameters were investigated: those of the standard deviation of the lognormal distribution, σ (the width of the spectrum) and the effective radius, r_e that is connected to the mode radius of the lognormal distribution r_0 by the following expression

$$r_e = r_0 \exp(5\sigma^2). \tag{4}$$

Fig. 1 shows the reflectivity pattern between $\Phi = 0°$ and 180° for four effective radii at 60° and 30° solar and satellite zenith angles respectively for standard deviations ranging between 0.20 and 0.50. The strengthening of the forward scattering with the increase of r_e is obvious. It is also clear that the reflectivity is sensitive to the width of the droplet spectrum, which can lead to retrieval errors in extreme situations. For example, at these solar and satellite zenith angles and $\Phi = 0$ the same reflectivity value (R = 21%) corresponds to both $r_e = 5$ μm, $\sigma = 0.20$ and $r_e = 10$ μm, $\sigma = 0.50$. However, using look-up tables calculated assuming a realistic mean value of $\sigma = 0.35$, this potential absolute error at such droplet sizes is generally not larger than 2–3 μm.

In *Fig. 2* the reflectivity pattern is shown as a function of the effective radius at the above viewing geometry and standard deviation (it is hereafter referred to as *reflection function*). With the increase of its slope one may suspect a decrease of the potential retrieval error towards the smaller droplets. This can be easily justified by scrutinizing Fig. 1, where a correspondence similar to the above example is depicted between $r_e = 3$ μm, $\sigma = 0.20$ and $r_e = 5$ μm, $\sigma = 0.50$ (R = 31%).

In addition, by investigating Fig. 1 it can also be observed that the sensi-

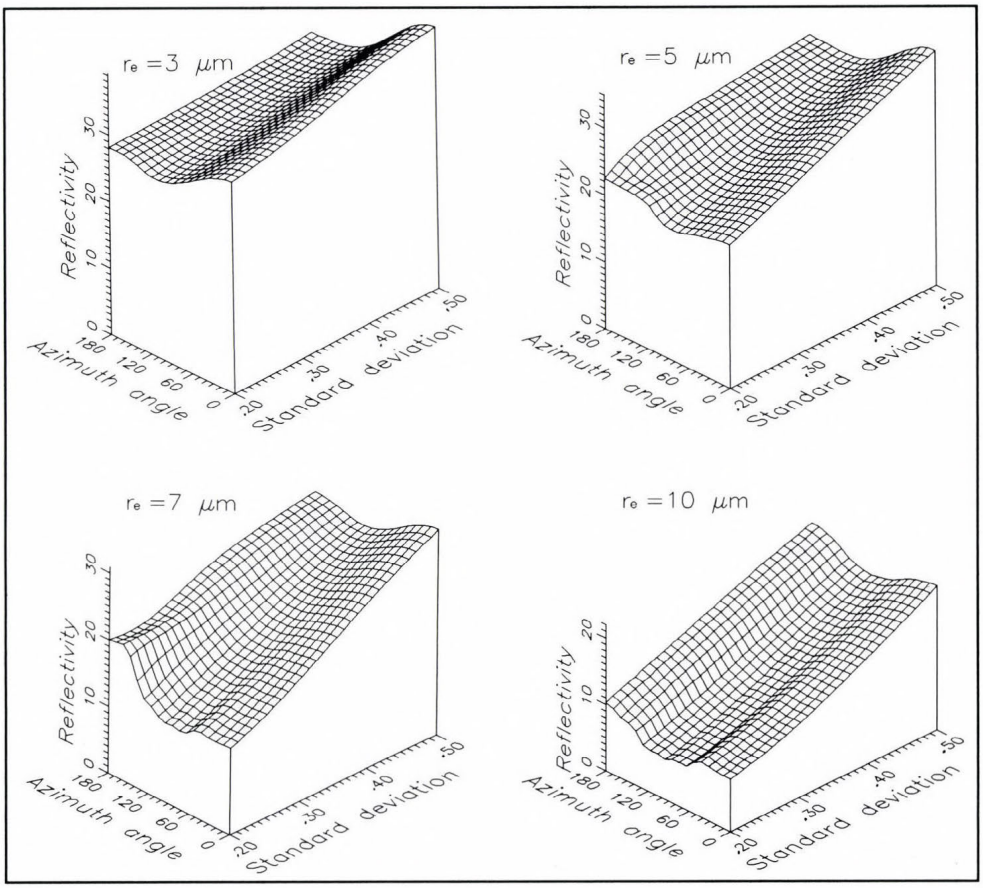

Fig. 1. 3.7 μm reflectivity patterns for lognormal droplet size distributions with $\sigma = 0.35$ and four effective radius values at $\Theta_0 = 60°$ and $\Theta = 30°$.

tivity of the reflectivity to the width of the droplet size spectrum depends on the effective radius itself. From the four cases shown it is highest for $r_e = 7$ μm. The reason of this phenomenon lies in the asymptotic theory developed by *King* (1987). According to this, at the water absorption bands in the near-infrared the reflectivity strongly depends on the single scattering albedo with a weaker dependence on the asymmetry factor. *Fig. 3* illustrates these parameters for three distributions and effective radii from 0.2 μm to 25 μm. There is a high variation of ϖ around 7 μm. This effect seems to be able to counteract the fact that the variability of g has a minimum at approximately the same wavelength. The dependence of the reflectivity on the spectrum width significantly weakens below $r_e = 4$ μm due to the decrease of the variability of ϖ. This results in a further decrease in the potential absolute retrieval error towards the smaller droplets.

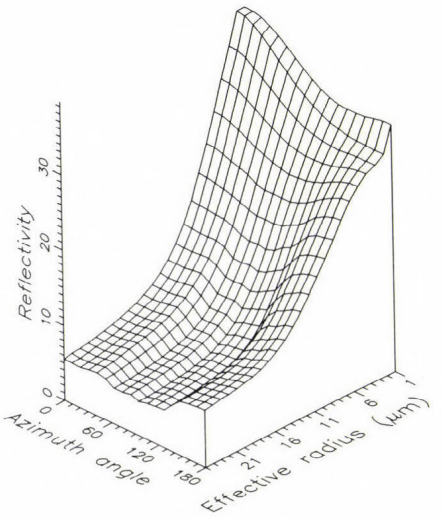

Fig. 2. Reflection function at 3.7 μm for σ = 0.35, Θ_0 = 60° and Θ = 30°, in dependence of the effective radius.

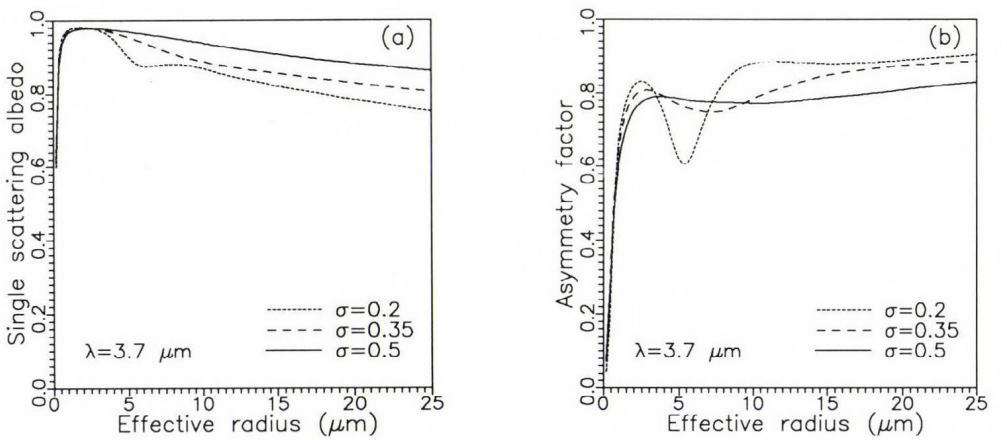

Fig. 3. Single scattering albedo (*a*) and asymmetry factor (*b*) at 3.7 μm as functions of the effective radius for three standard deviations of the lognormal droplet size spectra.

4. The effect of the horizontal cloud inhomogeneity on the remotely sensed reflectivity

Cahalan and *Snider* (1989) revealed that the liquid water path (or optical thickness) of marine stratocumulus clouds has a mesoscale fractal structure that can be characterized either by a lognormal probability density function or by a cascade model. They also showed that this inhomogeneity causes a decrease in the cloud albedo. *Nakajima et al.* (1991) observed a similar within-cloud inhomogeneity in microphysical properties over an area of several hundred square kilometres with no strong correlation between the effective radius and

the optical depth. Since this area is comparable to the HIRS FOV size, it is essential to investigate the effect of such spatial structure on the cloud reflectivity. In the present work the following assumptions were made about the cloud fractal structure and the radiative transfer processes:

— The probability density function of the effective radius is lognormal for an area comparable to the HIRS FOV size.
— The cloud optical thickness is high enough to assume opacity for all vertical cloud columns in the above area.
— There is no net photon transport between the adjacent cloud columns.

Thus, the reflectivity of the HIRS FOV can be obtained by the simple integration of the reflectivities of the separate cloud columns over the effective radius spectrum.

Fig. 4a shows the reflectivity pattern for $\Theta_0 = 60°$ for a FOV in which the horizontal distribution of the effective radius follows a lognormal spectrum with mode radius (r_{e0}) and standard deviation (σ_{e0}) of 10 μm and 0.10, respectively (these values are characteristic to the FIRE clouds). The standard deviation of the droplet spectra in the individual cloud columns was kept at 0.35.

The effective radius of this droplet population is 7.54 μm. If we now compute the reflectivity pattern for a horizontally homogeneous size distribution having $r_e = 7.54$ μm and $\sigma = 0.35$, we can estimate the retrieval error due to the neglect of the fractal structure of the cloud. These reflectivity values shown in *Fig. 4b* are systematically 6–12% higher than in the previous case. Thus, a cloud having the same effective radius but the above fractal structure produces

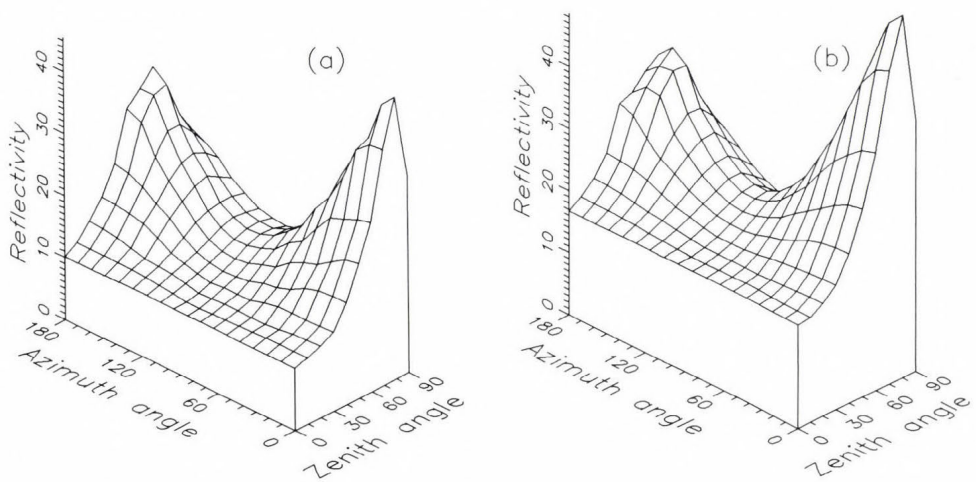

Fig. 4. (*a*) 3.7 μm reflectivity pattern at $\Theta_0 = 60°$ for a horizontally inhomogeneous cloud with $r_{e0} = 10$ μm and $\sigma_{e0} = 0.10$. (*b*) 3.7 μm reflectivity pattern for a homogeneous cloud with r_e=7.54 μm and $\sigma = 0.35$.

a reflectivity value that is lower than the one assigned to that particular effective radius and viewing geometry in the retrieval look-up table. This effect leads to the overestimation of the effective radius. The phenomenon is the consequence of the non-linearity of the reflection function and the asymmetry of the probability density function of the effective radius. Since the slope of the reflection function $\Delta R(\%)/\Delta r_e(\mu m) \approx -2$ in this region, the absolute error in the effective radius retrieval may reach 3–6 μm.

It is also important to see what the cloud reflectivity is if the same population of droplets, instead of having the fractal structure described above, is evenly distributed in the FOV. This may give us an idea of the behaviour of the reflectivity (and albedo) bias caused by the assumption of mesoscale horizontal homogeneity in, for example, general circulation models.

Now we had no assumption about the analytical form of the droplet spectrum; the mean Mie scattering parameters were determined from the normalized relative frequency corresponding to 0.1 μm wide bins of droplet radius. The calculations revealed again a systematic darkening in the case of the fractal cloud. *Fig. 5* shows the relative bias $100*(R_{hom} - R_{fr})/R_{fr}$. As it can be seen, the bias increases towards the higher satellite zenith angles.

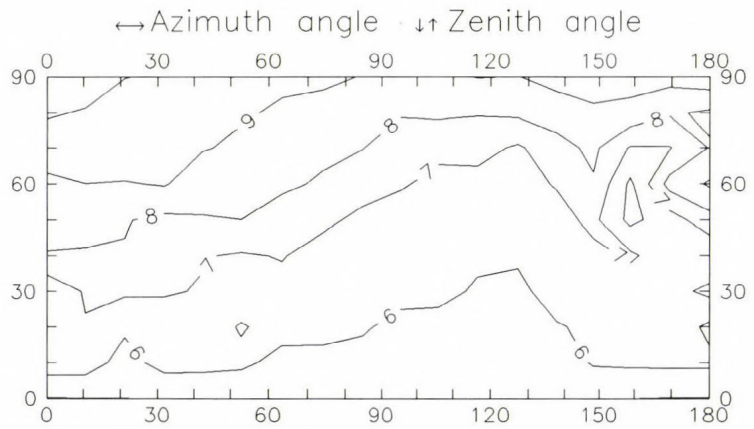

Fig. 5. Relative bias (%) between the 3.7 μm reflectivities of the horizontally inhomogeneous cloud (Fig. 4a) and a cloud containing the same droplet population evenly distributed.

To further clarify this point, we carried out a similar series of calculations for $r_e = 10$ μm and $\sigma = 0.20$. Such a widening of the spectrum may be a result of more intensive within-cloud dynamic processes or of the increase of the FOV size. The comparison of the reflectivity patterns (not shown) for the fractal cloud and the one corresponding to the effective radius of this droplet population (8.13 μm) at $\sigma = 0.35$ indicates a slightly bigger absolute bias

(7–15%) in this case, which results in the further increase of the potential absolute retrieval error.

More striking is, however, the increase in the relative bias between the reflectivities of the fractal and the corresponding homogeneous clouds; its characteristic value is about 25% (*Fig. 6*).

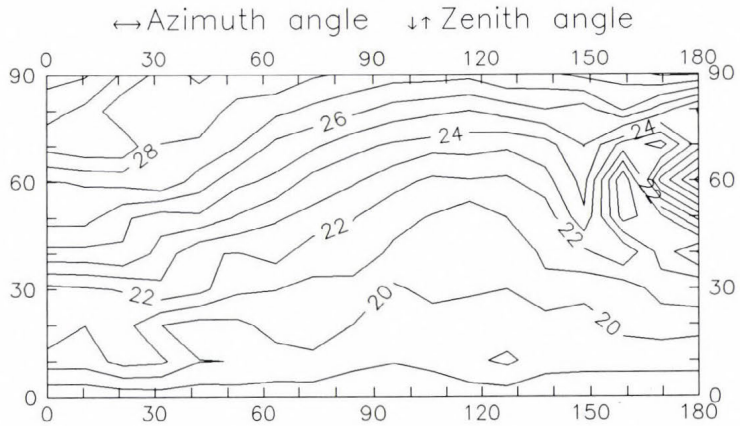

Fig. 6. Relative bias (%) between the 3.7 μm reflectivities of the horizontally inhomogeneous cloud with $r_{e0} = 10$ μm and $\sigma_{e0} = 0.20$ and a cloud containing the same droplet population evenly distributed.

It is also obvious that the magnitude of the reflectivity bias varies with the viewing geometry and r_{e0}. For clouds having larger droplets and hence characterized by a lower variability of the reflectivity the darkening is expected to be smaller. However, in this study these effects have not been investigated in details.

5. Conclusion and plans for the future

The effect of the droplet size distribution was investigated on the reflectivity of geometrically plane-parallel, low-level stratiform clouds. The principal aim of this study was to determine whether the near-infrared reflectivity measurements of the HIRS radiometer can be used for the accurate determination of the microphysical properties of such clouds. The main results can be summarized as follows:

— The cloud reflectivity is sensitive to the width of the droplet size spectrum. This sensitivity depends upon the effective radius, and is determined by the variability of the mean Mie scattering parameters of the droplet population. However, the potential absolute retrieval error caused by this effect is relatively small. This indicates an

acceptable retrieval accuracy whenever the horizontal variability of the effective radius is low on a scale comparable to the radiometer pixel size.

— The within-cloud horizontal inhomogeneity of the microphysical properties causes a darkening in the cloud reflectivity, and probably in the albedo too. This effect has two consequences. First, the use of look-up tables built up by assuming horizontal homogeneity causes a systematic overestimation of the effective radius of the droplet population by the low-resolution HIRS reflectivity measurements. Second, the parametrizations of the mesoscale near-infrared cloud albedo in climate models must also account for the within-cloud fractal structure even if the given gridbox is entirely overcast.

Of course, these results are based only on several simple examples. To achieve a better understanding of the phenomena it may be necessary to revise some of the simplifying assumptions made. For example, the choice of other statistical distributions or the consideration of the geometric inhomogeneity and non-zero cloud transmissivity may lead to a slight modification of the results, probably without changing, however, their main characteristics. Also, more detailed calculations would be needed for the whole range of sun-satellite geometry. The extension of our computational capabilities will hopefully enable us to perform this work.

Acknowledgements—We wish to express our gratitude to the *authors* of *MIEV0* and *DISORT* for making the programs available. The valuable discussions regarding the Mie scattering calculations with *Dr. M. Putsay* are also appreciated. *I. Ihász* and *G. Duska* were of great help in solving many computational problems.

References

Arking, B.A. and *Childs, J.D.*, 1985: Retrieval of cloud cover parameters from multispectral satellite images. *J. Climate Appl. Meteor. 24*, 322-333.

Cahalan, R.F. and *Snider, J.B.*, 1989: Marine stratocumulus fractal structure. *Remote Sens. Environ. 28*, 95-107.

Gu, J., Pincus, R., Austin, P. and *Szczodrak, M.*, 1992: Cloud optical depth estimates from satellite measurements. *Proceedings of the 11th International Conference of Clouds and Precipitation*, Montreal, Canada, 1992, 839-842.

King, M.D., 1987: Determination of the scaled optical thickness of clouds from reflected solar radiation measurements. *J. Atmos. Sci. 44*, 1734-1751.

Liou, K.N., 1980: *An Introduction to Atmospheric Radiation*. Academic Press, New York, London, Toronto, Sydney and San Francisco, 176-182.

Nakajima, T. and *King, M.D.*, 1990: Determination of the optical thickness and effective particle radius of clouds from selected solar radiation measurements. Part I: Theory. *J. Atmos. Sci. 47*, 1878-1893.

Nakajima, T., King, M.D., Spinhirne, J.D. and *Radke, L.F.*, 1991: Determination of the optical thickness and effective particle radius of clouds from selected solar radiation measurements. Part II: Marine stratocumulus observations. *J. Atmos. Sci. 48*, 728-750.

Paltridge, G.W. and *Platt, C.M.R.*, 1976: *Radiative Processes in Meteorology and Climatology*. Elsevier-Scientific Pub. Co., Amsterdam.

Rossow, W.B. and *Schiffer, R.A.*, 1991: ISCCP data products. *Bull. Amer. Meteorol. Soc. 72*, 2-20.

Slingo, A., 1990: Sensitivity of the Earth's radiation budget to changes in low clouds. *Nature 343*, 49-51.

Stamnes, K., Tsay, S.C., Wiscombe, W. and *Jayawera, K.*, 1988: A numerically stable algorithm for discrete-ordinate-method-radiative transfer in multiple scattering and emitting layered media. *Appl. Opt. 27*, 2502-2512.

Watts, P.D., 1993: Cloud microphysical Parameters from TOVS: a practical scheme and geometrical considerations. *Technical Proceedings of the Seventh International TOVS Study Conference*, 10-16 February, Igls, Austria, 543-554.

Wiscombe, W.J., 1979: Mie scattering calculations: advances in technique and fast, vector-speed computer codes. *NCAR Technical Note TN-140+STR*, National Center for Atmospheric Research, Boulder, Colorado.

IDŐJÁRÁS

Quarterly Journal of the Hungarian Meteorological Service
Vol. 98, No. 2, April–June 1994

Assessment of the impacts of climate change on the yields of winter wheat and maize, using crop models

Zs. Bacsi[1] and **M. Hunkár**[2]

[1]*Pannon University of Agricultural Sciences, Georgikon Faculty of Agronomy*
P.O. Box 71, H–8361 Keszthely, Hungary
[2]*Hungarian Meteorological Service, Agrometeorology Research Station*
P.O. Box 80, H–8361 Keszthely, Hungary

(Manuscript received 7 February 1994; in final form 20 May 1994)

Abstract—The climate change induced by the increase in atmospheric CO_2 due to human activities may lead to significant consequences for the human society and economy. Nowadays neither the extent of this climate change nor its effects on agriculture can be predicted with certainty. Many research papers have dealt with the analysis of these impacts on different crops in different regions of the Earth. The present paper aims at assessing the impacts of three well known climate change scenarios—the carbon-dioxide doubling scenarios from the GISS, GFDL and UKMO general circulation models—on wheat and maize yields in Hungary. For this purpose the outputs of the above three GCMs are used to create weather time series for Hungary. These are used together with the CERES-Wheat and the CERES-Maize crop growth simulation models, which simulate the growth and development processes of these crops using daily values of temperature, radiation and precipitation. These crop models facilitate the testing of the results of adaptation strategies such as adjusted sowing date, changed irrigation or fertilization patterns, or choice of a variety capable of better utilizing the environmental conditions of a new climate situation. The present paper uses field observations and weather data from Keszthely (Western Hungary). Simulation results indicate decreases both in winter wheat and maize yields with maturity occurring significantly earlier during the year.

Key-words: climate change impacts, simulation, crop models, wheat, maize, Hungary.

1. Introduction

Many climate scientists agree that the increase in atmospheric carbon-dioxide resulting from human activities will probably lead to changes in the Earth's climate. However, it is not possible at present to accurately forecast either the size or the temporal dynamics of this change. There are several

methods available which help us to estimate, under certain assumptions, the main features of this carbon-dioxide induced change. One of these methods is modelling the Earth's climate using General Circulation Models (GCMs) at various levels of atmospheric carbon-dioxide concentrations. Several such GCMs are known among the climate scientists, and these differ both in the climatic input variables considered and in the output variables produced. Until recently only results from so called 'equilibrium models' were published, that is, model outputs describing the Earth's climate after it has reached an equilibrium state at a given, higher level of atmospheric carbon-dioxide. (GCM results on the dynamics of the increase in the concentration of atmospheric carbon-dioxide—as well as other so-called 'greenhouse gases'—and on the temporal dynamics of the resulting climate change were not published until 1993. The climate research laboratory of the U.K. Meteorological Office at Bracknell has recently completed such a 'transient' model run, but the results of this were not available to the authors at the time of writing this paper.)

For the purposes of this study outputs from three general circulation models were used. Then the climate change scenarios predicted for Western Hungary were linked to wheat and maize simulation models, and the impacts on the development and yield of the two crops were estimated. The results describing the growth and development of the two crops were then compared to the corresponding values from the past 16 years at Keszthely, the location of the study, to analyse the size and direction of the changes.

2. Material and method

For the purposes of the present study daily maximum and minimum temperature values, daily global radiation and daily precipitation amounts were used for the years 1975 to 1990 measured at the Agrometeorology Station at Keszthely (county Zala, Western Hungary). Outputs from three General Circulation Models were used to create climate change weather scenarios. These are:

- GISS (Goddard Institute for Space Studies, New York, U.S.A.; *Hansen et al.*, 1988),
- GFDL (Geophysical and Fluid Dynamics Laboratory, Princeton, U.S.A.; *Wetherald* and *Manabe*, 1986),
- UKMO (United Kingdom Meteorological Office, Bracknell, U.K.; *Wilson* and *Mitchell*, 1987).

The crop growth and development rates were simulated using the CERES-Wheat (*Godwin et al.*, 1989) and the CERES-Maize (*Jones* and *Kiniry*, 1986) crop models.

3. The CERES simulation models

The growth and development of the winter wheat and maize crop were assessed using the Wheat and the Maize models of the CERES model group, developed in the United States. The two crop models are very similar regarding their structure, operation, input data requirements and modelled processes. They are capable of simulating the impacts of the following environmental factors:

- weather variables: daily maximum and minimum temperature values, global radiation and precipitation amount for each day from sowing till harvest;
- soil variables: parameters describing the physical and chemical composition and water holding capacity of each soil layer, and the initial soil water and nutrient content just before sowing;
- plant parameters: 5 parameters are used for maize and 6 parameters for wheat to describe the genetic characteristics of the actual crop variety used, some of these referring to the speed of phenological development, others to the speed of dry matter accumulation;
- agrotechnology data: sowing date, sowing depth, sowing density, date and amount of irrigation and fertilization, if any.

Based on the above input information the CERES crop models simulate the time of the crop's reaching each development stage, the amount of above ground biomass and its distribution among the various crop parts, the growth of the leaf area, the crop grain yield, the water and nitrogen balance of the soil, and the nitrogen content of the various crop parts.

Before starting the climate change experiments it was necessary to assess the performance of the Ceres-Wheat and Ceres-Maize models under the environmental conditions typical to the vicinity of Keszthely, and with crop varieties used in Hungary. For these so-called validation runs, relying on the experiments by *Hunkár* (1994) 3 years were chosen for maize from which field observations were available for a variety popular in Hungary. For winter wheat the field observations from 4 years by the Crop Production Institute of the Pannon University of Agricultural Sciences Keszthely were used. The field observations for both crops were compared to model outputs for Rammann-brown forest soil, the typical soil type around Keszthely, for the maize variety Pioneer 3901 and for the winter wheat variety Martonvásár-4. The results of the validation experiments are shown in *Table 1*.

As the above results show the model works with adequate accuracy, so it is suitable to be used in climate impact assessment studies. It has to be mentioned, that due to the inherent limitations of the simulation models available, the assessment of the climate change impacts has to be limited to the impacts caused by the changed weather characteristics resulting from the

increased carbon-dioxide concentrations, and the direct impacts of this increased carbon-dioxide level on the crop physiological processes (changed photosynthesis, transpiration and respiration) were not considered.

Table 1. Validation results for CERES-Maize and CERES-Wheat with field observations from Keszthely

CERES-Maize: Variety: Pioneer 3901

Difference between simulated and observed values

Year	Silking (day)	Maturity (day)	Grain yield (t/ha)	Biomass (t/ha)
1989	-4	-4	4.3	0.6
1990	-3	-5	0.006	-3.8
1991	-4	-4	-1.5	-1.8

CERES-Wheat: Variety: Martonvásár-4

Difference between simulated and observed values

Year	Anthesis (day)	Maturity (day)	Grain yield (t/ha)	Biomass (t/ha)
1984/85	+11	-3	0.4	-0.5
1985/86	+7	-11	0.6	1.1
1988/89	+1	-8	0.8	-0.4
1989/90	-2	-8	0.2	0.4

4. The creation of the climate change scenarios

All the three applied GCMs have their limitations regarding spatial resolution. The GISS handles the Earth's surface as gridboxes of the size 10° latitude × 7.9°longitude. The climate of each gridbox is considered to be homogeneous, and the climate characteristic are allocated to the gridbox centre. The GFDL works similarly with gridboxes of 4.5°latitude × 7.5°longitude, and the UKMO with gridboxes of 5°latitude × 7.5°longitude. In the present study the gridbox covering the location of Keszthely was used with each GCM, thus for GISS the gridbox with the centre 50°N;20°E, for GFDL the gridbox with the centre 46.7°N;15°E, for UKMO the gridbox with the centre 47.5°N;18.8°E (see *Fig. 1*).

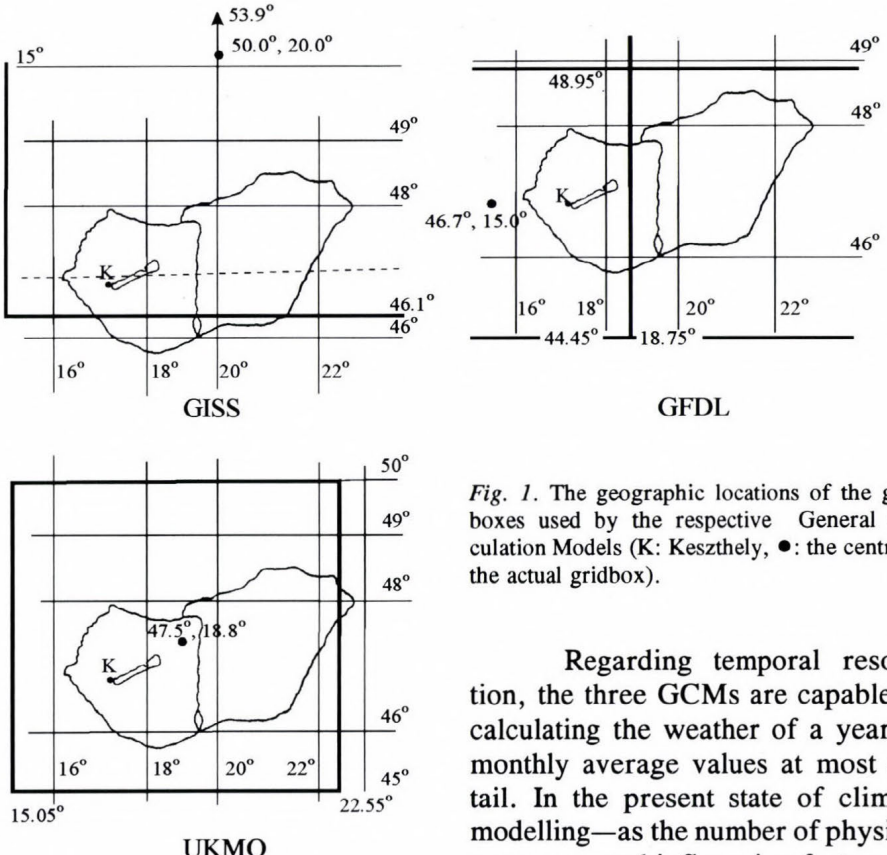

Fig. 1. The geographic locations of the gridboxes used by the respective General Circulation Models (K: Keszthely, •: the centre of the actual gridbox).

Regarding temporal resolution, the three GCMs are capable of calculating the weather of a year as monthly average values at most detail. In the present state of climate modelling—as the number of physical processes, and influencing factors included in the climate models are limited—the predictions coming from climate models are considerably inaccurate, e.g. the results from model experiments aiming at simulating the present climate of the Earth differ considerably from reality. So the climate characteristics simulated under changed greenhouse gas concentrations are also rather unreliable. Nevertheless, the predicted rate of changes can be accepted. For this reason in creating the climate change scenarios for the location of Keszthely a change factor between the modelled present and 'future' climates was generated for the various weather parameters, and then these change factors were used to modify the 'baseline' weather of the period 1975–1990. *Figs. 2* and *3* show the monthly average temperature values and precipitation amounts for the baseline weather in comparison with the same average values for the climatic standard period of 1951–1980. In the computation process of the change factors the 'present' climate means the modelled climate under the CO_2 concentration of the first half of the 1980s (300 ppm for GFDL and UKMO, 315 ppm for GISS), and the 'future' climate the modelled climate under doubled CO_2 concentration. The change factor was calculated as the difference between the

'future' and 'present' values for temperature, and as the ratio of these for radiation and precipitation, in agreement with the recommended methodology of many similar impact assessment studies (*Smith* and *Tirpak*, 1989; *Parry et al.*, 1988; *Adams et al.*, 1990).

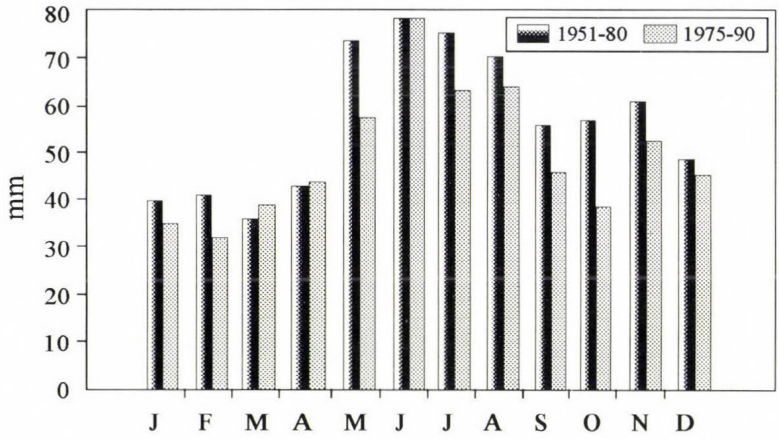

Fig. 2. Average monthly precipitation.

As the crop growth simulation models require daily weather data from sowing till harvest and the climate model outputs present the results only in

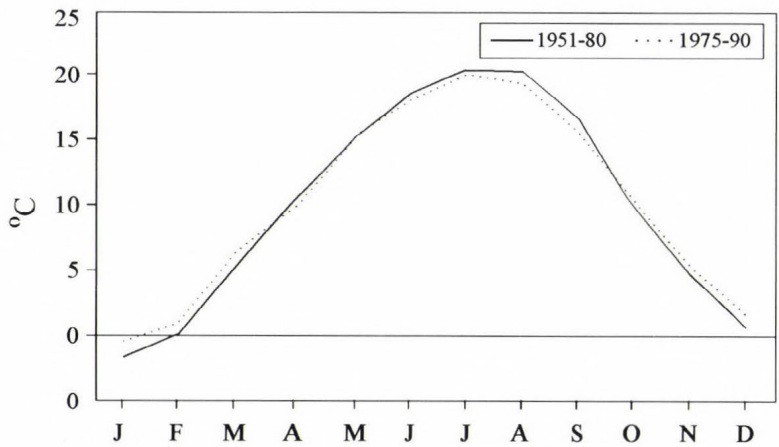

Fig. 3. Average monthly temperature.

monthly resolutions, the baseline daily weather data were modified by the change factor of the corresponding month, to create climate change scenarios with daily resolutions.

The change factors were calculated for each month of the year and for each GCM as follows:

$$\begin{aligned} \Delta T_j &= T_j\,(2 \times CO_2) - T_j\,(1 \times CO_2) && \text{for temperature,} \\ \Delta P_j &= P_j\,(2 \times CO_2) \,/\, P_j\,(1 \times CO_2) && \text{for precipitation,} \\ \Delta R_j &= R_j\,(2 \times CO_2) \,/\, R_j\,(1 \times CO_2) && \text{for radiation,} \end{aligned}$$

where $T_j\,(2 \times CO_2)$, $P_j\,(2 \times CO_2)$, $R_j\,(2 \times CO_2)$ are the average temperature, precipitation and radiation values respectively, calculated by the actual GCM for the month j in question for the modelled climate under doubled carbon-dioxide concentrations, and $T_j\,(1 \times CO_2)$, $P_j\,(1 \times CO_2)$, $R_j\,(1 \times CO_2)$ are the same for the modelled climate under normal carbon-dioxide concentrations, giving 12 sets ($j = 1 \ldots 12$, from January to December) of ΔT_j, ΔP_j and ΔR_j values for each GCM used.

The next step was to generate daily time series using the above change factors and the data of the baseline weather years of 1975–1990. So for all the three GCMs altogether 16 changed weather years were generated with daily maximum and minimum temperature, radiation and precipitation data as follows:

$$\begin{aligned} maxT_i\ (2 \times CO_2) &= maxT_i\ (1 \times CO_2) + \Delta T_j, \\ minT_i\ (2 \times CO_2) &= minT_i\ (1 \times CO_2) + \Delta T_j, \\ P_i\ (2 \times CO_2) &= P_i\,(1 \times CO_2) \times \Delta P_j, \\ R_i\ (2 \times CO_2) &= R_i\,(1 \times CO_2) \times \Delta R_j, \end{aligned}$$

where $maxT_i$, $minT_i$, P_i and R_i are the maximum and minimum temperature values, precipitation and radiation amounts respectively, for the actual day of the year in question, under the present and the doubled CO_2 concentrations. *Figs. 4, 5, 6* and *7* show the monthly average values of the weather variables for the baseline climate and for the doubled CO_2 scenarios from each GCM.

As described above, climate change scenarios were created using the three GCM outputs and the 16 baseline weather years from Keszthely. For the wheat simulation model altogether 15 baseline weather scenarios (from the 1975/76 growing period to the 1989/90 growing period), 15 GISS scenarios, 15 GFDL scenarios and 15 UKMO scenarios, and for the maize simulation model 16 baseline, 16 GISS, 16 GFDL and 16 UKMO scenarios were generated for the purpose of the climate impact assessments.

In order to compare the impact of the changed weather on the crops the agrotechnology was assumed constant for all simulation experiments. In the simulation runs the following agrotechnology parameters were used: sowing on 10 October with Martonvásár-4 winter wheat variety for the wheat model, and sowing on 10 April with Pioneer 3901 variety for the maize model. For both crops optimal nitrogen supply was assumed, and no irrigation was applied.

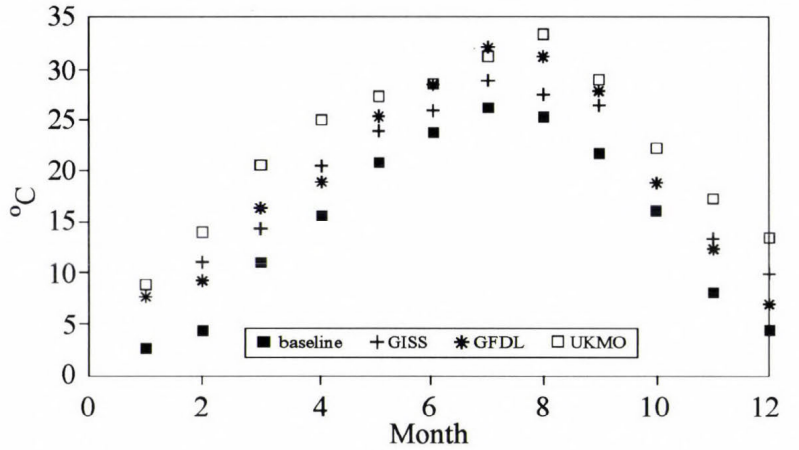

Fig. 4. Monthly averages of daily maximum temperature for 16 years.

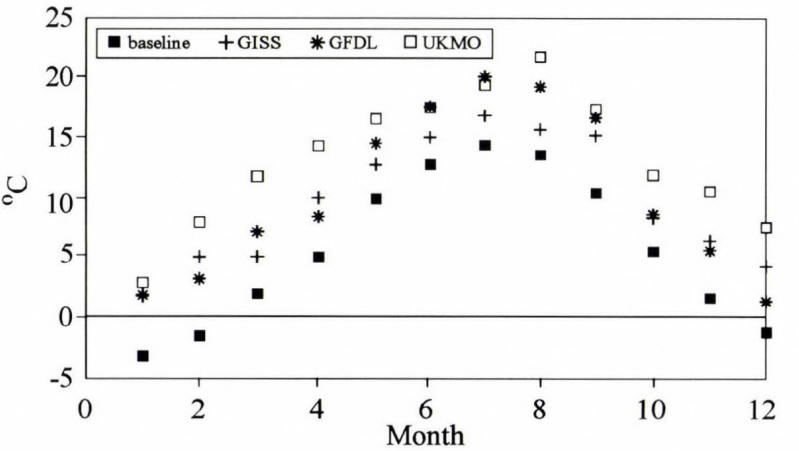

Fig. 5. Monthly averages of daily minimum temperature for 16 years.

5. Results

The outputs from the CERES crop models were used for the impact assessments, that is, for both wheat and maize the simulated values of resultant variables under the baseline weather were compared to the simulated values of the same variables under the climate change weather scenarios generated from the three GCMs.

5.1 Maize

In the maize experiments altogether 16 baseline weather years were available together with 16 GISS-years, 16 GFDL-years and 16 UKMO-years. So

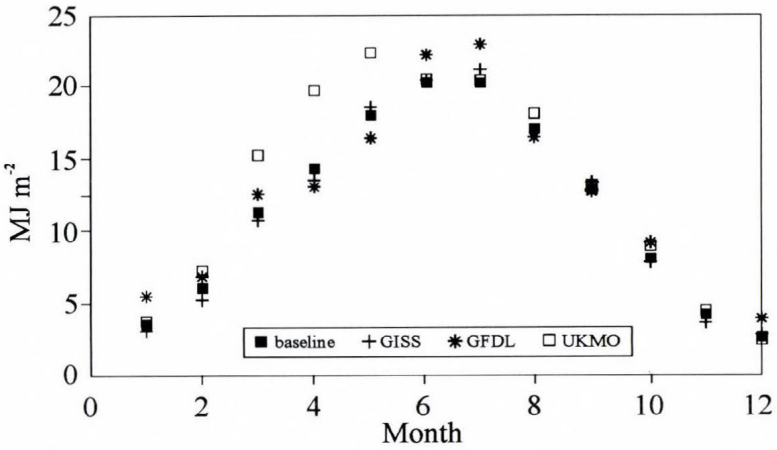

Fig. 6. Monthly averages of daily radiation for 16 years.

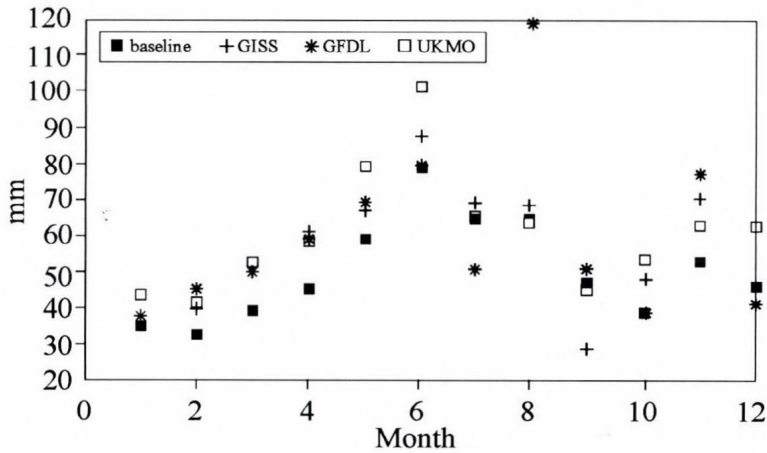

Fig. 7. Average monthly precipitation values for 16 years.

altogether 64 simulation experiments were carried out besides the validation runs described earlier.

The following resultant variables were considered in the assessment:

- the grain yield (t/ha),
- the amount of above ground biomass (t/ha),
- maximum leaf area index (LAI max),
- silking date,
- maturity date.

The climate change scenarios resulted in silking and maturity occurring much earlier, and thus the growing season became significantly shorter for all

the three different GCMs. The maize crop showed the fastest development under the 16 UKMO weather years, with maturity occurring 41 days earlier on average than under the baseline weather years. The GFDL scenario resulted in the crop's maturity occurring 35 days earlier on the average, while under GISS maturity occurred 20 days earlier.

Biomass and grain yield show somewhat less unanimous results. The GISS scenario resulted in a small, 8% yield increase on the average, while the GFDL resulted in a 7%, and the UKMO in a 14% average yield decrease. For all the three GCM scenarios the standard deviations of the yield are somewhat smaller than in the case of the baseline weather, so the yields though smaller, seem to become more stable under the changed weather, especially in the case of the GISS and the GFDL scenario. Biomass results showed similar characteristics to the yield. The average values of the maximum leaf area index increased a little for all the three GCM scenarios, while the standard deviations decreased. These results are shown in *Figs. 8* and *9*.

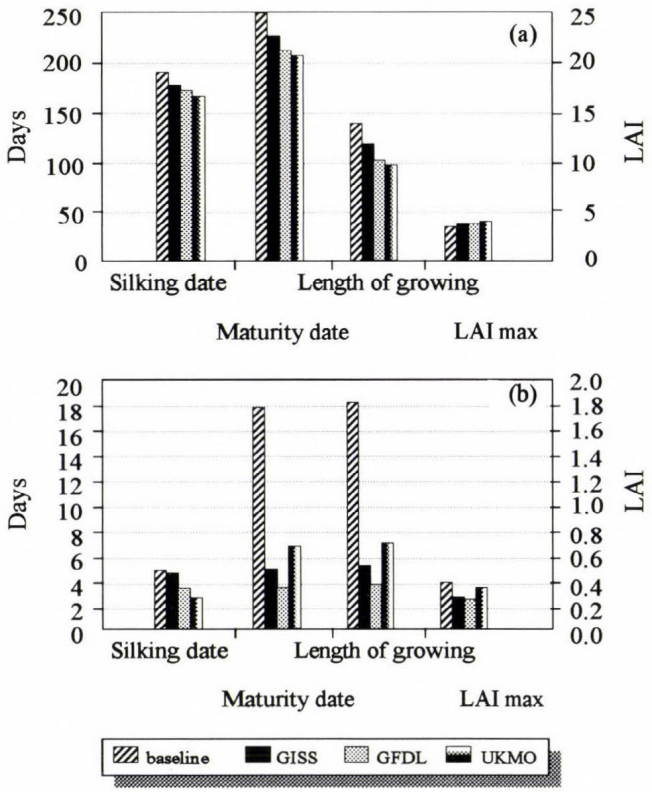

Fig. 8. Averages (*a*) and standard deviations (*b*) for the modelled development variables of maize for the various climate scenarios.

The above results may seem surprising, as maize, being a crop of tropical origin, was expected to utilize the increased temperature better, and produce higher yields under the changed weather, but the shortened growing season and the changed distribution of precipitation under this shorter growing season counteracted the results of the advantageous temperature patterns.

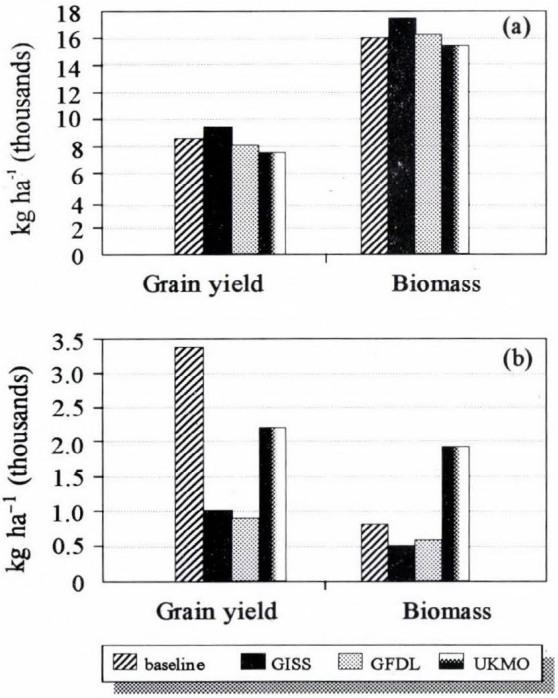

Fig. 9. Averages (*a*) and standard deviations (*b*) for the modelled production variables of maize for the various climate scenarios.

5.2 Wheat

In the wheat experiments altogether 15 baseline weather years were available together with 15 GISS-years, 15 GFDL-years and 15 UKMO-years. So altogether 60 simulation experiments were carried out above the validation runs described earlier.

The following result variables were considered in the assessment:

- the grain yield (t/ha),
- the amount of above ground biomass (t/ha),
- maximum leaf area index (LAI max),
- anthesis date,
- maturity date.

Results showed that similar to maize, the anthesis and maturity dates occurred earlier and the growing season became significantly shorter for all of the climate change scenarios. The fastest crop development occurred in the case of the UKMO scenario, with an average of 42 days shorter period from sowing to maturity in comparison to the baseline, while under the GFDL scenario maturity occurred 25 days earlier on the average, and under the GISS scenario 22 days earlier in average than under the baseline weather.

The average biomass production slightly increased for all the three climate change scenarios, and the standard deviation decreased. In the case of grain yield the GISS scenario resulted in a yield only 87%, the GFDL in a yield 72%, and the UKMO scenario in a yield 75% of the baseline average. It is true again that standard deviations of grain yield decreased for all the climate change scenarios, but it can be explained by the decrease in yield, and does not necessarily suggest more stable yields. It is also true for winter wheat that the 15 year average value for maximum leaf area index slightly increased while the standard deviation was somewhat reduced (see *Figs. 10* and *11*).

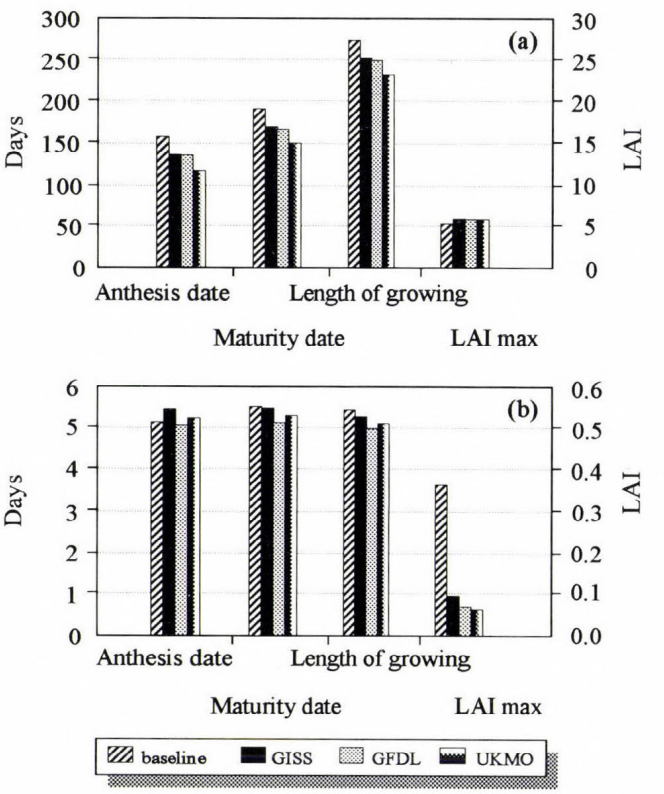

Fig. 10. Averages (*a*) and standard deviations (*b*) for the modelled development variables of wheat for the various climate scenarios.

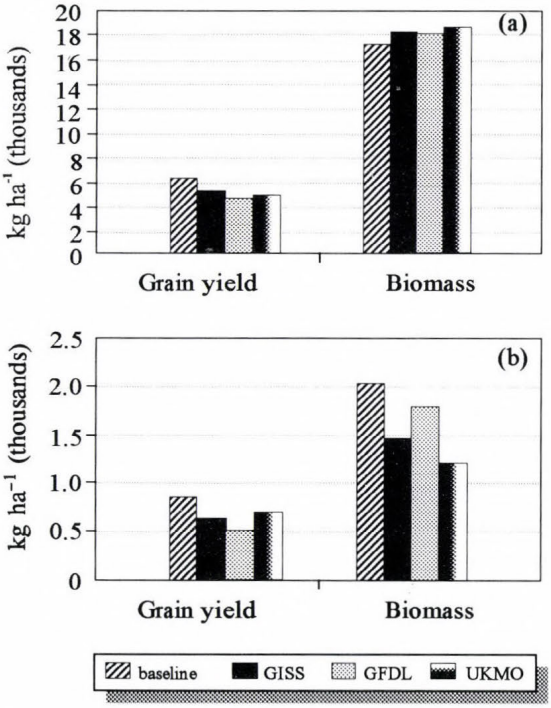

Fig. 11. Averages (*a*) and standard (*b*) deviations for the modelled development variables of wheat for the various climate scenarios.

5.3 Adjustment in agrotechnology to diminish unfavourable consequences

The present study also tried to assess whether modifications in agrotechnology could diminish the disadvantageous consequences of the climate change, or even turn them to advantageous results. These investigations were limited to the maize crop and for adjustments in sowing date and choice of variety.

In the original experiments the sowing date of 20 April and the variety Pioneer 3901 were used. In the sowing date adjustment experiments the impacts of 10 days earlier and 10 days later sowing were assessed.

Surprisingly, the three climate change scenarios produced different results. In the case of the GISS scenario neither the earlier nor the later sowing increased either grain yield or biomass production of the maize crop. For the GFDL scenario the later sowing at 30 April resulted in a slight increase in grain yield, which, however, was still lower than the baseline yield under the original sowing date. For the UKMO scenario the earliest sowing, that is, 10 April resulted in the best yield, but it is also lower, than the original baseline yield of 20 April (see *Table 2*).

In the variety choice experiments Pioneer 3382, a variety of longer growing

Table 2. The effect of sowing date on maize production under various weather scenarios

Variety: Pioneer 3901	Weather scenario			
Sowing date: 10 April	Baseline	GISS	GFDL	UKMO
Maturity date	2 Sep	6 Aug	28 Jul	20 Jul
Grain yield (kg/ha)	8261	8199	7749	7890
cv%	40.6	40.9	43.2	42.5
Biomass (kg/ha)	15726	15895	15655	16307
cv%	5.2	5.1	5.2	5.0
Sowing date: 20 April	Baseline	GISS	GFDL	UKMO
Maturity date	5 Sep	13 Aug	31 Jul	25 Jul
Grain yield (kg/ha)	8567	9285	7961	7354
cv%	39.1	36.1	42.1	45.6
Biomass (kg/ha)	15947	17285	16099	15251
cv%	5.1	4.7	5.1	5.4
Sowing date: 30 April	Baseline	GISS	GFDL	UKMO
Maturity date	13 Sep	18 Aug	5 Aug	2 Aug
Grain yield (kg/ha)	9096	8716	8254	7484
cv%	36.9	38.4	40.6	44.8
Biomass (kg/ha)	16349	16562	16694	16188
cv%	5.0	4.9	4.9	5.0

season was compared to Pioneer 3901 at the sowing date 20 April. Pioneer 3382 produced much higher grain yields and biomass results for all the three climate change scenarios than the baseline yield of Pioneer 3901, but in comparison with the yield of Pioneer 3382 under the baseline climate, only the GISS scenario led to a yield increase (see *Table 3*).

It has to be remarked, that the results of the variety choice experiments have to be handled with caution, because before having compared the performance of the two varieties the genetic parameters defining the variety characteristics should have been carefully tested, validated. The present study could not carry out this task due to lack of field observations for Pioneer 3382. Summarising the results of the present impact assessment it can be stated that adjustments in agrotechnology, such as careful choice of the sowing date and the variety sown, offer a possibility to compensate for, or at least diminish the unfavourable consequences of climate change.

Table 3. The impact of various climate scenarios on various maize varieties

Variety: Pioneer 3901	Weather scenario			
Sowing date: 20 April	Baseline	GISS	GFDL	UKMO
Maturity date	5 Sep	13 Aug	31 Jul	25 Jul
Grain yield (kg/ha)	8567	9285	7961	7354
cv%	39.1	36.1	42.1	45.6
Biomass (kg/ha)	15947	17285	16099	15251
cv%	5.1	4.7	5.1	5.4

Variety: Pioneer 3382	Weather scenario			
Sowing date: 10 April	Baseline	GISS	GFDL	UKMO
Maturity date	4 Oct	5 Sep	18 Aug	9 Aug
Grain yield (kg/ha)	14335	15703	13705	11964
cv%	23.4	21.3	24.4	28.0
Biomass (kg/ha)	21618	23873	22273	20728
cv%	3.8	3.4	3.7	3.9

6. Summary

The above assessment was aimed at assessing the impacts of a possible greenhouse gas-induced climate change on the winter wheat and maize yields in Western Hungary. As the forecasts regarding this future climate change are rather uncertain at present, three different climate change scenarios were used for the present study. There are serious inherent limitations in these climate scenarios, e.g. severe methodological problems arise in creating regional climate change scenarios from the outputs of global climate models. Another problematic issue is to construct daily weather time series from the outputs of climate models which produce results as seasonal, or at most detail, monthly averages for the changed climatic parameters. Another important research area would be to work with so-called 'transient' scenarios instead of the 'equilibrium' scenarios used here, which could describe the expected climate change as a gradual, dynamic process in time.

The application of crop growth simulation models as tools for climate change impact studies also present some difficulties. In the present assessment the location of the study was the Keszthely area, because field observations and historical weather data were available from this region. In order to use crop models for climate impact assessment studies it is necessary to test and validate

the genetic parameters describing the variety dependent characteristics of the crop varieties, and for this purpose many field observations from several locations would be necessary. A further research task could be to evaluate the impacts of nitrogen fertilization and the nitrogen balance of the crop, which may again lead to interesting conclusions under the changed water balance patterns of the changed climate.

A further issue is the choice of statistical methods to compare the present and 'future' performance of the crops in question. The present study used only a simple comparison of averages and standard deviations, though it might be more important to compare the distributions of the crop yield, and to analyse the probabilities of the occurrence of low and high yields. The techniques of risk assessment and stochastic dominance could be suitable tools for these analyses in the future.

References

Adams, R.M., Rosenzweig, C., Peart, R.M., Ritchie, J.T., McCarl, B.A., Glyer, J.D., Curry, R.B., Jones, J.W., Boote, K.J. and *Allen, L.H. Jr.*, 1990: Global climate change and US agriculture. *Nature 345*, 219-224.

Godwin, D.C., Ritchie, J.T., Singh, U. and *Hunt, L.* 1989: *A User's Guide to CERES Wheat-V2.10.* Muscle Shoals, Alabama: International Fertiliser Development Centre.

Hansen, J., Fung, I., Laces, A., Lebedeff, S., Rind, D., Ruedy, R. and *Russet, G.* 1988: Global climate changes as forecast by the GISS 3-D model. *J. Geophys. Res. 93*, 9341-9364.

Hunkár, M., 1994: Validation of crop simulation model CERES-Maize. *Időjárás 98*, 37-46.

Jones, S.A. and *Kiniry, J.R.*, 1986: *CERES-Maize: A Simulation Model of the Growth and Development of Maize.* Texas A&M University Press, College Station, Texas.

Parry, M.L., Carter, T.R. and *Konijn, N.T.* (eds.), 1988: *The Impact of Climatic Variations on Agriculture.* Vol. 1. Kluwer Academic Press.

Smith, J.B. and *Tirpak, J.A.* (eds.), 1989: *The Potential Effects of Global Climate Change on the United States.* EPA, Washington, DC.

Wetherald, R.T. and *Manabe, S.*, 1986: An investigation of cloud cover change in response to thermal forcing. *Climatic Change 8*, 5-23.

Wilson, C.A. and *Mitchell, J.F.B.*, 1987: A $2 \times CO_2$ climate sensitivity experiment with a global climate model including a simple ocean. *J. Geophys. Res. 92*, 13315-13343.

IDŐJÁRÁS

Quarterly Journal of the Hungarian Meteorological Service
Vol. 98, No. 2, April–June 1994

Cloud motion winds derived from METEOSAT infrared images

Á. T. Meszlényi

Satellite Research Laboratory, Hungarian Meteorological Service
P.O. Box 39, H–1675 Budapest, Hungary

(Manuscript received 14 February 1994; in final form 10 May 1994)

Abstract—A few attempts were made in Hungary about ten years ago for the estimation of wind fields from the displacement of clouds in successive METEOSAT infrared images. These techniques were not fully automatic and at that time the image information was converted into digital data. Now sequences of METEOSAT infrared data are available in digital form every half an hour. It enables the automatic derivation of cloud motion winds from carefully aligned successive satellite images. In this paper the first stage of this automatic method elaborated by us is described. The vectors derived from a twenty-day period are compared with radiosonde measurements and results are presented in this study.

Key-words: cloud motion winds, METEOSAT infrared images, automatic derivation.

1. Introduction

The basic principle of wind determination using geostationary satellite image data is quite simple. The starting point is always a sequence of satellite images, all covering the same area of the Earth's surface. These images are then standardized with each other very carefully, so that the coastlines and the earth horizons coincide from image to image. Then following the movement of clouds across the sequence with different techniques, the wind vectors can be derived.

These techniques include direct measurements of cloud motion from projected time lapse film loops, man machine interactive methods and automatic methods. The cloud motion winds were first determined from carefully aligned successive ATS visible pictures with a cross correlation technique by *Leese* and *Novak* (1971). The various stages of the automatic method were described in detail by *Bowen* (1979), *Rákóczi* and *Kovács* (1981), *Schmetz* and *Nuret* (1987), *Schmetz* (1991).

2. *Image data*

The geostationary METEOSAT satellites observe the Earth with an imaging radiometer in three channels:

VIS: solar spectrum between 0.4 and 1.1 μm,

IR: infrared window region between 10.5 and 12.5 μm,

WV: water vapour absorption band between 5.7 and 7.1 μm.

Images are taken at half hourly intervals and the spatial resolution is 2.5 $\times$ 2.5 km^2 in the VIS and 5 $\times$ 5 km^2 in the IR and WV channels.

METEOSAT IR images form the database for the automatic tracking of clouds with a cross-correlation. Three successive IR images are used to determine a wind vector. We used an image at the time 12 UTC and images at times h $\pm$30 min, that is an image at the time 11.30 UTC and an image at the time 12.30 UTC, in order to eschew inaccuracy proceeding from time difference, when the results are compared with radiosonde measurements. The basic square unit of processing is the segment. This is an array of 32 $\times$ 32 IR pixels called target area, which is cut out from the central image. The centre of each segment is always at a fixed geographical location.

Since the wind vectors are derived from the displacement of clouds, it is necessary that lands and seas, where pixels do not contain clouds, are left out of consideration. Empirically estimated threshold values are used for this purpose.

The wind vectors are computed for such locations, where radiosonde measurements are carried out regularly. Thus the inaccuracy proceeding from different locations of the calculated and measured vectors can be avoided, when the cloud motion winds are compared with radiosonde values.

If the wind vector is computed for a given station, the centre of segment is determined by its position. Then the φ, λ coordinates of the station are converted into x, y coordinates of satellite image, which are the coordinates of centre of segment.

3. *Wind vector determination*

The target area is cut out from the central image at time 12 UTC. The search area is an array of 3 $\times$ 3 segments cut out from the subsequent image at time 12.30 UTC. The search area is centered on the same pixel as the target area. The target area is moved stepwise over the search area. Correlation coefficients are computed for two pairs of the successive images.

If the best match is found between the target area and the central segment of the search area then there is a calm. If the match is good enough displaced from the centre, then the clouds have moved during the intervening period, and the displacement from the centre presents the wind velocity.

There are 65 × 65 possible displacements of the target area within the large search area. For each location the correlation coefficient between the target area and search area is computed. These correlation coefficients can be thought of as a correlation surface and its peak gives the best match between the two images. So the highest value of the correlation coefficients is searched. The distance and direction of the peak from the centre indicate the cloud motion wind vector.

Consequently, starting and extreme points of wind vector are known in the satellite image (x_1,y_1 ; x_2,y_2). Converting this coordinates into geographical coordinates x_1,$y_1 \rightarrow \varphi_1$,$\lambda_1$ and x_2,$y_2 \rightarrow \varphi_2$,$\lambda_2$, the speed ($v$) and direction ($\beta$) of the cloud motion wind are given by the following formulas (*Tänczer*, 1988):

$$\cos \varphi_c = \sin \varphi_1 \sin \varphi_2 + \cos \varphi_1 \cos \varphi_2 \cos (\lambda_2 - \lambda_1), \tag{1}$$

$$|v| = \frac{R\varphi_c}{t_2 - t_1}, \tag{2}$$

$$\beta = \arcsin \frac{\sin (\lambda_2 - \lambda_1) \cos \varphi_1}{\sin \varphi_c}, \tag{3}$$

where φ_c is the spherical distance between the two points, R is the Earth's radius, t_1 and t_2 are the image taking times.

4. Symmetry check

However, the cloud patterns can repeat themselves in the successive images, so there is a chance to find wrong local maximum. Therefore use of a quality check based on symmetry criteria is needed. The same process as outlined in the previous chapter is repeated, comparing the image at time h (12 UTC) with the image at time h -30 min (11.30 UTC). This symmetry check rejects all vectors for which the vector pair speeds or directions are not symmetrical within certain thresholds (*Schmetz* and *Nuret*, 1989).

5. Height assignment

The following step is to perform the height assignment of wind vector. The IR radiance is used for cloud height attribution. The brightness value of starting point of the wind vector is converted into a temperature by means of the Planck's relationship. The temperature of the cloud top can be converted into

a pressure or height if the atmospheric profile is known. The height of starting point of wind vector is computed using the TEMP data of the given station.

6. Results and conclusion

A twenty-day overcast period was selected. Each day the TEMP data and IR images at time 11.30 UTC, 12 UTC and 12.30 UTC were used for the study. Fourteen stations were selected in the vicinity of Hungary, where radiosonde measurements are performed regularly at these times. So 280 wind vectors have been produced. From these

— in 42 case there were no TEMP data at the given station;
— in 13 case there was no cloudy pixel in the segment;
— 96 vectors are removed by the symmetry check.

So in all 129 wind vectors have remained for comparing with radiosonde measurements.

It is remarkable that the use of a symmetry check has decreased the number of wind vectors from 225 to 129. Our examinations, however, prove that values removed by symmetry check are really very different from radiosonde values. If the calculations are performed to all segments of a greater area, then after the symmetry check enough wind vectors will remain to characterize the wind field.

The results obtained by comparing of the cloud motion winds and radiosonde measurements are presented in figures.

In *Fig. 1* the frequency distribution of differences between the wind speeds derived from images and measured by radiosonde can be seen. Small differences are observable in most cases, although large differences also occur (24 m/s $< \Delta v <$ 26 m/s) in some cases. The largest frequency of the distribution falls in to the interval of 2–4 m/s. So the peak is shifted to positive direction.

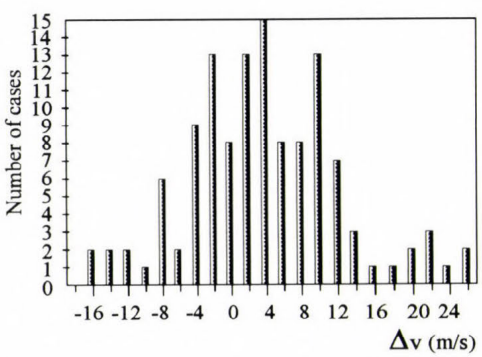

Fig. 1. Frequency distribution of differences (Δv (m/s)) between wind speeds from cloud motion and radiosonde in all cases of our examination.

Fig. 2 shows frequency distribution of differences in case of different level winds derived from low (<2000 m), medium (2000–7000 m) and high-level (>7000 m) clouds. The peak is shifted to positive direction in case of low-level clouds, however, the result cannot be considered too characteristic because of the small number of cases. The peak is situated closer to the 0 in the case

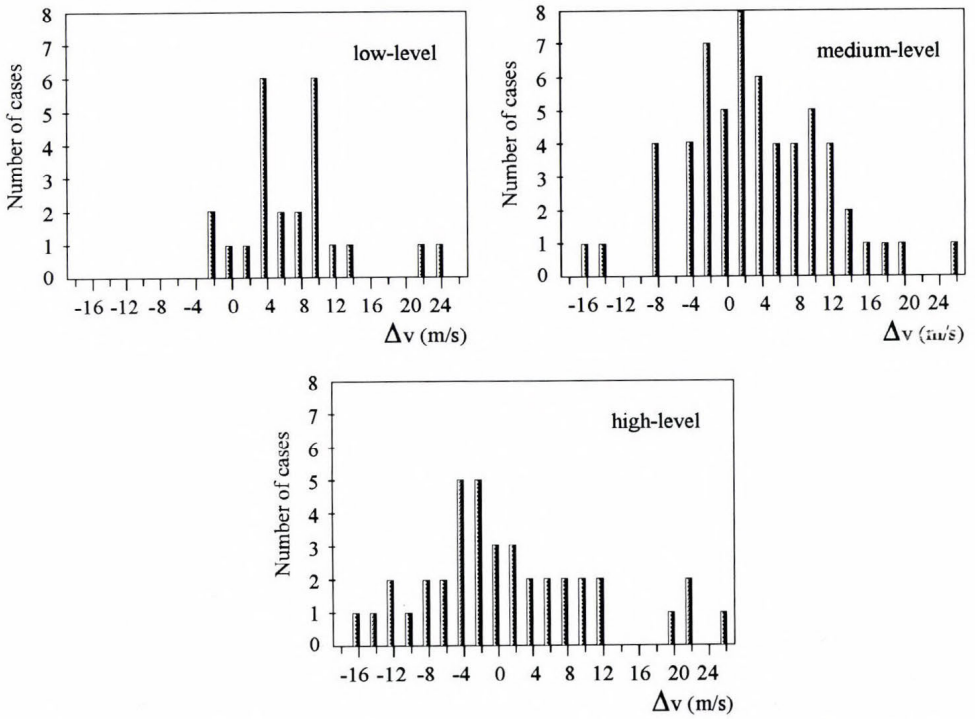

Fig. 2. Frequency distribution of differences (Δv (m/s)) between wind speeds from cloud motion and radiosonde in cases computed from low-level (< 2000 m), medium-level (2000–7000 m), high-level (> 7000 m) clouds.

of medium-level clouds comparing with Fig. 1. The smaller windspeed differences occur more frequently, but the great differences only in a few cases. It means that our calculation gives more accurate results in case of medium-level winds. There is a less significant peak of the windspeed differences in case of high-level clouds, which tends to negative direction, so the high-level winds are slightly underestimated.

The frequency distribution was examined in different windspeed categories (0–10 m/s, 10–20 m/s, 20–30 m/s) as well, which can be seen in *Fig. 3.* General shift to positive direction can be observed in case of windspeed under 10 m/s. The peak is between –4 m/s and –2 m/s in case of medium wind speed, but two secondary maximum occur at 4 m/s and 8 m/s. The shift to negative direction in case of strong winds follows from the underestimation of the high-level winds.

Frequency distribution of differences of the wind direction is represented in *Fig. 4.* Nevertheless, in *Fig. 5* the same is shown in cases of low, medium and high-level winds. The differences of wind directions are close to a normal

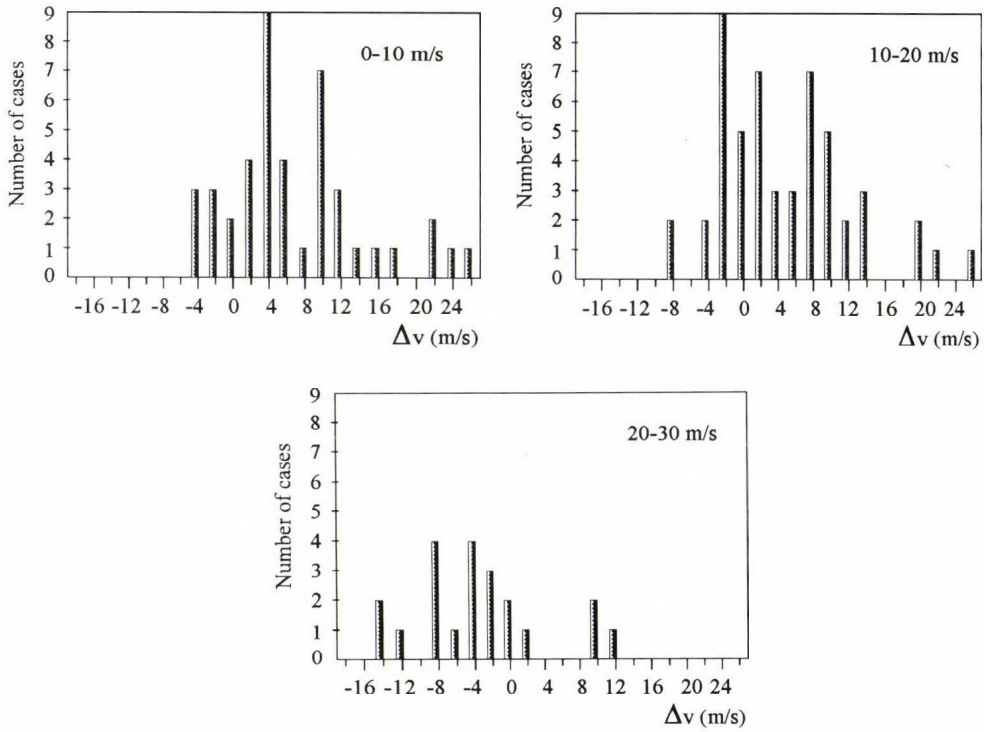

Fig. 3. Frequency distribution of differences (Δv (m/s)) between wind speeds from cloud motion and radiosonde in cases of measured wind speeds ranging 0–10 m/s, 10–20 m/s, 20–30 m/s.

distribution with a peak at 0. The separation of the three levels did not give more characteristic results.

Considering the simplicity of this method, rather good results have been achieved. Further improvement of the results can be expected by means of development of the method, for instance: application of multispectral image analysis and radiance slicing technique, refining the location of the peak on the correlation surface.

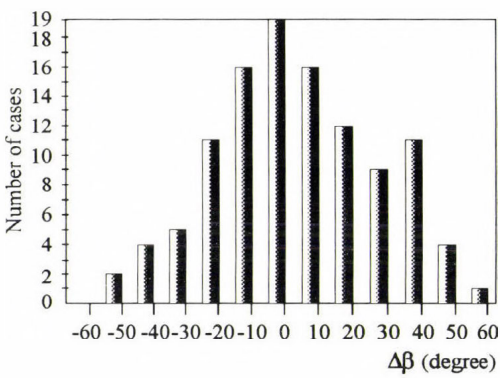

Fig. 4. Frequency distribution of differences (Δβ (degree)) between wind directions from cloud motion and radiosonde in all cases of our examination.

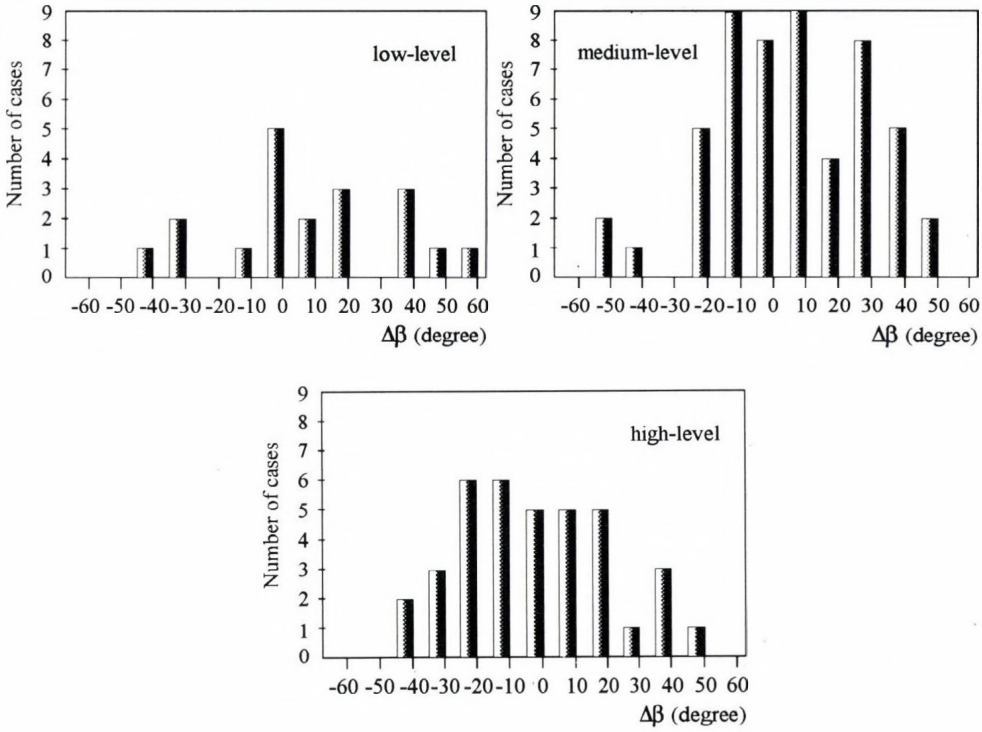

Fig. 5. Frequency distribution of differences ($\Delta\beta$ (degree)) between wind directions from cloud motion and radiosonde in cases computed from low-level (< 2000 m), medium-level (2000-7000 m), high-level (> 7000 m) clouds.

References

Bowen, R., Fusco, L., Morgan, J. and *Roeska, K.O.*, 1979: Operational production of cloud motion vectors (satellite winds) from METEOSAT image data. In *Proc. Use of Data from Meteorological Satellites*, ESA SP-143, 65-75.

Leese, L., Novak, S. and *Clark, B.*, 1971: An automated technique for obtaining cloud motion from geosynchronous satellite data using crosscorrelation. *J. Appl. Meteorol. 10*, 118-132.

Rákóczi, F. and *Kovács, E.*, 1981: Wind-field analysis on the basis of METEOSAT images. *Adv. in Space Research 1*, 133-137.

Schmetz, J., 1991: Cloud motion winds from METEOSAT: performance of an operational system. *Palaeogeogr., Palaeoclimatol., Palaeoecol.* (Global Planet. Change Sect.), 90, 151-156.

Schmetz, J. and *Nuret, M.*, 1987: Automatic tracking of high-level clouds in METEOSAT infrared images with a radiance windowing technique. *ESA Journal 11*, 275-286.

Schmetz, J. and *Nuret, M.*, 1989: Cloud motion wind estimates in Europe. In *The Use of Satellite Data in Operational Numerical Weather Prediction 1989-1993*. Proceedings of a workshop held at ECMWF, 9-12 May 1989, Vol. II, October 1989, 263-273.

Tänczer, T., 1988: *Műholdmeteorológia*. Akadémiai Kiadó, Budapest.

BOOK REVIEW

Meadows, D. H., Meadows, D. L. and *Randers, J.*: **Beyond the Limits**. Chelsea Green Publishing Company, Vermont (USA), 1992. pp. XIX and 300. ISBN 0-930031-55-5 (hard cover): 19.95 $.

More than twenty years ago the same authors published an international best-seller entitled '*The Limits to Growths*'. This book was sold 9 million copies in 29 languages. In this famous volume it was argued that the world economy goes towards its limits. In other words: if everything remains unchanged, the limits to physical growth on the planet-Earth would be reached during the next century. In the present book the authors express their view that in many respects the limit has already overshot: we are '*Beyond the Limits*'. They conclude, however, that the decline is not inevitable: a *sustainable society* is still technically and economically possible.

In the first chapter of the book the definition of the overshoot is given: it means that one goes beyond limits inadvertently, without meaning to do so. In the second chapter it is explained that the overshoot is due to exponential growth in world population and world industry. In many parts of the planet the population growth has resulted in poverty. There is a positive feedback between population growth and poverty. The situation is the worst in Africa, where the food production per capita has decreased since 1960.

The limits are overshot when the balance between sources and sinks is deteriorated. The problem is caused by the fact (Chapter 3) that both population and industrial capital (hardware, machines, factories etc.) have a potential for self-reproduction. For this, people need food, water, air and nutrients to grow, while machines need energy, water and air, minerals, chemicals and biological materials to produce goods and to make more machines. The quantity of these is limited in the Earth, more exactly it is in equilibrium because of the interaction of sources and sinks.

The sustainability is destroyed if the renewable resources are not regenerated, or the nonrenewable resources are not substituted by renewable resources at the rate of their use (e.g. when we use oil and the profit is not invested in solar collectors or in tree planting). Further, for a pollutant a sustainable rate of emission must be below the rate at which the pollutant is recycled. This indicates that we have to learn the dynamics of growth in a finite world as it is discussed in Chapter 4.

Chapter 5 of the book is devoted to the ozone story since the use of freons has already destroyed the balance of the formation and natural removal of stratospheric ozone. This example is applied by the authors to explain what does it mean that we are beyond the limit and how we can restore the natural state.

Chapter 6 is entitled: 'Technology, markets, and overshoot'. The main message of this chapter is that technology and free market can not solve alone the problem we face in spite of the spectacular development of technology and successes of the free market. This is illustrated by using a computer model called World3 elaborated by the authors. Thus, it is concluded that we have only two possibilities: the overshoot and collapse or 'controlled reduction of throughput by deliberate social choice'.

Chapter 7 of the book is interesting in particular. The meaning of a sustainable system is presented in detail. The authors cite the memorable words of the World Commission on Environment and Development according to which a sustainable society is one that 'meets the needs of the present without compromising the ability of future generations to meet their own needs'. In such a society the properties of the human heart and soul are different to the present ones. Thus, we have to change not the technologies, markets or governments but our own mentality. Finally, in the last chapter the authors express the hope of all of us that mankind is not before a collapse, but before the realization of a sustainable economic and social system.

It goes without saying that the present book can be proposed to everybody who cares about our present and future. Although the authors are economists, the text is readable by any educated person. The volume is recommended particularly to those meteorologists who are interested in climate variations and their relationships with world population and economic development.

E. Mészáros

NEWS

Scientific aspects of sustainable development

On the occasion of the General Assembly of the Hungarian Academy of Sciences a joint conference was organized on May 11, 1994 by the Department of Earth Sciences and the Commission of the Environmental Science of the Academy for discussing the scientific aspects of the concept of sustainable development. At the meeting Hungarian scientists of different disciplines outlined their view on the subject.

As it is known a *sustainable society* satisfies its needs in harmony with the environment. It can persist and makes the life for future generations possible. This simple definition becomes rather complicated if we want to define the word 'need'. The question is even more complex if one intends to say exactly what does 'development' mean. It is certain that a sustainable society cannot be poor. However, to cease the poverty on the Earth it would be necessary to increase considerably the standard of life of less developed part of the world. People in these country need a lot of energy, food and goods. How it is possible to meet this requirement without destroying further the environment, the biosphere and natural resources? On the other hand, how it is possible that people in more developed countries moderate their consumption without decreasing significantly the quality of their life? In other words: is the sustainable development a real concept?

During the conference it was more or less agreed that the evolution of our planet has been controlled by the presence of the biosphere. On the basis of physical and chemical principles we cannot simply explain why the planet-Earth is habitable (this point was stressed by *G. Marx*). It follows from this argument that the protection of the biosphere is of crucial interest for mankind. Thus, the conservation of the biodiversity is one of our most important tasks (*G. Vida*) for future. An other essential problem is to mitigate the global air pollution which can cause inadvertent climate modification. In this respect the scientific problems of climate forecasting was discussed. *G. Major* concluded that, beside the influence of greenhouse gases, anthropogenic changes in planetary albedo should also be considered to foresee more precisely climate of the next century.

Several speakers expressed the view that the continuation of the present growth in population and economy and – consequently – the present modification of the environment will lead to serious world-wide problems. Possible solutions were proposed to solve the economy-environment dilemma. *G. Vajda* spoke about the improvement of the energy production and air-cleaning technologies as well as about the necessity of a more efficient energy and material use. *G. Enyedy* stressed the need for a new taxation system which takes into account

the environmental effects of the production. The view generally accepted by the participants was formulated by *R. Czelnai* who argued that the concept of sustainable development is realizable only if the mentality of people can be modified. Such an 'impractical' philosophy is necessary which gives sense to human life without the continuous accumulation of material goods.

The conference was closed by *I. Láng*, session chairman, who mentioned, among other things, the difficulties of the present Hungarian economy which make the environmental management in the country even more complicated. However, he expressed his hope that the coming new Hungarian administration will do everything possible to take part in international efforts aiming to move human societies towards the realization of sustainable development.

E. Mészáros

ATMOSPHERIC ENVIRONMENT

an international journal

To promote the distribution of Atmospheric Environment *Időjárás* publishes regularly the *contents* of this important journal. For further information the interested reader is asked to contact *Dr. P. Brimblecombe,* School for Environmental Sciences, University of East Anglia, Norwich NR 7TJ, U.K.

Volume 28 Number 3 1994

Volume 28 Number 4 1994

Volume 28 Number 5 1994

Conference on Visibility and Fine Particles, Vienna, Austria, 15-18 September 1992

Section II: In-cloud transformation of particles

V. Ulevičus, S. Trakumas and *A. Girgždys*: Aerosol size distribution transformation in fog, 795-800.

Section III: Humidity influence on particle growth and visibility

W.E. Wilson and *P.C. Reist*: A PC-based Mie scattering program for theoretical investigations of the optical properties of atmospheric aerosols as a function of composition and relative humidity, 803-809.

E.-M. Uhlig, M. Stettler and *W. von Hoyningen-Huene*: Experimental studies on the variability of the extinction coefficient by different air masses, 811-814.

B.A. Nilsson: Model of the relation between aerosol extinction and meteorological parameters, 815-825.

M.L. Pitchford and *P.H. McMurry*: Relationship between measured water vapor growth and chemistry of atmospheric aerosol for Grand Canyon, Arizona, in winter 1990, 827-839.

K.A. Gebhart, W.C. Malm and *D. Day*: Examination of the effects of sulfate acidity and relative humidity on light scattering at Shenandoah National Park, 841-849.

J.F. Sisler and *W.C. Malm*: The relative importance of soluble aerosols to spatial and seasonal trends of impaired visibility in the United States, 851-862.

Section IV: Light absorption by aerosol particles

T. Raunemaa, U. Kikas and *T. Bernotas*: Observations of submicron aerosol, black carbon and visibility degradation in remote area at temoerature range from –24 to 20°C, 865-871.

G.W. Mulholland and *N.P. Bryner*: Radiometric model of the transmission cellreciprocal nephelometer, 873-887.

R.A. Dobbins, G.W. Mulholland and *N.P. Bryner*: Comparison of a fractal smoke optics model with light extinction measurements, 889-897.

Section V: Measuring methods and networks

M. Gazzi, V. Vicentini and *U. Bonafé:* A field experiment on contrast reduction law, 901-907.

W.H. White, E.S. Macias, R.C. Nininger and *D. Schorran*: Size-resolved measurements of light scattering by ambient particles in the southwestern U.S.A., 909-921.

W. von Hoyningen-Huene and *M. Wendisch*: Variability of aerosol optical parameters by advective processes, 923-933.

A. Thomas and *J. Gebhart*: Correlations between gravimetry and light scattering photometry for atmospheric aerosols, 935-938.

H. Tang, E.A. Lewis, D.J. Eatough, R.M. Burton and *R.J. Farber*: Determination of the particle size distribution and chemical composition of semi-volatile organic compounds in atmospheric fine particles with a diffusion denuder sampling system, 939-947.

Section VI: Airplane and space observations, solar photometry

R.F. Pueschel, J.M. Livingston, G.V. Ferry and *T.E. DeFelice*: Aerosol abundances and optical characteristics in the Pacific Basin free troposphere, 951-960.

J. Lukáč: Trend of solar radiation attenuation by atmospheric aerosols, 961-962.

V.E. Cachorro and *A.M. de Frutos*: Retrieval of atmospheric aerosol characteristics for visible extinction data at Valladolid (Spain), 963-971.

A.A. Galal and *R.H. Hamid*: On the instability of atmospheric optics in polluted areas, 973-976.

V. Cuomo, C. Serio, F. Esposito and *G. Pavese*: A differential absorption technique in the near infrared to determine precipitable water, 977-987.

Section VII: Trends in visibility and fine particles, including urban data

A. Trier and *L. Firinguetti*: A time series investigation of visibility in an urban atmosphere–I, 991-996.

V.N. Aref'ev and *V.K. Semenov*: Spectral transparency of the atmosphere in the center of the European-Asian continent, 997-999.

R.A. Stuart and *R.M. Hoff*: Airport visibility in Canada–revisited, 1001-1007.

Volume 28 Number 6 1994

NOTES TO CONTRIBUTORS

The purpose of *Időjárás* is to publish papers in the field of theoretical and applied meteorology. These may be reports on new results of scientific investigations, critical review articles summarizing current problems in certain subject, or shorter contributions dealing with a specific question. Authors may be of any nationality but papers are published only in English.

Papers will be subjected to constructive criticism by unidentified referees.

* * *

The manuscript should meet the following formal requirements:

Title should contain the title of the paper, the names(s) of the author(s) with indication of the name and address of employment.

The title should be followed by an *abstract* containing the aim, method and conclusions of the scientific investigation. After the abstract, the *key-words* of the content of the paper must be given.

Three copies of the manuscript, typed with double space, should be sent to the Editor-in-Chief: *P.O. Box 39, H-1675 Budapest,* Hungary.

References: The text citation should contain the name(s) of the author(s) in Italic letter or underlined and the year of publication. In case of one author: *Miller* (1989), or if the name of the author cannot be fitted into the text: *(Miller,* 1989); in the case of two authors: *Gamov* and *Cleveland* (1973); if there are more than two authors: *Smith et al.* (1990). When referring to several papers published in the same year by the same author, the year of publication should be followed by letters a,b etc. At the end of the paper the list of references should be arranged alphabetically. For an article: the name(s) of author(s) in Italics or underlined, year, title of article, name of journal, volume number (the latter two in Italics or underlined) and pages. E.g. *Nathan, K. K.,* 1986: A note on the relationship between photosynthetically active radiation and cloud amount. *Időjárás 90,* 10-13. For a book: the name(s) of author(s), year, title of the book (all in Italics or underlined with except of the year), publisher and place of publication. E.g. *Junge, C. E.,* 1963: *Air Chemistry and Radioactivity.* Academic Press, New York and London.

Figures should be prepared entirely in black India ink upon transparent paper or copied by a good quality copier. A series of figures should be attached to each copy of the manuscript. The legends of figures should be given on a separate sheet. Photographs of good quality may be provided in black and white.

Tables should be marked by Arabic numbers and provided on separate sheets together with relevant captions. In one table the column number is maximum 13 if possible. One column should not contain more than five characters.

Mathematical formulas and *symbols:* non-Latin letters and hand-written marks should be explained by making marginal notes in pencil.

The final text should be submitted both in manuscript form and on *diskette.* Use standard 3.5" or 5.25" DOS formatted diskettes for this purpose. The following word processors are supported: WordPerfect 5.1, WordPerfect for Windows 5.1, Microsoft Word 5.5, Microsoft Word for Windows 2.0. In all other cases the preferred text format is ASCII.

* * *

Authors receive 30 *reprints* free of charge. Additional reprints may be ordered at the authors' expense when sending back the proofs to the Editorial Office.

Published by the Hungarian Meteorological Service

Budapest, Hungary

INDEX: 26 361

HU ISSN 0324-6329

IDŐJÁRÁS

QUARTERLY JOURNAL
OF THE HUNGARIAN METEOROLOGICAL SERVICE

CONTENTS

VOL. 98 * NO. 3 * JULY–SEPTEMBER 1994

IDŐJÁRÁS

Quarterly Journal of the Hungarian Meteorological Service

Editor-in-Chief
E. MÉSZÁROS

Editor
T. TÄNCZER

Technical Editor
Mrs. M. ANTAL

Editorial Office: P.O. Box 39, H–1675 Budapest

Subscription from customers in Hungary should be sent to the Financial Department of the Hungarian Meteorological Service Kitaibel Pál u. 1, 1024 Budapest. The subscription rate is HUF 2000.

Abroad the journal can be purchased from the distributor: KULTURA, P.O. Box 149, H–1389 Budapest. The annual subscription rate is USD 56.

IDŐJÁRÁS

Quarterly Journal of the Hungarian Meteorological Service
Vol. 98, No. 3, July–September 1994

Experimental study on low-pressure aerosol filtration through fibrous filters

M. Attoui[1], **A. Renoux**[1], **C. Vauge**[2] and **D. Boulaud**[3]

[1] *Laboratoire de Physique des Aérosols et de Transfert des Contaminations, Université Paris XII, Avenue du Général de Gaulle, 94010 Creteil, France*
[2] *Laboratoire d'Instrumentation Physique, Université Paris XII*
[3] *CEA/IPSN/DPEI/SERAC/LPMA, Saclay, France*

(Manuscript received 21 June 1994; in final form 25 July 1994)

Abstract—This work concerns the efficiency of fibrous filters in the 'transition-flow regime'. We used filters with a mean fibre diameter of 2.7 μm, and a packing density, α, of 0.008, in a pressure range from 50 to 1000 hPa. Electrostatic classification was used to generate particles with a size distribution from 0.04 to 0.3 μm. The penetration was measured at a flow rate of 40 cm s^{-1}. Experimental results showed that the penetration decreased with pressure, while we also observed that the maximum penetration size shifted to larger particle sizes.

Key-words: aerosol, filtration, low pressure.

1. Introduction

When investigating, for instance, aerosol influence on the atmospheric radiative balance (*Lenoble*, 1993), it becomes more and more necessary to collect atmospheric particles at high altitude; consequently corresponding to low pressure. However, filtration models established for pressures close to atmospheric pressure, may no longer be valid. This is what prompted us to study the behaviour at low pressures of usual filters, down to one hectopascal.

Let us recall that the captation efficiency, E, of a filter is defined as the ratio of the number of retained particles to the number of incoming particles, i.e.:

$$E = (N_{up} - N_{do})/N_{up},$$

where N_{up} is the upstream particle concentration, and N_{do} the corresponding downstream one.

The penetration coefficient, P, is often preferentially used, defined as follows:

$$P = 1 - E = N_{do}/N_{up}.$$

The flow around the fibre, on which (among other factors) the penetration depends, is characterised by a dimensionless coefficient Kn, the Knudsen number of a fibre; defined as the ratio of twice the free mean path of the molecules of carrier gas, λ, to the fibre diameter, D_f:

$$Kn = 2\lambda/D_f.$$

According to the *Devienne* classification (1958), the flow regime can be subdivided into several domains:

1°– $Kn < 0.001$	Continuous flow regime
2°– $0.001 < Kn < 0.25$	Continuous flow regime with gas slip effect
3°– $0.25 < Kn < 10$	Transition flow regime
4°– $Kn > 10$	Molecular flow regime.

Our investigation is defined in the transition flow regime, or Knudsen regime, i.e. for Kn numbers ranging from 0.25 and 10, because very little work has been carried out so far within this field.

Actually, previous studies on low pressure filtration are scarce, be they theoretical or experimental. *Kirsch* and *Stechkina* (1978), and *Manson* (1984, 1988) have carried out studies, within the transitional flow regime, on the resistance (pressure drop) of a flow through a fibrous filter. *Zhang* and *Liu* (1992) have made experimental measurements of fibrous filter efficiencies in the pressure range of 1000 hPa–100 hPa.

2. *Experimental study and theory*

The classical method, illustrated in *Fig. 1*, involves sampling aerosols from a flow passing through the filter with both an upstream and a downstream concentration, and measuring those by means of a condensation nuclei counter (CNC).

However, this method can no longer be used when working at sub-atmospheric pressures. In fact, the loss in pressure would induce, more or less, rapid evaporation of the alcohol contained in the CNC saturator, and this would be drawn into the CNC—except model 3760 from T.S.I., which possesses a pressure equalization tube and can only operate correctly down to 100 hPa. This

counter has a further drawback of working solely with low particulate concentrations.

We subsequently developed an original method, allowing operation down to 10 hPa, in order to combat these restrictions (*Attoui et al.*, 1993a, b; *Attoui*, 1994).

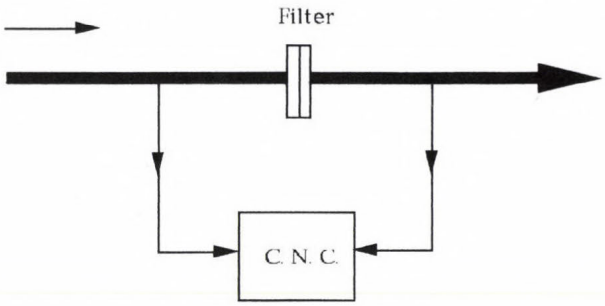

Fig. 1. Classical method for filter penetration measurement.

2.1 Principle of the method

An aerosol-loaded air flow is sent through the filter under study, being driven by a pressure gradient from one side of the filter to the other. This pressure gradient decreases exponentially and reaches zero after a relatively short time (*Fig. 2*).

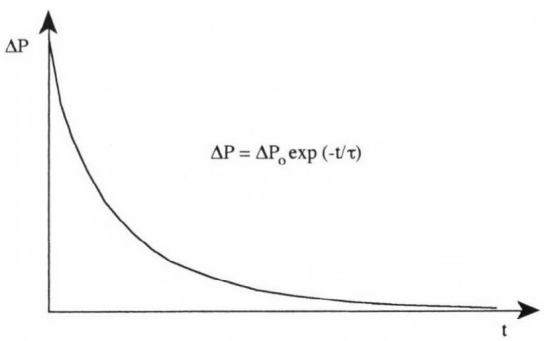

Fig. 2. Decrease in the pressure difference undergone by the filter.

This pressure gradient corresponds to an air velocity, which reaches zero at the same time as Δp. Every studied pressure possesses such a gradient. Those decreasing pressure gradients are obtained by emptying a tank into another through a cylindrical pipe, the whole set remaining totally isolated from the outside. For this purpose, two tanks (I and II) of equal volume are to be used, initially at different pressures P_1 and P_2. Their pressures reach an equilibrium value through the filter after opening the valve, V_a, as shown in *Fig. 3*.

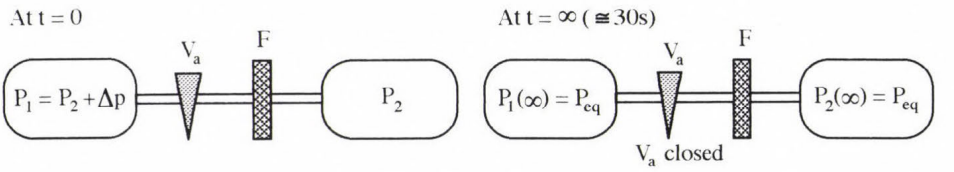

Fig. 3. Pressure in the two tanks at time, $t = 0$, and at equilibrium.

If we operate in laminar regime, the pressure difference, $\Delta p(t) = p_1(t) - p_2(t)$, decreases according to the exponential relationship:

$$\Delta p\,(t) = \Delta p\,(0)\,\exp\left[-\frac{t}{\tau}\right], \tag{1}$$

where τ is given by:

$$\tau = \frac{VM}{2KRT},$$

and R is the universal gas constant; T is the absolute temperature for the system; V is the volume of both tanks; K is the circuit resistance to flow. The derivation of the above relationship may be found in Appendix 1. Eq. (1) may also be written in terms of the flow velocity, as follows.

For this pressure gradient there corresponds a shift of matter, dm_1, from tank I towards tank II:

$$dm_1 = K\,[p_1(t) - p_2(t)]\,dt,$$

but:

$$dm_1 = \rho v s\,dt,$$

where ρ is the specific mass of the fluid (air); v is the flow velocity; s is the cross-sectional area of the fluid path.

$$\rho v s\,dt = K\Delta p = K\Delta p(0)\,e^{-t/\tau}\,dt,$$

hence:

$$v = \left[\frac{K\Delta p(0)}{\rho s}\right] e^{-t/\tau}.$$

Let us consider:

$$v_0 = \left[\frac{K\Delta p(0)}{\rho s}\right].$$

Thus v becomes:

$$v = v_0 e^{-t/\tau}. \tag{2}$$

2.2 Determination of the variation in air mass difference between tanks I and II as a function of time

The filter 'works' during transfer with a mean efficiency, $\bar{E}$, which may be approximated to $E(v_0)$. We only need to isolate the two tanks after the pressures are balanced by shutting valve, V_a, returning to atmospheric pressure by injecting clean nitrogen through an ULPA filter. It is then possible to count the number of particles having flowed through the filter and those remaining in the second tank, using the CNC at atmospheric pressure. The number of particles upstream of the filter is determined from the known mass concentration in tank I, under pressure p_1, and from the mass transferred, m. So that:

$$N_{up} = C_{m,p\,(up)} m,$$

where $C_{m,p}$ is the mass concentration of aerosol at pressure, p, given by:

$$C_{m,p\,(up)} = C_{m,P_{atm}^{(up)}} \times \frac{p}{p_{atm}}.$$

With $C_{m,P_{atm}^{(up)}}$ being the mass concentration of aerosol at atmospheric pressure in the upstream tank. The mass of gas transferred from tank I to tank II, m, is given by Eq. (3) below. Appendix 2 shows the derivation of this relationship.

$$m = \frac{VM}{2RT} \Delta P_0, \tag{3}$$

where ΔP_0 is the difference of pressures between tanks I and II at $t = 0$.

3. Experimental set-up

Our experimental set-up, shown in *Fig. 4*, consists of three distinct parts. The first of these is the generator system, composed of an atomizer, a dryer, a neutralizer and an electrostatic classifier. The second part is the testing bench, comprising of two stainless steel tanks of equal volume (20 litres) connected by a 70 cm long, 6 mm inside diameter stainless steel pipe. They are mounted on a support, which also contains:

— a filter holder, F, and a pneumatic valve, V_a, electrically operated to allow the air flow between the two tanks, or to isolate one from the other;

— a vacuum pump capable of evacuating both of tanks at the same time or separately, by means of manual valves, and equipped with a filter and a safety-check valve for oil vapour;
— a manometer on each of the two tanks, connected via a data processing card to a PC, and to a direct readout.

The final part is the counting system, consisting of a personal computer (PC) and a condensation nucleus counter (CNC). With the appropriate software, and use of the data processing card, particles may be counted one by one using the pulses issued by the CNC and collected by the card. This gives us a direct count of the number of particles having flowed through the filter.

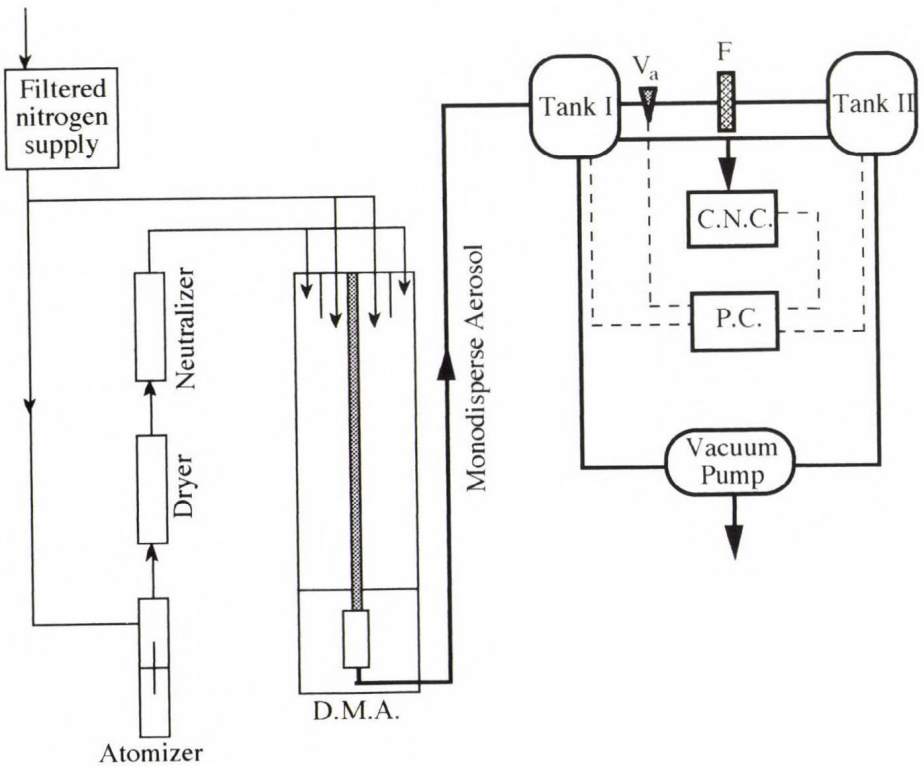

Fig. 4. Experimental set-up.

4. Experimental results

We tested 'formettes' (glass fibre filters) from *B. Dumas* company, at different pressures. The mean fibre diameter was 2.7 μm and the filter thickness was 0.3 mm. *Fig. 5* shows the variation in the particle number concentration

plotted as a function of pressure, for particles of 0.1 μm diameter in either of the other tanks. The relationship given by the equation:

$$C_{(p)} = C_{P_{atm}} \left[\frac{p}{p_{atm}} \right],$$

was confirmed by our results, so by measuring $C_{p_{atm}}$, we can easily go down to $C_{(p)}$.

Fig. 6 gives the variation of penetration, *P,* as a function of pressure, from 1000 hPa down to 50 hPa, for a filtration speed of 40 cm s^{-1}.

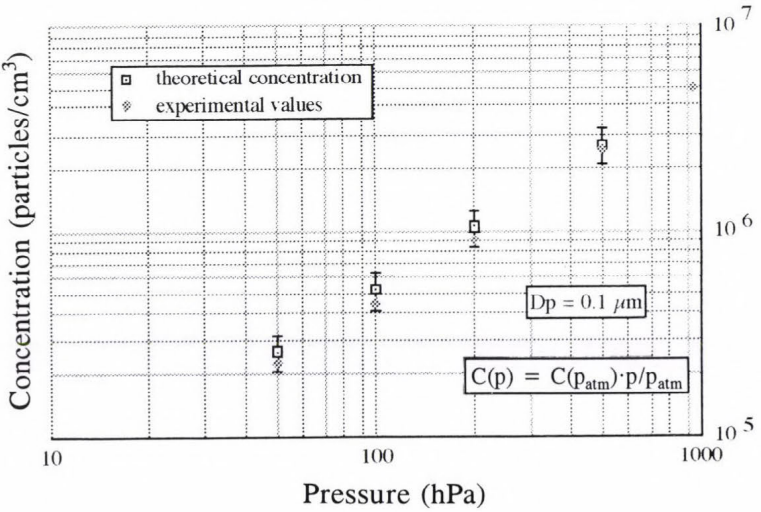

Fig. 5. Variation of the particle volumetric concentration as a function of pressure.

Fig. 7 illustrates the variation of penetration, *P,* as a function of the particle diameter, D_p, obtained for differing pressure conditions. As shown, six particulate diameters were studied: 0.04, 0.06, 0.1, 0.15, 0.2, and 0.3 μm.

5. Conclusion

Our first experimental readings clearly showed that the penetration, *P,* of a filter decreases significantly with pressure; i.e. when the Knudsen number of a filter increases.

We also noticed a slight shift of maximum penetration values towards the larger aerosol diameters, as already pointed out by *Zhang* and *Liu* (1992).

As a continuation of this work, we intend to carry out the same experiments at filtration speeds 10 times lower. A first comparison of our experimental results with the theory developed by *Payet* (1992), from *Rubow* works (1981), appears to give satisfactory results.

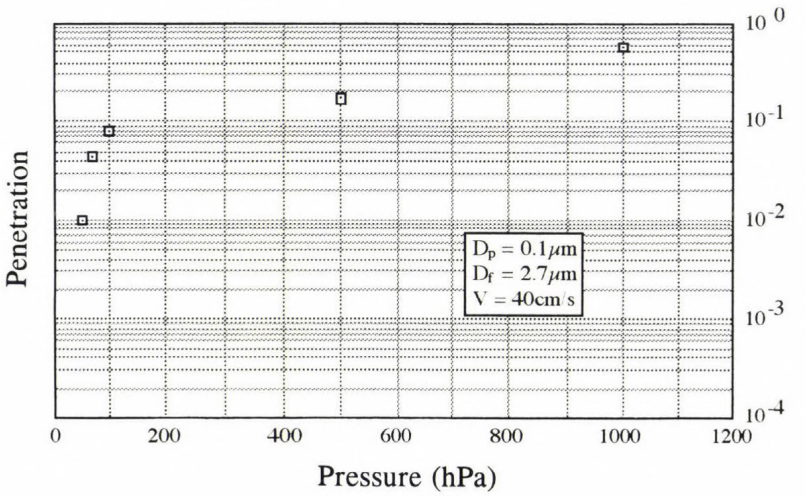

Fig. 6. Variation of penetration as a function of pressure for a given diameter.

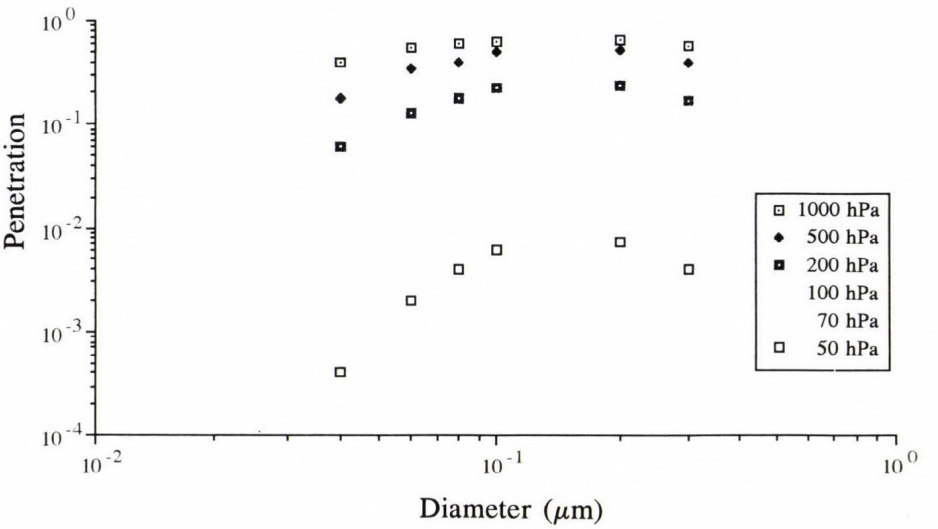

Fig. 7. Spectral variation of penetration for several pressures.

References

Attoui, M., Renoux, A. and *Madelaine, G.*, 1993a: Etude experimentale sur la filtration des aérosols par les filtres à fibres à basse pression. *COFERA Actes 1993.* GAMS, Paris.

Attoui, M., Renoux, A. and *Boulaud, D.*, 1993b: Fibrous filters efficiency in low pressure conditions. *Journal of Aerosol Science 24*, 37-39.

Attoui, M., 1994: *Une nouvelle approche experimentale de la mesure de l'efficacité des filtres à fibres à basse pression.* Thèse en science des aérosols, Université Paris XII.

Comolet, R., 1976: *Mécanique expérimental des fluides*. Masson, Paris.

Devienne, M., 1958: *Frottements et échanges thermiques dans les gaz raréfiés.* Gauthier-Villars, Paris.

Kirsh, A.A. and *Stechkina, I.B.*, 1978: In *Fundamentals of Aerosol Science* (ed.: *D.T. Shaw*). Wiley Intersci., New York.

Lenoble, J., 1993: Influence des aérosols atmosphériques sur le rayonnement: conséquences climatiques, possibilités de télédétection. *COFERA GAMS*, 75-80.

Manson, D.R., 1984: In *Aerosols: Science, Technology and Industrial Applications.* (eds.: *B.Y.H. Liu, D.Y.H. Pui* and *H.J. Fissan*). Elsevier, New York.

Monson, D.P., 1988: In *Proceedings of 1988 Annual Meeting of AAAR.* Chapel Hill, NC.

Payet, S., 1992: Filtration stationnaire et dynamique des aérosols liquides submicroniques. *Thèse de l'Université Paris XII. Rapport CEA-R-5589.*

Rubow, K.L., 1981: Submicron aerosol filtration characteristics of membrane filters. *Ph.D. Dissertation.* Mechanical Engineering Dept., Univ. of Minnesota, Minneapolis, MN.

Zhang, Z. and *Liu, B.Y.*, 1992: Experimental study of aerosol filtration in the transition flow regime. *Aerosol Science and Technology 15*, 228-238.

APPENDIX 1

Referring to Fig. 3., given in the text, *the derivation of the exponential relationship* given by Eq. (1) is as follows.

Operating in the laminar regime, the pressure difference, $\Delta p(t) = p_1(t) - p_2(t)$, decreases according to the exponential relationship:

$$\Delta p(t) = \Delta p(0) \exp\left[-\frac{t}{\tau}\right]. \tag{1}$$

Indeed, considering air as a perfect gas, we have inside each of the two tanks:

$$p_1 V_1 = \frac{m_1}{M} R T_1,$$

and

$$p_2 V_2 = \frac{m_2}{M} R T_2,$$

where R is the universal gas constant; m_1 is the mass of air in tank I; m_2 is the mass of air in tank II; T_1 and T_2 are the respective absolute temperatures in

tanks I and II; V_1 and V_2 are their respective volumes. The tanks are at the same temperature and have equal volumes.

Subsequently: $T_1 = T_2 = T,\ V_1 = V_2 = V.$

Which gives:

$$p_1 V = \frac{m_1}{M} RT \Rightarrow \frac{RT}{MV} = \frac{p_1}{m_1}, \tag{A1.1}$$

$$p_2 V = \frac{m_2}{M} RT \Rightarrow \frac{RT}{MV} = \frac{p_2}{m_2}. \tag{A1.2}$$

Therefore, for the relationship to be valid at any moment:

$$\frac{p_1}{m_1} = \frac{p_2}{m_2}. \tag{A1.3}$$

Our system (tanks I and II and their connecting pipes) is totally isolated from the 'outside', so that the total mass of air is constant, therefore:

$$\begin{aligned} m_1 + m_2 &= m_0, \\ m_2 &= m_0 - m_1. \end{aligned} \tag{A1.4}$$

Relationship (3) becomes:

$$p_2 = p_1 \left[\frac{m_0}{m_1} - 1 \right]. \tag{A1.5}$$

The total pressure is also constant, so:

$$p_1 + p_2 = \text{constant}. \tag{A1.6}$$

The mass flow, dm, leaving tank I towards tank II during a period of time, dt, is given by the equation:

$$dm = K(p_1 - p_2)\,dt. \tag{A1.7}$$

Where K is the circuit resistance to flow; a real constant in the laminar flow *(Comolet*, 1976).

In this case, tank I loses mass to the benefit of tank II. This means dm_1 is negative, so:

$$dm_1 = -K(p_1 - p_2)\,dt = K(p_2 - p_1)\,dt\,. \tag{A1.8}$$

By differentiating Eq. (1), we get:

$$dm_1 = \frac{VM}{RT}\,dp_1 = K(p_2 - p_1)\,dt\,, \tag{A1.9}$$

subsequently:

$$dm_1 = \frac{VM}{RT}\,dp_1 = K(p_2 - p_1)\,dt\,,$$

and: $$p_1 + p_2 = p_0 \Rightarrow p_2 = p_0 - p_1,$$

thus:

$$\frac{VM}{RT}\,dp_1\,K[(p_2 - p_1) - p_1]\,dt = K[p_0 - 2p_1]\,dt\,,$$

and then:

$$\frac{dp_1}{p_0 - 2p_1} = K\frac{RT}{VM}\,dt\,.$$

Which after integration gives:

$$(p_0 - 2p_1) = C_0^2 \exp\left[-2K\frac{RT}{VM}\,t\right].$$

The integration constant, C_0^2, is determined by the initial conditions for the pressures p_1 and p_2 inside each of the two tanks before their connection, and:

$$p_1(0) \text{ is known at } t = 0,$$
$$p_2(0) \text{ is known at } t = 0,$$

also known at $t = 0$:

$$p_1(0) + p_2(0) = p_0.$$

Then at $t = 0$:

$$p_0(0) - 2p_1(0) = C_0^2 \exp(0),$$

$$C_0^2 = p_0 - 2p_1(0)\,,$$

$$C_0^2 = p_2(0) - p_1(0)\,. \tag{A1.11}$$

Therefore:

$$2p_1(t) = p_0 \{p_2(0) - p_1(0)\} \exp\left[-2\frac{KRT}{VM}t\right],$$

$$p_1(t) = \frac{p_1(0)}{2}\left[1 - \exp\left[1 - 2\frac{KRT}{VM}t\right]\right] + \frac{p_2(0)}{2}\left[1 - \exp\left[-2\frac{KRT}{VM}t\right]\right]. \quad \text{(A1.12)}$$

We have: $p_0 = p_1(t) + p_2(t) = \text{constant},$

so: $p_2(t) = p_0 - p_1(t) = p_1(0) + p_2(0) - p_1(t),$

subsequently: $p_2(t) = p_1(0) + p_2(0) - p_1(t).$ (A1.13)

Replacing $p_1(t)$ by its expression given by Eq. (11) we get:

$$p_2(t) = p_1(0) + p_2(0) -$$

$$\left\{\frac{p_1(0)}{2}\left[1 - \exp\left[-2\frac{KRT}{VM}t\right]\right] + \frac{p_2(0)}{2}\left[1 - \exp\left[-2\frac{KRT}{VM}t\right]\right]\right\},$$

rearranging this equation we get:

$$p_2(t) = \frac{p_1(0)}{2}\left[1 - \exp\left[-2\frac{KRT}{VM}t\right]\right] + \frac{p_2(0)}{2}\left[1 - \exp\left[-2\frac{KRT}{VM}t\right]\right]. \quad \text{(A1.14)}$$

$\Delta p(t)$ is the pressure difference, $[p_2(t) - p_1(t)]$, between the two tanks at any moment:

$$\Delta p(t) = p_1(t) - p_2(t) = [p_1(0) - p_2(0)] \exp\left[-2K\frac{RT}{VM}t\right],$$

$$\Delta p(t) = \Delta p(0) \exp\left[-2\frac{RT}{VM}t\right].$$

Let us consider:

$$\tau = \frac{VM}{2KRT}.$$

Finally, $\Delta p(t)$ becomes:

$$\Delta p(t) = \Delta p(0) \exp\left[-\frac{t}{\tau}\right]. \tag{1}$$

APPENDIX 2 (derivation of Eq. (3))

Determination of the variation in air mass difference between I and II as a function of time ($m_1(t)$ and $m_2(t)$), and of the mass transferred from I to II

$$p_1(t) = m_1 \frac{RT}{MV} \quad \text{in tank I,} \tag{A2.1}$$

$$p_2(t) = m_2 \frac{RT}{MV} \quad \text{in tank II.} \tag{A2.2}$$

$$m_1 + m_2 = \text{constant} \Rightarrow \frac{dm_1}{dt} + \frac{dm_2}{dt} = 0 \Rightarrow \frac{dm_1}{dt} = -\frac{dm_2}{dt}. \tag{A.2.3}$$

Eq. (A2.1) gives:

$$\frac{dp_2}{dt} = \frac{RT}{MV}\frac{dm_2}{dt}. \tag{A2.4}$$

On the other hand, at any moment we have:

$$\frac{dm_1}{dt} = -K(p_1 - p_2).$$

Therefore, by replacing p_1 and p_2 with their values given by Eq. (2) and (A2.1), we get:

$$\frac{dm_1}{dt} = -K\frac{RT}{VM}(m_1 - m_2). \tag{A2.5}$$

From the derivation, Eq. (A2.5) gives:

$$\frac{d^2m_1}{dt^2} = -K\frac{RT}{MV}\left[\frac{dm_1}{dt} - \frac{dm_2}{dt}\right]. \tag{A2.6}$$

Eq. (A2.3) thus leads to:

$$\frac{d^2m_1}{dt^2} = -2K\frac{RT}{MV}\frac{dm_1}{dt}. \tag{A2.7}$$

Considering: $U = \frac{dm_1}{dt}$, Eq. (A2.6) becomes:

$$\frac{dU}{dt} = -2K\frac{RT}{MV}U. \tag{A2.8}$$

After integration, we get:

$$\frac{dm_1}{dt} = U_0 \exp\left[-2K\frac{RT}{VM}t\right].$$

Subsequently:

$$m_1 = -U_0\frac{MV}{2KRT}\exp\left[-2K\frac{RT}{MV}t\right] + A.$$

The integration constants, U_0 and A, are determined by the boundary conditions as follows:

at $t = 0$ $\quad m_1(0) = m_{1,0}$ and $m_2(0) = m_{2,0}$,

as $t \to \infty$ $\quad m_1(\infty) = \frac{m_{1,0} + m_{2,0}}{2} = m_2(\infty)$.

We then get:

$$m_1(t) = \frac{m_{1,0} + m_{2,0}}{2} + \left[\frac{m_{1,0} - m_{2,0}}{2}\right]\exp\left[-2K\frac{RT}{MV}t\right]. \tag{A2.9}$$

A similar calculation gives the evolution of air mass, m_2, in tank II as a function of time:

$$m_2(t) = \frac{m_{1,0} + m_{2,0}}{2} - \left[\frac{m_{1,0} - m_{2,0}}{2}\right]\exp\left[-2K\frac{RT}{MV}t\right]. \tag{A2.10}$$

The difference of mass (i.e., of matter) between I and II is given, at any moment, by:

$$\Delta m(t) = m_1(t) - m_2(t) = \left(m_{1,0} - m_{2,0}\right) \exp\left[-2\frac{KRT}{MV}t\right],$$

$$\Delta m(t) = \Delta m_0 \exp\left[-2\frac{KRT}{MV}t\right],$$

where: $\Delta m_0 = (m_{1,0} - m_{2,0})$.

In the end:

$$\Delta m(t) = \Delta m_0 \exp(-t/\tau), \tag{A2.11}$$

where:

$$\tau = \frac{MV}{2KRT}.$$

We have:

$$m_{1,0} = \frac{VM}{RT} p_{1,0},$$

and:

$$m_{2,0} = \frac{VM}{RT} p_{2,0},$$

where $p_{1,0}$ and $p_{2,0}$ are the pressures in tank I and II, respectively, at $t = 0$. Thus,

$$m = \frac{m_{1,0} - m_{2,0}}{2} = \frac{VM}{RT}\left[\frac{p_{1,0} - p_{2,0}}{2}\right].$$

Therefore:

$$m = \frac{VM}{2RT}\Delta P_0, \tag{3}$$

Δp_0 being the difference of pressures between tanks I and II at $t = 0$.

IDŐJÁRÁS

Quarterly Journal of the Hungarian Meteorological Service
Vol. 98, No. 3, July–September 1994

Ozone episodes in Hungary in March

V. Sándor, L. Haszpra and **Gy. Baranka**

Institute for Atmospheric Physics,
P.O. Box 39, H-1675 Budapest, Hungary

(Manuscript received 28 June 1994; in final form 26 September 1994)

Abstract—Every year there are a few days in March when the daily maximum 30 minutes average ozone mixing ratio exceeds 60 ppbv in Hungary. In this paper the reasons for these early spring ozone episodes are studied. It is found that the majority of the episodes is formed when the weather in the Carpathian Basin is controlled by anticyclones causing dry, sunny weather. However, long range transport of ozone and precursors, local ozone formation (urban plume) and intrusion of free tropospheric air into the surface layer may also result elevated ozone concentration. Meteorological factors characterizing the above processes can be reliably forecasted.

Key-words: ozone, ozone episodes, ozone forecasting, meteorological conditions.

1. Introduction

In the industrialised regions the majority of ozone observed in the surface layer is formed photochemically from ozone precursors like nitrogen oxides, carbon monoxide and reactive organic substances. The rates of the photochemical reactions directly depend on the incoming solar radiation. Therefore, the highest ozone concentrations are measured during the summer season. However, in certain cases rather high concentration can be observed as early in the year as March, while usually after late September elevated concentrations rarely occur. Most of the authors refer to the influence of the stratospheric ozone having its maximum over the northern mid-latitude in spring (*Haagenson et al.*, 1981; *Johnson* and *Viezee*, 1981; *Raatz et al.*, 1985; *Vaughan* and *Price*, 1989; *Ebel et al.*, 1991; *Oberreuter*, 1992; *Gruzdev* and *Sitnov*, 1993). However, this asymmetrical behaviour may also be caused by the interaction of the increasing insolation with the high amount of ozone precursors accumulated in the atmosphere during winter (*Penkett* and *Brice*, 1986—see also

Fig. 1 for Hungary). In this paper the meteorological conditions resulting in elevated ozone concentration in March are studied on the basis of the measurements carried out at K-puszta regional background air pollution monitoring station located in the centre of Hungary (46°58′N, 19°33′E, 125 m masl). Continuous ozone monitoring was started at this side in January, 1990.

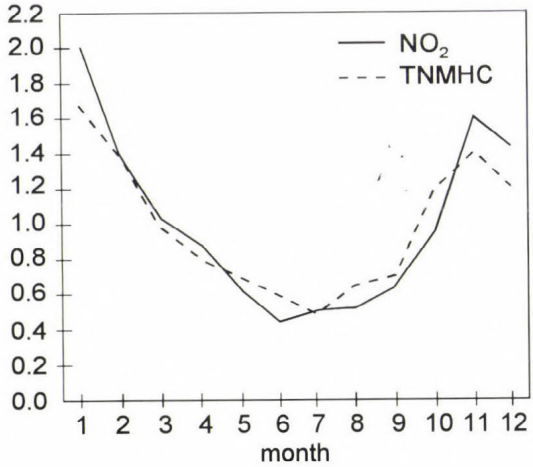

Fig. 1. Average relative (monthly average/annual average) annual cycles of NO_2 and total non-methane hydrocarbon concentrations at K-puszta (1987–1993).

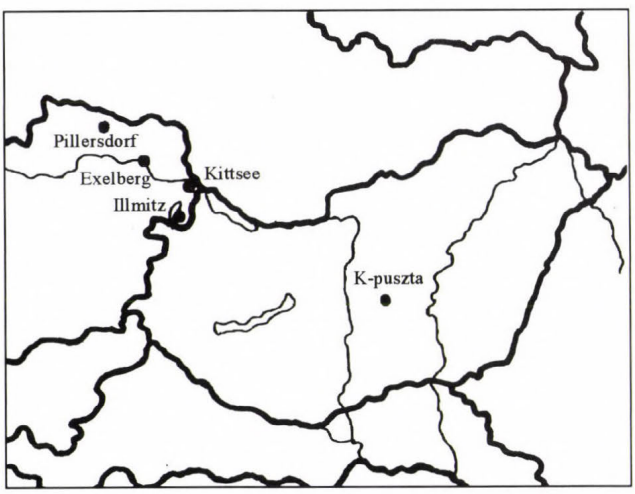

Fig. 2. Ozone monitoring stations in East-Austria and Hungary.

In this study to get a wider scope of the phenomenon measurements at a few ozone monitoring stations in East-Austria were also used (*Fig. 2*).

2. *Ozone episodes in March*

In this paper those days are studied when the maximum 30 minutes average ozone concentration value (mixing ratio) exceeds 60 ppbv for more than one day in succession. Most of these days clusters in 6 episodes (*Table 1*, *Fig. 3*).

Table 1. The periods of the episodes, 1990–1993

Period	O_3 maximum (ppbv)	Day of maximum
15–21 March, 1990	103.7	19 March
15–16 March, 1991	69.5	15 March
21–24 March, 1991	70.2	21 March
5– 7 March, 1993	68.3	6 March
10–17 March, 1993	71.9	16 March
20–23 March, 1993	69.5	22 March

On 21 and 24 March, 1991, the daily maximum 30-minutes ozone concentration exceeded 60 ppbv. However, between these days the measurement was interrupted, therefore, we could not be sure if that period was an episode. In addition to the above episodes there was a day in 1992 (28 March) when the daily maximum ozone concentration exceeded 60 ppbv (61.8 ppbv). The maximum concentration on the preceding day was also high, it reached 55 ppbv. The ozone concentration was governed by different processes on those two days. On the first one the influence of the upper tropospheric (indirectly stratospheric) air might be assumed. Therefore these days are also studied in this paper.

Episode 1: 15–21 March, 1990

March 1990 was drier and warmer than usual. Since 14 March the weather in the Carpathian Basin was influenced by an extended high pressure area (max. 1050 hPa) which had its centre over the Basin on 19 March (*Fig. 4*). The temperature gradually increased up to 9°C above the multiannual average and the sunshine duration was as long as 76–92% of the astronomically potential one. Only weak easterly wind was observed during the period. The meteorological condition was favourable for photochemical oxidant formation and accumulation in the whole region (*Fig. 5*). All monitoring stations in the region measured high concentration due to the similar meteorological conditions, however, the maximum values differed, which might reflect the importance of local effects (concentration of precursor and reductive compounds, dry deposition of ozone, etc.). The accumulation process was interrupted by a weak cold front passing the Carpathian Basin on 21 March.

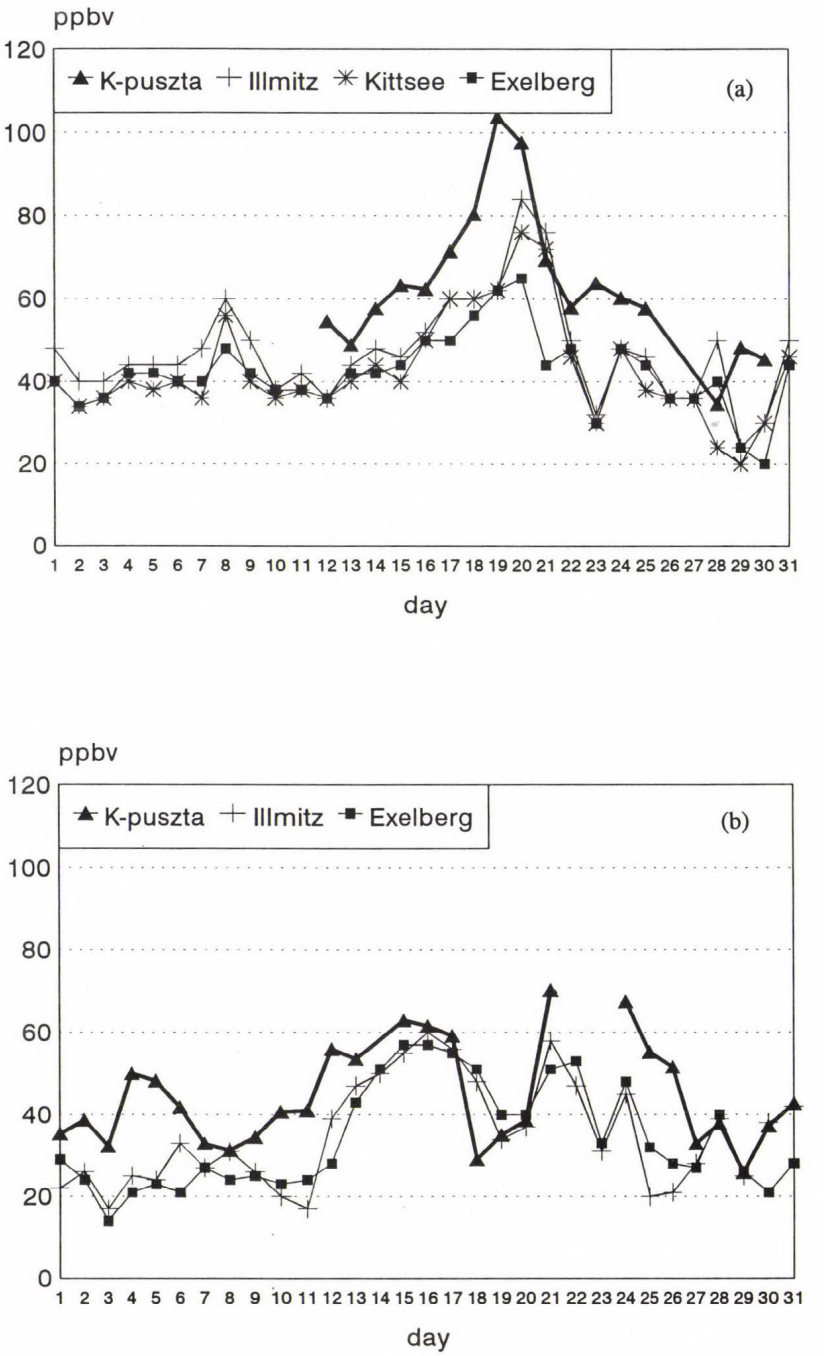

Fig. 3. The daily maximum 30 minutes ozone mixing ratios (*a*) March 1990, (*b*) March 1991.

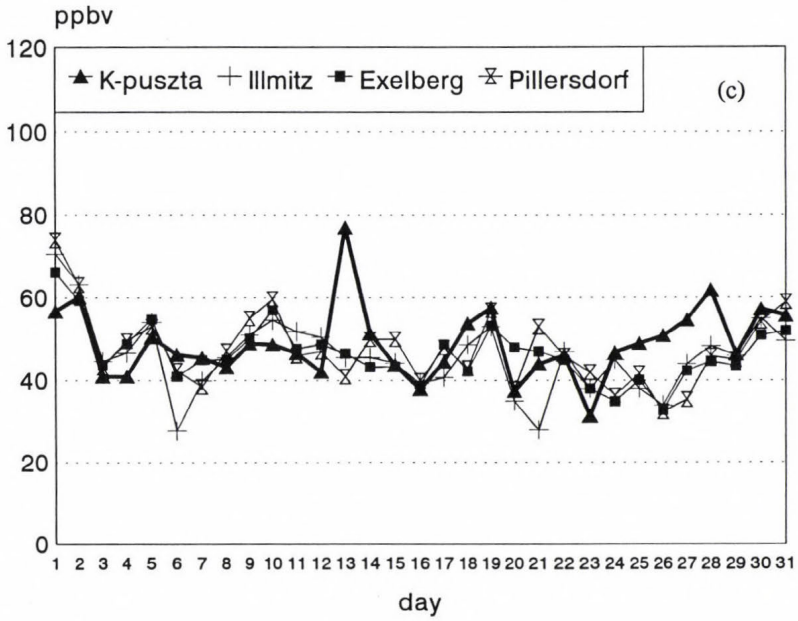

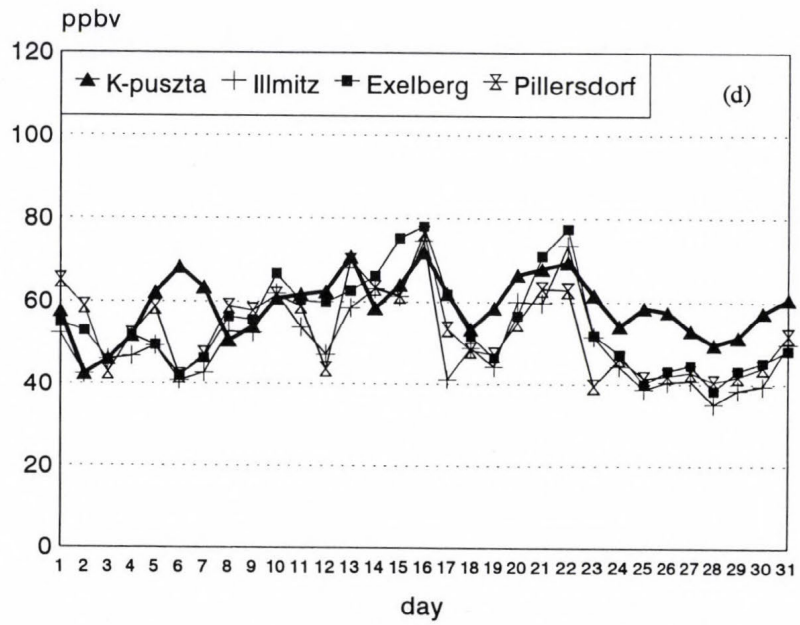

Continuation of *Fig. 3*.....(*c*) March 1992, (*d*) March 1993.

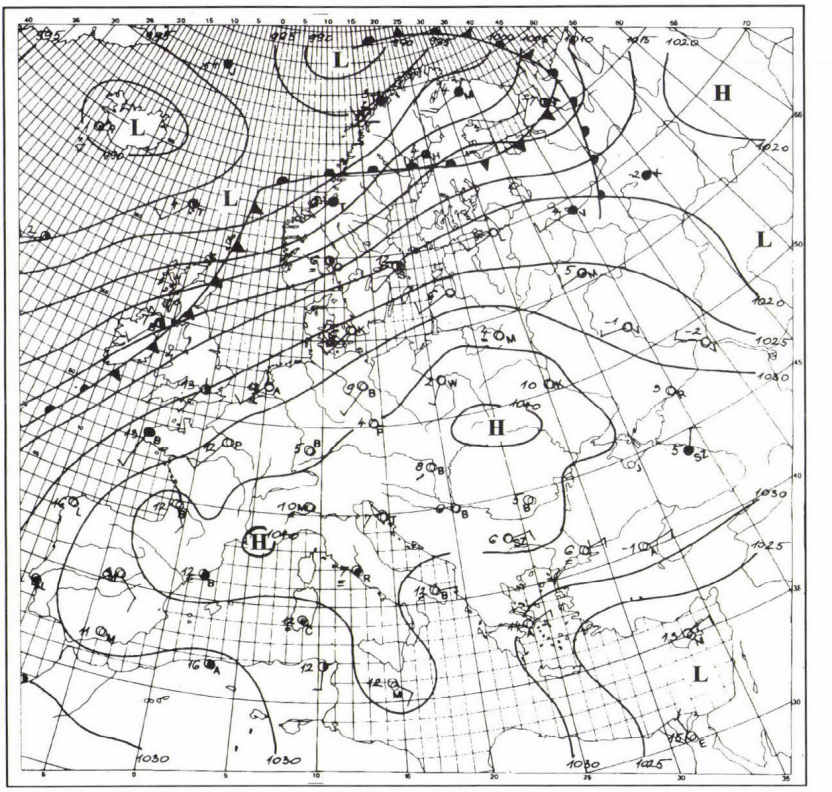

Fig. 4. Synoptic chart for 19 March, 1990, 00 UTC.

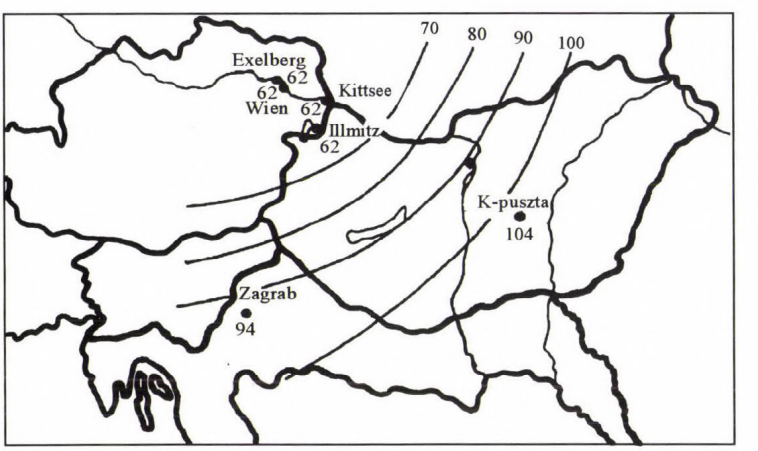

Fig. 5. Spatial distribution of the daily maximum 30 minutes ozone concentration on 19 March, 1990.

Episode 2: 15–16 March, 1991

Between 12 and 16 March a high pressure area controlled the weather in the Carpathian Basin. It resulted in a dry, a bit warmer than usual period. The accumulation of ozone in the surface layer started on 12th, however, the daily maximum concentration exceeded 60 ppbv only on 15 and 16 March. The changeable, rainy weather significantly decreased the ozone concentration after 17 March.

Episode 3: 21–24 March, 1991

Following the influence of a weak anticyclone the weather of the Carpathian Basin was determined by the forward side of a low pressure area having its centre over Western Europe. The resulted weak-to-moderate southwest air flow (later south, southeast) increased the temperature well above the usual. The dry, sunny period favoured the local ozone formation, however, the regional or long-range transport of ozone and its precursors from the sunny Southern Europe might also contribute to the high concentrations. The period was closed by the intrusion of cold air mass on the back side of the low pressure area moving slowly to east.

Episode 4: 27–28 March, 1992

Before the cold front passing over K-puszta at about 7 a.m. local time on 27 March the ozone concentration gradually increased up to 46 ppbv. However, right before the front it fell down 15 ppbv in one and a half hour. Behind the front, in spite of the early time of the day, the concentration quickly increased again and the daily maximum (55 ppbv) was reached before noon (*Fig. 6*).

The isentropic trajectory reaching K-puszta in the morning on 27 March (*Fig. 7*) reflects a remarkable transport of air from the upper troposphere (5–6000 m) to the lower layer from which it could be mixed into the surface layer. As the ozone concentration in the free troposphere increases with height (*Brühl* and *Crutzen*, 1989; *WMO*, 1990), this vertical transport might mix ozone rich air close to the ground causing the sudden increase of the ozone concentration observed.

The sunny weather on the next day promoted the local ozone formation.

Episode 5: 5–7 March, 1993

March 1993 was dry but cooler and less sunny than usual. The period of 5–7 March, which was not favourable for ozone formation in general, was characterized by moderate northerly wind. Elevated ozone concentration was observed only at K-puszta which reflects a local phenomenon. During the pe-

riod the station was covered by the plume of Budapest in which the chemical reactions might produce high amount of ozone in spite of the unfavourable photochemical condition. By means of mathematical models further studies are in progress for the determination of the essential meteorological conditions required by the significant ozone formation in the urban plume.

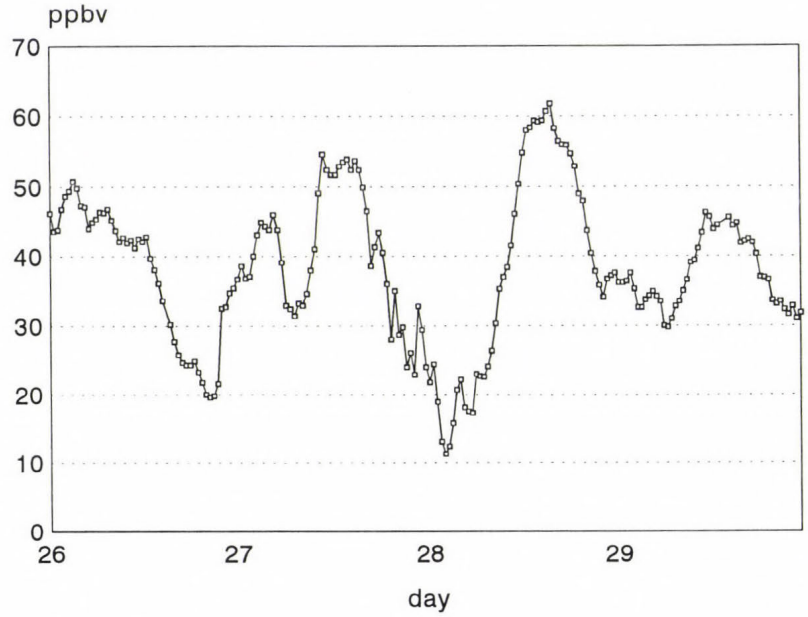

Fig. 6. Diurnal variation of ozone concentration at K-puszta, 26–29 March, 1992.

Episode 6: 10–17 March, 1993

This period was not favourable for ozone formation either. However, except for 14 March, the daily maximum concentration values at K-puszta were above 60 ppbv. The East-Austrian monitoring stations also reported elevated ozone concentrations.

During the period both the horizontal and vertical air motions were weak. The 96 h backward trajectories arrived at K-puszta originated within a region of 300–400 km around the station. Therefore, it is assumed that the regional scale ozone episode observed was the result of an accumulation process in the above region.

Episode 7: 20–23 March, 1993

After a cold front passing the Carpathian Basin on 19 March the weather was controlled by a weak anticyclone. The warm and sunny weather favoured

the oxidant formation. The accumulation process was interrupted by a cold front passing K-puszta in the afternoon on 23 March.

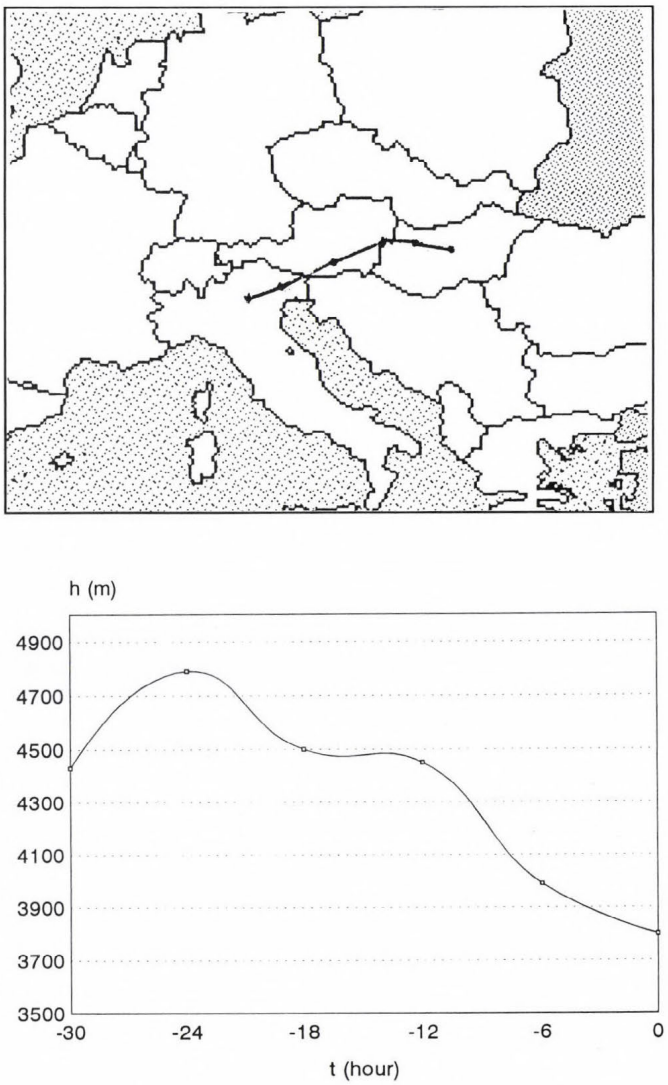

Fig. 7. (*a*) Isentropic trajectory arriving at K-puszta at 12 UTC, 27 March, 1992; (*b*) The height of the above isentropic trajectory.

3. Classification of the episodes

In the majority of the episodes presented here high ozone concentrations were formed when the weather in the Carpathian Basin was controlled by

anticyclones. The dry, sunny, calm weather characterizing these periods resulted in elevated ozone concentrations not only at K-puszta but in an extended region. This was the case in *Episodes 1, 2, 3* and *7*. The second day of *Episode 4* can also be listed here. In these cases the macrosynoptic conditions were the determining factors.

In the rest of the episodes different reasons led to elevated ozone concentration, or the reason could not be identified. On the first day of *Episode 4* the intrusion of upper tropospheric air forced by meteorological fronts can be made responsible for the high concentration. In *Episode 5* the ozone formation in the urban plume of Budapest covering the station may be the explanation for the elevated concentration. The spatially extended *Episode 6* needs further investigation.

Obviously the processes can support each other. For example, during *Episode 4* the downward ozone transport from the free troposphere contributed to the elevated ozone level on the second day when the local formation was also intensive.

Studying the relation between the macrosynoptic condition and the daily maximum ozone concentration we found that high ozone concentrations can be expected if the relative sunshine duration is larger than 60% of the potential one AND the weather is warmer than usual (deviation of the temperature from the multiannual average is positive) AND the pressure gradient remains below 1.0 hPa/100 km. On 60% of days satisfying this condition the daily maximum 30–minutes ozone concentration exceeds 60 ppbv (*Fig. 8*). The highest concentrations may occur when the weather is significantly warmer ($> 6°C$) than usual (multiannual average temperature at K-puszta is 6.5°C), the relative sunshine duration is longer than 70% of the astronomically potential one and the pressure gradient remains below 0.5 hPa/100 km. The meteorological parameters in the above condition can be forecasted reliably. This means that a significant portion of the early spring ozone episodes can also be forecasted with acceptable effectiveness.

The sunny weather alone is not enough for the formation of elevated ozone concentration. If the temperature anomaly is negative the daily maximum concentration rarely exceeds 60 ppbv (*Fig. 9*).

The meteorological conditions leading to high concentration are often satisfied when the weather of the Carpathian Basin is controlled by a high pressure area having its centre over the Basin or to the south of it. Taking into account the average frequency of occurrence of such a meteorological situation, there may be 4–5 days in March when the daily maximum concentration can be expected above 60 ppbv. In addition, every March there may be a few more days when other causes lead to ozone concentration exceeding this level at K-puszta.

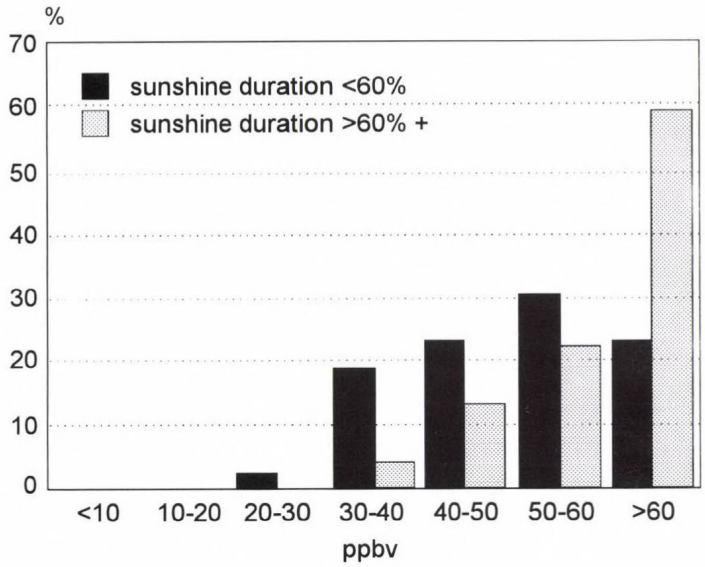

Fig. 8. Relative frequency distribution of the daily maximum 30 minutes average ozone concentration for < 60% relative sunshine duration (all cases) and for > 60% relative sunshine duration with positive temperature anomaly.

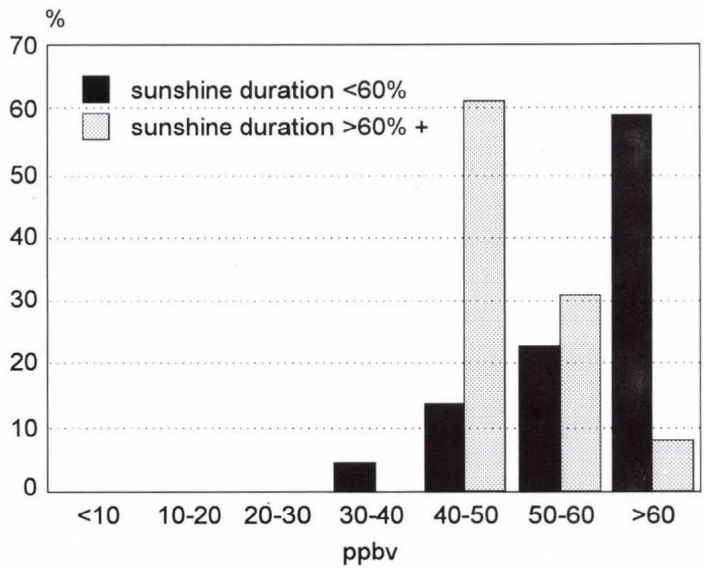

Fig. 9. Relative frequency distribution of the daily maximum 30 minutes average ozone concentration for positive and negative temperature anomaly, if the relative sunshine duration is higher than 60%.

Acknowledgements—The study was sponsored by the National Committee for Technological Development, Budapest, as part of an EUREKA/EUROTRAC/TOR contribution (PHARE ACCORD H9112-0400). The authors highly appreciate the East-Austrian and Croatian ozone data provided by *K. Radunsky* (Umweltbundesamt, Austria) and *L. Klasinc* (Ruđter Bošković Institute, Zagreb, Croatia). The isentropic trajectory was calculated by *I. Ihász* (Inst. for Atmospheric Physics, Budapest).

References

Brühl, C. and *Crutzen, P.*, 1989: On the disproportional role of tropospheric ozone as a filter against UV-B radiation. *Geophys. Res. Letters 16*, 703-706.

Ebel, A., Hass, H., Jakobs, H.J., Laube, M., Memmesheimer, M., Oberreuter, A., Geiss, H. and *Kuo, Y.-H.*, 1991: Simulation of ozone intrusion, caused by a tropopause fold and cut-off low. *Atmos. Environ. 25A*, 2131-2144.

Gruzdev, A.N. and *Sitnov, S.A.*, 1993: Tropospheric ozone annual variation and possible troposphere-stratosphere coupling in the Arctic and Antarctic as derived from ozone soundings at Resolute and Amundsen-Scott stations. *Tellus 45B*, 89-98.

Haageson, P.L., Shapiro, M.A. and *Middleton, P.*, 1981: A case study relating high ground level ozone to enhanced photochemistry and isentropic transport from the stratosphere. *J. Geophys. Res. 86*, 5231-5237.

Johnson, W.B. and *Viezee, W.*, 1981: Stratospheric ozone in the lower troposphere–I. Interpretation of aircraft measurements. *Atmos. Environ. 15*, 1309-1323.

Oberreuter, A., 1992: *Intrusion stratosphärischen Ozons in die Troposphäre durch Tropopausenfaltungen und Kaltlufttropfen.* Mitteilungen aus dem Institut für Geophysik und Meteorologie der Universität zu Köln, Köln.

Penkett, S.A. and *Brice, K.A.*, 1986: The spring maximum in photo-oxidants in the Northern Hemisphere troposphere. *Nature 319*, 655-657.

Raatz, W.E., Schnell, R.C., Shapiro, M.A., Oltmans, S.J. and *Bodhaine, B.A.*, 1985: Intrusions of stratospheric air into Alaska's troposphere, March 1983. *Atmos. Environ. 19*, 2153-2158.

Vaughan, G. and *Price, J.D.*, 1989: Ozone transport into the troposphere in a cut-off low event. Ozone in the Atmosphere. In *Proceedings of the Quadrennial Ozone Symposium 1988 and Tropospheric Ozone Workshop* (eds.: *R.D. Bojkov* and *P. Fabian*). A. Deepak, Hampton, Va., pp. 415-418.

WMO, 1990: WMO consultation on Brewer Ozone Spectrophotometer operation. Calibration and data reporting. *Global Atmosphere Watch, WMO Global Ozone Research and Monitoring Project*, No. 22.

IDŐJÁRÁS

Quarterly Journal of the Hungarian Meteorological Service
Vol. 98, No. 3, July–September 1994

Dry deposition of trace metals in Serbia: a contribution to the methodology of measurement

J. M. Marendić-Miljković, S. F. Rajšić and Z. B. Vukmirović

Institute of Physics,
Pregrevica 118, 11080 Belgrade-Zemun, Yugoslavia

(Manuscript received 22 June 1994; in final form 20 September 1994)

Abstract—An automatic wet/dry precipitation collector for trace metal deposition monitoring in rural and remote areas is constructed in the Institute of Physics, Belgrade. The aim is to simulate dry deposition to natural surfaces in order to estimate the impact of the atmospheric deposition on plants, mainly forests and crops. Dry deposition collector includes polyethylene holder, with two polycarbonate Petri dishes fixed upward and one downward-facing. This design allows both downward and upward fluxes to be measured. A timer for recording the dry period duration is also built in.

The dry deposition collector was tested in clean air of the Kopaonik mountain, Serbia, in two 5-day episodes (June and November 1991), and in Belgrade (November 1992 through October 1993). In the experiment at Kopaonik (site height 1225 m, 40 km downwind from the source), 24-hour mean fluxes were in the range of $\leq$0.02-2.44 ng m^{-2} s^{-1} for Pb, $\leq$0.02–3.5 ng m^{-2} s^{-1} for Cu, and $\leq$0.02–5.19 ng m^{-2} s^{-1} for Zn. Fluxes were very inhomogeneous: C_v (coefficient of variation of the mean) was 0.4–1.2. Ratio of the upward to downward flux, F_R was in the wide range from 0.01 to 16, more than 40% of values being $\geq$1.0. At a suburban Belgrade site, 7-day mean fluxes were measured. Average (n=38) downward fluxes were 0.40 (0.20) ng m^{-2} s^{-1} for Pb, 0.19 (0.14) for Cu, and 0.36 (0.23) ng m^{-2} s^{-1} for Zn (standard deviation in parenthesis). Fluxes were homogeneous, $\bar{C}_v$ was 0.10–0.14. $\bar{F}_R$ is found to be 0.18–0.22.

With a new-designed dry deposition collector an improvement in correspondence between dry deposition sampling and atmospheric processes is achieved.

Key-words: atmospheric deposition, dry deposition, trace metals, heavy metals, precipitation collector.

1. Introduction

It seems that dry deposition of atmospheric pollutants has lost its importance as an air quality indicator. It is not unusual that wet/dry precipitation collectors are used as wet-only collectors in routine measurements. However, measuring

dry deposition of species whose fluxes are dominated by large particles may be best conducted by assessing deposited material rather than focusing on airborne concentrations (*Davidson et al.*, 1985a; *Holsen* and *Noll*, 1992).

Although the number concentration of aerosol particles in the atmosphere is controlled by fine particles, total mass dry deposition may be dominated by sedimentation of the small fraction of coarse airborne particles. Such examples have already been documented for sulfur-containing particles (*Davidson et al.*, 1985a), as well as for Pb (*Davidson* and *Friedlander*, 1978; *Lin et al.*, 1993) and other trace metal-containing particles (*Lindberg* and *Harriss*, 1981; *Davidson et al.*, 1982).

Dry deposition measurements of trace metals are of special interest for investigation of the impact on the biosphere. For instance, deposition appears to be of particular importance in the biogeochemical cycle of Pb; nearly 100% of the estimated total growing-season flux to the forest floor can be accounted for in terms of the atmospheric deposition to the canopy alone. Besides, the estimated ratio of wet to dry deposition of Pb to the canopy during the growing season being 0.8 (*Lindberg et al.*, 1982) suggests a comparable contribution by each process. However, dry deposition of phytotoxic metals, like Pb, can be more harmful for plants than wet deposition. The reasons are longer exposition and interactions between moisture on vegetation and previously dry deposited material that can result in dissolved metal concentrations at the leaf surface which are significantly higher than those in rain alone (*Lindberg et al.*, 1982). Dry deposition measurements of trace metals can also play an important role in agriculture, in the high quality food production.

Wet/dry bucket samplers have been widely criticized (*Hicks*, 1986). Bucket samplers provide accurate measures of the dry deposition of rapidly falling particles. Questions arise regarding the performance of surrogate-surface devices used to measure deposition of small particles influenced by turbulence. An upward facing collection surface mounted above the natural surface might well collect particles carried by downdrafts, but not those carried by updrafts (*Hicks*, 1986). It has been documented that artificial collectors tend to overcollect coarse and undercollect fine particles, compared to the natural objects (*Ibrahim et al.*, 1983; *Lindberg* and *Lovett*, 1985). Efficiency of collecting coarse particles rises with the height of the vessel sides.

Considering the facts above, the need for a new designed wet/dry collector for trace metal monitoring has been imposed upon. An automatic wet/dry deposition sampler is designed in the Institute of Physics, Belgrade, to be used for trace metal deposition monitoring in rural and remote areas. Our work relies on the previous investigations of *Lindberg* and *Harriss* (1981), *Lindberg et al.* (1982), *Lindberg* and *Lovett* (1985), who also used two upward-facing polycarbonate Petri dishes in an automatic sampler of a different design. On the other hand, our experiment is related to the results of *Noll* and *Fang* (1989), *Noll et al.* (1990), who proposed a model for dry deposition of coarse particles

based on their measurements in the atmosphere. They used an aerodynamically shaped surface and measured both downward and upward fluxes. On the basis of these experiences, we constructed an original sampler and developed a method, the performances of which we still investigate.

The basic idea is to simulate dry deposition to the natural surface in order to estimate the impact of the atmospheric deposition on plants, mainly forests and crops. The construction is a compromise between an aerodynamically shaped surface and the demand of simplicity and practicability in routine use.

Both top and bottom surfaces of the vegetation leaf are exposed to the dry deposition. Bottom surface has greater aerodynamical roughness than top surface, and is not exposed to the wet deposition washout so, it is possible that deposited particles shall be retained for a longer time. Moreover, the sizes of the particles deposited on the bottom surface can significantly exceed 1 μm. At an urban site, *Noll et al.* (1988) obtained mass median diameter (MMD) of 70 μm for total particles deposited to the lower plate. *Noll* and *Fang* (1989) estimate the maximum of the deposition velocity on the bottom surface for particle sizes of 20–40 μm.

Therefore, one of the aims of this work is to emphasize the significance of the upward deposition flux measurements.

2. Experimental

2.1 Sampling

Wet and dry collectors are mounted at 2 m height (the height is adjustable) on an aluminum pole (*Fig. 1*). This height has been chosen according to the methodology of dry deposition measurement in forest clearings proposed by *Lindberg* and *Turner* (1988).

The dry deposition collector is a surrogate surface sampler with minimized aerodynamic effects of the walls. The surface is a polycarbonate Petri dish of 94-mm inner diameter with a 13-mm rim. This choice offers several advantages: low substrate background for trace elements in deposition; minimized contamination during handling due to the presence of the rim, ease of efficient extraction by using ultrasonic bath; ready availability at low cost. Besides, the small rim precludes dew and fog drip, even small amount of which result in loss of soluble components from rimless surfaces (*Lindberg* and *Lovett,* 1985). The collector consists of an especially designed holder, made of polyethylene, with two Petri dishes fixed upward-facing and one downward-facing.

An electronically operated rain shield is positioned 1 cm above Petri dishes in the closed (rain protected) position. In the open position this rain shield covers wet deposition collector, protecting the sample from dry deposition contamination.

A rain sensor, heated resistance grid, is placed at the top of the pole. Once

the rain shield is set in a closed position, it stays in that position for at least 5 min. This electronically programmed period prevents numerous opening-closing actions at the beginning of the rain events. (Most rain events begin with scattered rain drops; also, after the rain stops there is, very often, a high relative humidity which may give a false signal.)

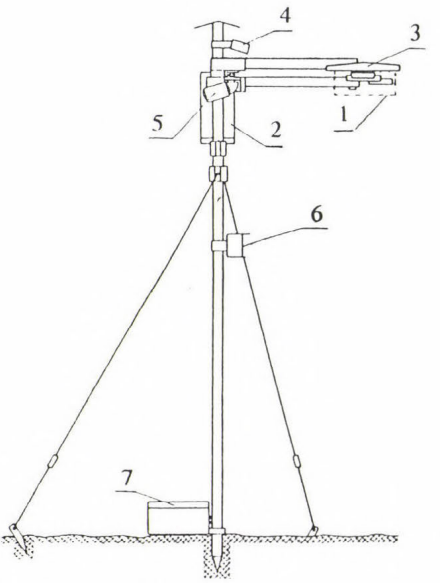

Fig. 1. Automatic wet/dry precipitation collector. (1) dry deposition collector; (2) wet deposition collector; (3) rain shield; (4) rain sensor; (5) motor; (6) control unit; (7) storage battery.

The sensing circuit also controls a timer for recording the dry period duration, expressed in minutes.

The wet deposition collector consists of polyethylene bottle with a funnel, altogether placed in a cylindric housing. A quantitative cellulose filter, fastened in the funnel, filters rainwater removing locally generated wind-blown dust, suspended in raindrops.

In order to minimize the heating and evaporation of the sample, the housing is coated with mirror layer which reflects sunlight. Funnel diameter is related to the minimum sample volume needed for analysis. For a more detailed description see *Marendić-Miljković* and *Vukmirović* (1994).

2.2 *Analytical procedures*

All of the preparatory lab work was conducted in a class 100 clean laboratory. Petri dishes were soaked for 48 hr in dilute nitric acid, and then

thoroughly rinsed with ultrapure water. The purified dishes were wrapped in polyethylene bags and sealed, to be opened just prior to use. All handling of Petri dishes was done using clean polyethylene gloves. After the sampling, dishes were packed back in bags and transported to the clean room.

Particles deposited on Petri dishes were eluted by 10 ml of 0.1 M HNO_3, (pH $\approx$ 1.2) using ultrasonic bath. Nitric acid (Merck suprapure) was diluted with the double distilled, deionized water.

The amount of particulate matter to be collected in a sampling procedure, is determined by the detection limit of the subsequent analytical technique. The analytical technique, chosen according to the aim and the object of the investigation, is one of the most sensitive for heavy metals analysis: electrochemical method named differential pulse anodic stripping voltammetry (DPASV). The instrument used was an EDT anodic stripping voltammeter, model ECP 140, with hanging mercury drop electrode. The samples were analysed for Pb, Cu, Zn and Cd, by the method of standard addition.

An important advantage of DPASV, compared to the other analytical methods, such as atomic absorption spectrometry (AAS), is that it does not contaminate the working place atmosphere with flue gases. With this feature the previously achieved high class clean-air conditions could be maintained.

In ordinary conditions the sensitivity threshold of 0.002 ng m^{-2} s^{-1} in a weekly dry event was reached for the fluxes of metals studied in this work. Consequently, the sensitivity threshold was higher in 24-hour samples for one order of magnitude. It was surprising that Cd flux was under the detection limit in Belgrade weekly samples.

2.3 Site description

The wet/dry precipitation collector made in the Institute of Physics, Belgrade, was tested in clean atmosphere of the Kopaonik mountain in two episodes (June and November 1991), and in Belgrade under the UN sanctions (November 1992 through October 1993).

The Kopaonik mountain, Serbia, (the highest peak Pančićev vrh, 43°16′21″N, 20°49′26″E, 2017 m amsl), is a 80 km long and 40–60 km wide massif, spreading in the NNW-SSE direction (*Fig. 2*). With this space and height Kopaonik is dominating surrounding area. Deep valleys of the rivers Ibar and Z. Morava surround the mountain from the west and north, while several smaller river valleys penetrate the massif laterally. Such complex orography strongly influences the flow of the air masses producing a transversal jet. Concretely, when the air flow on higher altitudes changes its direction from the S to the NW, the wind at Kopaonik will have stable SW direction, orthogonal to the ridge. These facts are connected with the unfavorable conditions of ventilation and transport of air pollutants in the valleys around Kopaonik, and their elevation from the valleys to the bigger heights (*Gburčik*, 1990).

Kopaonik is rich in ore deposition, especially lead and zinc. At the foot of the mountain there is a Lead and Zinc Refinery, with the 312 meters high stack, built in the period of 1982–1984. The stack height is projected to be greater than the inversion height in most weather situations during the whole year. It has been found that a plume from this stack impinges on the south-southwest slopes and the upper regions of Kopaonik (*Tasić* and *Vukmirović*, 1994).

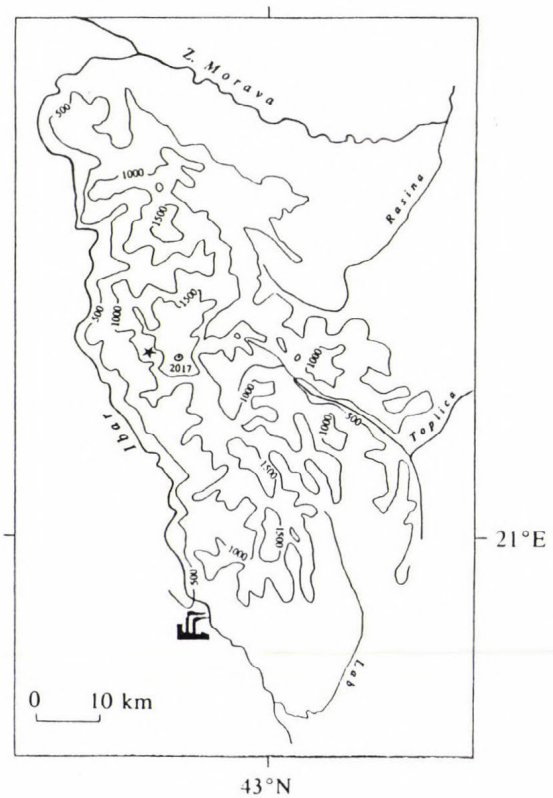

Fig. 2. The Kopaonik mountain. ★ Experimental site Glog (1225 m); ⊙ Pančićev vrh (2017 m); The Lead and Zinc Refinery is indicated as major industrial source.

In our experiment, the site was on the northwest slope of the mountain, at 1225 m amsl height, about 40 km far from the source. It is a location named Glog, in a rural area (500 m distant from little village Lisina). In the vicinity, (100 m), there is a non-asphalt road with very rare traffic. There are no local emission sources. The sampling device was placed above a grassy terrain, height of the grass was about 50 cm in June and 1 cm in November. According to *Sehmel* (1980) the aerodynamic surface roughness, $z_0 \approx 0.15$ h, was 7.5 and 0.15 cm, respectively).

In the Belgrade experiment, the site was in a recreative area of new Belgrade (44°48′N, 20°24′E). Actually, it is a large clearing in the park. It is a flat terrain at the confluence of the Sava and Danube rivers. A flat island lies in the Danube dividing the flow where it meets the Sava. The old city lies on the ridge across the Sava river. The characteristics of the air flow combining orographyc complexity, heat island effects, and changes in surface, are difficult to contemplate. The site may be classified as suburban.

3. Results and discussion

The exposure time of the downward-facing Petri dish is different from this of the upward-facing Petri dishes. While the latter are protected during the rain and fog periods, the former is exposed all the time. So, some contribution of the wet and cloud-water deposition to the total deposition on the downward-facing surface cannot be excluded.

Petri dishes with dry deposition samples were taken every day at 12^h during the episodic measurements at Kopaonik. In the Belgrade experiment Petri dishes were changed after 7 days, also at 12^h. Thus, fluxes measured at Kopaonik are 24-hour mean values, while fluxes measured in Belgrade are 7-day means.

Wind speeds in the June episode were low to moderate (daily averages were 1–4 m s^{-1}) with a stable SSW direction. Friction velocities, according to *Sehmel* (1980), were 20–50 cm s^{-1}. In the November episode the wind speeds were very low (daily av. 0.17–1.20 m s^{-1}), wind direction changed from the SSW to WSW and W. Estimated friction velocities were 2–8 cm s^{-1}.

Dry deposition fluxes obtained in two episodes at the Kopaonik site are presented in *Table 1*. There are several features to be pointed out:

(a) fluxes are generally high for the rural area (maximum value of 2.44 ng m^{-2} s^{-1} of Pb approaches urban levels);

(b) values of fluxes vary over two orders of magnitude, 24-hour mean downward fluxes were in the range of $\leq$0.02–2.44 ng m^{-2} s^{-1} for Pb, $\leq$0.02–3.5 ng m^{-2} s^{-1} for Cu, and $\leq$0.02–5.19 ng m^{-2} s^{-1} for Zn;

(c) there are significant differences between the results on two adjacent upward-facing Petri dishes, in some cases they differ in one (Pb, Cu) and even two (Zn) orders of magnitude. Obviously, fluxes were very inhomogeneous: coefficients of variation of the mean were: 0.4–0.7 for Pb; 0.4–1.1 for Cu and 1.1–1.2 for Zn (in the first episode in June 1991 besides two Petri dishes on the automatic sampler, there were additional four Petri dishes operated manually);

(d) the most interesting feature in *Table 1* is the upward flux: some of these values are extremely high, and even higher than the downward flux values; this needs an explanation.

The upward-facing surfaces generally collect more material than downward-facing ones. It was particularly surprising that in the Kopaonik experiment there

were many exceptions to the rule. In approximately 40% cases downward-facing Petri dish collected equal or more measured metals than the upward-facing dish. A particle deposition flux ratio F_R (defined as the ratio of the upward flux to the downward flux) is expected to be < 1. Values of F_R were in the vide range from 0.01 to 15, about 40% of values being ≥ 1.0. Extreme value obtained was $F_R > 15$ for Pb.

Table 1. Dry deposition fluxes. Episodes of June and November 1991, Kopaonik. The arrows indicate the direction of the flux

Date	Dry deposition flux (ng m^{-2} s^{-1})					
12^h–12^h	↓ Pb	↑	↓ Cu	↑	↓ Zn	↑
1991						
06/18–19	1.22	≤0.02	0.28	0.12	1.06	≤0.02
	2.12		0.25		1.06	
06/19–20	0.90	≤0.02	0.15	0.24	0.74	1.06
	1.22		0.29		0.74	
06/20–21	0.35	≤0.02	0.28	0.13	≤0.02	3.89
	0.23		0.06		1.53	
06/21–22	0.24	0.23	0.09	0.36	0.10	1.30
	0.59		1.81		0.84	
11/19–20	0.68	2.13	1.31	1.84	n.a.	≤0.02
	2.44		0.98		n.a.	
11/20–21	2.38	1.77	0.84	2.69	5.19	0.41
	2.32		2.26		3.84	
11/21–22	0.64	0.70	0.48	1.75	0.43	2.32
	0.64		2.27		n.a.	
11/22–23	0.74	≤0.02	0.73	0.12	0.41	≤0.02
	≤0.02		≤0.02		≤0.02	
11/23–30	0.34	0.02	0.01	0.01	0.0-	≤0.02
	0.63		0.02		80.59	

n.a. – not available
Exposure time: $1300 < t \leq 1440$ min

These characteristics are probably due to the presence of a small number of very large particles. Simultaneously measured concentration by the filtration method with two filters in series, one for coarse (> 2 μm) and an other for fine (0.35–2 μm) particles, confirmed this thesis: coarse fraction contained significantly more metals measured than fine fraction, in all samples, see

Marendić-Miljković et al., (1994). It should also be mentioned that the airborne concentrations were high too: e.g. for Pb they ranged from 27–284 ng m^{-3} (*ibid.*). Knowing that deposition velocities are much higher for coarse particles, it is expected that the mass of dry deposited metals in this experiment will be dominated by coarse particles. Moreover, fly ash coarse particles containing Pb and Zn, collected on filters, were identified by scanning electron microscopy (*Tasić* and *Vukmirović,* 1994).

In the only one 7-day sample (11/23–30 1991) there were no high values of the upward fluxes. It is possible that large particles deposited on the downward-facing Petri dish cannot hold on for a longer period of time.

High and inhomogeneous fluxes obtained at Kopaonik indicate that the sampling site is on the direct impact of a major emission source. The reason for this situation is probably by-passing of the filters, the phenomenon that could only be found in 'the Eastern Europe's Environment' (the concept introduced by *Alcamo,* 1992).

The results obtained at a suburban site in new Belgrade give a rather different image. In *Table 2* flux data of a series of 38 weekly samples, for which the exposure time is precisely determined, are presented. There were only 3 dry periods and 5 periods with unmeasurable (< 0.1 mm) precipitation. The average ratio of dry deposition exposure time to total time was 0.77 (standard deviation 0.17).

In contrast to the results from Kopaonik, in Belgrade:

(a) fluxes were low, average downward fluxes were 0.40 (0.20) ng m^{-2} s^{-1} for Pb, 0.19 (0.14) ng m^{-2} s^{-1} for Cu, and 0.36 (0.23) ng m^{-2} s^{-1} for Zn (standard deviation in parenthesis). It should be noted that in all samples the amount of Cd deposited on Petri dishes was not sufficient for analysis. Cd flux was under the detection limit of 0.02 ng m^{-2} s^{-1} for 1 day exposure time (Kopaonik) and 0.002 ng m^{-2} s^{-1} for 7 days exposure time (New Belgrade). In order to 'catch' Cd, sampling time should be increased. Low level fluxes of Pb in Belgrade are due to drastically reduced traffic and industrial activities. An overall decrease of air pollution has been noticed since UN sanctions have been imposed upon Yugoslavia;

(b) values of fluxes are more uniform, even though obtained over much longer period; fluxes are in the range 0.06–0.880 ng m^{-2} s^{-1} for Pb, 0.091-0.580 ng m^{-2} s^{-1} for Cu, and 0.054–1.068 ng m^{-2} s^{-1} for Zn;

(c) fluxes were homogeneous, flux values before March, 17 are arithmetic means of the results obtained on two Petri dishes. Coefficients of variation of the mean were: $\bar{C}_v = 0.13 \pm 0.21$ for Pb, $\bar{C}_v = 0.14 \pm 0.23$ for Cu, and $\bar{C}_v = 0.10 \pm 0.23$ for Zn (errors were calculated according to the Student's distribution, on 95% confidence level). After March, 17 only one of the two upward-facing Petri dishes was analysed, while the other was left for microscopic analysis.

Table 2. Dry deposition fluxes at the new Belgrade site (ng m^{-2} s^{-1}). The arrows indicate the direction of the flux

Period	↓ Pb	↑	↓ Cu	↑	↓ Zn	↑
1992						
11/20–27	0.621	0.066	0.507	0.032	0.782	0.045
12/02–09	0.188	0.087	0.201	0.038	0.189	0.048
12/09–16	0.204	0.021	0.144	0.011	0.667	n.a.
12/16–23	0.880	0.010	0.177	0.012	1.068	0.024
1993						
01/20–27	0.576	0.017	0.340	0.010	0.306	0.018
1/27–2/4	0.347	0.012	0.162	0.005	0.389	0.014
02/04–10	0.304	0.012	0.185	0.024	0.242	0.012
02/10–17	0.274	0.048	0.182	0.027	0.500	0.036
02/17–24	0.159	0.020	0.580	0.022	0.192	0.025
2/24–3/3	0.376	0.013	0.130	0.011	0.148	0.006
03/03–10	0.442	0.012	0.072	0.004	0.347	0.042
03/10–17*	0.45	≤0.02	0.29	≤0.02	0.34	≤0.02
03/17–24	≥0.76	0.24	0.24	≤0.02	0.25	0.24
03/24–31	0.10	≤0.02	0.06	0.045	0.78	0.06
3/31–4/7	0.74	0.10	0.145	0.025	≥0.84	0.09
04/07–14	0.36	≤0.02	0.39	≤0.02	0.10	≤0.02
04/21–28	0.40	≤0.02	≥0.60	0.03	0.20	0.04
4/28–5/5	0.41	0.12	0.17	0.07	≥0.67	0.03
05/05–12	0.52	0.09	0.19	0.05	0.45	≤0.02
05/12–19	0.12	0.10	0.055	0.04	0.30	0.04
05/19–26	0.06	0.06	0.065	0.03	0.17	0.15
5/26–6/2	0.41	0.17	0.12	0.025	0.48	0.31
06/09–16	≥0.62	0.05	0.13	0.04	0.16	≤0.02
06/23–30	0.149	0.082	0.045	0.022	0.054	0.014
07/07–14	0.245	0.034	0.081	0.012	0.248	0.014
07/14–21	0.158	0.037	0.145	0.027	0.054	0.036
07/21–28	0.138	0.030	0.060	0.025	0.279	0.032
08/04–11	0.238	0.007	0.074	0.005	0.205	0.010
08/11–18	0.311	0.008	0.091	0.007	0.307	0.007
8/25–9/1	0.188	0.005	0.065	0.006	0.263	0.005
09/01–08	0.410	0.031	0.096	0.021	0.367	0.005
09/08–15	0.354	0.021	0.137	0.012	0.072	0.026
09/15–22	0.458	0.013	0.109	0.006	0.231	0.007
09/22–29	0.369	0.014	0.099	0.026	0.104	0.008
9/29–10/6	0.797	0.297	0.379	0.059	0.571	0.049
10/06–13	0.823	0.029	0.398	0.008	0.555	0.020
10/13–20	0.376	0.037	0.139	0.016	0.327	0.032
10/20–27	0.375	0.017	0.081	0.023	0.316	0.023

n.a.– not available; * By this date till June 16 sensitivity came down

(d) in the Belgrade experiment, out of 42 weekly samples only one had equal amount of Pb on both downward and upward-facing surfaces, the other one had more (20%) Zn, and the third had 50% more Cu on the downward-facing surface. Average ratio of the mass collected on the downward-facing to the mass collected on the upward-facing Petri dish was found to be: 0.21 (0.23) for Pb; 0.25 (0.26) for Cu, and 0.21 (0.26) for Zn (standard deviation in parenthesis). Flux ratio (n = 38) was in the range 0.01–1.00 for Pb, 0.03–0.49 for Cu, and 0.02–0.88 for Zn. Only 8% of F_R values for Pb and Zn were greater than 0.5. In order to calculate mean flux ratio, only those samples with the ratio of dry to total time $\geq$ 0.75, (n = 23) have been taken into account. $\bar{F}_R$ is found to be 0.22 $\pm$ 0.54 for Pb, 0.18 $\pm$ 0.27 for Cu, and 0.20 $\pm$ 0.47 for Zn (errors were calculated according to the Student's distribution, on 95% confidence level).

Because of the boundary layer structure complexity in this location beside the river, it is difficult to comment the Table 2 in the light of meteorological conditions.

Let us again consider the paradox that Pb fluxes were higher in a rural than in an urban area. A short review of trace metal dry deposition fluxes, obtained on surrogate surfaces, is given in *Table 3*. Out of many various surfaces, only flat and Petri dishes are considered. It seems that fluxes obtained at Kopaonik are among the highest rural values in Table 3. Our results, compared to the results of other authors are closest to the results of *Lindberg et al.* (1982) and *Lindberg* and *Turner* (1988), obtained on a rural type site, exposed to acid precipitations. One should bear in mind that deposition rate on Petri dish is normally greater than on a flat surface, and that teflon flat surface would yield the smallest values (see e.g. *Davidson et al.*, 1985b). On the other hand, shortening of the exposure time from seven to only one day may also result in the higher flux values (see e.g. *Noll et al.* 1990). Nevertheless, the main cause for the extremely high flux values is the high level of the air pollution originating from smelter facilities.

There are not too many direct measurements of dry deposition trace metal fluxes reported in the literature. It is common that these fluxes are estimated from the measured airborne concentrations and modeled deposition velocities (*Lin et al.*, 1993; *Bozó et al.*, 1992; *van Daalen*, 1991; *Dulac et al.*, 1989). Various models for predicting dry deposition velocities (*Sehmel* and *Hodgson*, 1978; *Slinn* and *Slinn*, 1980; *Noll* and *Fang*, 1989) as their inputs include wind speed, atmospheric stability, surface aerodynamic roughness, particle density and particle size distribution. Such procedure is much more reliable when particle size distribution is measured too. Difficulties arise in measuring particles over 10 μm diameter which may have substantial influence on dry deposition mass (*Holsen* and *Noll*, 1992). Incomplete information about complete size distribution of atmospheric particles has a much larger influence on the prediction of flux than the use of different models to predict deposition

velocities *(ibid.)*. Models which use only fine particles concentration (even for Pb in rural areas), and MMD deposition velocity to calculate flux rate, severely underestimate the measured flux *(ibid.)*.

Table 3. Trace metal dry deposition fluxes obtained on surrogate surfaces – a review

Flux (ng m^{-2} s^{-1})	Exp (d)	Surface	Site	Reference
Pb				
<2.3			rural	*Schroeder et al.*, '87
0.13–<6			urban	(review)
0.04–0.17	4–7	polyethylene-flat	rural	*Lindberg & Harriss*, '81
2.0–10	4–11	polyethylene–Petri	rural	*Lindberg et al.*, '82
0.28		leaf		
0.0008–0.0049	7	teflon-flat	remote	*Davidson et al.*, '85b
0.028–0.047	7&14	polycarbonate–Petri	rural	*Lindberg & Turner*, '88
2.7	1	mylar-flat	urban	*Noll et al.*, '90
	5			
<0.02–2.44	1	polycarbonate–Petri	rural	this work
0.06–0.88	7		urban	
Cu				
0.38			urban	*Schroeder et al.*, '87 (review)
0.0054–0.036	7	teflon-flat	remote	*Davidson et al.*, '85b
2.0	1	mylar-flat	urban	*Noll et al.*, '90
1.1	5			
<0.02–3.5	1	polycarbonate-Petri	rural	this work
0.04–0.60	7		urban	
Zn				
<6.4			rural	*Schroeder et al.*, '87
0.17–18.8			urban	(review)
0.009–0.027	4–7	polyethylene-flat	rural	*Lindberg & Harriss*, '81
0.53–1.6	4–11	polyethylene-Petri	rural	*Lindberg et al.*, '82
0.97		leaf		
0.011–0.035	7	teflon-flat	remote	*Davidson et al.*, '85b
0.083–0.10	7&14	polycarbonate–Petri	rural	*Lindberg & Turner*, '88
6.7	1	mylar-flat	urban	*Noll et al.*, '90
4.4	5			
<0.02–5.19	1	polycarbonate–Petri	rural	this work
0.05–1.07	7		urban	

Exp – exposure time in days.

It is interesting to mention that *Bozó et al.* (1992) estimated annual average of dry deposition fluxes, for the former Yugoslavia, as follows: 0.28 ng m^{-2} s^{-1}

for Pb, 0.17 ng m^{-2} s^{-1} for Zn and 0.0073 ng m^{-2} s^{-1} for Cd. All these values are of the same order as the correspondig average values in Table 2 (i.e. 0.40 ng m^{-2} s^{-1} for Pb, 0.36 ng m^{-2} s^{-1} for Zn and $\leq 0.002 - \leq 0.02$ ng m^{-2} s^{-1} for Cd).

There are few data, obtained on surrogate surfaces in the field, concerning upward to downward flux ratio. *Dash* (1983) obtained the ratio of the downward to upward-facing results varying from about 0.2–0.5. *Holsen* and *Noll* (1992) obtained a relatively constant flux ratio of 0.3 in a suburban area of Chicago. These results agree fairly well with our results from the site in new Belgrade.

According to the dry deposition model for atmospheric coarse particles proposed by *Noll* and *Fang* (1989), flux ratio F_R is indicative for the sizes of deposited particles. When F_R is greater than 0.1 it is likely that dry deposition mass is dominated by particles having aerodynamic diameter greater than 5 μm. Another indication for coarse particles could be great dissipation of deposition flux values. Highly inhomogeneous flux may be caused by small number of very large particles.

Coe and *Lindberg* (1987) obtained mass median diameter (MMD) for total particles deposited on leaves about 10 μm; fly ash particles (NMD 2.6–3.4) having MMD of the range 5.6–11 μm. Such particles, deposited on leaves by dry deposition mechanism, are potentially harmful for plants. Especially when dissolved in contact with high acidic fog or cloud droplets. This is particularly important for forests growing above the average cloud-base height.

Plants have not developed their self-protecting system for coarse particles, like human beings and animals. So, we cannot exclude coarse particles from dry deposition monitoring, if we are interested in the trace metals impact on the biosphere.

4. Conclusions

A new designed dry (and wet) precipitation collector with Petri dishes, seems to be an improvement compared to the previous bucket-like design. It is recognized that bucket-like samplers overcollect coarse and undercollect fine particles *(Ibrahim et al. 1983)*. Trapping of coarse particles in the bucket sampler is mainly avoided by using Petri dishes with low rim. The downward-facing Petri dish yield information of the upward flux, which involves small particles influenced by turbulence. In that sense a better correspondence between dry deposition sampling and atmospheric processes is accomplished.

Two adjacent upward-facing Petri dishes give possibility of estimating the homogeneity of the flux and better accuracy of the results.

The upward flux is found to be about 20% of downward flux of Pb, Cu and Zn, for 7-day averaging time in a fairly clean air of Belgrade suburban area.

At the site on the slope of the Kopaonik mountain, which is under the impact of a Lead and Zinc Refinery, and with shorter averaging time of only one day, upward flux varied from $\leq$ 0.01 to 15.9 times downward flux. There is not enough data to estimate the mean flux ratio, but it is indicative that upward flux was greater than downward in 40% of all cases. There are two probable causes for this feature: high inhomogeneity of the flux and short averaging time. At this point, question arises regarding proper averaging time related to the dose and the receptor answer.

It is not a simple task to combine the data obtained in order to estimate the net flux to the underlying surface. Workers familiar with turbulent exchange might rely on the difference between upward and downward fluxes; it is likely that this is appropriate for smooth surfaces, like water surface. However, when the surface in question is deciduous forest in vegetational period, it may be more appropriate to take the sum of the two fluxes.

References

Alcamo, J., 1992: *Coping with Crisis in Eastern Europe's Environment.* Parthenon Publ. Group, New York.

Bozó, L., Alcamo, J., Bartnicki, J. and *Olendrzynski,K.*, 1992: Total deposition budgets of heavy metals over Eastern Europe. *Időjárás 96*, 61-80.

Coe, J.M. and *Lindberg, S.E.*, 1987: The morphology and size distribution of atmospheric particles deposited on foliage and inert surfaces. *JAPCA 37*, 237-243.

Daalen, J. van, 1991: Air quality and deposition of trace elements in the province of South-Holland. *Atmos. Environ. 25A*, 691-698.

Dash, J. M., 1983: *Precipitation Scavenging, Dry Deposition, and Resuspension.* Elsevier Press, New York, p. 883.

Davidson, C.I. and *Friedlander, S.K.*, 1978: A filtration model for aerosol dry deposition: Application to trace metal deposition from the atmosphere. *J. Geophys. Res. 83*, 2343-2352.

Davidson, C.I., Miller, J.M. and *Pleskow, M.A.*, 1982: The influence of surface structure on predicted particle dry deposition to natural grass canopies. *Water Air Soil Pollut. 18*, 25-43.

Davidson, C.I., Lindberg, S.E., Schmidt, J.A, Cartwright, L.G. and *Landis, L.R.*, 1985a: Dry deposition of sulfate onto surrogate surfaces. *J. Geophys. Res. 90(D1)*, 2123-2130.

Davidson, C.I., Goold, W.D., Mathison, T.P., Wiersma, G.B., Brown, K.W. and *Relly, M.T.*, 1985b: Airborne trace elements in Great Smoky Mountains, Olympic, and Glacier National Parks. *Environ. Sci. Technol. 19*, 27-35.

Dulac, F., Buat-Menard, P., Ezat, U., Melki, S. and *Bergametti, G.*, 1989: Atmospheric input of trace metals to the Western Mediterranean: uncertainties in modelling dry deposition from cascade impactor data. *Tellus 41B*, 362-378.

Gburčik, P., 1990: Air circulations over Kopaonik and its surroundings. *Proc. Nature of Kopaonik—Protection and Exploatation. Simp.*, Kopaonik, 19-21 April 1990, Fortuna, Beograd (in Serbian), 113-118.

Hicks, B.B., 1986: Measuring dry deposition: a re-assessment of the state of the art. *Water Air Soil Pollut. 30*, 75-90.

Holsen, T.M. and *Noll, K.E.*, 1992: Dry deposition of atmospheric particles: application ambient data. *Environ. Sci. Technol. 26*, 1807-1813.

Ibrahim, M., Barrie, L.A. and *Fanaki, F.* 1983: An experimental and theoretical investigation of the dry deposition of

particles to snow, pine trees and artificial collectors. *Atmos. Environ. 17,* 781-788.

Lin, J.-M., Fang, G.-C., Holsen, T.M. and *Noll, K.E.*, 1993: A comparison of dry deposition modeled from size distribution data and measured with a smooth surface for total particle mass, lead and calcium in Chicago. *Atmos. Environ. 27A,* 1131-1138.

Lindberg, S.E. and *Harriss, R.C.*, 1981: The role of atmospheric deposition in a deciduous forest. *Water Air Soil Pollut. 16,* 13-31.

Lindberg, S.E., Harriss, R.C. and *Turner, R.R.*, 1982: Atmospheric deposition of metals to forest vegetation. *Science 215,* 1609-1611.

Lindberg, S.E. and *Lovett, G.M.*, 1985: Field measurement of particle dry deposition rates to foliage and inert surfaces in a forest canopy. *Environ. Sci. Technol. 19,* 238-244.

Lindberg, S.E. and *Turner, R.R.*, 1988: Factors influencing atmospheric deposition, stream export, and landscape accumulation of trace metals in forested watersheds. *Water, Air and Soil Pollut. 39,* 123-156.

Marendić-Miljković, J. and *Vukmirović, Z.*, 1994: A newly designed automatic wet/-dry precipitation collector. 2nd International Symposium on Environmental Contamination in Central and Eastern Europe. Budapest, September 20-23, 1994 (accepted).

Marendić-Miljković, J., Rajšić, S. and *Vukmirović, Z.*, 1994: Calibration of the dry part of wet/dry collector in clean air. 2nd International Symposium on Environmental Contamination in Central and Eastern Europe, Budapest, September 20-23, 1994 (accepted).

Noll, K.E., Fang, K.Y.P. and *Watkins, L.A.*, 1988: Characterization of the deposition of particles from the atmosphere to a flat plate. *Atmos. Environ. 22,* 1461-1468.

Noll, K.E. and *Fang, K.Y.P.*, 1989: Development of a dry deposition model for atmospheric coarse particles. *Atmos. Environ. 23,* 585-594.

Noll, K.E., Yuen, P.F. and *Fang, K.Y.P.*, 1990: Atmospheric coarse particulate concentrations and dry deposition fluxes for ten metals in two urban environments. *Atmos. Environ. 24A,* 903-908.

Schroeder, W.H., Dobson, M., Kane, D.M. and *Johnson, N.D.*, 1987: Toxic trace elements associated with airbone particulate matter: a review. *JAPCA 37,* 1267-1285.

Sehmel, G.A. and *Hodgson, W.H.*, 1978: A model for predicting dry deposition of particles and gases to environmental surfaces. DOE Report PNL-SA-6721, Pacific Northwest Laboratory, Richland, WA.

Sehmel, G.A., 1980: Particle and gas dry deposition: a review. *Atmos. Environ. 14,* 983-1011.

Slinn, S.A. and *Slinn, W.G.N.*, 1980: Predictions for particle deposition to natural waters. *Atmos. Environ. 14,* 1013-1016.

Tasić, M. and *Vukmirović, Z.* 1994: Identification of particles emitted from a 312 meters high stack of the Lead and Zinc Refinery in Trepča. 2nd International Symposium on Environmental Contamination in Central and Eastern Europe. Budapest, September 20-23, 1994 (accepted).

IDŐJÁRÁS

Quarterly Journal of the Hungarian Meteorological Service
Vol. 98, No. 3, July–September 1994

Temporal variation of the daily extreme high precipitation in Hungary

I. Schirok-Kriston

Hungarian Meteorological Service,
P.O. Box 38, H-1525 Budapest, Hungary

(Manuscript received 5 April 1994; in final form 25 June 1994)

Abstract—This study presents an examination of the daily precipitation amounts above 30 mm during the 20th century. The basic data used consist of the 90 years (1901–1990) daily precipitation data separated into three periods of 30 years from 6 stations in Hungary. Furthermore, the daily precipitation amounts from all the raingauge network of Hungary (about 800 stations) for the period of 1961–1990 were examined as well. It can be said that the occurrence of the daily high and extreme high precipitation in Hungary during the 20th century does not show a decrease or an increase which would exceed the natural climate variability. A further examination is directed to the annual variation of the daily high precipitation. We can conclude that there is a change in timing of maximum of the frequency occurrence of the daily extreme high precipitation from early summer to the second half of summer. This change of annual variation can be related to the appearance of the seasonal change.

Key-words: climate variability and change, daily precipitation, extreme precipitation, Hungary.

1. Introduction

The global climate change has come worldwide into the limelight of interest of the specialists; and the possibility and the rate of its existence has been studied in a lot of climate models. Some large-scale climate anomalies with severe consequences and the observed changes in concentrations of some atmospheric trace gases have led to intense research in the recent 25 years. These studies include the investigation of reasons of the changes, the interactive processes within the climatic system and the climatic impacts, respectively. The results of the studies about the climate change and its possible regional consequences have been summarized in two volume of 'Climate Variability and Change' edited by *Faragó et al.* (1990, 1991).

On the one hand, these publications give a brief review of the international research activities on variability and change of climate, on the other hand, they give an account on the beginning of the research in Hungary and the first results: 'Using regional estimates for this region derived from large-scale climate scenarios by empirical-statistical methods (that is, a moderate warming of about 0.5°C in annual means which corresponds to the 'low' scenario), the preliminary estimations were concluded as follows: an increase in sunshine-duration by about 10%, decrease of annual precipitation amounts by 10–15%, reduction of frost frequencies in autumn and spring' (*Faragó et al.*, 1990). This change qualitatively corresponds to the simultaneous change in the circulation patterns (i.e., the circulation is expected to become more anticyclonic).

Besides the change of the average values (*Mika*, 1991, 1993), a big importance must be devoted to change of frequencies of the extreme meteorological events (*Schirok-Kriston*, 1983). The extreme meteorological events are risk factors, and the changes of their frequencies must be taken into account either during a durable climate variability or during a climate change. These changes can be the consequences and the indicators of the global change.

A question arises, whether any change of extreme meteorological events, the daily extreme high precipitation amounts, ensue as a result of the global climate change.

2. Data and area for the study

This study presents an examination of the daily precipitation above 30 mm during the 20th century. We use the term *high precipitation*, when the daily rainfall is above 30 mm; and the term *extreme high precipitation* when it is above 70 mm.

The basic data used in this study consist of the 90 years (1901–1990) daily precipitation data from six stations of Hungary (*Table 1*). A long series of stored and controlled daily precipitation data is available only for six stations in the climate data base of the Hungarian Meteorological Service. In our further examination the daily precipitation amounts from about 800 stations were used for the shorter period of 1961–1990.

3. Occurrence of daily high precipitation

Table 1 shows the absolute frequencies of the daily high precipitation above 30, 40, 50, 70 and 80 mm, which were recorded by six stations between 1901–1990. The numbers of the last two column including the daily high precipitation of 30 and 40 mm are related to the regional climatological distribution of the precipitation: the precipitation of 30 and 40 mm in Sopron (West–Hungary)

Table 1. The absolute frequencies of the daily high and extreme high precipitation above 30, 40, 50, 70 and 80 mm in Hungary between 1901–1990

Station	≥ 80	≥ 70	≥ 50	≥ 40	≥ 30
Sopron	2	6	32	87	205
Budapest	1	4	15	41	138
Pécs	1	4	22	50	147
Szeged	–	–	10	34	110
Debrecen	1	2	18	43	103
Miskolc	2	2	27	56	151
Σ	7	18	124	311	854

occurs twice more than in Debrecen representing the Great Hungarian Plain, poorly supplied with rain. This regional difference disappears in case of the daily high and extreme high precipitation above 50 mm.

Since our aim is to examine, whether any change of the frequent occurrence of the daily high precipitation in Hungary during the 20th century exists or not, it is reasonable to separate the data of Table 1 during 1901–1990 into three periods of 30 years. *Table 2* shows the absolute frequency of the daily high and extreme high precipitation above 30, 40, 50, 70 and 80 mm recorded by six stations between 1901–1930, 1931–1960 and 1961–1990, respectively. The numbers (percentages) in the last line of Table 2 show all the observations of six stations during 1901–1990, which are distributed into the three periods of 30 years. The percentage is insignificant when the occurrence of the daily extreme high precipitation is very low. Therefore the first and second coloums of the last line are empty within the three periods. Furthermore, it can be seen that 30–36 percent of all cases falls into each three 30-year periods. It is unnecessary to make a significance test to decide whether does any increase or decrease of occurrence of the daily high precipitation take place. The answer is unambiguous, it can not be verified with statistical methods.

Had we made a comparison only between the observations of the last 30-yearly period (1961–1990) and the data of the directly preceeding 30-yearly period (1931–1960), we would have come to an other conclusion (*Table 3*). In this case, we should have come to the conclusion that the difference between the percentage of the two 30-yearly periods during 1931–1990 are 6–8%.

The beginning third of the century was followed by a second 30-year period with a lot of cases of daily high precipitation. Occurrence of the daily high precipitation was less frequent in the latest 30-year period than in the beginning

Table 2. The absolute frequencies of the daily high and extremely high precipitation

Station	1901–1930					1931–1960					1961–1990				
	≥ 80 mm	≥ 70 mm	≥ 50 mm	≥ 40 mm	≥ 30 mm	≥ 80 mm	≥ 70 mm	≥ 50 mm	≥ 40 mm	≥ 30 mm	≥ 80 mm	≥ 70 mm	≥ 50 mm	≥ 40 mm	≥ 30 mm
Sopron	2	3	11	41	80	–	1	13	24	69	–	2	8	22	56
Budapest	–	–	6	15	45	1	3	3	14	53	–	1	6	12	40
Pécs	–	–	4	19	53	–	2	10	15	46	1	2	8	16	48
Szeged	–	–	2	7	33	–	–	3	19	45	–	–	5	8	32
Debrecen	–	–	3	8	26	–	–	5	15	30	1	2	10	20	47
Miskolc	1	1	13	20	48	1	1	11	22	59	–	–	3	14	44
Σ	3	4	**39**	110	285	2	7	**45**	109	302	2	7	**40**	92	267
%	–	–	**31.4**	35.4	33.4	–	–	**36.3**	35.0	35.4	–	–	**32.3**	29.6	31.2

third of the century. But the number of flash floods was much lower in the latest 30-year period (between 1961–1990) than in the period of the middle of the century (between 1931–1960).

Table 3. The absolute and relative frequencies of the daily high precipitation in Hungary

	1931–1960			1961–1990		
	≥ 50 mm	≥ 40 mm	≥ 30 mm	≥ 50 mm	≥ 40 mm	≥ 30 mm
Σ	45	109	302	40	92	267
%	53	54	53	47	46	47

4. Occurrence of the days of high precipitation

The climate data base of the Hungarian Meteorological Service gives a long series of data only for six stations. We should like to use all the raingauge observations, but those are available only from 1951 in our computerized data bank. The quantity of the data earlier used is shown in Table 1. For the six stations the summed numbers of cases with daily precipitation above 80 mm are

7, above 70 mm: 18, and above 50 mm: 124. These case numbers are not enough for further examination.

It was reasonable to rely on *Péczely*'s (1962) work, who studied the occurrence of daily precipitation above 80 mm, during 1931–1960, in all the raingauge network of Hungary. In this study the daily precipitation amounts from about 800 stations were examined for the periods of 1961–1990.

Table 4 shows the absolute frequencies specified for 10 mm intervals of the daily precipitation above 80 mm on the whole territory of Hungary during 1931–1960 (after *Péczely*) and during 1961–1990, as well. From the earlier period to the latter one, the number of cases of daily precipitation above 80 mm reduces from 521 to 417, that makes 20 percent. It seems that the decrease of the event's number appears almost uniformly at all intervals.

Table 4. The absolute frequencies specified for 10 mm intervals of the daily precipitation above 80 mm based on 800 stations in Hungary during 1931–1960 (after Péczely) and during 1961–1990

Intervals	1931–1960	1961–1990
81– 90 mm	241 cases	208 cases
91–100 mm	128 cases	101 cases
101–110 mm	56 cases	42 cases
111–120 mm	42 cases	29 cases
121–130 mm	24 cases	15 cases
131–140 mm	15 cases	6 cases
141–150 mm	5 cases	5 cases
151–160 mm	4 cases	4 cases
161–170 mm	2 cases	3 cases
171–180 mm	1 case	2 cases
181–190 mm	–	–
191–200 mm	2 cases	1 case
201–210 mm	–	1 case
...	–	–
251–260 mm	1 case	–
All cases	521 cases	417 cases

In *Table 5* the daily precipitations above 150 mm during 1961–1990 are listed. The date of 8 cases from the 11 extremes is: September 8, 1963. The date of 63 cases from the all 417 extremes during 1961–1990 is September 8, 1963, as well.

Furthermore, we introduced a new term: *the day of high precipitation above a given precipitation amount*. The definition is as follows: if the daily precipitation above a given precipitation amount (80, 70, ... or 30 mm) is observed at least at *one* station from all raingauge stations of the country, this day is referred as *high precipitation's day*. Accordingly, during the 1961–1990 period only 4 days may be named *extreme high precipitation's days above 150 mm*.

Table 5. List of the daily precipitation above 150 mm in Hungary during 1961–1990

Stations	Daily precipitation (mm)	Date
Gyömrő	203	Sep 8, 1963
Hatvan	191	Jul 27, 1963
Kartal	176	Sep 8, 1963
Mende	173	Sep 8, 1963
Apostag	168	Jul 26, 1982
Valkó	163	Sep 8, 1963
Isaszeg	162	Sep 8, 1963
Ócsa-Felsőbabád	158	Sep 8, 1963
Parádsasvár	156	Aug 3, 1974
Ócsa	154	Sep 8, 1963
Csévharaszt	151	Sep 8, 1963

In this way, the information-content of the original data significantly decreases, so that we can not say anything about all the precipitation amounts of the high precipitation's days, and the territorial extension of flash floods, respectively.

Table 6 shows the numbers of cases of daily precipitation above 30, 40, ... 150 mm, and the numbers of high *precipitation's days* above given values, during 1961–1990. The extension of rainfall above 30 mm is large enough, so it may be observed at a lot of raingauge stations. Had we did not consider the territorial extension of precipitation, the number of cases between 1961–1990 would have reduced from 36,059 to 1,991, that makes 5.5 percent. The territorial extension of the extreme high precipitations producing flash floods is smaller, so the differences between the two columns in Table 6, aren't as big as in the case of lower precipitation.

To reproduce such a table for the period of 1931–1960, after *Péczely*'s

study was impossible. But *Péczely* had made the data independent from the density change of raingauge stations. This gave possibility to ascertain the number of days called *extreme high precipitation's days above 80 mm* during 1931-1960 based on his figure, that is 162.

The number of extreme high *precipitation's days* above 80 mm is 167 during 1961–1990. Consequently, had we disregarded the territorial extension of precipitation, and had we examined only its frequency distribution in country, we would have established more occurrence of extreme high precipitation's day above 80 mm in the latest 30-yearly period (between 1961–1990) than in the middle period of the century (between 1931–1960).

Table 6. The absolute frequencies of the number of all cases of daily precipitation and the number of precipitation's days above 30 mm in Hungary during 1961–1990

Threshold (mm)	Cases	Precipitation's days
> 30	36,059	1,991
> 40	12,840	1,223
> 50	5,010	763
> 60	2,034	457
> 70	897	273
> 80	**417**	**167**
> 90	209	95
> 100	108	54
> 110	66	31
> 120	37	14
> 130	22	6
> 140	16	5
> 150	11	4

We have come to the conclusions based on results in Table 4 that the number of cases of daily extreme high precipitation above 80 mm reduces by 20 percent (from 521 to 417), and after aforesaid establishments that the occurrence of extreme high *precipitation's day* above 80 mm grows from 162 to 167. But these deviations are not considerable. Furthermore, it can be said that *the occurrence of the daily high and extreme high precipitation in Hungary during the 20th century does not show a decrease or an increase which would exceed the natural climate variability.*

5. Annual variation of the daily high precipitation

Our further examination is directed to the annual variation of the daily high precipitation. We have examined its monthly frequency occurrences. The relative frequencies of monthly occurrence of the daily extreme high precipitation above 80 mm are shown in *Fig. 1*, between 1931–1960 (after *Péczely*) and 1961–1990 according to our investigation. Fig. 1 also indicates the relative frequencies of numbers of all cases (527 and 417 cases). The 70 percent of the daily extreme high precipitation (examined by *Péczely*) has fallen in June-July, and its 93 percent in May-August, between 1931–1960. Their annual variation distorts towards the left, it suddenly rises and slowly damps. The annual variation of the daily extreme high precipitation in the period of 1961–1990 shows symmetry: more than half of all cases occurred in July-August (nearly at the same rate), and 93 percent was found in 4 months, from June to September. It seems that in the annual variation of the daily high precipitation there is one-monthly discrepancy. However, we have to consider that data of all observations are taken into account, for example September 8, 1963 is included when 63 stations reported extreme precipitation.

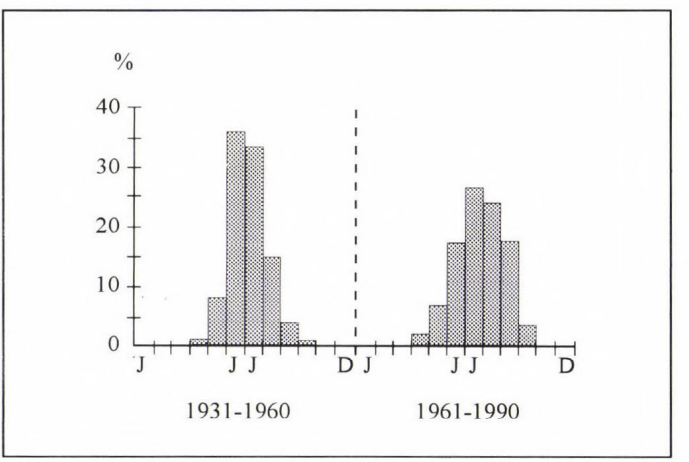

Fig. 1. The relative frequencies of monthly occurrence of the daily extreme high precipitation above 80 mm in Hungary during 1931–1960 (after *Péczely*) and 1961–1990 (present study).

Fig. 2 shows the relative frequencies of monthly occurrence of the *precipitaton's days* above 50, 60, 70, 80, 90 and 100 mm, between 1961–1990. Here, the extreme precipitation amounts observed in the same days on several stations have not been taken into account with multiple weight. In Fig. 2 the maxima of the histograms fall in July-August, and they represent a greater

frequency with increasing of extremity. So, we can conclude that there is a change in timing of maximum of the frequency occurrence of the daily extreme high precipitation from early summer to the second half of summer. This change of annual variation can be related to the appearance of the seasonal change.

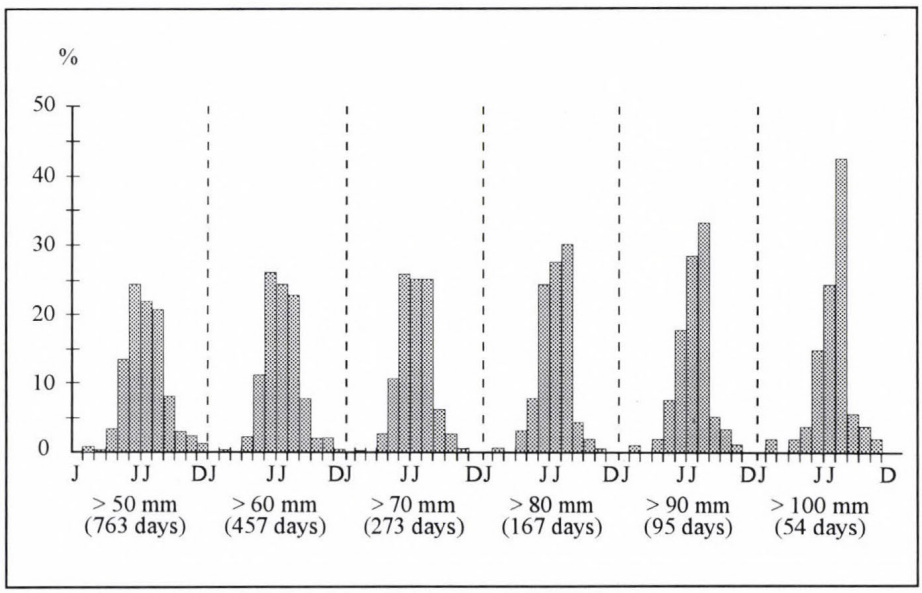

Fig. 2. The relative frequencies of monthly occurrence of the precipitation's days above various thresholds in Hungary during 1961–1990.

Acknowledgements—The author wishes to thank *T. Tänczer* for revising this manuscript. This paper was supported by contract OTKA-443 with the Hungarian Academy of Sciences.

References

Faragó, T., Iványi, Zs. and *Szalai, S.* (eds.), 1990, 1991: Climate variability and change, Vol. I., Vol. II. (in Hungarian). Környezetvéd. és Területfejl. Min., Orsz. Meteorológiai Szolgálat, Budapest.

Mika, J., 1991: Regional features of a stronger global warming over Hungary (in Hungarian). *Időjárás 95*, 265-278.

Mika, J., 1993: Effects of the large-scale circulation on local climate anomalies in relation to GCM outputs. *Időjárás 97*, 21-34.

Péczely, G., 1962: Frequency of the daily precipitation above 80 mm in Hungary (in Hungarian). *Időjárás 66*, 197-204.

Schirok-Kriston, I., 1983: Frequency analysis of storm rainfalls and estimation of the probable maximum precipitation (in Hungarian). Vízügyi Közlemények LXV., 167-187.

BOOK REVIEWS

Frakes, L. A., Francis, J. E. and *Syktus, J. I.:* **Climate Modes of the Phanerozoic**. Cambridge University Press, 1992. pp. 272, 11 chapters.

This book first describes, in a concise way, the salient features of Earth climates over the last 600 mil. years. With this background information in hand its purpose is to recognize and then compare similar climatic states in history. So the changes in the Earth's climate from the Cambrian (partly late Precambrian as well) to Quaternary come under scrutiny in this book. Geological evidence for ancient climates is examined, such as the distribution of climate-sensitive sediments, including coals, evaporites, and glacial deposited.

The Earth's climate has changed many times throughout the Phanerozoic. Thus in this book the climate history has been divided into Warm and Cool Modes, intervals when either the Earth was in a 'greenhouse' state with higher levels of atmospheric CO_2 and polar regions free of ice, or the global climate was cooler and ice was present in high latitudes.

The Cool Modes are defined as times of global refrigeration during which the polar regions were covered by large permanent ice caps or when the high-latitude regions were only seasonally sufficiently cold for the formation of ice during winter. The record of ancient glaciations, represented by such well-known features as tillites, striated pavements, is not difficult to confirm.

The Warm Modes are defined as times when climates were globally warm, as indicated by abundance of evaporites, geochemical data, faunal distribution, and little or no polar ice. As more climate data are collected in future, it may be shown that these divisions into climate modes are far too simple or completely wrong—write the authors. Because these Modes span rather long intervals of approximately 150 mil. years, they do include brief intervals of contrasting climates.

What are the causes of climate change? The studies presented here highlight the complex interactions between the carbon cycle, continental distribution, tectonics, sea level variations, ocean circulation and temperature change as well as other parameters. In particular, the potential of the carbon isotope records as an important signal of the past climates of Earth is explored.

The book consists of eleven, most of them describing the Warm and Cool Modes in chronological order. At the end of the book, there are approximately 850 references, but excluding such authors as *M. Schwarzbach, W. Köppen, A. Wegener, H. Lamb* and others.

G. Koppány

Houghton, J.: **Global Warming. The Complete Briefing.** Lion Publishing, Oxford, 1994. pp. 192, 12 chapters.

Sir John Houghton, the author of this book, is co-chairman of the Science Assessment Working Group of the Intergovernment Panel on Climate Change (IPCC), chairman of the Royal Commission on Environmental Pollution, and a member of the British Government's Panel on Sustainable Development. Besides: his name is well-known in meteorological literature, he has published a great number of excellent books and papers.

The book consists of twelve chapters, a very useful and up to date glossary including references to UN Conference on Environment and Development at Rio de Janeiro in June 1992, and an index. Perhaps the most important initiatory facts of writing this book have been as follow.

For the Earth as a whole, seven of eight warmest years on record have occurred in the 1980-s and early 1990-s. The storm which swept western Europe in October 1987 was the worst in the area since 1703. In 1988 the highest flood levels recorded affected 80 per cent of Bangladesh.

There is a consensus among the world scientific community about the fact of global warming, but there is fierce debate about the scale of the problem and what, if anything, should be done about it. This important new book—the most comprehensive work ever written on the subject for a non-specialist readership—moves no debate on.

The author explores the whole theory of global warming and sets out the findings of the world scientific community. His clear exposition of current scientific understanding, including the uncertainties, provides a balanced account which will be welcomed by students and general readers alike. The author uses the latest research to investigate the likely consequences of the world's current course if no action would be taken.

This book addresses the questions that lie at the heart of political and social concern about the environment. Is the current lifestyle of modern, industrial society sustainable? What kind of world will our grandchildren inherit?

G. Koppány

NEWS

Joint Meeting on Global Atmospheric Chemistry

The Commission on Atmospheric Chemistry and Global Pollution (CACGP) of the International Association of Meteorology and Atmospheric Physics and the International Global Atmospheric Chemistry Project (IGAC) of the International Geosphere-Biosphere Programme held a joint conference in Fuji-Yoshida (Japan) between September 5 and 9, 1994. This was the 8th regular conference of CACGP, while the meeting was the second in a series initiated by IGAC. The host organization was the Department of Earth and Planetary Physics of the University of Tokyo headed by *T. Ogawa*. Into the conference program (chairman of the Program Committee: *S. A. Penkett, U.K.*) the following sessions were included: (1) Greenhouse Gases; (2) Tropospheric Ozone; (3) Sulfur and Nitrogen Cycles; and (4) Aerosol and Cloud Chemistry. While many lectures were given orally, the major part of the papers was presented on posters.

The lectures of the first session made it clear that the global concentration of some greenhouse gases has decreased or at least it has been stabilized during the last years. This very important fact is observed mainly in the level of methane, carbon monoxide and some freons. It was a great discussion, without final conclusions, about the possible reasons for these observations. Thus, it was proposed that this phenomenon is due to the decrease of emissions, to changes in oxidation capacity of the atmosphere or to the modifications of global atmospheric circulation. Many new observational facts were presented at the conference on tropospheric ozone. These measurements were carried out in areas where our knowledge was rather poor like the North Atlantic, South Atlantic and several African regions. These latter programs were mainly made to gain further evidences concerning the effects of biomass burning on the ozone formation in the troposphere.

The session on sulfur and nitrogen cycles was mainly devoted to problems (e.g. acidity) in Asia and to the role of oceanic biogenic sulfur emission in the control of the global sulfur budget. Some new precipitation chemistry data were discussed, based on samplings in Asian regions (e.g. Siberia, Thailand) not yet studied. Among other things the main aim of the last session was to evaluate the possible role of anthropogenic aerosol particles in the climate variations. It was concluded that sulfate particles caused by fossil fuel burning will regionally reduce the effects of man-made greenhouse gases in industrialized areas (north-eastern part of North America, Europe and China). Further research is needed, however, to confirm this conclusion.

The organization of the conference was excellent. About 250 participants from all over the world enjoyed not only the scientific presentations—partly from high levelled Japanese scientists—, but also the beautiful environment of the Fuji mountain and the warm Japanese hospitality. It was a good decision to hold for the first time the conference of CACGP outside Europe and North America.

At the conference it was announced that the next scientific meeting of CACGP will take place in Seattle, Washington (U.S.A.) during 1998. Finally, one has to note that new officers and members were elected by CACGP. The new president is *I. Galbally* (Australia), while the commission secretary is *L. A. Barry* (Canada).

E. Mészáros

ATMOSPHERIC ENVIRONMENT

an international journal

To promote the distribution of Atmospheric Environment *Időjárás* publishes regularly the *contents* of this important journal. For further information the interested reader is asked to contact *Dr. P. Brimblecombe,* School for Environmental Sciences, University of East Anglia, Norwich NR 7TJ, U.K.

Volume 28 Number 7 1994

Volume 28 Number 8 1994

The Glen E. Gordon Memorial Issue

A.E. Sheffield, G.E. Gordon, L.A. Currie and *G.E. Riederer*: Organic, elemental, and isotopic tracers of air pollution sources in Albuquerque, NM, 1371-1384.

Xudong Huang, I. Olmez, N.K. Aras and *G.E. Gordon*: Emissions of trace elements from motor vehicles: potential marker elements and source composition profile, 1385-1391.

M.S. Germani and *W.H. Zoller*: Solubilities of elements on in-stack suspended particles from a municipal incinerator, 1393-1400.

D.L. Anderson, M.E. Kitto, L. McCarthy and *W.H. Zoller*: Sources and atmospheric distribution of particulate and gas-phase boron, 1401-1410.

D.M. Glover and *P.K. Hopke*: Exploration of multivariate atmospheric particulate compositional data by projection pursuit, 1411-1424.

M.P. Zelenka, W.E. Wilson, J.C. Chow and *P.J. Lioy*: A combined TTFA/CMB receptor modeling approach and its application to air pollution sources in China, 1425-1435.

Y. Hashimoto, Y. Sekine, Hui Kang Kim, Zong Liang Chen and *Zhi Min Yang*: Atmospheric fingerprints of East Asia, 1986-1991. An urgent record of aerosol analysis by the JACK Network, 1437-1445.

Ning Gao, Meng-Dawn Cheng and *P.K. Hopke*: Receptor modeling of airborne ionic species collected in SCAQS, 1447-1470.

Zhong Yu Wu, Ming Han, Zhi Chao Lin and *J.M. Ondov*: Chesapeake Bay atmospheric deposition study, Year 1: sources and dry deposition of selected elements in aerosol particles, 1471-1486.

J.R. Scudlark, K.M. Conko and *T.M. Church*: Atmospheric wet deposition of trace elements to chesapeake Bay: CBAD Study Year 1 results, 1487-1498.

D.L. Leister and *J.E. Baker*: Atmospheric deposition of organic contaminants to the Chesapeake Bay, 1499-1520.

E.G. Burkhard, V.A. Dutkiewicz and *L. Husain*: A study of SO_2, SO_4^{2-} and trace elements in clear air and clouds above the midwestern United States, 1521-1533.

G.J. Keeler and *W.R. Pierson*: Regional trace element and sulfate transport, 1535-1548.

N.Z. Heidam: Arctic aerosol factor models: validation by marginally detected elements, 1549-1555.

F.A. Akeredolu, L.A. Barrie, M.P. Olson, K.K. Olkawa, J.M. Pacyna and *G.J. Keeler*: The flux of anthropogenic trace metals into the Arctic from the mid-latitudes in 1979/80, 1557-1572.

Volume 28 Number 9 1994

A. Malyschew, H.-J. Schmidt, K.G. Weil and *P. Hoffmann*: Methods for characterization of colloid particles in rain water, 1575-1581.

H. Skov, Th. Benter, R.N. Schindler, J. Hjorth and *G. Restelli*: Epoxide formation in the reactions of the nitrate radical with 2,3-dimethyl-2-butene, *cis*- and *trans*-2-butene and isoprene, 1583-1592.

R.M. Harrison, M.I. Msibi, A.-M. N. Kitto and *S. Yamulki*: Atmospheric chemical transformations of nitrogen compounds measured in the North Sea Experimental, September 1991, 1593-1599.

A.C. Comrie: A synoptic climatology of rural ozone pollution at three forest sites in Pennsylvania, 1601-1614.

I.Y. Lee and *H.M. Park*: Comparison of microphysics parameterizations in a three-dimensional dynamic cloud model, 1615-1625.

S. Kutsuna, M. Kasuda and *T. Ibusuki*: Transformation and decomposition of 1,1,1-trichloroethane on titanium dioxide in the dark and under photoillumination, 1627-1631.

R. Bellasio and *M. Tamponi*: MDGP: a new Eulerian 3D unsteady state model for heavy gas dispersion, 1633-1643.

S. Loranger and *J. Zayed*: Manganese and lead concentrations in ambient air and emission rates from unleaded and leaded gasoline between 1981 and 1992 in Canada: a comparative study, 1645-1651.

Volume 28 Number 10 1994

Volume 28 Number 11 1994

5th International Wind and Water Tunnel Dispersion Modelling Workshop, 30 October–1 November, 1991, Warren Spring Laboratory, Stevenage, U.K.

Volume 28 Number 12 1994

Volume 28 Number 13 1994

The Kuwaiti Oil Fires

Short Communication

NOTES TO CONTRIBUTORS

The purpose of *Időjárás* is to publish papers in the field of theoretical and applied meteorology. These may be reports on new results of scientific investigations, critical review articles summarizing current problems in certain subject, or shorter contributions dealing with a specific question. Authors may be of any nationality but papers are published only in English.

Papers will be subjected to constructive criticism by unidentified referees.

* * *

The manuscript should meet the following formal requirements:

Title should contain the title of the paper, the names(s) of the author(s) with indication of the name and address of employment.

The title should be followed by an *abstract* containing the aim, method and conclusions of the scientific investigation. After the abstract, the *key-words* of the content of the paper must be given.

Three copies of the manuscript, typed with double space, should be sent to the Editor-in-Chief: *P.O. Box 39, H-1675 Budapest,* Hungary.

References: The text citation should contain the name(s) of the author(s) in Italic letter or underlined and the year of publication. In case of one author: *Miller* (1989), or if the name of the author cannot be fitted into the text: *(Miller,* 1989); in the case of two authors: *Gamov* and *Cleveland* (1973); if there are more than two authors: *Smith et al.* (1990). When referring to several papers published in the same year by the same author, the year of publication should be followed by letters a,b etc. At the end of the paper the list of references should be arranged alphabetically. For an article: the name(s) of author(s) in Italics or underlined, year, title of article, name of journal, volume number (the latter two in Italics or underlined) and pages. E.g. *Nathan, K. K.,* 1986: A note on the relationship between photosynthetically active radiation and cloud amount. *Időjárás 90,* 10-13. For a book: the name(s) of author(s), year, title of the book (all in Italics or underlined with except of the year), publisher and place of publication. E.g. *Junge, C. E.,* 1963: *Air Chemistry and Radioactivity.* Academic Press, New York and London.

Figures should be prepared entirely in black India ink upon transparent paper or copied by a good quality copier. A series of figures should be attached to each copy of the manuscript. The legends of figures should be given on a separate sheet. Photographs of good quality may be provided in black and white.

Tables should be marked by Arabic numbers and provided on separate sheets together with relevant captions. In one table the column number is maximum 13 if possible. One column should not contain more than five characters.

Mathematical formulas and *symbols:* non-Latin letters and hand-written marks should be explained by making marginal notes in pencil.

The final text should be submitted both in manuscript form and on *diskette.* Use standard 3.5" or 5.25" DOS formatted diskettes for this purpose. The following word processors are supported: WordPerfect 5.1, WordPerfect for Windows 5.1, Microsoft Word 5.5, Microsoft Word for Windows 2.0. In all other cases the preferred text format is ASCII.

* * *

Authors receive 30 *reprints* free of charge. Additional reprints may be ordered at the authors' expense when sending back the proofs to the Editorial Office.

Published by the Hungarian Meteorological Service

Budapest, Hungary

INDEX: 26 361

HU ISSN 0324-6329

IDŐJÁRÁS

QUARTERLY JOURNAL
OF THE HUNGARIAN METEOROLOGICAL SERVICE

CONTENTS

VOL. 98 * NO. 4 * OCTOBER–DECEMBER 1994

IDŐJÁRÁS

Quarterly Journal of the Hungarian Meteorological Service

Editor-in-Chief
E. MÉSZÁROS

Editor
T. TÄNCZER

Technical Editor
Mrs. M. ANTAL

Editorial Office: P.O. Box 39, H–1675 Budapest

Subscription from customers in Hungary should be sent to the Financial Department of the Hungarian Meteorological Service Kitaibel Pál u. 1, 1024 Budapest. The subscription rate is HUF 2000.

Abroad the journal can be purchased from the distributor: KULTURA, P.O. Box 149, H–1389 Budapest. The annual subscription rate is USD 56.

IDŐJÁRÁS

Quarterly Journal of the Hungarian Meteorological Service
Vol. 98, No. 4, October–December 1994

Recalculation of EMEP photolysis rates as a function of total ozone using LOWTRAN 7 code

D. Bilčík[1], **E. Závodská**[1] and **D. Závodský**[2]

[1] *Geophysical Institute of Slovak Academy of Sciences,*
842 28 Bratislava, Dúbravská cesta 9, Slovakia
[2] *Slovak Hydrometeorological Institute,*
833 15 Bratislava, Jeséniova 17, Slovakia

(Manuscript received 3 May 1994; in final form 18 July 1994)

Abstract—The results of photolysis rates calculation as a function of both the total ozone amount and the solar zenith angle for the EMEP photochemical reactions set are presented. To calculate actinic flux the computer code LOWTRAN 7 was used. The regression expressions were derived to specify the photodissociation rate dependence upon total ozone amount for each of reactions considered.

Key-words: actinic flux, photodissociation rate, total ozone amount.

1. Introduction

Ozone and other photochemical oxidants are natural constituents of the atmosphere. About 90% of the atmospheric ozone is found in the stratosphere. It absorbs most of the solar ultraviolet radiation (UV) before the troposphere is reached. The sources of the tropospheric ozone are influxes from the stratosphere and photochemical production involving nitrogen oxides, hydrocarbons and carbon monoxide from natural and anthropogenic sources.

Up to about 1970 it was thought that photochemical air pollution was concentrated mainly to some urban areas, while the abundance of the tropospheric ozone was predominantly controlled by natural processes. Today is well established that the growing tropospheric ozone level, the most pronounced in middle latitudes of the Northern Hemisphere, results from the increasing emissions of the anthropogenic ozone precursors (*Bojkov,* 1993).

Elevated ozone concentrations are produced by a complex series of the photo and thermal chemical reactions. The representation of these complex reactions is not straightforward in chemical computer models because of the widespread spatial distribution of the precursors and because of the many hundreds of chemical species and reactions believed to be involved. Nevertheless, despite of their apparent complexity, the computer models appear to offer the only approach to gaining the necessary understanding of the ozone creation process and to accepting a national ozone control strategy.

Perturbations to stratospheric O_3 and resulting increase of the UV solar radiation also significantly influence the rates of the key tropospheric photochemical processes. It is believed that feedbacks resulting from the future ozone layer depletion will intensify the tropospheric photochemistry (*Thompson*, 1992; *Závodský* and *Závodská*, 1992). This effect should also be taken into account by formulation of ozone control strategy.

Tropospheric chemistry model simulations often apply the photodissociation rates which are calculated for the typical summer total ozone amount (350 DU). This paper brings the results of photolysis rates calculation as a function of the both total ozone amount and the solar zenith angle for the EMEP photochemical reactions set (*Simpson*, 1992, 1993).

2. Photochemistry in EMEP model

The Meteorological Synthesizing Centre-West of the Co-operative Programme for Monitoring and Evaluation of the Long-range Transmission of Air Pollutants in Europe (EMEP) have developed an ozone model capable of addressing both the problem of short-term episodic ozone and long-term (growing season) ozone (*Simpson*, 1992, 1993). The chemical scheme of this model is updated version of the old EMEP model (*Eliassen et al.*, 1982; *Hov*, 1987). The full scheme of the model includes 45 chemical species, about 100 thermal and 16 photochemical reactions (*Table 1*).

The results of comparison of 25 chemical mechanisms from various photochemical models were recently published (*Derwent*, 1990, 1993). An evaluation of the EMEP chemical mechanism has revealed that it generates the results for ozone, peroxyacetylnitrate and hydrogen peroxide which lie within the central range expected if any of 25 chemical mechanisms had been implemented.

Photodissociation rates of 16 photochemical reactions in EMEP model are the same as those used in the Harwell photochemical model (*Hough*, 1986, 1988). In this work we used the atmospheric transmission and radiance model LOWTRAN 7 (ONCORE, 1991) to recalculate the Harwell photolysis rates. This computer code more realistic considers the important physical processes in cloudless aerosol atmosphere that control the transfer of solar radiation.

Table 1. Photolytic reactions of the EMEP model

Reaction No.	Process	Effective wavelength region
1	$O_3 \rightarrow O_2 + O(^1D)$	290–320 nm
2	$O_3 \rightarrow O_2 + O(^3P)$	290–660 nm
3	$NO_2 \rightarrow NO + O(^3P)$	290–420 nm
4	$NO_3 \rightarrow NO + O_2$	585–635 nm
5	$NO_3 \rightarrow NO_2 + O(^3P)$	400–635 nm
6	$N_2O_5 \rightarrow NO_2 + NO_3$	290–360 nm
7	$HNO_3 \rightarrow NO_2 + OH$	290–330 nm
8	$HCHO \rightarrow HCO + H$	290–335 nm
9	$HCHO \rightarrow H_2 + CO$	290–360 nm
10	$H_2O_2 \rightarrow 2OH$	290–370 nm
11	$CH_3OOH \rightarrow CH_3O + OH$	290–350 nm
12	$CH_3CHO \rightarrow CH_3 + CO + H$	290–340 nm
13	$HCOCHO \rightarrow HCHO + H_2 + CO$	290–470 nm
14	$CH_3COCHO \rightarrow CH_3CO + CO + H$	290–470 nm
15	$CH_3COCOCH_3 \rightarrow CH_3CO + CH_3CO$	290–470 nm
16	$C_2H_5COCH_3 \rightarrow C_2H_5 + CH_3CO$	290–335 nm

3. *Photolysis rates calculation*

3.1 Theoretical assumptions

For each photoactive molecule the photodissociation rate coefficient J is calculated by integrating over the effective wavelength interval (λ_1, λ_2) the product of the spectral actinic flux F_A (λ), the spectral absorption cross section σ (λ), and the photodissociation quantum yield φ (λ) (*Madronich*, 1987):

$$J = \int_{\lambda_1}^{\lambda_2} \varphi(\lambda)\, \sigma(\lambda)\, F_A(\lambda)\, d\lambda \,. \tag{1}$$

The actinic flux F_A (λ) is defined as the spherically integrated solar photon flux incident onto an infinitesimal volume element in the atmosphere. F_A (λ) must be in units of photons per unit area per unit time per unit wavelength interval. It depends on many factors: ozone and molecular oxygen absorption, aerosol absorption, molecular (Rayleigh) and aerosol (Mie) scattering, Earth's surface reflection.

The actinic flux F_A (λ) may be split into a direct and a diffuse part:

$$F_A(\lambda) = F_0(\lambda) + F\downarrow(\lambda) + F\uparrow(\lambda). \tag{2}$$

The first component $F_0(\lambda)$ is the directly transmitted solar irradiance, while the rest two components $F\downarrow(\lambda)$ and $F\uparrow(\lambda)$ represent the downward and the upward diffuse contributions. Whereas the direct component $F_0(\lambda)$ can be calculated using a simple exponential formula, the diffuse components require angular integration over hemisphere:

$$F\downarrow(\lambda) = \int_0^{2\pi}\int_0^{1} L\downarrow(\lambda,\mu,\varphi)\, d\mu\, d\varphi, \tag{3}$$

$$F\uparrow(\lambda) = \int_0^{2\pi}\int_{-1}^{0} L\uparrow(\lambda,\mu,\varphi)\, d\mu\, d\varphi, \tag{4}$$

where μ and φ are the cosine of zenith angle and the azimuthal angle, respectively. Even if angular distribution of both the downward $L\downarrow$ and the upward $L\uparrow$ radiance is known, the calculation is too much time consuming from practical applications point of view. Therefore appropriate approximations of angular integrals in Eqs. (3) and (4) are useful. The most common approximation used in the radiation model calculations for the upward radiance is an asumption of isotropic surface reflection (Lambertian surface), i.e. $L\uparrow(\mu,\varphi)$ = constant. In this case the upward component of the actinic flux can be calculated as (*Madronich*, 1987)

$$F\uparrow(\lambda) = A(2\mu_0 F_0(\lambda) + F\downarrow(\lambda)), \tag{5}$$

where A is the surface albedo and μ_0 is cosine of solar zenith angle.

The downward radiance $L\downarrow$ in the atmosphere with aerosol particles is highly anisotropic. However, according to *Ruggaber et al.* (1993) for the diffuse part of the actinic flux only the azimuthally independent radiance is relevant. Therefore the azimuthally dependent radiance in Eq. (3) can be replaced either by its mean value or by a value at a fixed azimuth angle φ_r, which represents approximately the mean radiance. To avoid the integration over all zenith angles in Eq. (3) a similar approximation is necessary, i.e. to use the irradiance value at a fixed zenith angle $\theta_r = \cos^{-1}\mu_r$, which corresponds to mean radiance (*Madronich*, 1987). We can then write for downward diffuse part of the actinic flux:

$$F\downarrow(\lambda) = 2\pi L\downarrow(\lambda,\theta_r,\varphi_r). \tag{6}$$

θ_r and φ_r are the zenith angle and the relative azimuth (to the Sun position),

respectively. The angle of 1 radian for θ_r (*Hough*, 1988) and the same value for a relative azimuth φ_r was used in our calculation. *Figs. 1a, b* illustrate the comparison of downward radiance values calculated at a reference point (φ_r = 1 rad, θ_r = 1 rad) with azimuthally averaged values calculated using 20 points Gaussian quadrature for the azimuth integral. It can be seen that in UV region the differences are negligible. At the longer wavelenghts ($\lambda > 400$ nm) these differences are small and depend upon the Sun position.

Using above mentioned approximations with combination of Eqs. (2) and (5) we can determine the actinic flux as

$$F_A(\lambda) = F_0(\lambda)(1 + 2A\mu_0) + F\downarrow(\lambda)(1 + A). \tag{7}$$

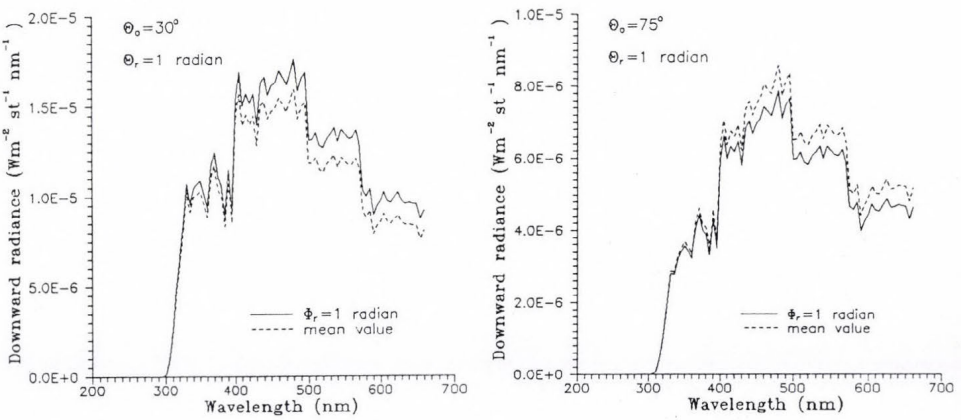

Fig. 1. Comparison of downward radiance values calculated for θ_r and φ_r (1 rad) with azimuthally averaged values; solar zenith angle (*a*) $\theta_0 = 30°$, (*b*) $\theta_0 = 75°$.

3.2 Radiative transfer model and input data

The computer code LOWTRAN 7 was utilized to calculate the directly transmitted solar irradiance and the path radiance ($L\downarrow$ in Eqs. (3) and (6)) in the inhomogeneous aerosol cloudless atmosphere with spectral resolution of 50 cm^{-1}. In addition to Rayleigh scattering and molecular absorption this code includes the aerosol extinction. The contributions of multiple scattered photons to the total path radiance are also included. Scattering caused by air molecules and aerosol particles is treated separately using different phase functions. The Mie generated phase functions corresponding to the different aerosol models are used for aerosol scattering.

The model atmosphere is composed of 31 homogeneous plane-parallel layers of unequal thickness. The top of the atmosphere is situated at 50 km hight.

Table 1 contains the list of 16 photochemical reactions with the effective wavelength intervals for which the calculations have been made. To calculate the photolysis rates of the reaction i Eq. (1) can be evaluated by summation over finite wavelength intervals:

$$J_i = \sum_{n=1}^{N_i} \varphi_{i,n} \sigma_{i,n} F_{A,n}, \tag{8}$$

where N_i is the total number of 5-nm intervals covering the effective wavelength region of reaction i (see Table 1). All values of φ_n, σ_n for each photochemical reaction are taken from *Hough* (1988). $F_{A,n}$ represent the integrated values of the actinic flux over individual 5-nm intervals.

The actinic flux was calculated at 0.5 km level for five total ozone amounts (200, 250, 300, 350, and 400 DU) and for five Sun positions. Although the relation Eq. (5) is valid only for a level close to the Earth's surface, we used it at level of 0.5 km, because the contribution of layer below the 0.5 km level to the upwelling diffuse radiation is small compared to the total downwelling radiation.

Vertical ozone profiles follow the Mid-Latitude Summer profile (*Ellingson et al.*, 1991). We considered a Lambertian surface with albedo of 0.10. We used the LOWTRAN 7 boundary layer (0–2 km) rural (visibility of 23 km) and stratospheric background aerosol models.

4. Results and discussion

Figs. 2–17 show the calculated photodissociation rates as a function of both the solar zenith angle and the total ozone column for each of 16 photochemical processes listed in Table 1. All J_i calculations are made at level of 0.5 km above surface with albedo 0.10 (summer conditions). The present results are compared with those of *Hough* (1988) for 350 DU total ozone. Generally, fairly good agreement is found between these two sets of calculation. The differences increase with spreading the effective wavelength region toward the visible part of solar spectrum. In most cases the differences change from positive to negative with increasing solar zenith angle. The dependence of J_i on the solar zenith angle is more intensive in present work. It may be explained by the different method of the radiance calculations. The dependence upon the solar zenith angle may be enhanced due to aerosol particles anisotropic scattering. The solar zenith angle dependence is decreasing with decreasing effective wavelengths, due to an increasing effect of multiple scattering.

Ozone absorption is the dominating process in the wavelength region between 290 and 320 nm (UVB region) and therefore the downward radiance

is less affected by aerosol particles than in other wavelength intervals. This explains why the photolysis rates for ozone photolysis ($O_3 \rightarrow O_2 + O(^1D)$) and HNO_3 photolysis calculated by *Hough* are in excellent agreement with present results (Figs. 2 and 8).

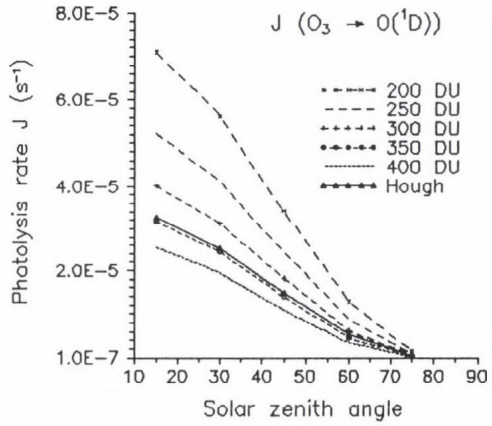

Fig. 2. The calculated photolysis rate $J(O_3 \rightarrow O(^1D))$ as a function of solar zenith angle and total ozone amount under clear sky, 0.5 km above surface, 0.10 surface albedo. *Hough* assumed condition clear sky, 0.5 km above land, 350 DU total ozone.

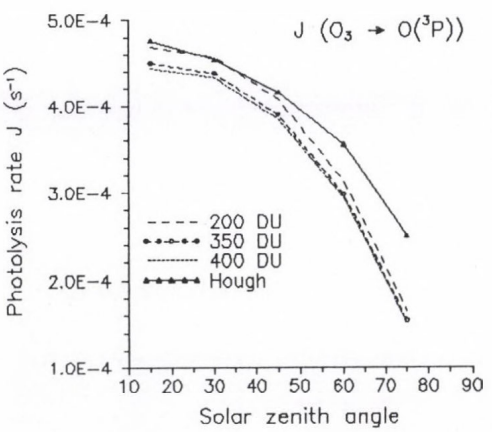

Fig. 3. As Fig. 2, but for $J(O_3 \rightarrow O(^3P))$.

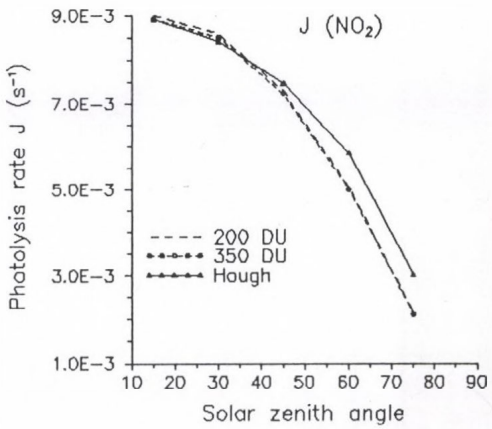

Fig. 4. As Fig. 2, but for $J(NO_2)$.

The effect of variations of the total ozone amount is largest at the photochemical processes with the effective wavelengths in UVB region. The strong ozone absorption in this part of the solar spectrum (Hartley band) results in a strong dependence of the actinic flux as well as the photolysis rates on the total ozone amount (Figs. 2, 7, 8 and 17). The influence of the Chappius band at about 600 nm is smaller (Figs. 5 and 6).

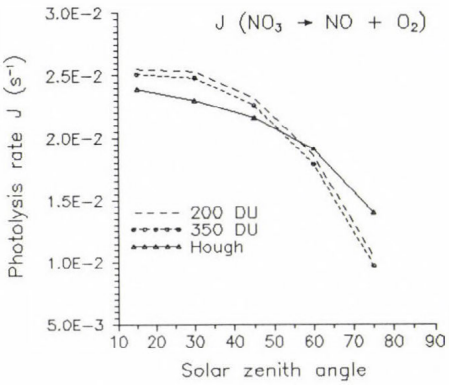

Fig. 5. As Fig. 2, but for $J(NO_3 \rightarrow NO + O_2)$.

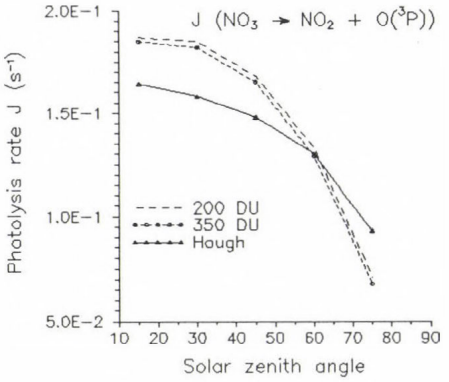

Fig. 6. As Fig. 2, but for $J(NO_3 \rightarrow NO_2 + O(^3P))$.

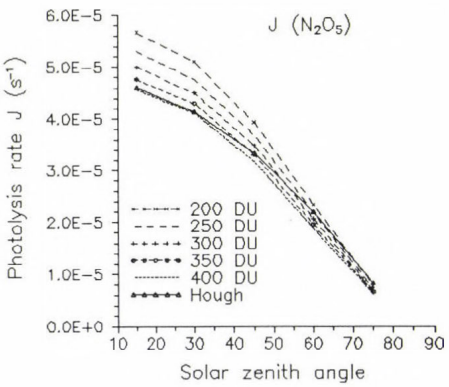

Fig. 7. As Fig. 2, but for $J(N_2O_5)$.

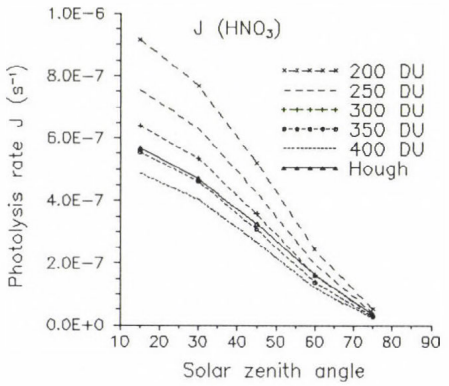

Fig. 8. As Fig. 2, but for $J(HNO_3)$.

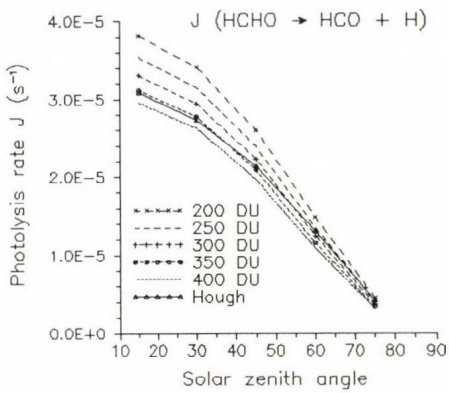

Fig. 9. As Fig. 2, but for $J(HCHO \rightarrow HCO + H)$.

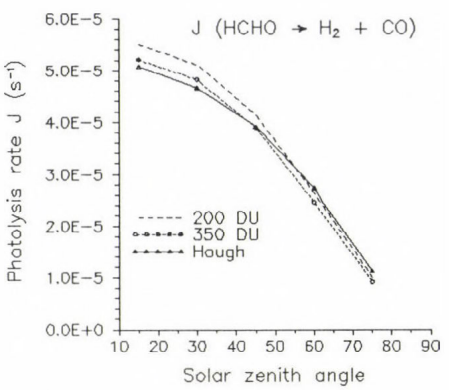

Fig. 10. As Fig. 2, but for $J(HCHO \rightarrow H_2 + CO)$.

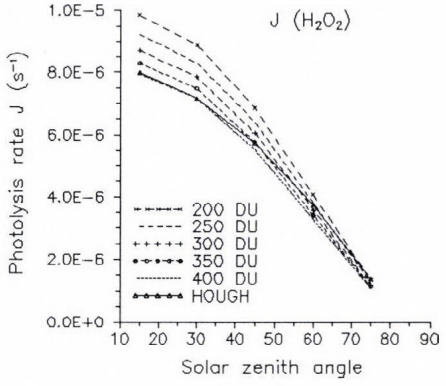

Fig. 11. As Fig. 2, but for $J(H_2O_2)$.

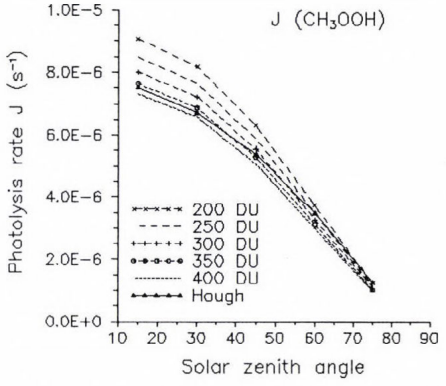

Fig. 12. As Fig. 2, but for $J(CH_3OOH)$.

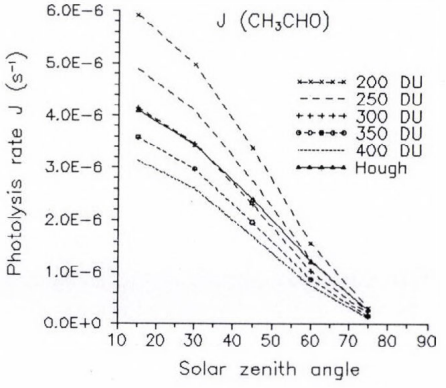

Fig. 13. As Fig. 2, but for $J(CH_3CHO)$.

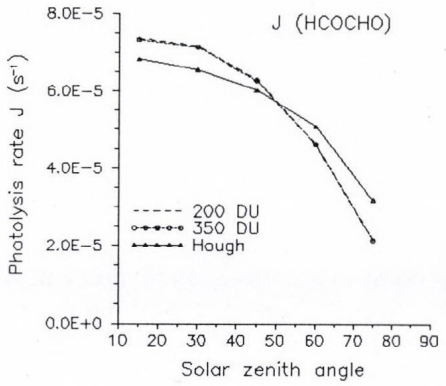

Fig. 14. As Fig. 2, but for J(HCOCHO).

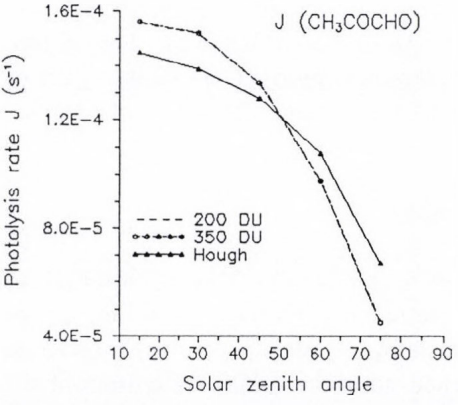

Fig. 15. As Fig. 2, but for $J(CH_3COCHO)$.

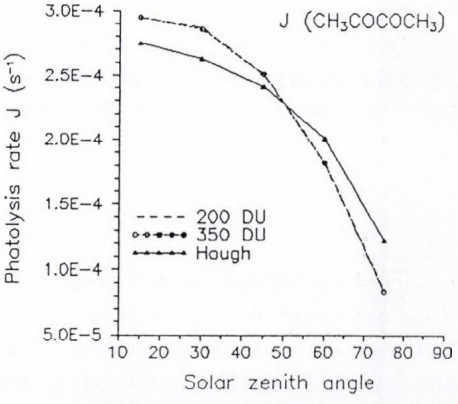

Fig. 16. As Fig. 2, but for $J(CH_3COCOCH_3)$.

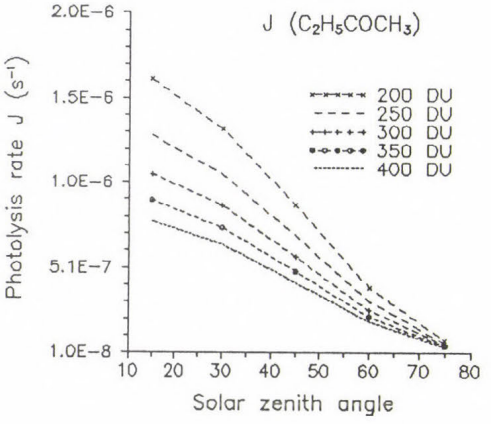

Fig. 17. The calculated photolysis rate $J(C_2H_5COCH_3)$ as a function of solar zenith angle and total ozone amount under clear sky, 0.5 km above surface, 0.10 surface albedo.

For use in tropospheric chemistry model photodissociation rates are specified as a function of both the solar zenith angle (θ_0), and the total ozone column (*Simpson*, 1993):

$$J = a \exp(-b \sec \theta_0). \tag{9}$$

Here a and b are coefficients which for clear sky depend upon the total ozone amount in the atmosphere. In order to indicate this dependence, we used the present photodissociation rate calculations. For the solar zenith angle between 15° and 75° and for the total ozone amount between 200 and 400 DU we derived the exponential expressions for coefficients a and b:

$$a = A_a \exp(B_a x), \quad b = A_b \exp(B_b x), \tag{10}$$

where x is the total ozone amount in DU. *Table 2* presents the regression coefficients A_a, B_a, A_b and B_b for each of reactions considered. The photochemical processes with the effective wavelength region in the visible part of solar spectrum are practically independent of total ozone amount.

5. *Conclusions*

The transmission and radiance model LOWTRAN 7 were applied to recalculate the photolysis rates of 16 photochemical reactions used in long-range transport air pollution models. The regression expressions were derived to specify the photodissociation rate dependence upon the total ozone amount for each of reactions considered. The calculations were made for the level of 0.5 km above surface with the albedo of 0.10. The calculated data were compared

with those used in EMEP model for 350 DU total ozone. Generally good agreement but some differences were found. These may be explained by the different method of the actinic flux calculation.

Table 2. Regression coefficient values in relations (10)

Reaction No.	Regression coefficient			
	A_a	B_a	A_b	B_b
1	5.108E-4	-3.937E-3	1.129E+0	8.245E-4
2	7.182E-4	-2.184E-4	3.642E-1	1.270E-4
3	1.516E-2	-4.895E-5	5.115E-1	+
4	3.654E-2	-2.576E-5	3.086E-1	2.980E-4
5	2.717E-1	*	3.572E-1	*
6	7.791E-5	-1.059E-3	1.518E+0	2.356E-5
7	4.024E-6	-2.940E-3	9.603E-1	2.421E-4
8	9.510E-5	-1.090E-3	7.106E-1	2.636E-4
9	1.040E-4	-2.876E-4	5.885E-1	1.246E-4
10	2.307E-5	-1.063E-3	6.952E-1	+
11	2.127E-5	-1.044E-3	7.021E-1	+
12	2.501E-5	-2.603E-3	9.258E-1	5.228E-4
13	1.165E-4	*	4.427E-1	*
14	2.487E-4	*	4.461E-1	*
15	4.722E-4	*	4.538E-1	*
16	8.275E-6	-3.704E-3	1.030E+0	+

* in this case a and b are independent of total ozone amount ($a = A_a$, $b = A_b$)
\+ in this case b is independent of total ozone amount ($b = A_b$) coefficients A_a are in s^{-1}

References

Bojkov, R.D., 1993: Changes in ozone distribution: European aspects. *Extended Abstracts, WMO Region VI Conference on the Measurement and Modelling of Atmospheric Composition Changes Including Pollution Transport.* 4-8 October, Sofia, Bulgaria, 13-16.

Derwent, R.G., 1990: Evaluation of photochemical mechanisms for their application in models describing the formation of photochemical ozone in Europe. *Atmos. Environ. 24A*, 2615-2624.

Derwent, R.G., 1993: Evaluation of the chemical mechanism employed in the EMEP photochemical oxidant model. *Atmos. Environ. 27A*, 277-279.

Eliassen, A., Hov, O., Isaksen, I.S.A., Saltbones, J. and *Stordal, F.*, 1982: A Lagrangian long-range transport model with atmospheric boundary layer chemistry. *J. Appl. Meteor. 21*, 1645-1661.

Ellingson, R.G., Ellis, J. and *Fels, S.*, 1991: The intercomparison of radiation codes used in climate models: Long-wave results. *J. Geophys. Res. 96*, 8929-8953.

Hough, A.M., 1986: The production of photochemical pollution in Southern England and the effects of vehicle exhaust emis-

sion control strategies. Harwell Laboratory. *Report* AERE R 12069.

Hough, A.M., 1988: The calculation of photolysis rates for use in global tropospheric modelling studies. Harwell Laboratory. *Report* AERE R 13259.

Hov, O., 1987: Models for photochemical processes. In *Regional and Long-range Transport of Air Pollution*. Elsevier, Amsterdam, pp. 391-412.

Madronich, S., 1987: Photodissociation in the atmosphere. 1. Actinic flux and the effects of ground reflections and clouds. *J. Geophys. Res. 92*, 9740-9752.

ONCORE, 1991: *Personal Computer Version of the LOWTRAN 7 Atmospheric Model, Version 2a*. Ontar Corporation.

Ruggaber, A., Forkel, R. and *Dlugi, R.*, 1993: Spectral actinic flux and its ratio to spectral irradiance by radiation transfer calculations. *J. Geophys. Res. 98*, 1151-1162.

Simpson, D., 1992: Long-period modelling of photochemical oxidants in Europe. Model calculations for July 1985. *Atmos. Environ. 26A*, 1609-1634.

Simpson, D., 1993: Photochemical model calculations over Europe for two extended summer periods: 1985 and 1989. *Atmos. Environ. 27A*, 921-943.

Thompson, A.M., 1992: The oxidizing capacity of the Earth's atmosphere: Probable past and future changes. *Science 256*, 1157-1165.

Závodský, D. and *Závodská, E.*, 1992: Air quality and climate change (in Slovak). In *National Climate Programme CSFR No. 7*, CHMI, Prague, pp. 3-52.

IDŐJÁRÁS

Quarterly Journal of the Hungarian Meteorological Service
Vol. 98, No. 4, October–December 1994

Temperature variation in Europe and North America since the beginning of instrumental observations

G. Koppány

Department of Climatology, József Attila University,
H-6722 Szeged, P.O. Box 661, Hungary

(Manuscript received 22 June 1994; in final form 20 November 1994)

Abstract—With the intention of analysis, 19 climatological stations were selected possessing annual mean temperature series longer than 150 years. The running 9-year mean temperatures were used in order to determine the coincidences of simultaneous warmings and coolings at different places in central, western and northern Europe, as well as in the eastern U.S.A. Several short periods were found with simultaneous maxima or minima at many different locations. Comparing these periods with volcanic activity,it is pointed out that the temperature minima are close to high volcanic activities, and maxima to calm volcanic episodes. It were also found that in 9 stations out of 19, temperature maxima before 188O were higher than those after 188O. It is likely that the global mean temperature had relatively low value around 188O.

Key words: long-term temperature variations, volcanic activity.

1. Introduction

It is widely known that the global near surface temperature has increased by cca 0.5°C since the 1880-s (*Götz*, 1983; *Lockwood*, 1986; *Brazdil et al.*, 1987). The warming was as much as 0.8°C in the Northern Hemisphere, and reached its maximum in years 1938–1940. Many authors concluded that this warming is the response of the atmosphere to increasing CO_2 after beginning of industrialisation and technical development from late 19-th century (*Energy and Climate*, 1977). Moreover, according to numerical climate model experiments the global warming may reach 2–5°C by 21-st century, if the increase of atmospheric CO_2 will continue with present rate (*Bach* and *Jain*, 1991; *Houghton*, 1994). This warming may result in shifts of climatic zones.

However, the question is, whether the temperature variations could be explained by means of a single factor, namely the change of atmospheric CO_2

and other greenhouse-gases (CH_4, N_2O etc.). It is also well known that the energy flux density of anthropogeneous sources in area as large as several 100 km (megapolises, industrial centres) approaches the net solar radiation density, which is about 100 W/m^2 (*Lockwood*, 1986; *Koppány*, 1989). On the other hand, many climatic stations are located in areas with dense population. Thus, at least a fraction of the global warming is apparent and may be the consequence of urbanization.

It is also noteworthy that the global mean temperature decreased by around 0.3°C from 1940 to 1979, while cooling in the Northern Hemisphere was as much as 0.5°C. This fact suggests that the atmospheric temperature is influenced by other factors besides the greenhouse effect since the atmospheric carbon-dioxide has grown after 1940 continuously.

Therefore it is reasonable to investigate temperature series of length more than 150 year in order to decide: whether significant warming took place before 1880, too, and if yes, then these pre-industrial warmings were higher or lower, than those in the 20-th century. 19 climatic stations were selected possessing more or less continuous temperature series from early 19-th century or further back. The records available from these stations are insufficient for calculation mean global or hemispheric temperature variations. Still the early instrumental measurements might provide some information on regional temperature changes occured in last 2 or 3 centuries mainly from great part ot Europe, and from eastern United States.

2. Data sources

The temperature records have been taken mostly from Bracknell data basis up to 1960 in form of magnetic tapes. Some additional series were obtained from *Ch. D. Schönwiese*, Goethe University of Frankfurt am Main, among others the records of Central England (*Schönwiese*, 1988), and the data period 1961-70 from *World Weather Records* (1971). The series of Budapest since 1780 are available in *A. Réthly*'s work (*Réthly*, 1947), and in file of the Hungarian Meteorological Service. The list of climatic stations is presented in *Table 1*.

The majority of stations (14) is located between 46–56°N latitudes, i.e. in temperate zone, three stations are in subtropical zone, and two stations in subpolar zone, respectively. 16 stations have continuous temperature series, two stations have interrupted series (Charleston and Copenhagen), in these cases either only the continuous part was used or the short interruptions were completed by interpolation. The records of Prague from 1939 to 1950 were added to those obtained from Bracknell.

Table 1. Geographical positions and observation periods of climatic stations

Station	Latitude	Longitude	Observation period(s)
Central England	52.8°N	2.5°W	1659–1987
De Bilt	52.6°N	5.1°E	1706–1970
Charleston (U.S.A.)	32.9°N	80.0°W	1741–1759, 1823–1965
Edinburgh	55.9°N	3.2°W	1764–1970
Basel	47.6°N	7.6°E	1755–1970
Geneva	46.2°N	6.2°E	1753–1970
Trondheim	63.4°N	10.4°E	1761–1969
Stockholm	59.4°N	18.0°E	1757–1970
Copenhagen	55.6°N	12.5°E	1768–1776, 1782–1788, 1798–1970
Greenwich	51.5°N	0.0°	1763–1970
Berlin	52.6°N	13.4°E	1769–1970
Paris	48.8°N	2.5°E	1764–1970
Prague	50.1°N	14.4°E	1771–1989
New Haven (U.S.A.)	41.3°N	72.9°W	1781–1970
Hohenpeissenberg	47.8°N	11.0°E	1781–1970
Vienna	48.3°N	16.4°E	1775–1970
Budapest	47.5°N	19.0°E	1780–1970
Kremsmünster	48.1°N	14.1°E	1796–1985
Genova	44.5°N	3.5°E	1833–1986

3. Method and results

As a first step decadal mean temperatures were calculated for all available climatic stations. By analyzing such rough materials synchronous warmings or coolings appeared in some stations, e.g. the decade of *1731–1740* proved warm both in Central England and De Bilt with positive decadal temperature anomaly (+ 0.4°C). Similar relative *warming* occured in *1791–1800* at twelve stations, in *1861–1870* at eleven stations etc. On the other hand, relatively great negative anomalies were found in *1811–1820* at eight stations, in *1881–1890* at 13 climatic stations etc.

In order to get more exact periods of local warming and cooling at various stations, running 9-year averages were determined. The standard deviations of 9-year mean temperatures and the mean values of the whole series were also calculated for each station. The secular temperature variations are presented in *Fig. 1 a-f.* The arrows directing upwards denote warming, 'M' marks the maxi-

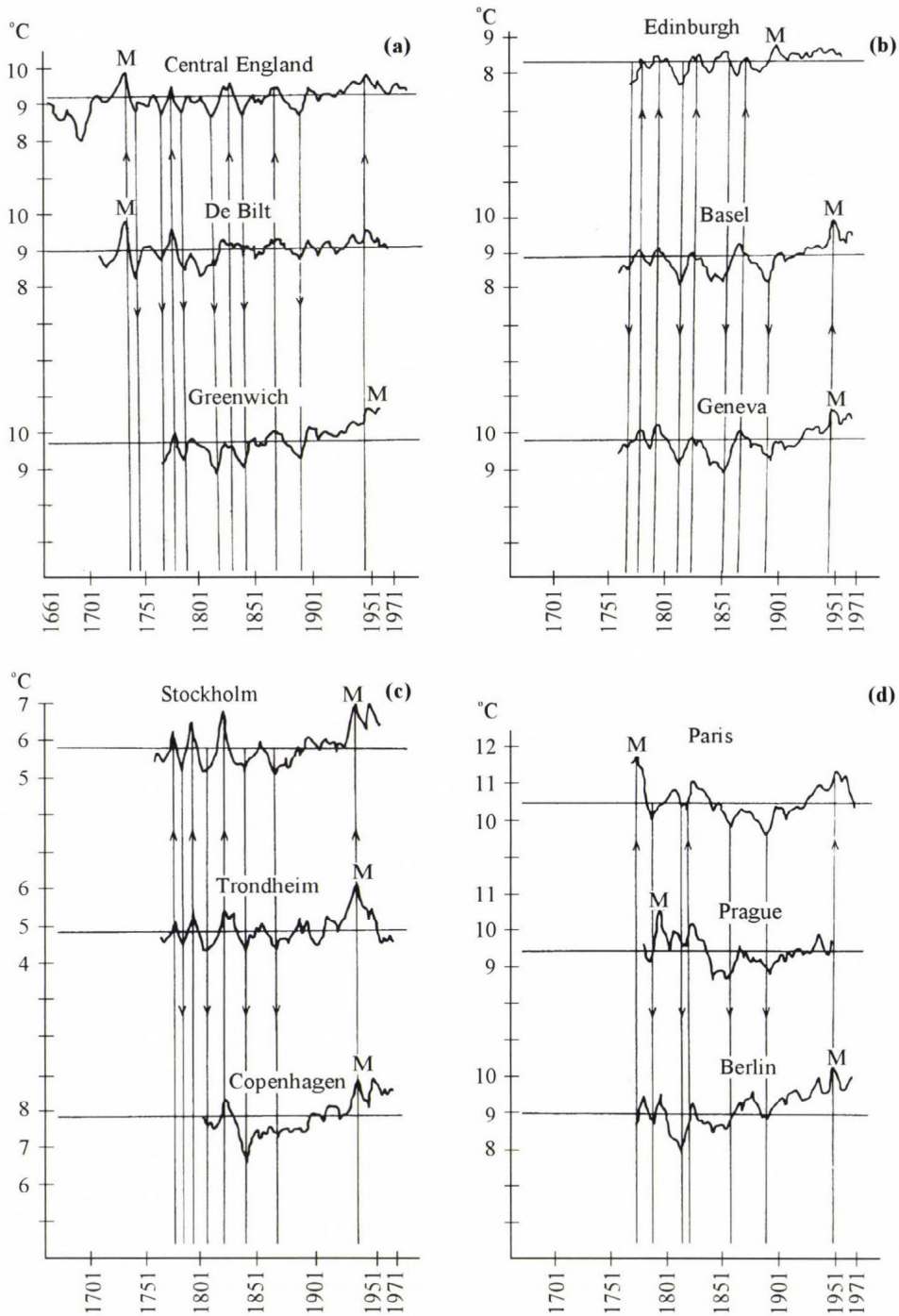
°C
(a)
Central England
De Bilt
Greenwich
M
10
9
8
1661
1701
1751
1801
1851
1901
1951
1971
(b)
Edinburgh
Basel
Geneva
(c)
Stockholm
Trondheim
Copenhagen
(d)
Paris
Prague
Berlin

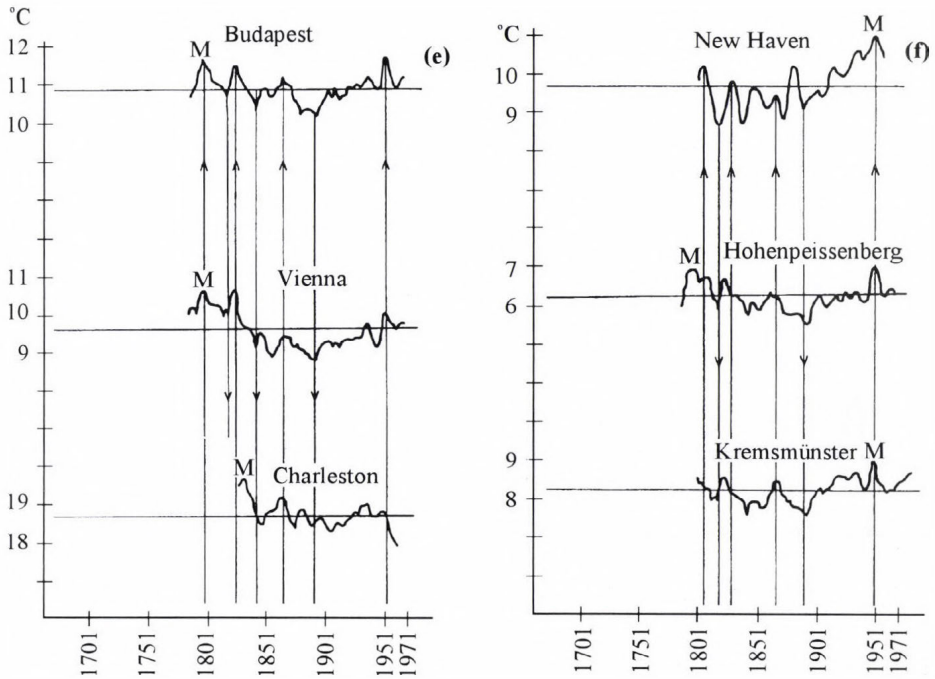

Fig. 1a-f. Running 9-year mean temperature since beginning of instrumental observation at different station.

mum value in whole series of a given station, the arrows directing downwards denote cooling. One can recognize *synchronous maxima* in some stations in periods of 1772–1779, of 1790–1794, of 1822–1830, of 1859–1865, of 1893-1897, of 1930-s and 1940-s. On the other hand, *minima* can be found in some stations in periods of 1767–1770, of 1812–1816, of 1836–1841, of 1888–1891, of 1903–1905 and 1960-s.

Schönwiese (1988) has found significant negative correlation between the mean temperature of Northern Hemisphere and several kinds of volcanic indices. In *Fig. 2* the spells of synchronous warmings and coolings are presented during the period of 1731–1970 (above), while the dust vail index (DVI) is shown below since 1750, with the names of greater volcanic eruptions. According to the DVI data the calm volcanic periods were: (1) 1770–1780, (2) 1790–1810, (3) 1820–1831, (4) 1845–1880 and (5) 1913–1962. These calm periods coincided with the years of temperature maxima mentioned above. Unusually long *volcanic* silence appeared between 1912 and 1963, which coincided with the significant warming in the 20-th century. On the other hand

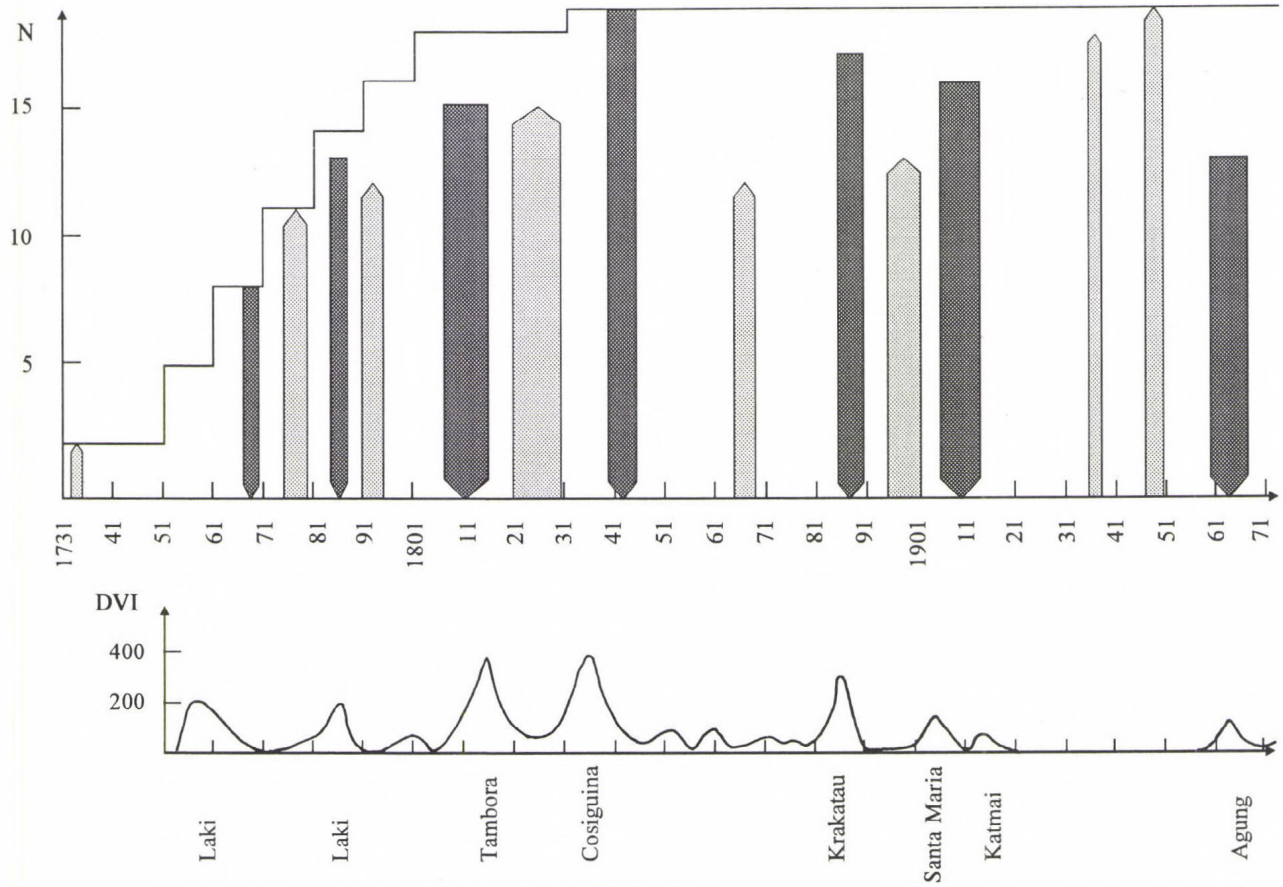

Fig. 2. Above: Number of climatic stations (N) possessing data since 1731; arrows upwards denote the number of stations with synchronous maxima, downwards denote the number of stations with simultaneous minima. The widths of the arrows indicate the lengths of spells with synchronous extreme temperature. *Below*: dust veil index with the names of greater volcanic eruptions.

several strong volcanic eruption occured since 1756 over the period included in this investigation (e.g. Laki, Iceland in 1756 and 1785; Tambora between 1815 and 1822; Krakatau in 1875–83; Santa Maria, Mount Pelee, and Colima in 1902; Katmai, Alaska in 1912; Agung, Bali 1963). The coincidences of active volcanic spells with cooling in the majority of climatic stations are evident in Fig. 2. Besides the direct insolation has weakened by around 5 per cent after 1950 due to *increasing atmospheric turbidity* as a probable consequence of increased aerosol emitted by human activity (*Pivovarova*, 1970; *Budyko*, 1982; *Budyko et al.*, 1987). A similar cooling effect was pointed out by *Houghton* (1994).

One of the main purpose of this study is to investigate the temperature maxima *before 1880* and to reveal the evidence of warmer periods comparing with those in the *20-th century*. *Table 2* contains the highest running 9-year mean temperature anomalies at each station, before and after *1880*. In the first column one can find the mean temperature for the whole series, and in the second column the standard deviation of running 9-year averages (s). The next column presents the maxima years and the temperature anomalies in form of the ratio k = anomaly per standard deviation i.e. signal per noise, both concerning the warmings before *1880*. The next column contains the same characteristics but after *1880*, while in last column *dt* denotes the difference between the maximum annual temperature in 20-th century and the maximum annual temperature before 1880. If the difference is positive that means relative warming in the 20-th century, if it is negative, the stronger warming took place before 1880. The latter cases are marked with exclamation point. Nine stations out of 19 have proved relative greater warming before 1880, among others Charleston and Prague, Paris, Vienna, De Bilt, Genova etc.

Hence it seems, that there were significant warmings in the both 18-th and the 19-th century, i.e. before the significant increase of atmoshperic carbon-dioxide started due to industrialization. *Keil* (1961), analyzing long temperature series of Basel, Hohenpeissenburg, Jena and Prague, has got similar results using 30–40–50–60-year smoothed temperature data.

After maxima in the 1930-s or the 1940-s an overall cooling was observed during the 1950-s or the 1960-s in all stations (*Table 3*). The ratio k = (difference between maximum and minimum per standard deviation) exceeds 1 at 16 stations, 2 at 7 stations and 3 at 2 stations.

4. Conclusions

— The temperature series over a period longer than 150 years exhibit minima between 1886 and 1891 at the majority of the climatic stations (see Fig. 2).
— Temperature maxima occured many times before 1880, and at 45

percent of the stations these maxima were higher, than those in 1930-s and 1940-s.

— The warming in the 1930-s or the 1940-s coincides with the longest calm volcanic period since 1750.
— A uniform cooling took place by the 1950-s or the 1960-s.
— In the light of these facts the global temperature variations may not be explained exclusively with greenhouse effect.

Table 2. The warmest running 9-year mean temperature

Station	°C	s °C	Before 1880 (k)		After 1880 (k)		dt °C
Basel	8.9	0.38	1794	+0.87	1947	+2.95	+0.67
			1865	+1.18			
Berlin	8.9	0.36	1794	+1.44	1947	+1.28	- 0.50 !
			1876	+1.69			
Budapest	10.9	0.33	1794	+2.52	1949	+2.45	- 0.20 !
Charleston	18.7	0.35	1831	+2.86	1935	+0.94	- 0.70 !
New Haven	9.7	0.59	1790	+1.57	1949	+2.19	+0.73
Central England	9.2	0.33	1734	+2.36	1947	+2.00	- 0.12 !
			1830	+1.33			
Copenhagen	7.8	0.49	1922	+1.04	1947	+2.20	+0.57
De Bilt	9.0	0.33	1733	+2.87	1947	+2.10	- 0.23 !
			1777	+2.03			
Edinburgh	8.3	0.26	1794	+0.65	1936	+1.65	+0.12
			1854	+1.19			
Geneva	9.8	0.38	1794	+1.32	1947	+2.53	+0.46
Genova	15.7	0.36	1865	+2.50	1946	+1.67	- 0.30 !
Greenwich	9.7	0.39	1779	+0.69	1947	+2.38	+0.66
Hohenpeissenberg	6.2	0.33	1794	+2.39	1949	+2.45	+0.02
Kremsmünster	8.2	0.31	1800	+1.13	1947	+2.45	+0.41
Paris	10.5	0.46	1772	+2.67	1949	+1.76	- 0.42 !
Prague	9.5	0.52	1793	+2.11	1949	+1.35	- 0.40 !
Stockholm	5.8	0.48	1794	+1.48	1947	+2.67	+0.28
			1822	+2.08			
Trondheim	4.8	0.37	1794	+1.43	1934	+3.38	+0.70
			1822	+1.49			
Vienna	9.6	0.50	1798	+2.18	1949	+1.04	- 0.57 !

Table 3. Maxima and subsequent minima (years and values) of 9-yr running averages of temperature in the 20th century and the magnitude of the cooling after 1930s or 1940s; *k* is the difference between maximum and minimum per standard deviation

Station	Year	°C	Year	°C	°C	k
Central England	1947	9.8	1966	9.2	-0.6	-1.91
De Bilt	1947	9.6	1966	8.9	-0.7	-2.37
Greenwich	1947	10.7	1954	10.5	-0.2	-0.51
Edinburgh	1936	8.8	1954	8.4	-0.4	-1.23
Basel	1947	10.0	1959	9.3	-0.7	-1.79
Geneva	1947	10.7	1954	10.2	-0.5	-1.26
Stockholm	1947	7.1	1954	6.3	-0.8	-1.56
Trondheim	1934	6.1	1954	4.4	-1.7	-4.49
Copenhagen	1947	8.9	1966	8.3	-0.6	-1.14
Paris	1949	11.3	1966	10.2	-1.1	-2.37
Prague	1949	10.2	1959	9.5	-0.7	-1.35
Berlin	1947	9.4	1958	8.7	-0.7	-1.89
Budapest	1949	11.7	1958	10.9	-0.8	-2.45
Vienna	1949	10.1	1959	9.6	-0.5	-1.00
Charleston	1935	19.0	1959	17.9	-1.1	-3.26
New Haven	1949	11.0	1956	10.4	-0.6	-1.03
Hohenpeissenberg	1949	7.0	1966	6.1	-0.9	-2.82
Kremsmünster	1947	9.0	1959	8.1	-0.9	-2.74
Genova	1946	16.3	1958	15.4	-0.9	-2.50

References

Bach, W. and *Jain, K.*, 1991: From climate crisis to climate protection. Greenpeace Germany, Muenster Univ.

Brazdil, R., Kozuchowsky, K., Marciniak, K. and *Tam, T.N.*, 1987: Variation of annual air temperature in Europe in the period of 1881-1980. Climatic Changes, Brno, 115-130.

Budyko, M.I., 1982: The Earth's Climate: Past and Future. Academic Press, London.

Budyko, M.I., Ronov, A.B. and *Yashin, A.L.*, 1987: *History of the Earth's Atmosphere*. Springer Verlag, Berlin.

Energy and Climate, 1977: National Academy of Sciences, Washington D.C.

Götz, G., 1983: Introduction to general climatology. Lecture notes, Orsz. Meteorológiai Szolgálat, Budapest.

Houghton, J., 1994: *Global Warming. The Complete Briefing*. Lion Publishing, Oxford.

Keil, K., 1961: Zum Thema Klimaschwankun-

Keil, K., 1961: Zum Thema Klimaschwankungen. *Meteorologische Rundschau 14*, Jg. Heft 6, 180-182.

Koppány, Gy., 1989: *Atmospheric Resources* (in Hungarian). JATE, Szeged.

Lockwood, J.G., 1986: *World Climatic Systems*. Edward Arnold Ltd., London.

Pivovarova, Z.I., 1970: Study of the regime of atmospheric transparency. Radiation including satellite techniques. *WMO Technical Note 104*, 181-185.

Réthly, A., 1947: Climate of Budapest (in Hungarian). A Budapesti Központi Gyógy- és Üdülőhelyi Bizottság Rheuma- és Fürdőkutató Intézete Kiadványa, Budapest.

Schönwiese, Ch. D., 1988: Volcanic activity parameters and volcanism-climate relationship within the recent centuries. *Atmosfera 1*, 141-156.

World Weather Records, 1971. Washington, D.C.

IDŐJÁRÁS

Quarterly Journal of the Hungarian Meteorological Service
Vol. 98, No. 4, October–December 1994

Determination of the value of atmospheric drought

G. Szász

Debrecen Agricultural University,
P.O. Box 36, H-4015 Debrecen, Hungary

(Manuscript received 4 August 1994; in final form 7 December 1994)

Abstract—The value of atmospheric drought is determined by the temperature and the relative air humidity. Its value expresses the deviation of a given potential evaporation from the ecologically adequate standard value.

The value of atmospheric drought (D_a) under different climates ranges between 0–200. The diurnal course and the intervals of its values are directly proportional to the enthalpy. The reference values of the equations used for estimation can be chosen optionally. The atmospheric drought value can be considered as a meteorological and ecological index. This paper presents tables and nomograms which demonstrate how to calculate it.

Key-words: atmospheric drought, atmospheric dryness, enthalpy, potential evaporation, Debrecen.

1. Introduction

When speaking about drought, a distinction has to be made between soil drought and atmospheric drought (or atmospheric dryness). Soil drought is an extreme case of the water balance in the soil, while the atmospheric drought is an extreme event of the physical conditions of boundary layer. There are great differences between the duration of soil and atmospheric drought. If considered by its harm causing effects, the duration of soil drought averages $2–10 \times 10^2$ hours, whereas the same average for atmospheric drought is 2–6 hours/day and usually is formed around noon. Atmospheric drought in ecological and agricultural sense is when the relative humidity falls below 40%. It has to be remarked that this critical value is not considered constant either in climatological or in ecological respect. Below, the possible way of the numerical estimation of the atmospheric drought will be discussed.

2. *Theoretical basis*

The specific enthalpy of air under about the same pressure is the sum of the sensible and latent heat:

$$E = c_p \cdot \rho_a \cdot T + [L_a(0.622 \cdot e/p)] \qquad (\mathrm{J\ kg^{-1}\ K^{-1}}), \tag{1}$$

where c_p is specific heat at constant pressure (1 J $\mathrm{kg^{-1}\ K^{-1}}$), ρ_a air density (1.2 kg $\mathrm{m^{-3}}$), e vapour pressure (hPa), L water evaporation heat (20°C = 2.5 MJ $\mathrm{kg^{-1}}$), T is temperature (K). This equation corresponds to the first axiom of thermodynamics (*Götz* and *Rákóczi*, 1981). The degree of atmospheric drought (D_a) can be characterized by the quotient of the latent and sensible heat:

$$D_a = \frac{c_p \cdot \rho_a \cdot T}{L \cdot \rho_a (0.622 \cdot e/p)}. \tag{2}$$

This quotient has a minimum for each T which is formed at a saturation vapour pressure (E) when $e = E(T)$. The value of air humidity at this point:

$$D_{a\ \max} = \frac{\rho_a \cdot c_p \cdot T}{L \cdot \rho_a (0.622\, E(T)/p)}. \tag{2.a}$$

To express the joint value of sensible and latent heat, the equivalent temperature (Θ) is used (*Gates*, 1980):

$$\Theta = T + e/\gamma, \tag{3}$$

where γ is psychrometrical constant:

$$\gamma = \frac{c_p \cdot p}{0.622 \cdot L} = 0.66 \quad (\mathrm{hPa\ °C^{-1}}).$$

So, by the equivalent temperature, the humidity of air can be determined:

$$D_a = t/(e \cdot 0.66). \tag{4}$$

The expression above is a ratio based on thermodynamics and is particularly well suited to determine the degree of the atmospheric drought if the temperature in the numerator is expressed in K. The denominator in Eq. (4) will grow in range as temperature rises, and, so, the function will tend to fall if the e/E ratio is low. This means that with the increase of air drought, the D_a value will proportionally fall. Consequently, the quotient of the two terms determining the

value of equivalent temperature in Eq. (4) expresses a specific thermodynamical state, which, on the one hand, is inversely proportional to relative air humidity and, on the other, effects the numerical value of humidity to a slight extent only. Therefore, it is not fitted for the practical definition of air drought, since it does not express the sensible and latent heat extractions and, so, can only be considered as a stationary characteristic.

The value of atmospheric dryness is a very significant value in physical and also in ecological sense. To determine its value, the formula of potential evaporation (PE_0) can be used as a starting point, which is (*Szász*, 1973):

$$PE_0 = a[f(v) \cdot 0.0054\,(t + 21)^2\,(1 - e/E)^{2/3}] \quad \text{mm}, \tag{5}$$

where t is daily mean temperature (°C), e/E saturation ratio, v daily average wind speed (m s^{-1}), $f(v)$ effect of wind speed, a the factor correcting the microadvectional effect. The latter is needed because the constant of the formula was determined by pan evaporation measurements (a = 0.85–1.00). This equation is valid for 2 m s^{-1}. So, the calculation is made by the evaporation according to the temperature and the water vapour saturation ratio. A parabola function can be used to describe the potential evaporation determined by the temperature:

$$PE_0\,(t) = a\,(t - t_0)^2. \tag{6}$$

In this function the apex of the parabola is on axis x. This criterion expresses that the minimum of PE_0 (t) equals 0. If the square roots of both sides of the equation are extracted:

$$\sqrt{PE_0} = \sqrt{a} \cdot t - \sqrt{a} \cdot t_0, \tag{7}$$

i.e. $\sqrt{PE_0}$ is a linear function of t temperature. The line characteristics fitting the experimental measurements perfectly are $r^2 = 0.9990$, $a = 0.005356$, $t_0 = 20.89 \approx 21$ °C. For relative humidity the following relationship was found to be adequate:

$$\log PE_0\,(e/E) = \log a' + b \log (1\text{–}e/E),$$

i.e. the logarithm of PE_0 is the linear function of the logarithm of the (1–e/E) value. The test of the calculation results shows that

- the correlation can be considered linear,
- by the fittings based on experimental measurements the lines are parallel, i.e. the direction tangent of the lines in the examined interval is independent of the temperature (5–40 °C).

Based on the statements above, $b = 0.06645$, the determination coefficient $r^2 = 0.005$.

These calculations led us to the interpretation of the role of temperature and saturation ratio in the degree of evaporation.

3. The definition of atmospheric dryness

There exists no physically defined value for atmospheric drought used in practical sense in agrometeorology and in other related fields of science, though there has been a high demand for it (*Munn*, 1970; *van Eimern* and *Häckel*, 1979). The frequency of parallelism between temperature (= 30°) and relative humidity (= 40%) was examined by *Rákócziné Wagner* (1976) in 12 data series between 1930–1960. She concluded that, in Hungary, the frequency is the highest in July and August in 10–25% intervals. *Slatyer* (1963) and *Cary et al.* (1968) investigated the water movement in plants under dry conditions. They found that the physical state and mobility of the water in the plant, in the vascular tissues in particular, are closely correlated with atmospheric dryness. The hydrical state, the growth and, consequently, the productivity of a plant are determined by the frequency value of the water potential in the air and plant foliage *(Kreeb*, 1963; *Bierhuzien* and *Slatyer*, 1965; *O'Leary* and *Knecht*, 1971). Results of national and international research support the view that the numerical expression of the atmospheric dryness is an actual demand by meteorologists and ecologists. To define the numerical value of the atmospheric dryness, we used the product of the following proportions as a starting point

$$D_a = 100 \frac{t_a}{t_{25}} \cdot \frac{(e/E)_a}{(e/E)_{40}} = \frac{PE_a}{PE_{0\,ref}}, \tag{9}$$

where D_a is a value without dimension to express the degree of atmospheric dryness, t_a and $(e/E)_a$ are air temperature and saturation ratio, t_{25} and $(e/E)_{40}$ the temperature and saturation ratio at a given time, PE_a potential evaporation with different temperature and saturation ratio values, PE_{0ref} potential evaporation with temperature: 25 °C and saturation ratio: 0.4. As atmospheric dryness tends to be formed around noon, the reference values were selected accordingly. The reference values can be optional, depending, though, on the type of the ecological system (e.g. hydromorph, xeromorph). As the drying effect of the various elements is different, instead of their direct values, the proportions of the values of Eq. (5) are being compared,

$$t_{25} = 0.0054\ (25 + 21)^2 = 11.43$$

$$(e/E)_{40} = (1 - 0.4)^{0.67} = 0.71.$$

In the estimations these two reference values were used. The product of the temperature and of the evaporation value (determined by the saturation ratio) expresses the evaporation conditions of these two values and the size of resultant evaporation. Eq. (5) proves that the effect of the two elements in the process of evaporation is different, which is expressed by the difference in the exponents and by the order of magnitude of the coefficient of the two elements *(Fig. 1)*. The above impact functions are fitted for the numerical expression of atmospheric dryness:

$$D_a = 100 \frac{(0.0054 \cdot t + 21)^2}{11.43} \frac{(1 - e/E)^{0.67}}{0.71} .$$

The denominator involves the function of the temperature (25°C) and the saturation ratio (0.4), which supply the basis of the correlation.

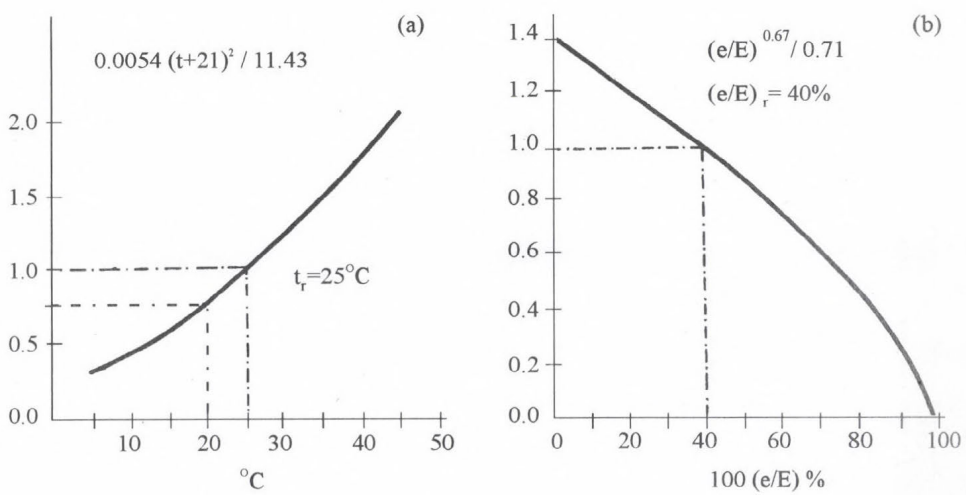

Fig. 1. Calibration curve for effectivity of the temperature (*a*), effectivity of the saturation ratio (*b*).

According to the estimations, relative atmospheric dryness is increased by a decrease in temperature and by an increase in relative humidity. *Table 1* shows the impact function of temperature and saturation ratio (in percentage), well representing the contraversary changes that go with the increases of the two elements. It can be concluded that the atmospheric dryness value (D_a) expresses an evaporation ratio compared to any optional reference value, as the numerator represents atmospheric evaporation potential, whereas the denominator is a standard value (25°C, 40%). The quotient expresses the deviation from the standard value.

Table 1. Atmospheric dryness values in Debrecen

°C	e/E (percentage)									
	10	20	30	40	50	60	70	80	90	100
5	0.42	0.38	0.36	0.32	0.28	0.24	0.20	0.15	0.10	0
10	0.59	0.54	0.50	0.45	0.40	0.34	0.28	0.22	0.14	0
15	0.80	0.74	0.68	0.61	0.54	0.46	0.38	0.29	0.18	0
20	1.03	0.96	0.88	0.79	0.70	0.60	0.50	0.38	0.24	0
25	1.31	1.21	1.11	1.00	0.89	0.76	0.63	0.48	0.30	0
30	1.61	1.49	1.37	1.23	1.09	0.93	0.77	0.59	0.34	0
35	1.94	1.81	1.64	1.48	1.32	1.12	0.93	0.71	0.44	0
40	2.29	2.12	1.94	1.75	1.56	1.33	1.10	0.84	0.53	0
45	2.70	2.49	2.29	2.06	1.83	1.57	1.30	0.99	0.62	0

The atmospheric dryness value is a complex climatic parameter whose graphical representation facilitates estimation making (*Fig. 2*).

As the formula exists for temperatures down to –11 °C, the dryness value can be used in a diversity of regions.

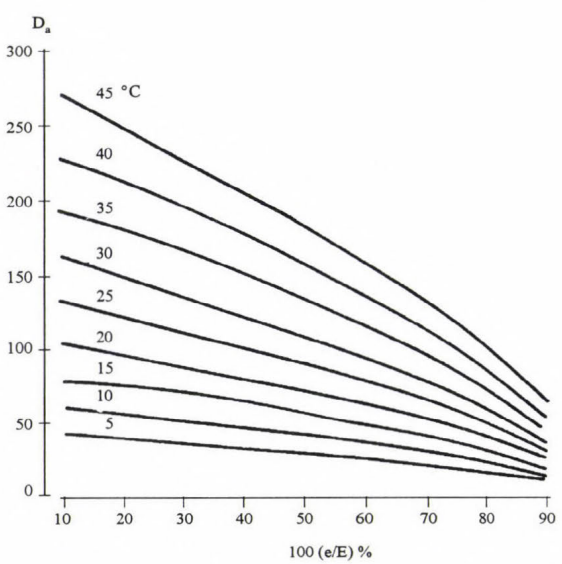

Fig. 2. Nomogram for the determination of the atmospheric dryness (D_a) from the temperature and relative humidity values.

4. Discussion

The atmospheric dryness value introduced above is well fitted for climatic and agro-meteorological investigations. Dryness is usually described by the

deficiency of rainfall. It has to be stressed, however, that the deficiency of rainfall could be seriously worsened by atmospheric dryness which is manifested by high temperature and low relative humidity. Atmospheric dryness is usually very heavy at midday, which produces adverse climatic and ecological conditions for plants with high water requirement. There are significant regional differences in this respect, especially in dry and hot periods. The values of air humidity and atmospheric dryness are considerably different in various climatic zones. Let us consider some examples proving the feasibility of the value in question.

Atmospheric dryness value strongly depends on the climatic zones and is closely related to rainfall. *Fig. 3* shows the precipitation and temperature data of representative areas of 8 different climatic zones (*Péczely*, 1984). The part of the figure dealing with temperature represents annual average fluctuation. The fluctuations of the atmospheric dryness values, determined by the monthly temperature average of the coldest and warmest months can be seen at the bottom figure (*c*). The covering curve involving the lower and upper values gives a synoptical representation of the annual fluctuations in the different climatic zones. Giving a detailed global analysis of the examined value does not belong to the subject of this paper, this figure, however, convincingly proves

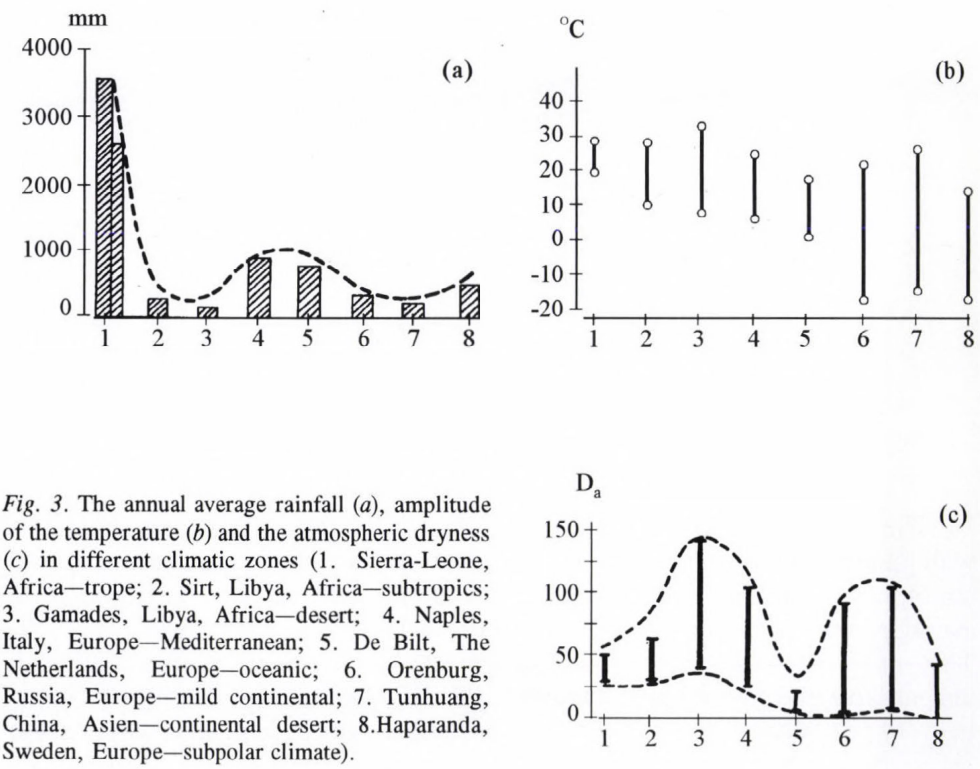

Fig. 3. The annual average rainfall (*a*), amplitude of the temperature (*b*) and the atmospheric dryness (*c*) in different climatic zones (1. Sierra-Leone, Africa—trope; 2. Sirt, Libya, Africa—subtropics; 3. Gamades, Libya, Africa—desert; 4. Naples, Italy, Europe—Mediterranean; 5. De Bilt, The Netherlands, Europe—oceanic; 6. Orenburg, Russia, Europe—mild continental; 7. Tunhuang, China, Asien—continental desert; 8.Haparanda, Sweden, Europe—subpolar climate).

its feasibility. The regional distribution of atmospheric drought values can help to draw the boundaries of the different plant-ecological regions. Each fraction of the family of curves in Fig. 2, in fact, represents different climatic characteristics. *Fig. 4* is an attempt to locate the different climatic and ecological regions according to their atmospheric dryness values and the fluctuation of temperature.

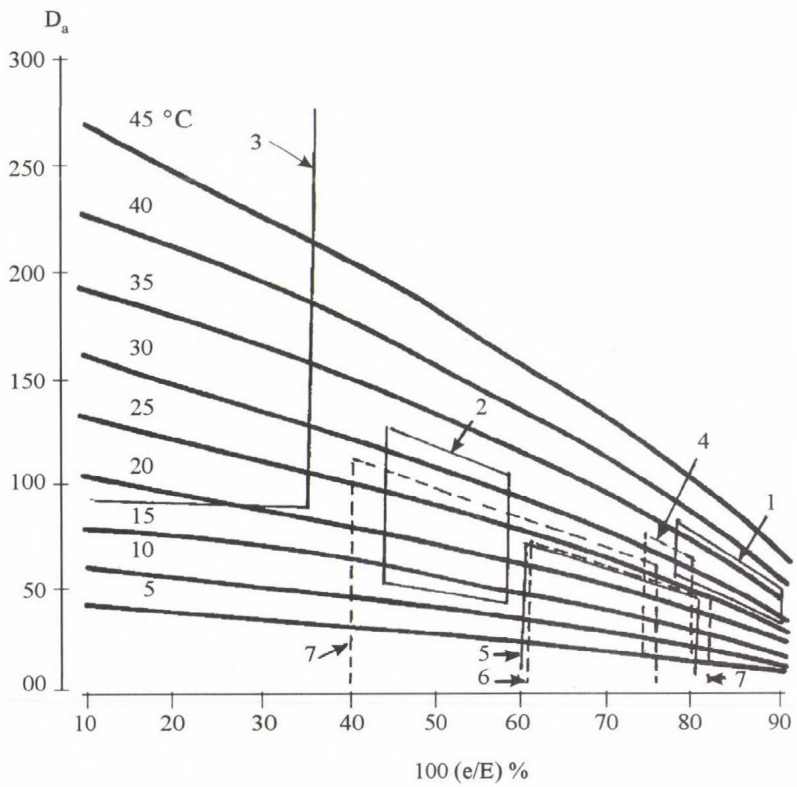

Fig. 4. Surfaces and dividing boundaries of different climatic zones in the D_a nomogram.

The atmospheric dryness values provides scopes for analyses in a given area with heterogenous climate. *Fig. 5* shows the regional distribution of the atmospheric dryness value calculated from the daily maximum temperature averages and the average relative humidity at 14 UTC in July from 1901–50. This map gives a good representation of the consequent effect of high temperature and low relative humidity. The highest atmospheric dryness value in every two maps is formed in the southernmost parts of Hungary, whereas the

lowest relative humidity values come from the middle but not the hottest parts of the country. A similar conclusion can be drawn from Fig. 5a. In this case the value of temperature was calculated from the average absolute maximum and the 14 UTC relative humidity values reduced by 5%. Compared with Fig. 5b, it can be concluded that in the Fig. 5a the dryness values are 50–60 units higher, but there is no significant difference between their geographical distribution. It is commonly known, that in the Carpathian-basin the highest atmospheric drought values are formed in July, that is why our attention was basically focused on the detailed analysis of this period.

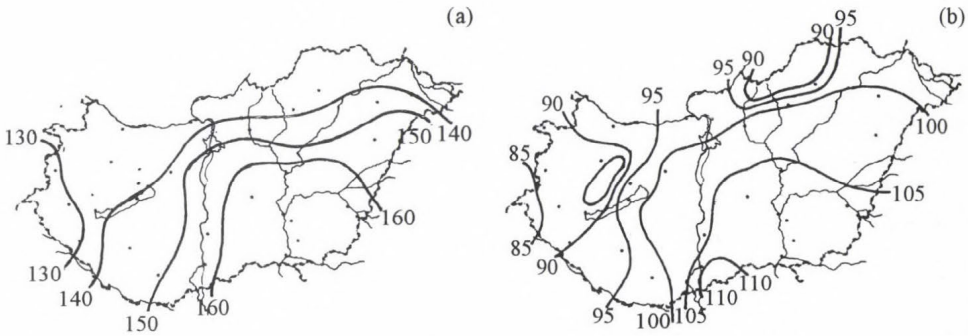

Fig. 5a. Values of the atmospheric dryness from the average absolute temperature maximum and minimum relative humidity (14 UTC) in Hungary (1901–1950).

Fig. 5b. Values of the atmospheric dryness from the average temperature maximum and relative humidity (14 UTC) in Hungary (1901–1950).

The atmospheric drought values for Debrecen are fairly near the average values common in the Hungarian Great Plain. This is why the data observed in Debrecen are demonstrated here:

July:

daily temperature average:	20.7°C
daily fluctuation average:	±6.1°C
average relative humidity:	68%
daily fluctuation average:	±15%
daily average maximum dryness value:	92.5
daily average minimum dryness value:	44.1
average atmospheric dryness:	68.3

A comparison made between the latter value and the D_a interval in column six, Fig. 4, suggests that the continental character of the Hungarian plain in summer is regulated by influences of continental climate.

Atmospheric dryness values vary within a wide range. To increase information in this respect, the frequency of daily dryness averages for the years 1951–1990 was established (*Table 2*). The estimated values are placed in vary wide intervals, which indicates that there is an alteration of continental and ocean predominance.

Table 2. Frequency of atmospheric dryness value calculated by daily averages

D_a	Number of day	Frequency, %
> 10	1	0.08
11 - 20	28	2.26
21 - 30	74	5.97
31 - 40	167	13.47
41 - 50	239	19.27
51 - 60	254	20.48
61 - 70	239	19.27
71 - 80	143	11.53
81 - 90	49	3.95
91 - 100	35	2.82
101 - 110	8	0.65
111 - 120	2	0.16
121 - 130	1	0.08
Sum	1240	100.00

The extremes of drought values in Hungary (*Climatic Atlas of Hungary*, 1967) run between 0–193. The dryness values reflect the climatic conditions, so, high extremes may follow each other. The very heavy drought spell of the summer of 1983 was characterized by sharp fluctuations in temperature and moderate changes in the relative air humidity. The quick change in the atmospheric drought values can be attributed to the effect of advection regulated by synoptic weather processes. *Fig. 6* is an example of this, showing the atmospheric dryness values estimated by values measured at 14 UTC on 17 days of a very hot summer (1983). On the first 7 days there was dominated subtropical continental air mass (NE-Africa), its predominance was broken by an attack of cold air front from the North-Atlantics.

The diurnal change in the atmospheric dryness values is the result of temperature cycles, as shown in *Fig. 7*. The solid curve demonstrates the average diurnal course in July, with the parameters belonging to the extreme values also are represented. The dashed curve indicates the diurnal course of the atmospheric dryness in a hot, dry period. The difference between the two diurnal courses supports the extreme character of the climatic conditions in Debrecen.

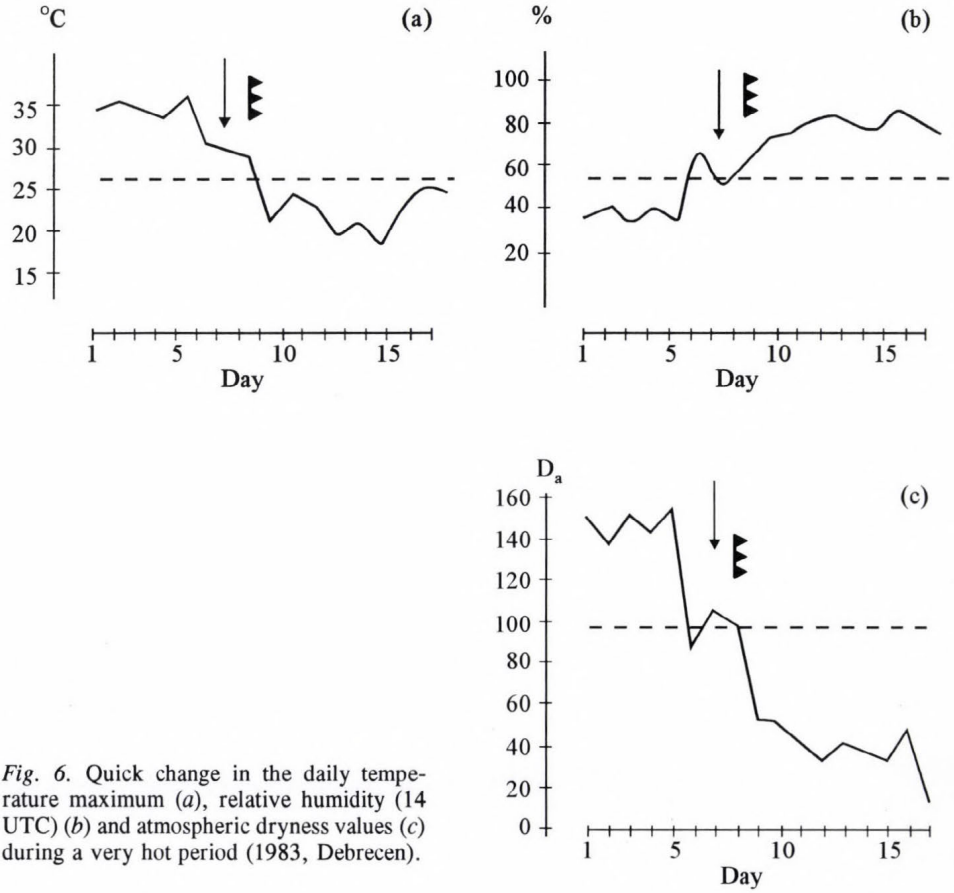

Fig. 6. Quick change in the daily temperature maximum (*a*), relative humidity (14 UTC) (*b*) and atmospheric dryness values (*c*) during a very hot period (1983, Debrecen).

5. Conclusions

The atmospheric dryness value is a proportion which can physically be deduced: in fact, it is the ratio between the value calculated by the $t = 25°$ and $e/E = 0.4$ and the existing potential evaporation. We assume that relative air humidity exclusively does not provide sufficient basis to determine the atmospheric dryness value. The definition should be based on the theory that increasing temperature results an increase in the water vapour saturation interval. That is, the degree of dryness is effected by the temperature as well, the saturation water vapour pressure, which is increasing as the temperature is rising. Air water potential is dependent on the air temperature and the vapour saturation ratio. The temperature component of the water potential: $(\rho W/M \cdot RT)$, where W is water molecule weight, R gas constant (8.3143 J K^{-1} mol^{-1}). This value is only slightly affected by the temperature. The water potential value changes according to the logarithm of the saturation ratio mainly, and so,

of two factors determining evaporation, vapour saturation ratio should be taken priority. To bridge this difference in their importance we used Eq. (5), which contains the product of temperature and air humidity evaporation potential. This multiplicative linkage makes the widening of the scales also possible. So, the product of the effect ratio of the two meteorological elements is fit to truely express atmospheric drought conditions.

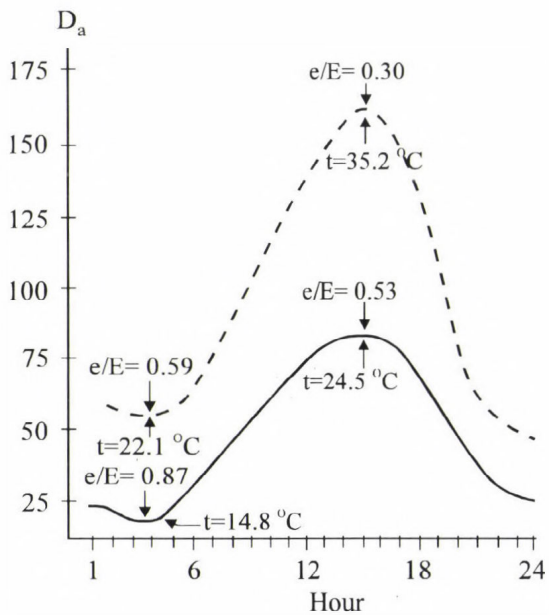

Fig. 7. Diurnal course of the average (solid) and maximum (dashed) atmospheric dryness in Debrecen.

Atmospheric dryness is a relative value in ecological sense as well. The atmospheric dryness value, naturally, allows high temperature and low relative humidity for drought-resistant plants, the inverse of which is true for plants with high water requirement. Taking temperate zone conditions, 25°C and a relative humidity of 40% can be considered as reference values for mezophyte requirements, so they are fit for general use. The advantage of estimation is that the product of atmospheric dryness ratio is applicable for different ecological conditions, however, the value intervals calculated by the previously discussed method also fit into the hydric cathegories:

— hydrophytic $D_a = 0 - 75$,
— mezophytic $D_a = 25 - 100$,
— xerophytic $D_a = 50 - 200$.

The above intervals vary in a wide interval for the reason that temperature has also been involved.

The above mentioned results are well applicable for agrometeorological, agroclimatological and ecological researches.

References

Bierhuzien, J.F. and *Slatyer, R.O.*, 1965: Effect of atmospheric concentration of water wapor and CO_2 in determining transpiration – photosynthesis relationships of cotton leaves. *Agric. Meteorol. 2*, 259-270.

Cary, J.W., Jensen, M.E. and *Fisher, H.D.*, 1968: Physical state of water in plant xylem vessels. *Agron. Journ. 60*, 167-169.

Climatic Atlas of Hungary, vol. II, 1967. Akadémiai Kiadó, Budapest.

Eimern, van J., Häckel, H., 1979: *Wetter- und Klimakunde*. Ulmer Verlag, Stuttgart.

Gates, M.D., 1980: *Biophysical Ecology*. Springer Verlag, New-York-Heidelberg-Berlin.

Götz, G., Rákóczi, F., 1981: *A dinamikus meteorológia alapjai*. Tankönyvkiadó, Budapest. 483 p.

Kreeb, K., 1963: Hydrature and plant production. In The Water Relations of plants (eds.: *A.J. Rutter* and *F.H. Wintehead*). Blackwell Sci. Publ., London.

Munn, R.E., 1970: *Biometeorological Methods. Environmental Methods*. Academic Press, New-York and London.

O'Leary, J.W. and *Knecht, G.N.*, 1971: The effect of relative humidity on growth, yield and water consumption of bean plants. *J. Amer. Soc. Hortic. Sci. 96*, 263-265.

Péczely, Gy., 1984: *Climate of the Earths* (in Hungarian). Tankönyv Kiadó, Budapest.

Rákócziné Wágner, M., 1967: *Complex-Climatological Investigation of Atmospheric Drought* (in Hungarian). *Időjárás 71*, 34-39.

Stocker, O., 1960: Physiological and morphological changes in plants due to water deficiency. In *Arid Zone Research*. UNESCO XV., Paris, 63-104.

Szász, G., 1973: A new method of estimating potential evapotranspiration (in Hungarian). *Hidrológiai Közlöny*, 435-442.

IDŐJÁRÁS

Quarterly Journal of the Hungarian Meteorological Service
Vol. 98, No. 4, October–December 1994

Brief survey on recurrences of extreme rainfalls in Genoa, Italy

G. Russo and **A. Sacchini**

Department of Earth Science, University of Genoa,
V. le Benedetto XV 5, Genoa, Italy

(Manuscript received 17 February 1994; in final form 16 November 1994)

Abstract—This paper is a brief survey on extreme rainfalls (considered as precipitations of remarkable intensity with overflowing phenomena) recorded at the University Meteorological Observatory of Genoa in the last 100 years. We found that meteorological phenomena similar for causes (intense precipitation) and effects (floods) don't follow any particular cycle as regards their return periods and they are not linked to climatic periods particular for their rainfall or droughtiness. The years of the events, associated with different intensity of precipitation in the Standardized Distribution are distributed into 4 'pairs'. Temporal steps between events of the same 'pair' or extreme rainfalls cycle (λ = 8, 15, 22, 25 years) increase with the growing up of the annual precipitation; these intervals can be associated with a precise exponential sequence. Finally, according to this survey method, return periods of new possible extreme events are proposed.

Key-words: standardized distribution of annual precipitations, flood events, Genoa.

1. Introduction

On September 27th, 1992 a torrential precipitation caused the overflow of many streams flowing through Genoa; there were deads and damages. Meteorological characteristics of last flood have been rather similar to other tragic events occurred in the last 40 years; the meteorological causes of these exceptional rainfalls were studied by many authors (*Bossolasco et al.*, 1970, 1971; *Dagnino et al.*, 1975, 1978). Flood events from 1957 to 1992 developed according to the same dymanics represented in *Fig. 1*:

— an Atlantic disturbance over Spain, bringing cold air as joined to a deep depression in the north-western sectors of Europe;
— stopping action towards the eastern sectors by an anticyclonic ridge located over Balcans;

— this blocked disturbance conveys warmer and wetter southern air, flowing towards this frontal system against Ligurian Appenninic range so that very intense and concentrated orographic and frontal precipitations fall over on north-western Italy.

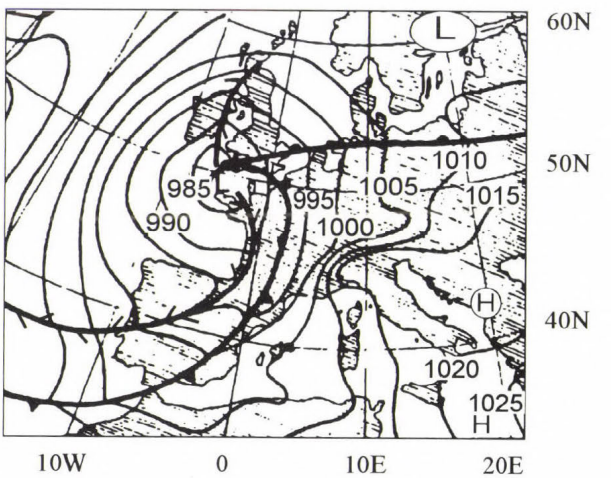

Fig. 1. Weather map during 1977 event and typical of extreme rainfalls events in Genoa (after Europäischer Wetterbericht of Deutscher Wetterdienst).

In this work we don't consider the already studied mechanisms generating these phenomena, but we investigate their recurrences and the possibility to forecast the existence of particular climatological epochs favouring these events. Considering return frequences of extreme rainfalls, we can say these events are not so rare in Genoa and a planetary control system, not even surely known, exists. The possibility of forecasting long term returns of these events is very complex; floods are the consequence of more circumstances like 'a prolonged period, or close succession of periods, of large-scale precipitation; severe transitory storm; violent convective activity' (*WMO, GARP,* 1975).

2. Data and methods of analysis

In *Table 1* all the years and months are shown in which heavy precipitations occurred; we consider those events memorable for their unusual intensity (mm/h) and for damages brought about to the community, such as stream overflowings, landslides and victims.

Table 1. Extreme rainfalls in Genoa, precipitation amount and intervals in years between the successive events from 1892

Year	Date	Day	Event	Total precipitation (mm)		Breaks
				Month (1)	Year (2)	
1892	October	6	181.3	358.3	1445.2	0
1907	October	24–25	246.1	599.4	1362.9	15
1926	October	21–22	86.7	215.7	2008.8	19
1945	October	29–30	275.8	352.0	1127.8	19
1951	November	7–8	396.4	597.6	1990.8	6
1953	September	19	218.6	489.0	1210.0	2
1970	October	7–8	449.2	454.4	1641.6	17
1977	October	6–7–8	370.0	490.6	2189.8	7
1992	September	27–28	450.8	551.0	1690.0	15

(1) Monthly averages: September 113.6 mm, October 202.4 mm, November 170.6 mm
(2) Annual mean: 1287.9 mm

It may be observed that the probability of rainy days with extreme precipitation amounts in Genoa is very high in the beginning of autumn; in particular, October presents the higher occurrence for extreme rainfall events. At the end of dry season (from the end of September to the beginning of November), the Azore's high pressure, bringing a long period of good weather in summer, in the Mediterranean area, is subject to a rapid collapse (equinoctial perturbations) with infiltrations of polar maritime air under complex interactions of different oceanic and continental effects and violent circulation between land and sea (*Bossolasco et al.*, 1973). In October, in particular, the unstable air masses (northern polar maritime air and southern warm, wet maritime air) happens to bear intense frontal and orographic precipitations in the Ligurian Appennine.

As a matter of fact in October six of nine flood events were recorded in the last 100 years; the others occurred about the end of September or the first days of November. Even ancient Genoese chronicles report big flood events in 1402 and 1822, both of them in October (*Giustiniani*, 1407; *Gazzetta di Genova*, 1822).

In Table 1 there are also included total precipitations, occurred in the month and in the year of the event; this helps to understand the importance of the events compared to monthly and annual precipitation amounts. It is worth

underlying on October 7–8, 1970 there was a rainfall of 449.2 mm equivalent to the 98.9% of the precipitation fallen in all the month. In the last column interval periods among floods are shown; evident recurrences are not present. Other authors applied numerical analysis to the precipitation series of Genoa looking for periodic recurrences (*Flocchini et al.*, 1981; *Flocchini*, 1983) by using the DFT (Discrete Fourier Transform); they found maximum spectral densities around 22 years, generally ascribed to sunspots cycles and planetary phenomena.

We wanted to verify the hypotesis that each event is associated with a climatic discriminant linked to the historical trend of precipitation series, i.e. the event occurs in a very rainy year or that happens in a rather normal or drought year. So we analysed the trend of annual departure of precipitations from the mean for the historical series of Genoa (*Fig. 2*). Arrows point out the years of the events with their annual departure from the mean (1287.9 mm). Comparisons between Fig. 1 and Table 1 allow to say that there are not climatic periods in which flood events exclusively occur. The curve of Standardized Cumulative Distribution of total annual precipitation amounts has been built (*Fig. 3*). This is the procedure we follow to point out whether a correlation between floods and particularly distinguishable climatic periods (rainfall or droughtiness) exists.

In the curve we group single events according to precipitation amount of the year of occurrence (see Table 1) to verify single event position in comparison with the mean value, considering their variability or standard deviation from the mean. The curve shows a slight asymmetry towards maximum values of precipitation; in 1872 the absolute maximum value of the whole historical series (2872 mm) was recorded, although without flood events.

Fig. 3 points out that the events occur irregularly in the curve but they seem to group in 'pairs' or 'trios', distant from the mean with a different standard deviation; the arrows show distances λ (years) among events of the same cluster (λ = 8, 15, 22, 25-26 years). The clusters ('pairs') are distributed in the curve prevalently joined to annual precipitation amounts superior to the mean; in fact, the main recorded events (1970, 1977, 1992) took place during many rainy periods; the 'pair' 1945-1953 has an exception, because it's associated with annual precipitations a little inferior to the mean.

The following *list* has been worked out to classify different climatic periods, which analysed flood clusters are associated with:

1. * 1945-1953, two events:
- pair W.D. (Weakly Dry):
- recurrences in the cluster every 8 years;
- precipitation amount of the year of occurrence a little inferior to the mean; standard deviation 0.5;
- this series ended in 1953.

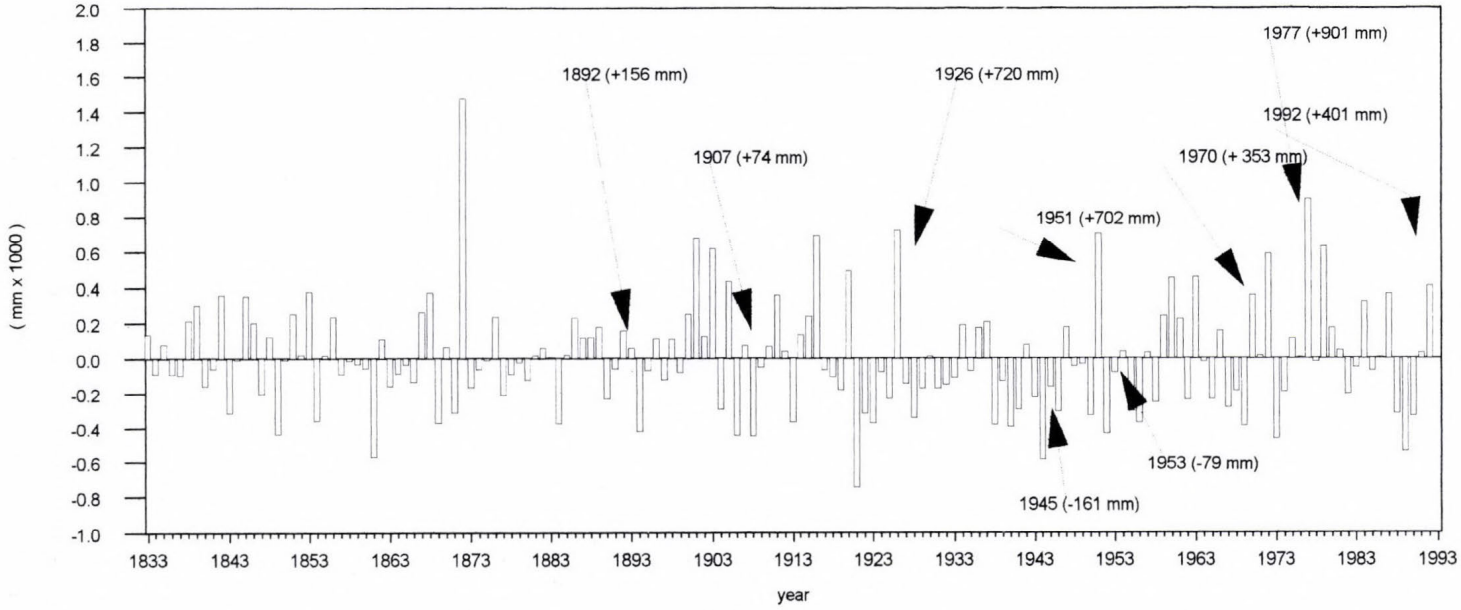

Fig. 2. Departure from the mean of annual precipitation amounts in Genoa (1833–1992); arrows point out last hundred year flood events.

2. * 1892-1907, two events:
- pair W.R. (Weakly Rainy):
- recurrences in the cluster every 15 years;
- annual precipitation amounts a little superior to the mean; standard deviation 0.5;
- this series ended in 1907.

3. * 1970-1992, two events:
- pair I.R. (Intensively Rainy):
- recurrences in the cluster every 22 years;
- annual precipitataion amounts superior to the mean; standard deviation 1.5;
- events which could probably appear 22 years after 1992 event, in 2014.

4. * 1926-1951-1977, three events:
- pair V.I.R. (Very Intensively Rainy):
- recurrences in the cluster every 25 years;
- annual precipitation amounts much superior to the mean; standard deviation 2.5;
- there is the possibility that periodicity has not still ended: probably the next flood event of this kind may verify in 2003-2004.

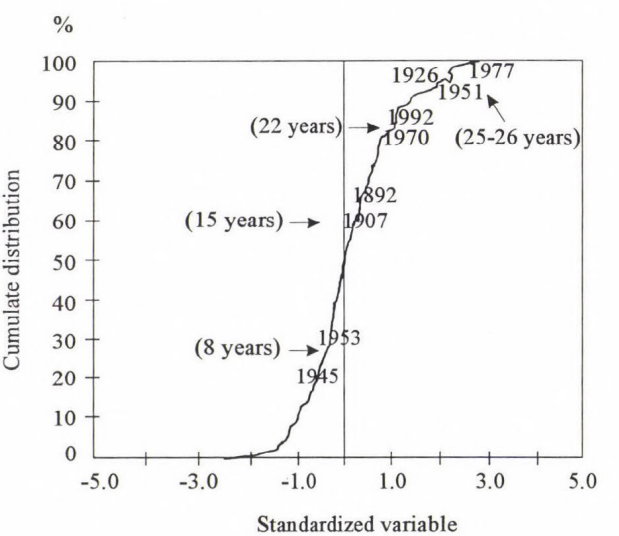

Fig. 3. Representation on the Standardized Cumulative Distribution of total annual precipitation and positions of extreme rainfalls; in parentheses intervals between the successive events similar for distance from the mean of their total annual precipitation are given.

Results show that extreme events, even if equivalent in their metorological background, are different for three factors:

(1) these events are clusterizable according to climatic periods different for annual precipitation amount;
(2) the events distribute in 'pairs' pointing out the beginning and the end of a single flood cycle: all pairs are ended except for 1977 ($\lambda = 25$ years: this pair will be likely to end in 2003);
(3) recurrences periods of every cycle increase with the growing up of the precipitation amount of the year of occurrence.

Sequence T between intervals of similar events seems to follow an exponential progression like $n^{\sqrt{2}}$ where $n = 1, 2, 3...$(*Table 2* and *Fig. 4*); in Table 2 comparisons among theoretical and experimental intervals are reported together with a classification of the events. It's intersting to note that, in the series we can analyse that extreme rainfall events don't fill in the 'n' positions available in the table; we suppose that, if the criterion we adopted (that every event may belong to different climatic patterns measurable through annual trend of precipitation amount) is associated with a physical reality of temporal successions, other 'n' extreme rainfalls cycles, we could not verify, may virtually exist.

Table 2. Clusters of extreme rainfall events according to rainfall or droughtiness of the year of occurrence, intervals in years between elements of the same group and their positions on the extrapolation curve

n	Intervals		Clusters		Years
	Computed	Real			
1	1.0	?	V.I.D.	(very intensive dry)	
2	2.7	?	I.D.	(intensive dry)	
3	4.7	?	V.D.	(very dry)	
4	7.1	8	W.D.	(weakly dry)	1945, 1953
5	9.7	?	U.D.	(usually dry)	
6	12.6	?	U.R.	(usually rainy)	
7	15.7	15	W.R.	(weakly rainy)	1892, 1907
8	18.9	?	V.R.	(very rainy)	
9	22.4	22	I.R.	(intensive rainy)	1970, 1992
10	26.0	26	V.I.R.	(very intensive rainy)	1926, 1951, 1977
11	29.7	?	U.R.	(unusually rainy)	

Return periods and cycles, presenting periodicities similar to those ones we found, were already ascertained at least for as concerning some river floods in the northern Italy and generally some earth phenomena, such as variations in geomagnetic field declination, annual precipitations, river flows, atmosphere composition (*Rima*, 1962). In particular, we can remember *Mosetti* (1956), who summarized periodicities he found in earth phenomena, establishing a relation between the mean of the observed periods and a theoretical succession according to a geometrical progression of kind $\sqrt{2}$. Besides, it is important to

stress the presence of the 22 year cycle already mentioned, which seems to demonstrate the possible relationship between sunspot cycles and the weather and climate. However, as return periods of found events are also rather different from this particular cycle, we cannot draw precise conclusions in this sense according to the indications of other authors (*Pittock*, 1978a, b).

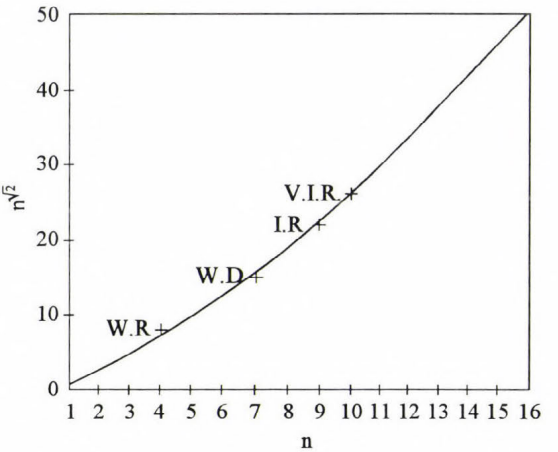

Fig. 4. Positions of clusters of extreme rainfalls events on the extrapolation curve.

3. Conclusive remarks

Even if the number of events is little, results presented lead us to point out some main elements:

(a) flood precipitations occur independently from the climatic period: they are present both in very intensively rainy and in drought periods;
(b) the criterion which associates every annual precipitation amount with the year of occurrence of the extreme rainfall, allows to distinguish 4 different flood clusters;
(c) these clusters appear in 'pairs' marking the beginning and the end of each flood cycle;
(d) distances in years between events of each 'pair' are proportional to the growing up of the Standardized Cumulative Distribution curve of the annual precipitation amount;
(e) distances in years among each flood cluster seem to follow a characteristic numerical succession.

Characteristics of this model don't allow absolute forecastings; anyhow, the method we used can be a contribution to the future research in the field of flood phenomena forecasting.

APPENDIX

On September 23, 1993 another torrential precipitation with overflowing phenomena ensued in Genoa (456.0 mm the precipitation in the event, 519.2 mm monthly amount). The meteorological conditions causing the event were the same of last ones. Trying to include this event in our model, we inserted the annual precipitation amount (1159.6 mm) in the Standardized Distribution. This value inserts the event between 1945 and 1953 in a year W.D. belonging to the 'pairs' with $\lambda = 8$ years. In *Fig. 5* clusters are represented in horizontal layers according to precipitation amount of the occurrence year of events and to their intensity.

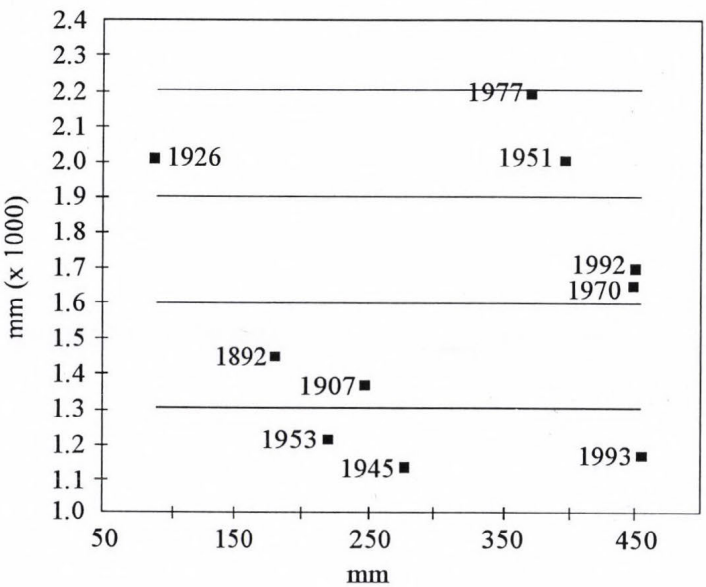

Fig. 5. Representation of years of extreme rainfall events according to their total annual precipitation (abscissa) and intensity of the event (ordinate).

We can suppose that events of the cluster W.D. have started again and so next event will likely ensure in 2001; that, together with the event of cluster V.I.R., expected for 2003, will be likely to lead to appearence of two different 'pairs' in very close years.

Characteristics of this model don't allow absolute forecastings; anyhow, the method we used can contribute to future research in the field of flood phenomena forecasting.

References

Bossolasco, M., Dagnino, I., Flocchini, G., 1970: Situazioni meteorologiche tipiche di precipitazioni forti ed estese sull'Italia Settentrionale. *Geof. e Meteor. XIX, 5-6*, 143-151.

Bossolasco, M., Cicconi, G., Dagnino, I., Flocchini, G.,1971: Le cause meteorologiche della alluvione su Genova del 7-8 ottobre 1970. *Geof. e Meteor. XX, 3-4*, 122-132.

Bossolasco, M., Dagnino, I. and *Flocchini, G.*, 1973: On sea and land climate differences. *Bonner Meteor. Abhandlungen 17*, 467-473.

Dagnino, I., Flocchini, G., Palau, C., 1975: Sulle cause meteorologiche che determinano precipitazioni anomale sulla Liguria. *Atti Acc. Ligure Scienze e Lettere XXXI*, 149-168.

Dagnino, I., Flocchini, G., Palau, C., 1978: Le precipitazioni del 6-10 ottobre 1977 sulla Liguria centrale. *I.T.A.M. 1978*, 267-270.

Flocchini, G., Palau, C., Repetto, I. and *Rogantin, M. P.*, 1981: A mathematical model of the field of precipitation. *Il Nuovo Cimento 1*, 673-681.

Flocchini, G., 1983: On the regularization of the pluviometric series. *2nd Int. Meet. Stat. Climat., Lisbon, September 1983.*

Gazzetta di Genova, 1822: Alluvione. 26 ottobre 1822.

Giustiniani, A., 1407: Annali della Repubblica di Genova; libro IV. vol. II.

Mosetti, F., 1956: Considerazioni preliminari per una legge sulle periodicità naturali. *Tecn. It., Rivista di Ingegneria e Scienze, 8.*

Pittock, A.B., 1978a: A critical look at long term sun-weather relationships. *Rev. of Geoph. and Space Physics 16*, 400-415.

Pittock, A.B., 1978b: Solar cycles and the weather: successful experiments in autosuggestion? In *Solar and Terrestrial Influences on Weather and Climate*. D. Reidel, Dordrecht, pp. 181-191.

Rima, A., 1962: Considerazioni sul periodo undecennale dei fenomeni terrestri. *Geof. e Meteor. X, N. 1, 2*, 34-44.

WMO, GARP, 1975: The physical basis of climate and climate modelling. No. 16, 33.

NEWS

ANNOUNCEMENT

International Conference on Environment and Informatics (EN-IN) in Budapest, Hungary, June 29 – July 1, 1995

International Conference on Environment and Informatics will be organized in Budapest between June 19th and lst July 1995 by the Computer and Automation Research Institute, the Hungarian Academy of Sciences and SCOPE Meeting Co. Ltd. The sponsor of the Conference is the Hungarian Academy of Sciences (HAS) and co-sponsors are Institute for Economic and Environmental Development in Central and Eastern Europe, International Biometric Society, International Council of Scientific Unions (ICSU), International Federation of Automatic Control (IFAC), International Federation of Operations Research (IFORS), International Institute of Applied Systems Analysis (IIASA). The Conference Chairman is academician *I. Láng* (HAS).

The scope of the conference may be formulated as follows:
The management, protection and changes of environment are the most timely, exciting, dynamically developing problems of the day all over the world. In the past years, several global and regional programs have been started in the field of climatic changes, global and environmental changes, acid rains, biosphere, etc. Informatics, information systems, decision support models and mathematical methodology play fundamental role in these research projects.

One of the most significant impediments of the research work is the lack of information on the state and changes of environment. Although projects for the integration of information systems have also been launched, e.g. CORINE, they are in fact, restricted to the developed European countries and do not cover the less-developed Middle- and East-European countries. Considerable progress can only be expected if

— people working on the problems of environment will have a wide overlook on the achievements and the existing information systems, and
— will co-ordinate their work and find new areas of environmental sciences to explore.

Beside the global and regional research, a wide international co-operation would considerably help the scientific investigations running now isolatedly in the countries or regions.

The aim of the EN-IN Conference is to provide a forum for the experts

involved in environmental research and informatics to exchange ideas, views, information and initiate a better co-operation.
Topics to be concerned are the followings:

Information systems of environmental management
- — environmental indicators, standards
- — local and regional information and their interrelations
- — networks of information systems.

Environmental monitoring systems
- — characterization of the environmental state and its changes
- — methodological tools for the evaluations of the environmental state and change.

Environmental modelling
- — simulation models
- — stochastic models
- — risk analysis
- — decision support system.

Environmental impact assessement
- — methodological tools and techniques
- — case studies.

Informatics in the environmental management
- — implementations of the information systems, software and hardware
- — geographical information systems
- — networks
- — managing of environmental hazards.

Deadlines for contributors. Submission of abstracts: January 31, 1995; proposal for invited sessions: January 31, 1995; notification of acceptance: March 15, 1995 and submission of full papers: May 15, 1995.

Two copies of abstracts (max. 200–300 words) in English should be sent to the Conference Secretariat, indicating the author(s) name, the title of the paper, the affiliation and the mailing address of the contact author.

Proposals for invited sessions must include a brief description of the topics and a list of prospective authors and titles.

Proceedings containing all accepted papers will be published and available for all registered participants.

An *exhibition* will be held during the Conference. Whoever is interested in exhibiting, please inform the Secretariat.

The Conference will take place at the *Hotel Agro* (H–1121 Budapest, Normafa út 54), situated on Szabadság Hill, a quiet, nice part of the capital, offering beautiful panoramas of the city. The Hotel has excellent conference facilities and can accommodate all participants at reasonable prices. Attractions include an indoor swimming pool and fitness centre; a scenic forest is close by.

Address of the Conference Secretariat:

EN + IN Conference
Viktor Richter
Computer and Automation Research Institute
H-1518 Budapest, P.O. Box 63, Hungary
Phone: +361 181 0511, 166-5644
Fax: +361 186 9378, 166-7503
E-mail: h8746 ric @ella.hu

Workshop on Regional Climatology
organized on the occasion of the 90th anniversary
of the Milešovka Observatory foundation

The workshop is organized by the Institute of Atmospheric Physics, and the National Committee for the National Climate Programme of the Czech Republic, under the auspices of the Czech Meteorological Society.

The workshop will be held on 11–15 September 1995 in Prague. One day excursion to the Milešovka Observatory is planned within the workshop.

It is intended to hold the following sessions:

— mountain climatology,
— climate variability,
— advanced methods in climatology,
— regional climate change scenarios,
— methods for assessing climate change impacts,
— adaptation and mitigation strategies.

If you intend to participate, please contact as soon as possible Dr. Ivana Nemešová at the following address:

Institute of Atmospheric Physics
Boční II 1401, 141 31 Praha 4, Czech Republic
Tel.: 42 2 769703
Fax: 42 2 763745

ATMOSPHERIC ENVIRONMENT

an international journal

To promote the distribution of Atmospheric Environment *Időjárás* publishes regularly the *contents* of this important journal. For further information the interested reader is asked to contact *Dr. P. Brimblecombe,* School for Environmental Sciences, University of East Anglia, Norwich NR 7TJ, U.K.

Volume 28 Number 14 1994

Volume 28 Number 15 1994

Short Communications

Volume 28 Number 16 1994

N. Dombrowski, E.A. Foumeny, D.B. Ingham and *Y.D. Qi*: Prediction of 'blowout' from deposition gauges, 2685-2690.

D.S. Lee, J.A. Garland and *A.A. Fox*: Atmospheric concentrations of trace elements in urban areas of the United Kingdom, 2691-2713.

L.A. Gundel, W.H. Benner and *A.D.A. Hansen*: Chemical composition of fog water and interstitial aerosol in Berkeley, California, 2715-2725.

R.C. Musselman, T. Younglove and *P.M. McCool*: Response of *Phaseolus vulgaris* L. to differing ozone regimes having identical total exposure, 2727-2731.

A. Eldering, G.R. Cass and *K.C. Moon*: An air monitoring network using continuous particles size distribution monitors: connecting pollutant properties to visibility via Mie scattering calculations, 2733-2749.

T.R. Quackenbush, M.E. Teske and *C.E. Polymeropoulos*: A model for assessing fuel jettisoning effects, 2751-2759.

Volume 28 Number 17 1994

J. Kukkonen, M. Kulmala, J. Nikmo, T. Vesala, D.M. Webber and *T. Wren*: The homogeneous equilibrium approximation in models of aerosol cloud dispersion, 2763-2776.

D.P. Chock, S.L. Winkler, T.Y. Chang, S.J. Rudy and *Z.K. Shen*: Urban ozone air quality impact of emissions from vehicles using reformulated gasolines and M85, 2777-2787.

L.A. Moy, R.R. Dickerson and *W.F. Ryan*: relationship between back trajectories and tropospheric trace gas concentrations in rural Virginia, 2789-2800.

A.E. Milionis and *T.D. Davis*: Regression and stochastic models for air pollution—I. Review, comments and suggestions, 2801-2810.

A.E. Milionis and *T.D. Davis*: Regression and stochastic models for air pollution—II. Application of stochastic models to examine the links between ground-level smoke concentrations and temperature inversions, 2811-2822.

N. Kumar, A.G. Russel, T.W. Tesche and *D.E. McNally*: Evaluation of CALGRID using two different ozone episodes and comparison to UAM results, 2823-2845.

O. Klemm and *E. Schaller*: Aircraft measurement of pollutant fluxes across the borders of Eastern Germany, 2847-2860.

R.F. Griffiths: Errors in the use of the Briggs parameterization for atmospheric dispersion coefficients, 2861-2865.

E. Ganor: The frequency of Saharan dust episodes over Tel Aviv, Israel, 2867-2871.

R. Chester, G.F. Bradshaw and *P.A. Corcoran*: Trace metal chemistry of the North Sea particulate aerosol; concentrations, sources and sea water fates, 2873-2883.

B. Telenta, N. Aleksic and *M. Dacic*: Application of the operational synoptic model for pollution forecasting in accidental situations, 2885-2891.

Volume 28 Number 18 1994

D.A. Westenbarger and *G.B. Frisvold*: Agricultural exposre to ozone and acid precipitation, 2895-2907.

A.C. Ward: A simple procedure for ranking the performance of several air-quality models across a number of different sites, 2909-2915.

H.W.M. Witlox: The HEGADAS model for ground-level heavy-gas dispersion—I. Steady-state model, 2917-2932.

H.W.M. Witlox: The HEGADAS model for ground-level heavy-gas dispersion—II. Time-dependent model, 2933-2946.

H.W.M. Witlox and *K. McFarlane*: Interfacing dispersion models in the HGSYSTEM hazard-assessment package, 2947-2962.

D.J. Hall, S.L. Upton and *G.W. Marsland*: Designs for a deposition gauge and a flux gauge for monitoring ambient dust, 2963-2979.

H.H. Suh, G.A. Allen, B. Aurian-Blăjeni, P. Koutrakis and *R.M. Burton*: Field method comparison for the characterization of acid aerosols and gases,2981-2989.

H.E. Jeffries and *S. Tonnesen*: A comparison of two photochemical reaction mechanisms using mass balance and process analysis, 2991-3003.

Xiaoming Zhang and *A.F. Ghoniem*: A computational model for the rise and dispersion of wind-blown, buoyancy-driven plumes—II. Linearly stratified atmosphere, 3005-3018.

Xiaoming Zhang and *A.F. Ghoniem*: A computational model for the rise and dispersion of wind-blown, buoyancy-driven plumes—III. Penetration of atmospheric inversion, 3019-3032.

J.W. Spence and *J.N. McHenry*: Development of regional corrosion maps for galvanized steel by linking the RADM engineering model with an atmospheric corrosion model, 3033-3046.

J.F. Hopper, D.E. Worthy, L.A. Barrie and *N.B.A. Trivett*: Atmospheric observations of aerosol black carbon, carbon dioxide, and methane in the high Arctic, 3047-3054.

Volume 28 Number 19 1994

B.J. Turpin, J.J. Huntzicker and *S.V. Hering*: Investigation of organic aerosol sampling artifacts in the Los Angeles basin, 3061-3071.

R.W. Simpson and *Hongchang Xu*: Atmospheric lead pollution in an urban area—Brisbane, Australia, 3073-3082.

V. Subramanyam, K.T. Valsaraj, L.J. Thibodeaux and *D.D. Reible*: Gas-to-particle partitioning of polycyclic aromatic hydrocarbons in an urban atmosphere, 3083-3091.

D.J. Moschandreas and *P.E. Chang*: On the use of a risk ladder: linking public perception of risks associated with indoor air with cognitive elements and attitudes toward risk reduction, 3093-3098.

D.J. Wilson and *B.K. Lamb*: Dispersion of exhaust gases from roof-level stacks and vents on a laboratory building, 3099-3111.

P. Goyal, M.P. Singh and *T.K. Bandyopadhyay*: Environmental studies of SO_2, SPM and NO_x over Agra, with various methods of treating calms, 3113-3123.

Yu-Mei Kuo and *Chih-Shan Li*: Seasonal fungus prevalance inside and outside of domestic environments in the subtropical climate, 3125-3130.

J.K. Mishra, R. Aarathi and *M.D. Joshi*: Remote sensing quantification and change detection of natural resources over Delhi, 3131-3137.

Chih-Shan Li: Elemental composition of residental indoor PM10 in the urban atmosphere of Taipei, 3139-3144.

L.T. Khemani, G.A. Momin, P.S.P. Rao, A.G. Pillai, P.D. Safai, K. Mohan and *M.G. Rao*: Atmospheric pollutants and their influence on acidification of rain water at an industrial location on the west coast of India, 3145-3154.

G. Lorenzini, C. Nali and *A. Panicucci*: Surface ozone in Pisa (Italy): a six-year study, 3155-3164.

O. Massambani and *F. Andrade*: Seasonal behavior of tropospheric ozone in the Sao Paulo (Brazil) Metropolitan Area, 3165-3169.

N. Mikac and *M. Branica*: Wet deposition of ionic alkylleads and total lead in urban areas of Croatia, 3171-3179.

J.G. Kretzschmar: Particulate matter levels and trends in Mexico City, Sao Paulo, Buenos Aires and Rio de Janeiro, 3181-3191.